OPTICAL POINTING SYSTEM

FOR STRATOSPHERIC

BALLOON-BORNE MULTI-SLIT

OSIRIS-DM

A Thesis

Submitted to the College of Graduate Studies and Research

In Partial Fulfillment of the Requirements

For the Degree of

Master of Science

In the Department of Physics and Engineering Physics

By

Matthew N. Kozun

Saskatoon, Saskatchewan

Permission to Use

In presenting this thesis in partial fulfilment of the requirements for a Postgraduate degree from the University of Saskatchewan, I agree that the Libraries of this University may make it freely available for inspection. I further agree that permission for copying of this thesis in any manner, in whole or in part, for scholarly purposes may be granted by the professor or professors who supervised my thesis work or, in their absence, by the Head of the Department or the Dean of the College in which my thesis work was done. It is understood that any copying or publication or use of this thesis or parts thereof for financial gain shall not be allowed without my written permission. It is also understood that due recognition shall be given to me and to the University of Saskatchewan in any scholarly use which may be made of any material in my thesis.

Requests for permission to copy or to make other use of material in this thesis in whole or part should be addressed to:

Head of the Department of Physics and Engineering Physics

116 Science Place

University of Saskatchewan

Saskatoon, Saskatchewan

Canada

S7N 5E2

ABSTRACT

The Optical Spectrograph and InfraRed Imaging System (OSIRIS) satellite instrument spearheaded by a team of researchers at the University of Saskatchewan has provided scientists with 13 years of information about the state of the atmosphere. The success of the mission has motivated further development of the technology in a next generation instrument called the Canadian Atmospheric Tomography System (CATS) to provide better spatial and spectral resolution through a successive satellite mission.

This work details the development of a proof-of-concept prototype built to test the validity of the CATS optical design. This thesis project utilized the developmental model built for the OSIRIS mission. The major modification made to the instrument replaced the optical element that defines the instrument's field of view. This new development transformed the original single line of sight utilized by the satellite based OSIRIS instrument into three separate fields of view, which increased the imaging capabilities of the instrument. The new system has improved spatial resolution by collecting spectral information from three separate regions in the atmosphere in a single exposure, as opposed to the single region imaged by the original system.

The newly developed prototype was tested on the platform of a stratospheric balloon. This test platform offered the capabilities to make limb scattered measurements similar to those that are made by a satellite based instrument. However, from the balloon geometry, the instrument required an additional pointing system to redirect the line of sight over stratospheric tangent altitudes. The design and test of this pointing system is also detailed in this work.

ACKNOWLEDGMENTS

This project was made possible through funding from the Canadian Space Agency through the FAST initiative. Additional financial support was supplied by the University of Saskatchewan and the Institute of Space and Atmospheric Studies.

I would like to extend my extreme gratitude to my supervisors, Doug Degenstein and Adam Bourassa. Their care and dedication to my work throughout this project has been incredible, and it has motivated further pursuits in the field of Atmospheric Physics. I would also like to thank Paul Loewen for helping me take my designs and turn them into reality. In addition to this, I'd like to thank Nick Lloyd for always helping me see where these realities could use some modifications. My other office mates were also a great asset throughout this work. In particular, Barrett Taylor has been a great office mate, lab mate, travel mate and most of all, a great friend.

I could not have completed this project without the guidance and skills of Ted Toporowski, Blair Chomyshen and Jill Cornish in the Physics Machine Shop. In addition to this, the knowledge and assistance of Sandy Beaton, Ashley McColgan and Craig Haley of COM DEV were assets to building this system. The teams involved in the Timmins Stratospheric Balloon Base made up of CSA and CNES representatives also helped make this project a success.

Lastly, I'd like to thank my family and friends for their never ending support throughout my work.

To my family: Merle, Lorrie and Breann Kozun

Do you wanna know what?

TABLE OF CONTENTS

page

LIST OF TABLES

LIST OF FIGURES

Figure page

LIST OF ABBREVIATIONS

CAD	Computer Aided Design
CATS	Canadian Atmospheric Tomography System
CCD	Charge Coupled Device
CNES	Centre national d'études spatiales
CSA	Canadian Space Agency
DC	Direct Current
DN	Digital Number
FOP	Field-Flattener/Order Sorter/Prism
MART	Multiplicative Algebraic Reconstruction Technique
OSIRIS	Optical Spectrograph and InfraRed Imaging System
OSIRIS-DM	OSIRIS Developmental Model
OSIRIS-FM	OSIRIS Flight Model
SAGE	Stratospheric Aerosol and Gas Experiment
SBB	Stratospheric Balloon Base
TOMS	Total Ozone Mapping Spectrometer

1. INTRODUCTION

The Earth's atmosphere is in an ever changing state of photochemical processes. These processes involve the absorption, transmission and scattering of sunlight in the atmosphere. The concentrations of various atmospheric species depend upon numerous factors such as altitude, geographic location and the amount of light interacting with the region based on the time of day. The absorption and scattering of the solar spectrum can be used to study the composition of the atmosphere. Different constituents of the atmosphere affect the passage of specific wavelengths through it. Therefore, by measuring the light as it interacts with the atmosphere, the composition can be inferred through a variety of modelling techniques. Ozone concentrations for instance can be measured by observing the absorption of light in the Hartley-Huggins band which absorbs wavelengths between 200 to 325 nm, or the Chappuis band from 500 to 700 nm (*Roth*, 2007). Although measurements of ozone can be made from ground based platforms, they are limited to the area where the instrument is set up, and therefore can only cover a finite region of the atmosphere around that position. Remote sensing from a space craft however provides global coverage and allows for robust retrieval of vertical profile information about the atmosphere.

The legacy of satellite based remote sensing instruments spans over 50 years, with numerous Earth orbiting satellite based instruments making measurements of the regions below. These instruments provide global coverage of the processes that take place both on the surface of the Earth and its oceans, as well as in the atmosphere. With regard to atmospheric measurements, the primary viewing geometry implemented in the early days of satellite measurements was nadir based viewing, which sets the field of view directly downward from the satellite platform. This viewing geometry provides very good global coverage, but relatively poor vertical resolution of measurements within the atmosphere. The Total Ozone Mapping Spectrometer (TOMS) is an instrument that uses the nadir viewing geometry (*McPeters et al*., 1998). TOMS provides high

horizontal resolution measurements of the total amount of ozone in a column of the atmosphere. It yields very good global coverage, but has only very course resolution of the vertical profile of the ozone column.

Solar occultation is a second viewing geometry utilized by satellite instruments, which images the sun directly as it either rises or sets through the atmosphere during the course of an orbit. This provides high resolution vertical measurements of the different layers of the atmosphere that the sunlight penetrates during the measurements. The downfall of this viewing geometry is that only two measurements can be made per orbit, and therefore the global coverage suffers. Lunar occultation is a similar method that measures the direct line of sight aimed towards the moon. Examples of a solar/lunar occultation instruments are the Stratospheric Aerosol and Gas Experiment (SAGE) instruments (*Thomason et al*., 1997).

A compliment found between these two viewing geometries is the limb scattering geometry. For this, instruments view sideways through the illuminated atmosphere. By scanning the field of view in this region, vertical resolution of the atmosphere can be obtained. Additionally, because these measurements do not require the rising or setting of the sun through the atmosphere, they can be performed throughout the entire illuminated part of the satellite orbit. Therefore, limb scattering viewing geometry has increased vertical resolution and global coverage when compared to the previous two geometries. With this viewing geometry however comes the tradeoff of more complicated data analysis as a result of the multiple scattering events that can occur within a single measurement. The Optical Spectrograph and InfraRed Imaging System (OSIRIS) is an example of an instrument that utilizes the limb scattering geometry (*Llewellyn et al.*, 2004).

The OSIRIS instrument on board the Odin satellite is a Canadian remote sensing mission with strong ties to the University of Saskatchewan. The instrument was built through collaboration of a team from the University, the Canadian Space Agency, and the Canadian space industry. The project was originally spearheaded by Dr. E.J. (Ted) Llewellyn, who has since passed the reigns of Principal Investigator to Dr. Doug Degenstein and Dr. Adam Bourassa (Deputy). Along with a dedicated team of researchers, this project has provided 13 years of global coverage of atmospheric data that can be used to better understand the composition and processes that occur in the atmosphere. The success of the mission has brought about discussions of a successor to the instrument, which will build upon the OSIRIS legacy.

A new instrument now under study at the Canadian Space Agency, known as the Canadian Atmospheric Tomography System (CATS), will have a similar optical design to the OSIRIS instrument but will result in greater spatial and temporal resolution in the measurements made. This will be achieved by making modifications to the slit plate within the instrument, which defines the field of view, and through improvements made to the detector and optical technology.

As part of this thesis project, the developmental model built for the OSIRIS mission was modified to include a slit plate similar to the one proposed for CATS to better understand the system operation from an optical performance point of view. The developmental model of OSIRIS is the predecessor of the OSIRIS flight model which is currently in orbit. The validity of the new system was tested on board a stratospheric balloon, with a custom optical pointing system, designed and tested as part of this work, to verify the operation of the instrument in the limb scattering geometry.

Further detail will be given in Chapter 2 about the OSIRIS mission and the developmental model which was used. It also highlights how SASKTRAN, a radiative transfer model developed

at the University of Saskatchewan as part of the OSIRIS project, can be utilized to analyze the data that is currently being collected by the OSIRIS instrument, and explain how it is used both to help design the new prototype system as well as analyze the data that was collected during the balloon mission.

The design and analysis of the new slit plate is examined in Chapter 3. First, a detailed analysis of the original slit plate in the OSIRIS instrument is examined using optical ray tracing software to better understand the operation of the optical system within the instrument. The same software is then used to analyze the effects of a new slit geometry on the slit plate to verify the internal operations of the instrument. The replacement of the slit plate is also examined, and then the modified system is analyzed. Chapter 4 details the design process required to ready the instrument to be launched on a stratospheric balloon. The key component to this process was building a system that redirects the line of sight of the instrument to cover stratospheric tangent attitudes when it is mounted on the gondola and floating at an altitude of 36 km. Additional constraints are also resolved. These primarily revolve around ensuring high quality images are collected on the Charge Coupled Device (CCD) with respect to exposure times and reduction of any smearing effects caused by the multiple fields of view that are imaged by the multi-slit system.

Chapter 5 details the stratospheric balloon mission for the instrument. The performance of the different systems and their operation from a balloon is analyzed. The data collected during the mission is validated through comparison to the SASKTRAN radiative transfer model. Finally, an ozone retrieval from the balloon flight spectra is performed and compared to nearly coincident ozone profiles measured by the OSIRIS instrument from orbit on board the Odin satellite.

Chapter 6 summarizes the effectiveness of the new optical system, and analyzes the overall success of the balloon mission, as well as highlights future work that to be done on this project.

2. BACKGROUND

This project was focused on modifications made to the developmental model of the OSIRIS instrument, which will be explained in the following section. A number of modelling tools were used to analyze and design the new prototype system. These included optical, mechanical and radiative transfer modelling software, which were used extensively throughout this project. These tools are also discussed in the following sections.

2.1 OSIRIS Instrument

OSIRIS is a Canadian built instrument designed to measure scattered sunlight in the upper troposphere and lower stratosphere. The instrument was built by Routes AstroEngineering Ltd., which has since been purchased by COM DEV International Ltd. Some members of the engineering team that built the original system are currently working for COM DEV. The instrument was designed in part by Dr. Llewellyn of the University of Saskatchewan, who was also the first Principal Investigator on the project.

As the name suggests, the instrument is composed of two main systems. The InfraRed Imaging System is a three channel infrared telescope designed to measure vertical profiles of atmospheric limb emissions in the near infrared. This system will not be discussed in this work. The Optical Spectrograph system is a single line of sight spectrograph that covers a wavelength range from 280 - 800 nm. The system utilizes a folded optical system that features a diffraction grating to spectrally disperse the incoming light. Further description of the instrument operation will be given in a Chapter 3.

The OSIRIS instrument was designed to make measurements on board the Swedish satellite Odin. The orbit of the satellite is 600 km above the Earth. In anticipation of the satellite mission, a developmental model (DM) of the instrument was built in the mid to late 1990's. This developmental model is referred to as OSIRIS-DM. OSIRIS-DM was built as a proof-of-

performance model before building the flight model (FM), which will be referred to as OSIRIS-FM in this work. As a result, the OSIRIS-FM is almost an exact replica of OSIRIS-DM, therefore, the optical elements have all been sized for operation on a satellite. Specifically, this impacts the instruments field of view. The developmental model was intended for lab based testing only, and was never expected to go on board the satellite, nor on board a stratospheric balloon.

OSIRIS-FM was launched on February 20th, 2001 (*Murtagh et al*., 2002). Shortly after launch, the instrument started making atmospheric measurements. The instrument was designed to last for a minimum of two years. The OSIRIS-FM system on board Odin is still operational to date. It has provided global coverage of the state of the atmosphere for more than 13 years. In this time, extensive work has been performed on refining techniques to retrieve profiles of atmospheric species concentrations from the data measured by the instrument. One specific species that has been focused on over this period is ozone. Ozone has been a hot topic with regards to atmospheric trends, and therefore concentrated efforts have been put forth to retrieve highly accurate profiles from the OSIRIS-FM measurements.

After the OSIRIS-DM was used in the lab to validate the operation of the systems and the OSIRIS-FM was launched, the developmental model was transported to the University of Saskatchewan. The system came with the required ground support equipment to be fully operational in a lab setting. It has since been used for two projects, which were centered on making ground based measurements of the atmosphere from the roof-top of the Physics building at the U of S (*Wilcox*, 2002 and *Stoicesu*, 2006). The instrument was used in this thesis project in an all-new capacity. The internal optical system was modified, from having a single field of view

to having multiple fields, and the system was tested in the limb scatter geometry using a stratospheric balloon based experiment.

2.2 Limb Scattering Geometry

A variety of viewing geometries are available for measuring scattered sunlight in the Earth's atmosphere. The simplest example of this is ground-based measurements with the instrument looking upwards into the atmosphere to collect light that is scattered into the line of sight of the instrument. With regards to remote sensing from a satellite, the compliment to the ground based viewing geometry is the nadir geometry, which implements a downward look direction towards the Earth. A second viewing geometry, known as occultation, involves the instrument directly imaging either the sun or the moon. In addition to these, the limb scattering geometry can be implemented from remote airborne platforms, as shown in Figure 2.1. This is the viewing geometry utilized by OSIRIS-FM on Odin.

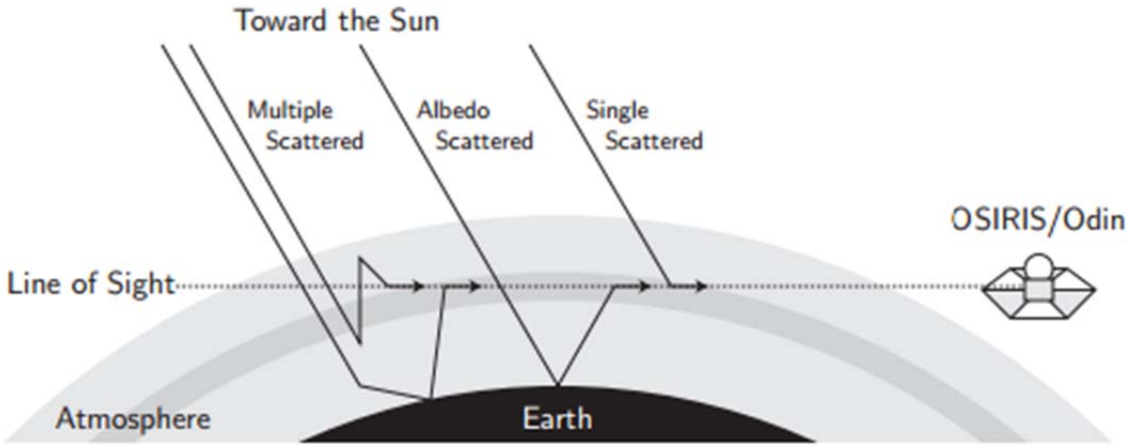

Figure 2.1: Limb scattering geometry implemented by OSIRIS-FM on the Odin satellite. Multiple scattering events are shown. Adapted from *Bourassa* (2007).

Figure 2.1 shows the OSIRIS-FM onboard the Odin satellite in orbit above the surface of the Earth. The line of sight in the image indicates the direction that the field of view extends from

the aperture of the instrument. As shown, the sun is located in a direction that differs from the direct line of sight of the instrument. Therefore, there are no rays entering the system directly from the sun in this geometry. The instrument instead measures sunlight that is scattered by the atmosphere into the line of sight of the instrument. Four examples of this phenomenon are shown in Figure 2.1. In the first case, the light has entered the atmosphere from the direction of the sun, and it has been scattered by a particle in the atmosphere directly into the line of sight in the instrument. This is referred to as a single scattering event. In the second case, the light from the sun has penetrated the atmosphere all the way to the Earth. The light in this case is scattered at the surface of the Earth back upward into the atmosphere, and then scattered by a particle in the atmosphere into the line of sight of the instrument. This is defined as an albedo scattered event. In this situation, two scattering events have occurred, so this is referred to as second order scattering. Second order scattering can also occur as a result of the two instances of the first case. The light may scatter from a particle in the atmosphere, then from a second particle, which results in the ray travelling in the line of sight of the instrument. Finally, the last two examples shown display multiple order scattering events occurring. Multiple scattering events occur when any combination of the previous two examples occur. These multiple scattering events may or may not include scattering from the surface of the Earth.

As shown, a single line of sight penetrates various layers of the atmosphere, which correspond to various altitude ranges directly above the Earth. It is therefore helpful to define a single tangent altitude that is observed by any line of sight. The tangent altitude is then defined as the altitude at which the instrument line of sight is tangent to the surface of the Earth. It is also the lowest altitude along the direct line of sight.

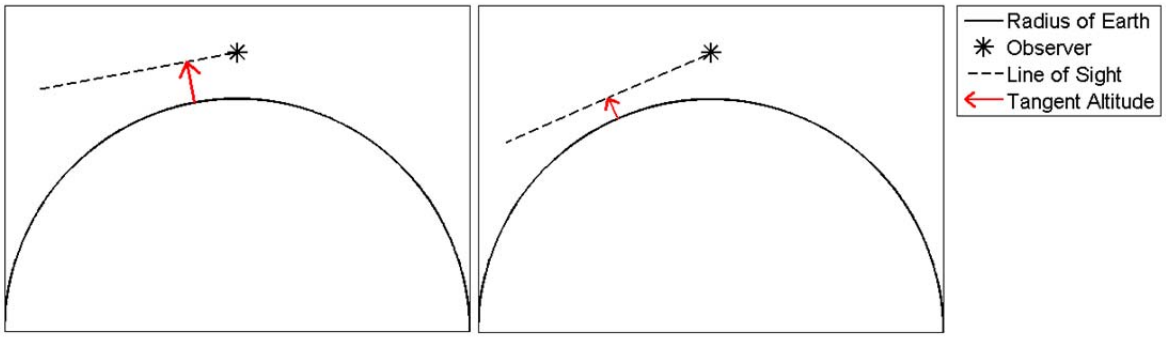

Figure 2.2: Two tangent altitudes defined by separate lines of sight from a single airborne platform.

Figure 2.2 illustrates the concept of a tangent altitude. A single point is chosen for the observer, but two lines of sight are shown. In the sketch on the left, the tangent altitude is relatively similar to the height of the observer above the Earth, whereas the sketch on the right shows a much lower tangent altitude.

Figure 2.2 demonstrates that lines of sight with lower tangent altitudes look through sections of the atmosphere that are closer to the Earth. These lower sections have higher atmospheric density, and therefore scatter more light. As a result of this, lower tangent altitudes are generally "brighter" than higher altitudes, because more light is scattered from these sections as a result of increased density.

Figure 2.1 shows that the Odin satellite is beyond the reaches of the atmosphere. However, a similar limb scattering geometry can also be achieved if the instrument is within the atmosphere, such as from a high altitude balloon or aircraft. The path length of the line of sight is however shorter within the atmosphere in this case.

2.3 SASKTRAN

SASKTRAN is a radiative transfer model used to predict optical scattering in the atmosphere for the limb scatter geometry described previously (*Bourassa*, 2007). It utilizes uniform spherical

atmospheric shells and multiple orders of scatter to determine the predicted limb scattered measurements over the optical wavelengths observed by the OSIRIS instruments.

SASKTRAN solves the radiative transfer equation

$$I(\overrightarrow{r_0}, \hat{\Omega}) = \int_{s_1}^{0} J(s, \hat{\Omega}) e^{-\tau(s,0)} ds + \tilde{I}(s_1, \hat{\Omega}) e^{-\tau(s_1,0)} \quad \text{(Eq. 2.1)}$$

which is based on an Earth centered coordinate system. In this equation, I is the observed radiance at a location, $\overrightarrow{r_0}$, in the propagation direction defined by $\hat{\Omega}$, which is a unit vector along the line of sight, s. J is the scattered source term and $\tilde{I}$ is the radiance at the end of the path. These two values have been attenuated along the path to the observer by τ, the optical depth.

The scattering source term is defined by

$$J(s, \hat{\Omega}) = k_{scat}(s) \int_{4\pi} I(s, \hat{\Omega}') \overline{p}(s, \Theta) d\Omega' \quad \text{(Eq. 2.2)}$$

where k_{scat} is the extinction value due to scattering, $\overline{p}$ is the scattering phase function, which is a function of the angle between incoming, $\hat{\Omega}'$, and outgoing, $\hat{\Omega}$, directions, which is defined as Θ.

The model solves the radiative transfer equation based on uniform shells in the atmosphere by taking into account multiple scattering events. Further details on the model can be found in in *Bourassa et al*. (2008).

The model can be used to perform inversions of spectra collected in the limb scattering geometry to retrieve atmospheric components such as ozone. This method is detailed in Chapter 5.

When using SASKTRAN, parameters must be set for the observer position and the look direction, as well as the date and time to be modelled. This sets up the geometries required between the line of sight of the instrument and the direction of light coming from the sun. This

offers the flexibility to move the observer from the satellite platform that the model is primarily used for to a ground based or balloon based viewing geometry.

SASKTRAN is used in three capacities for this work. Firstly, ground based measurements are modeled for a test scenario that was performed with the instrument positioned on the roof of the Physics building at the University of Saskatchewan. Radiance profiles are also modeled from the altitude expected for a balloon-borne measurement. These two data sets are used to determine the ratio between ground based and balloon based measurement radiances, in order to assist with the optical design for the balloon experiment. The second use of SASKTRAN is to model the spectra that are collected during the balloon mission, with location and time parameters set to match those from the mission. Finally, SASKTRAN is used in combination with a non-linear inversion technique to perform an ozone retrieval from the balloon spectra that were collected.

2.4 Canadian Atmospheric Tomography System

CATS is a proposed project by the Canadian Space Agency (CSA) to build on the legacy of OSIRIS. The instrument is currently under development by the CSA with involvement from COM DEV. This new instrument is an improvement on the optical design of OSIRIS-FM, which aims to improve the spatial and temporal resolution of collected data. This new instrument will utilize a multi-slit plate that defines multiple fields of view for the instrument (*Degenstein*, 2013). These multiple fields of view will allow the instrument to collect light from different tangent altitudes simultaneously, which will require less time to complete a single profile. Each slit will image a separate section of the atmosphere to be combined into a single overall profile.

The multi-slit plate that was installed into OSIRIS-DM as part of this thesis work was used as a proof-of-concept test for the new CATS instrument. The goal was to verify that the multiple fields of view defined by the new slit configuration could accurately image the atmosphere in the limb scattering geometry discussed previously. The data collected in this project was analyzed

and compared to that collected by OSIRIS-FM to verify operation. This project will help validate an important optical parameter for the design of the future CATS satellite instrument.

2.5 Flights for the Advancement of Science and Technology (FAST) and Timmins Stratospheric Balloon Base

FAST is a grant program facilitated by the Canadian Space Agency with aims of giving graduate students hands-on experiences with space technology on suborbital platforms (*Canadian Space Agency,* 2013a). The program recognizes the limited opportunities available for access to orbital space platforms, so it focuses on projects involving nanosatellites, sounding rockets or in the case of this project, stratospheric balloons. The CSA hopes that through this initiative, it can develop a capable workforce to maintain Canada's capacity in space science. To compliment this, the initiative also strives to develop new technologies that can be used in future CSA projects. This allows the trainees to have hands-on experience with the technologies of the future.

In the summer of 2012, the CSA announced that it would be partnering with Centre national d'études spatiales (CNES), the French space agency, to launch stratospheric balloons from a new base to be located in Timmins, Ontario (*Canadian Space Agency*, 2012). One goal of the partnership is to offer hands-on learning experience for Canadians to train the next generation of space scientists and engineers. This partnership means that the CSA has the opportunity to learn from CNES, which has had experience with more than 3500 balloon launches in the past 40 years. In September of 2013, the collaboration launched its first balloon, which completed a ten-hour flight with great success (*Canadian Space Agency*, 2013b).

2.6 Ray Tracing Software

A ray tracing software package was used to model and analyze optical systems. It was used to model the modifications made to the interior optics of OSIRIS-DM as well as to aid in the design of the external pointing system. A quick overview of some of the tools provided by the software is presented.

2.6.1 Modelling a Simple Single Lens System

The ray tracing software utilized in this thesis work can be used to easily define an optical system. The required parameters deal with the various surfaces that rays of light will interact with as they travel along the optic axis. Each optical system model begins with the same three surfaces: the object, the stop and the image. The optical system is then built by adding surfaces between these default surfaces and applying properties to each surface that will meet the properties of the optical elements intended for the system. A simple single lens system model is shown in Figure 2.3.

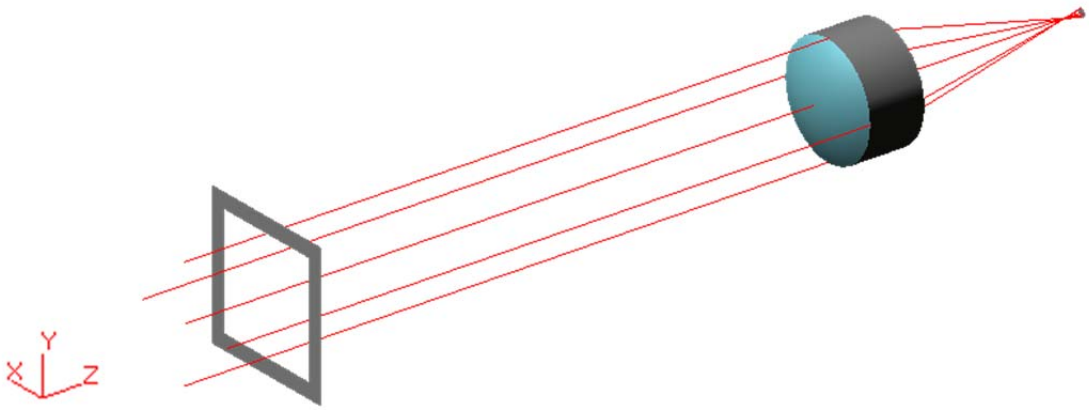

Figure 2.3: Ray trace model of simple plano-convex lens system.

In Figure 2.3, there are 5 surfaces defined. The object surface is located infinitely far away, so it is not shown in the figure. The stop surface is the square aperture shown on the left side of this image. In this software, this surface dictates which rays will pass through the system. Rays are traced such that they start before the stop, but then pass through the stop at well-defined locations. The rays then continue to be traced past the stop based on the positions which they crossed the plane of the stop. In this case, a 4 mm × 4 mm aperture is defined. The image plane is

finally shown on the far right side of the image, where the rays are finally focused for this particular system.

In the area between the stop and the image surfaces, two surfaces have been added. These two surfaces define the two surfaces of a plano-convex lens. The inputs required to build this lens are the radii of the two surfaces, the distance from one surface to the next and the material to fill between the surfaces.

2.6.2 Analysis of a Simple Single Lens System

To start, the optic axis of the system must be understood. The optic axis is the axis that each of the elements in this system is centered upon. The starting position for the optic axis is always along the z axis as it passes through the aperture stop. When an element is rotated about the incoming optic axis, which is known as a decenter, the outgoing optic axis is typically rotated in a similar fashion to exit normal to the surface. In the case of this simple system, there are no decenters and therefore the optic axis is not altered throughout the system. In Figure 2.3, the ray that passes through the center of the aperture lies along the optic axis throughout the system.

The angles of light entering the system are defined with respect to the optic axis. There are two directional angles that the user has control over, θ_x and θ_y. This is displayed in Figure 2.4.

In Figure 2.4a, two sets of rays are shown. The red rays have θ_x defined as 0°, and the green rays have θ_x defined as 5°. The angle between these two sets of rays is therefore 5°. The location where these rays intersect is the location of the aperture. Figure 2.4b shows a side view of the same system to demonstrate the effects of θ_y. In this case, the red rays have a θ_y set to 0° and the green rays have θ_y defined as 5°. Once again, the rays intersect at the aperture and the angle between the rays is 5°. When analyzing an optical system, these values can be altered to understand how the system reacts to various incoming angles of light into the system.

(a)

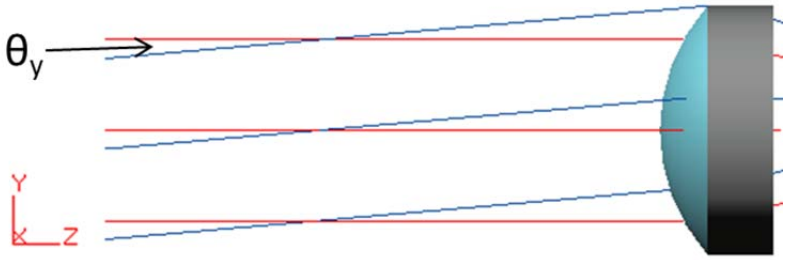

(b)

Figure 2.4: (a) Top view of lens system to show effect of changing θ_x. (b) Side view of lens system to show effect of changing θ_y.

An important tool that was used for much of the analysis for this project was the "spot diagram" feature. This tool defines a pattern of rays across the entrance aperture and traces the rays through the system to a defined surface. For analysis in this project, the pattern of rays was an equally spaced square grid, which will be referred to as a raster scan. Figure 2.5 defines the raster scan pattern used for the simple lens example, which is representative of only a single θ_x and θ_y direction.

An example spot diagram for rays entering the aperture at $\theta_x = 0°$ and $\theta_y = 0°$ with the raster scan defined previously is shown in Figure 2.6. This analysis is for the lens system shown in Figure 2.3, and the spot diagram is shown as it appears on the image plane.

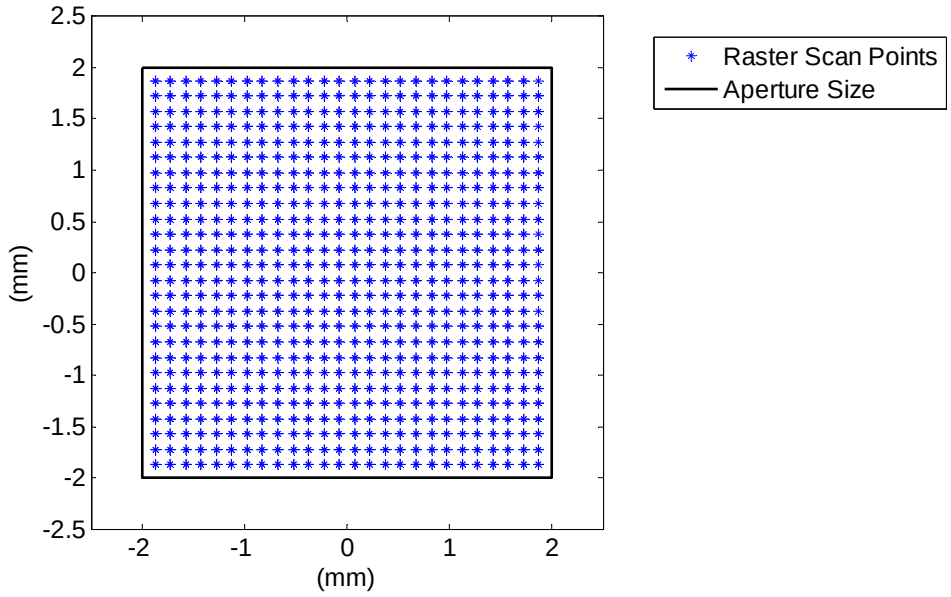

Figure 2.5: Raster scan points defined within aperture. Each point represents the intersection point of an incoming ray with the plane of the aperture.

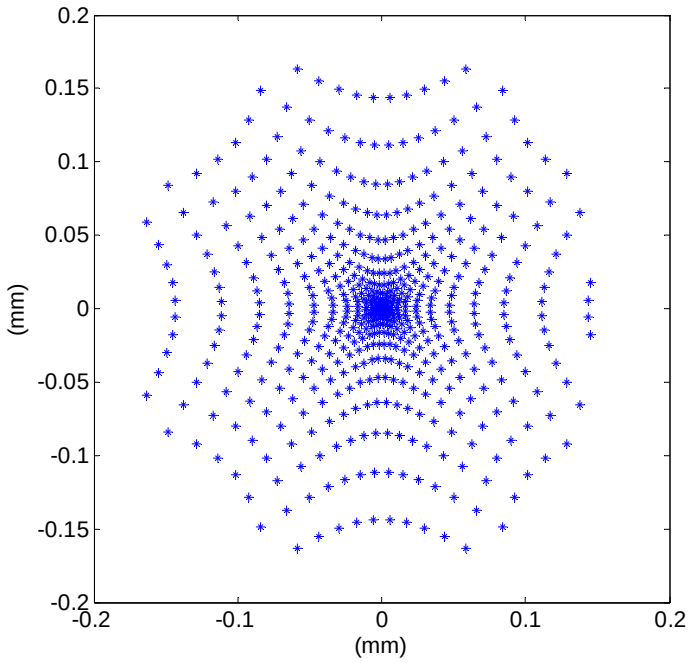

Figure 2.6: Spot diagram on image plane of simple lens system with $\theta_x = 0°$ and $\theta_y = 0°$.

In Figure 2.6, the rays that entered in a square grid have now been focused towards a single point on the image plane. Each ray has been individually traced through the lens surfaces based on their starting position in the aperture raster scan. The rays traced through the lens experienced varying amounts of refraction before finally reaching the image plane. The software takes into account all aberrations associated with the lenses modelled and therefore these aberrations are visible in the spot diagram. Examples of the aberrations that are modeled include spherical, chromatic, comatic and others. If these aberrations were ignored in the ray trace, then the entire raster scan of rays would be focused to a single point for this example.

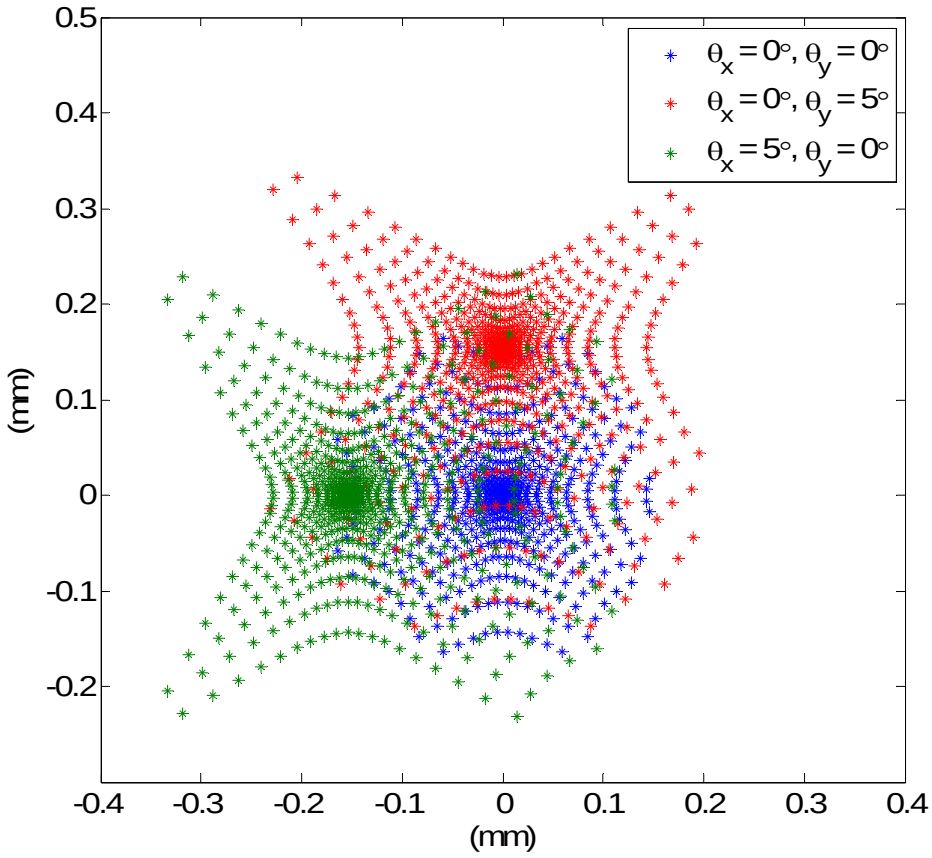

Figure 2.7: Spot diagram showing three input angles and their location on the image plane.

Now, in Figure 2.7, the image plane is shown with three different directions of incoming light. The sets of rays from a single direction will be referred to as ray bundles when they strikes the image plane. In this figure, three ray bundles are displayed, defined by the three directions that light has entered from. Each ray bundle is shown in a different color. It is shown that the ray bundle from light entering parallel to the optic axis is centered about the point (0, 0) on the image plane. The rays entering with $\theta_x = 5°$ are shown to be focused slightly to the side of the on axis rays. Similarly, the rays entering at $\theta_y = 5°$ are focused slightly above the on axis rays.

This figure helps show how the software is used to trace rays through an optical system. This is useful when analyzing OSIRIS-DM through the analysis of the new slit plate. In this case, the light only interacted with a single optical element before it was imaged. For the OSIRIS-DM instrument analysis however, the ray bundles may interact with up to 9 elements before they are finally imaged. Of these 9 elements in the OSIRIS-DM, one is a diffraction grating. The ray trace software has the capability to take wavelength into account, so it will model the effects of the diffraction grating as well as any chromatic aberrations incurred through refraction.

2.7 SolidWorks

SolidWorks is a computer-aided design (CAD) program that is used extensively for the mechanical design of this project. The working philosophy is to break a system into a number of individual, detailed parts, and then combine them into modeled assemblies. Assemblies can then be merged together to form assemblies of assemblies. With this philosophy in mind, the pointing system required for this project is broken into a number of parts and subassemblies, which combine to make the final product.

With these tools, a system was built to test the new CATS prototype. The first step towards development of the new system was to fully understand the effects of the slit plate. The original slit plate was first examined before designing the multi-slit plate for this project.

3. OSIRIS-DM MULTI-SLIT OPTICAL DESIGN

The multi-slit OSIRIS-DM system was intended as a proof-of-concept test for the CATS instrument. The OSIRIS-DM however required certain refurbishments before it could start testing the new technology CATS intends on utilizing. The first and most important modification that needed to be made to the system was to change the slit plate housed within the instrument from a plate with only a single slit, to a plate with multiple slits. This is the aspect of CATS that will provide increased vertical resolution. However, before any alterations were made, the current instrument had to be investigated to understand how the rest of the optical system performed in order to design the new multi-slit plate.

3.1 Introduction to OSIRIS-DM Ray Trace Model

OSIRIS-DM has 9 optical elements used to capture the spectra of light visible from its aperture, as described by *Warshaw et al.* (1996). These elements are shown in Figure 3.1. The light first enters through the 36 mm × 36 mm aperture (1) before reaching the objective mirror (2). The objective mirror is a 43 mm × 43 mm off axis parabolic mirror with a radius of curvature of 508.0 mm. It was manufactured by Space Optics Research Laboratories. The objective mirror is placed 260 mm from the entrance aperture and reflects the optic axis of the outgoing light at an angle of 7.88° to the incoming optic axis. As the light continues along the optic axis, it becomes focused 254 mm from the objective mirror. Before reaching this point however, it strikes the fold mirror (3) and the direction is changed. At the focal point of the objective mirror is the slit plate (4). The slit plate is used to define the field of view for the instrument, and limits the light that makes its way through the rest of the instrument. The slit plate will be discussed in further detail in Section 3.2. After the slit plate, the light strikes a second parabolic mirror located 254 mm further down the optical axis. This collimating mirror (5) is used to counteract the effects of the objective mirror. Once the light reflects off the

collimating mirror, the original incoming angles of the light are restored. In this way, the two parabolic mirrors and the slit plate have effectively limited the light passing through the entire system without disrupting the direction that the light rays were originally travelling with respect to one another.

Following the collimating mirror, light in OSIRIS-DM strikes the diffraction grating (6). This element is a first order, aspherized, blazed diffraction grating with 600 lines per mm. The grating is the element that spectrally disperses the collected light and thus is the heart of the spectrometer. Following the grating is the camera mirror (7), which focuses the spectrally dispersed light. After the camera mirror is a compound element called the Field-Flattener/Order Sorter/Prism, or more simply the FOP (8). The FOP is made up of four elements: Two plano-spherical lenses, an order sorter and total internal reflection prism. This piece is used to block unwanted higher orders of diffracted light from travelling through the rest of the instrument, and to redirect the light towards the out of plane imaging element. The out of plane imaging is a design feature that is somewhat unique to OSIRIS and was incorporated to improve its stray light rejection. This element is the charge-coupled device (CCD), which measures the resolved light (9). The CCD has an active area of 143 × 1353 pixels. The CCD is oriented such that the wavelengths are diffracted along the rows of 1353 pixels. Figure 3.1 shows the ray trace model of the OSIRIS-DM optics with rays entering the input aperture and finally landing on the CCD. This model will be extensively tested for the design of a new slit plate.

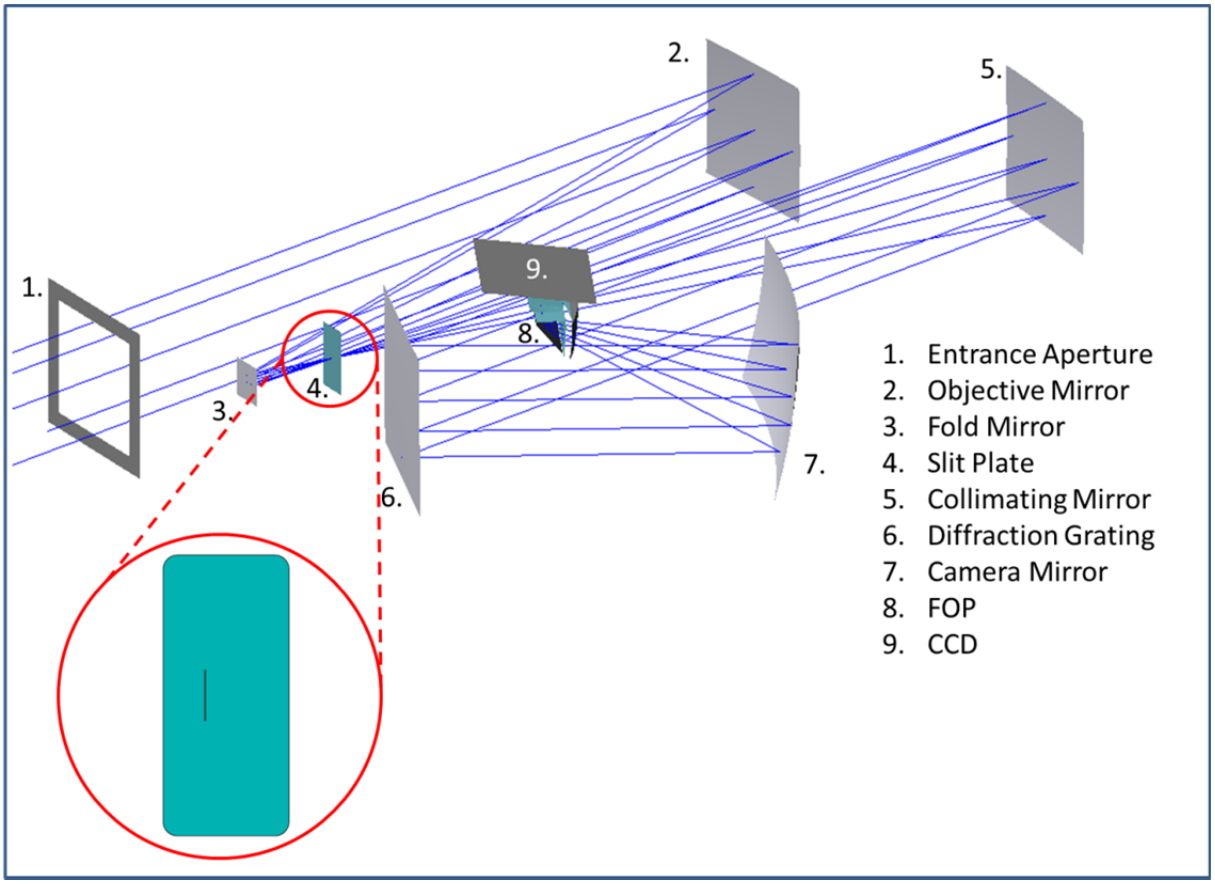

Figure 3.1: Ray trace model of OSIRIS-DM with original slit plate.

The ray trace model used in this analysis was provided by the engineers who originally built the system; therefore no additional modifications were required. The model is used strictly for analysis. The instrument, which was built from this model, has one flaw with respect to the model. The diffraction grating in OSIRIS-DM is overaspherized (*Warshaw et al.*, 1996). This causes slight differences between the modelled data that will be shown and that which is measured with OSIRIS-DM.

The original slit on the slit plate installed in OSIRIS-DM had dimensions of 90 µm × 1200 µm. The size of this slit defines an illuminated area on the CCD covering approximately 18 pixel rows as shown in Figure 3.2.

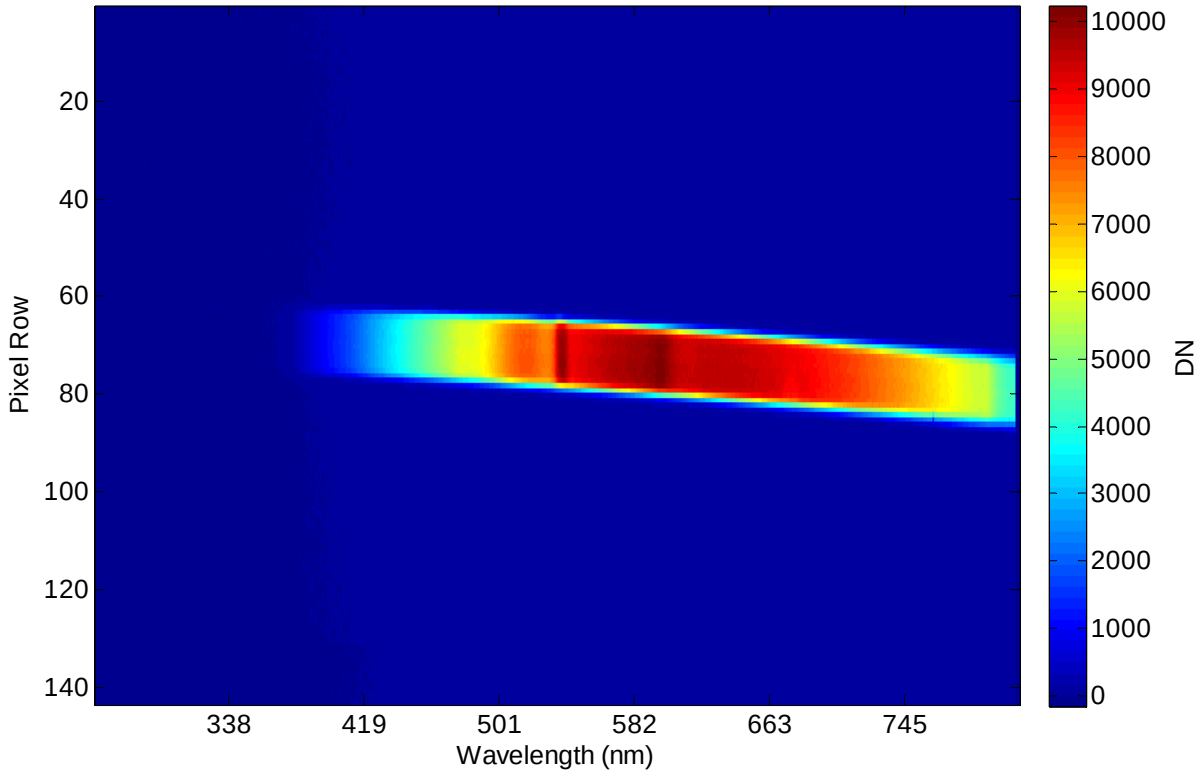

Figure 3.2: Tungsten-Halogen spectrum measured with original OSIRIS-DM slit. The color bar is in units of Digital Number (DN). The DN is proportional to the number of photons striking a pixel over a given exposure time. Single slit illuminated band of 18 pixels across CCD for all wavelengths.

Figure 3.2 displays the spectra collected from the original OSIRIS-DM using a simple Tungsten-Halogen light source at the time when this project was started. The shape of the rectangular slit is projected through the instrument until it reaches the CCD. Before reaching the CCD however, the light is dispersed by a diffraction grating, which results in a convolution of the rectangular slit projection spanning the CCD according to wavelength. The CCD converts incoming photons on each pixel into electrons, which then provides a voltage potential associated with each pixel. These pixel voltages are then converted into a digital number (DN), with 14 bit resolution. The DN, which may also be referred to as the counts on the CCD, is proportional to the number of photons striking a pixel over a given exposure time, hence the

spectral radiance. In the center of the image is the illuminated area of the CCD. The instrument is designed such that there are no light paths striking the CCD outside the illuminated area. The spectral separation is mapped to the horizontal direction on the CCD image shown; hence the pixel columns represent a narrow wavelength range. The horizontal rows define a single spectrum of light that ranges from approximately 280 nm to 800 nm. The pixel rows in the illuminated region are typically binned together to find the average spectrum imaged on the CCD. The pixel rows are also binned together to increase the signal -to-noise ratio of the instrument. The pixel row orientation is arbitrary.

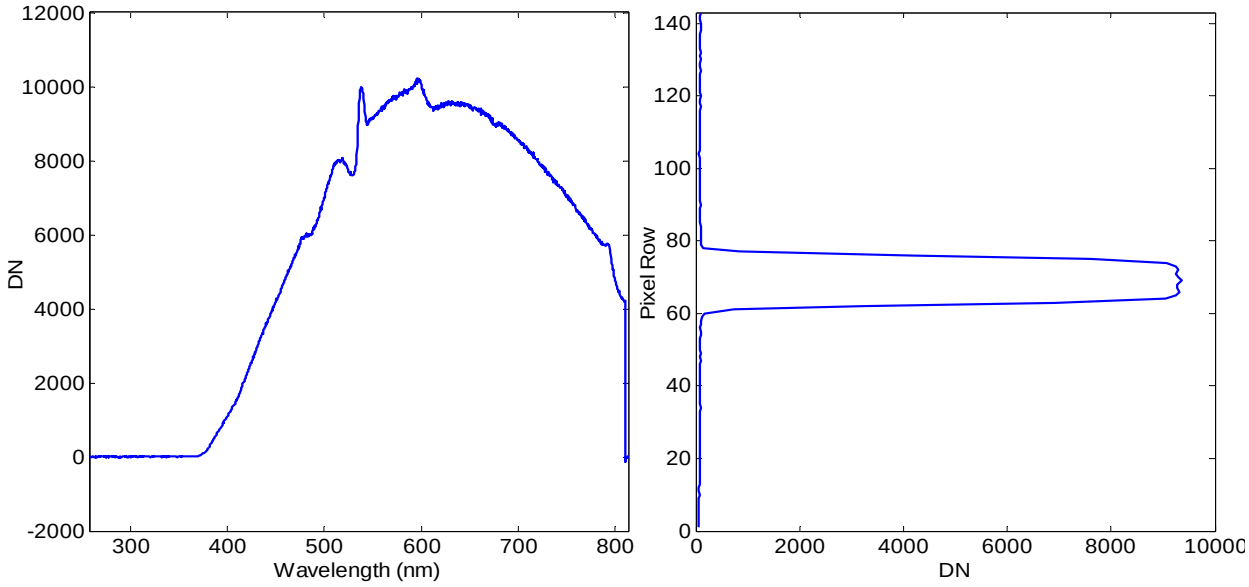

(a) (b)

Figure 3.3: (a) Horizontal cross section of Figure 3.2. (b) Vertical cross section of Figure 3.2.

Figure 3.3 shows two cross sections of the Tungsten spectrum measured by the instrument in Figure 3.2. Figure 3.3a shows a horizontal cross section, selected at row 70. This shows the blackbody curve associated with the Tungsten spectrum, with the instrument's spectral

sensitivity superimposed. An interesting feature in this figure is located between 500-550 nm. This instrument artifact is a result of the boundary of the order sorter in the FOP. As was mentioned, the pixel rows may be binned in order to better estimate the spectrum being measured. Figure 3.3b shows a vertical cross section of the Tungsten spectrum. This figure shows that the only rows illuminated lie between pixel rows 61 and 79. These are the 18 pixel rows that are illuminated by the slit in the original slit plate, as mentioned earlier. This vertical cross section was taken around 650 nm.

For this particular spectrum, a Tungsten-Halogen bulb is used to illuminate a diffusing plate. The diffusing plate is then imaged by OSIRIS-DM. The diffusing plate is an important tool for lab based measurements because it provides a uniform imaging surface with uniform light in all directions. This is important because all the angles that fill the field of view of the instrument must be illuminated. The field of view will be investigated further in Section 3.1.1.

3.1.1 Ray Tracing Analysis of Original Slit Plate

The slit within OSIRIS-DM is the optical element that determines the field of view of the instrument. Figure 3.1 shows the original slit plate in OSIRIS-DM. As shown, the slit on the plate has a finite height and width. These two dimensions translate into angular fields of view that define the system. Although the entrance aperture to OSIRIS-DM is open to the full range of angles covering 2π, only a certain range of angles, described as θ_x and θ_y, pass through the slit, while light from all other angles entering the system strikes the solid portion of the slit plate and are absorbed or reflected. Defining the field of view for the original slit plate as well as designing a new multi-slit version is the focus of this section.

The original slit was assumed to be centered about the optical axis of OSIRIS-DM. This means light entering the instrument in the same direction as the optical axis would pass straight

through the center of the slit plate unaffected. Light entering the instrument at any other angle strikes other areas of the slit plate. Off axis light is not focused to a single point on the slit plate but rather has finite spread due to aberrations. A combination of these two aspects results in a fraction of the light entering the aperture of the instrument making it past the slit plate. The vignetting effect, which will be discussed in detail in Section 3.3.1, is a result of this issue. The ray trace model is used to analyze the optical system and define its field of view. It was determined that the field of view for the original slit plate was approximately ±0.010° in the θ_x direction and ±0.134° in the θ_y direction. This is explained further with reference to Figure 3.4. Spot sizes are analyzed with regards to where they strike the slit plate in Figure 3.4a and then their location on the CCD is shown in Figure 3.4b.

Using the ray trace model shown in Figure 3.1, a raster scan of input rays across the aperture was traced through the system until it reached the plane of the slit plate. Figure 3.4a shows the location of five sets of ray bundles at the slit plate, each defined by a unique color. Each of these ray bundles represents the spot size of rays coming in at a specific angle, similar to the method described in Section 2.6. In the middle of the image, the rays that have come in along the optical axis are shown as a single point. This is because there are no spherical aberrations associated with the objective mirror, and therefore these rays get tightly focused. The four remaining ray bundles have come in at differing angles, which strike a different portion of the slit plate as mentioned earlier. These four ray bundles define the field of view for this slit. A fraction of the rays from each of these directions manage to pass through the slit plate, while most rays are blocked by the slit plate. If either directional angle is increased any further, then no rays in the ray bundle will pass through the slit. The inset in Figure 3.4a shows a zoomed view of the top right corner of the slit to show the spot size of rays defined by $\theta_x = 0.010°$ and $\theta_y = 0.134°$. This

figure displays the vignetting effect mentioned previously. Some of the rays coming in at this specific angle will pass through the slit in the lower left hand area, but the majority strike the slit plate and therefore are blocked.

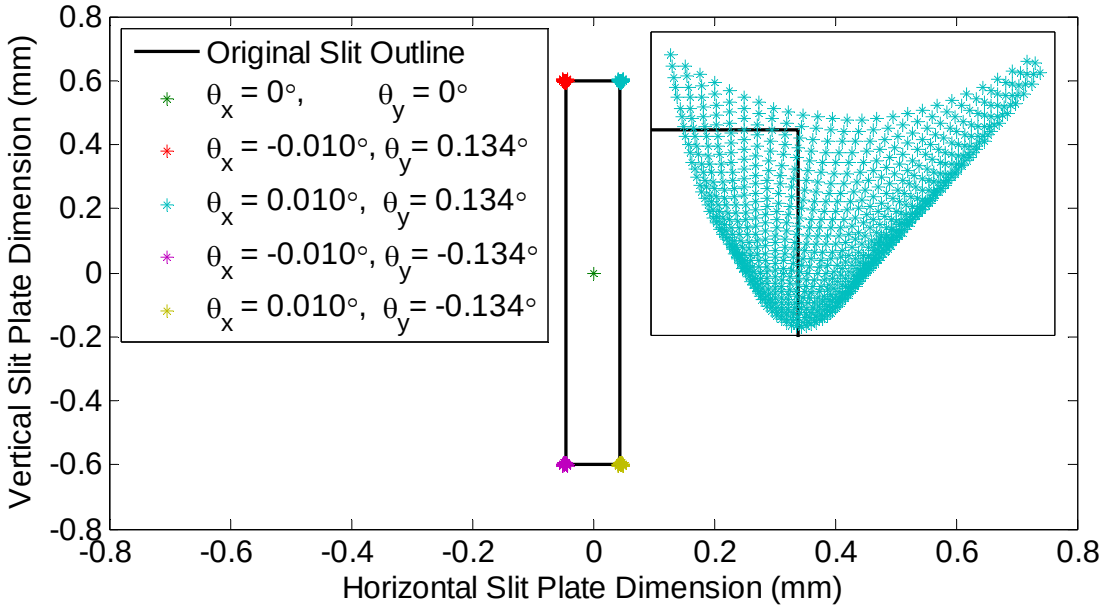

(a)

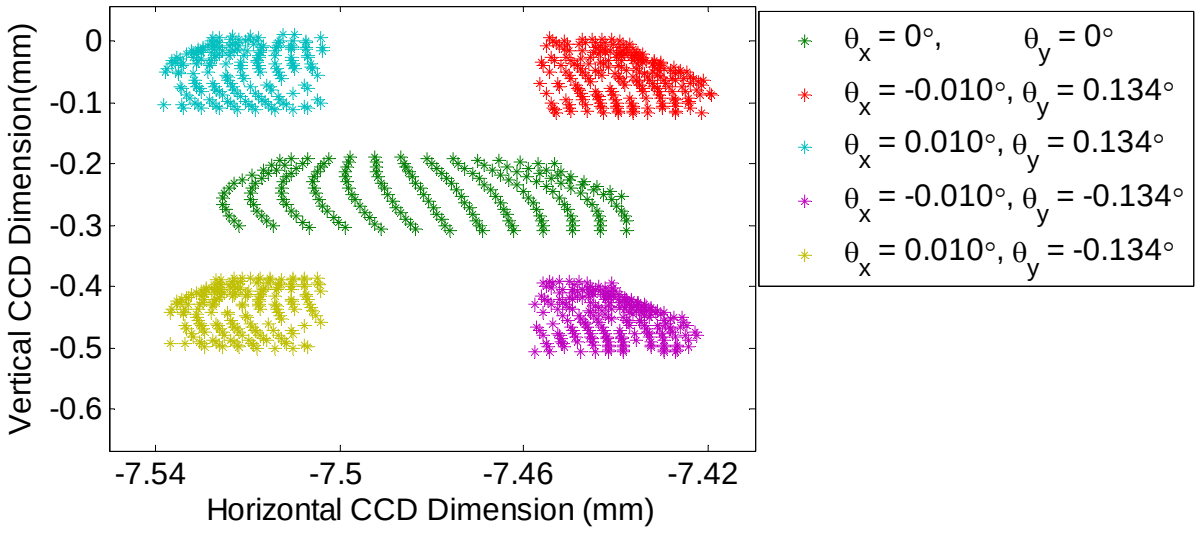

(b)

Figure 3.4: (a) Ray bundle locations on original OSIRIS-DM slit plate. Inset shows zoomed in view of original slit plate locations for rays defined by $\theta_x = 0.010°$ and $\theta_y = 0.134°$. (b) Ray bundle interactions with CCD through original OSIRIS-DM slit at 400 nm.

It is evident from this image that if light enters the system at an angle that differs greatly from the optic axis, then the rays are blocked by the slit plate. This demonstrates how the slit plate defines the field of view for the instrument; light entering within the accepted angular range will pass through the slit plate while all other light will not. This figure also demonstrates that off axis light experiences an aberration effect and therefore the ray bundles are not packed as tightly as those on the optic axis. Figure 3.4b shows the same ray bundles at the intersection with the image plane, i.e. the CCD. These points represent only the light that has passed through the opening in the slit plate. This is representative of the shape of the light as it is captured on the CCD. The rays that had the greatest θ_y deviations from the optic axis extend furthest in the vertical pixel direction on the CCD. It should also be noted that for all rays in Figure 3.4, only 400 nm light is represented.

In Figure 3.5 additional wavelengths are shown as they strike the CCD. The same spot size analysis was performed at the surface of the CCD with the same θ_x and θ_y values, but the wavelength of light was changed. Short wavelength rays all strike the CCD on the leftward side of the CCD whereas the longer wavelength rays strike the rightward side. It is also evident from this image that there is a great deal of chromatic aberration for the shorter and longer wavelengths. This results in a widening of the area captured on the CCD on the two ends of the spectrum. This widening is not an indication of more light from these wavelengths reaching the CCD; it is solely the result of imperfections in the optics within the instrument.

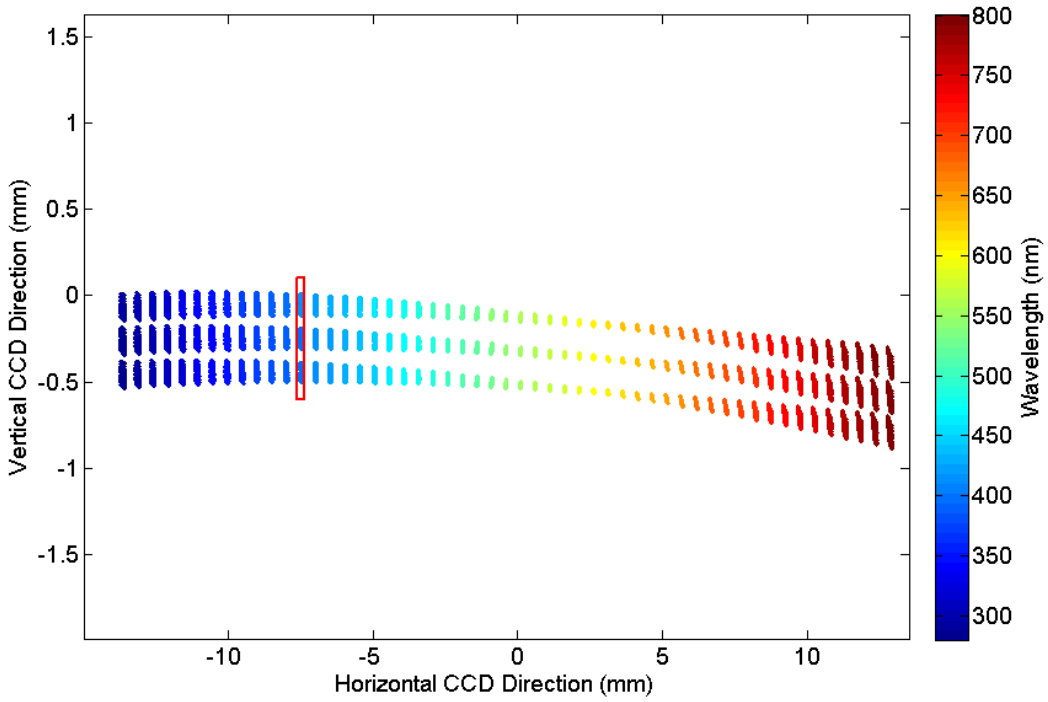

Figure 3.5: Ray trace model of various wavelengths passing through original OSIRIS-DM slit. The points representing 400 nm shown in Figure 3.4 are indicated in the red box.

In Figure 3.5, only discrete wavelengths ranging from 280 nm to 800 nm are shown in 10 nm steps. Also, only three angular directions in the θ_y dimension have been shown. This is why there are distinct bands traversing the wavelength range. The data shown in this figure represents how white light should interact with the CCD, as defined by the field of view of the original slit plate. Finally, the ray trace model is shown superimposed upon the measured spectrum of a Tungsten-Halogen bulb in Figure 3.6. This figure shows fairly good agreement between the modeled and measured data. As mentioned, it is known that the grating in the OSIRIS-DM is overaspherized by as much as 18% (*Warshaw et al.*, 1996), which is not accounted for in the ray trace model. For this reason, there are some discrepancies between the two data sets.

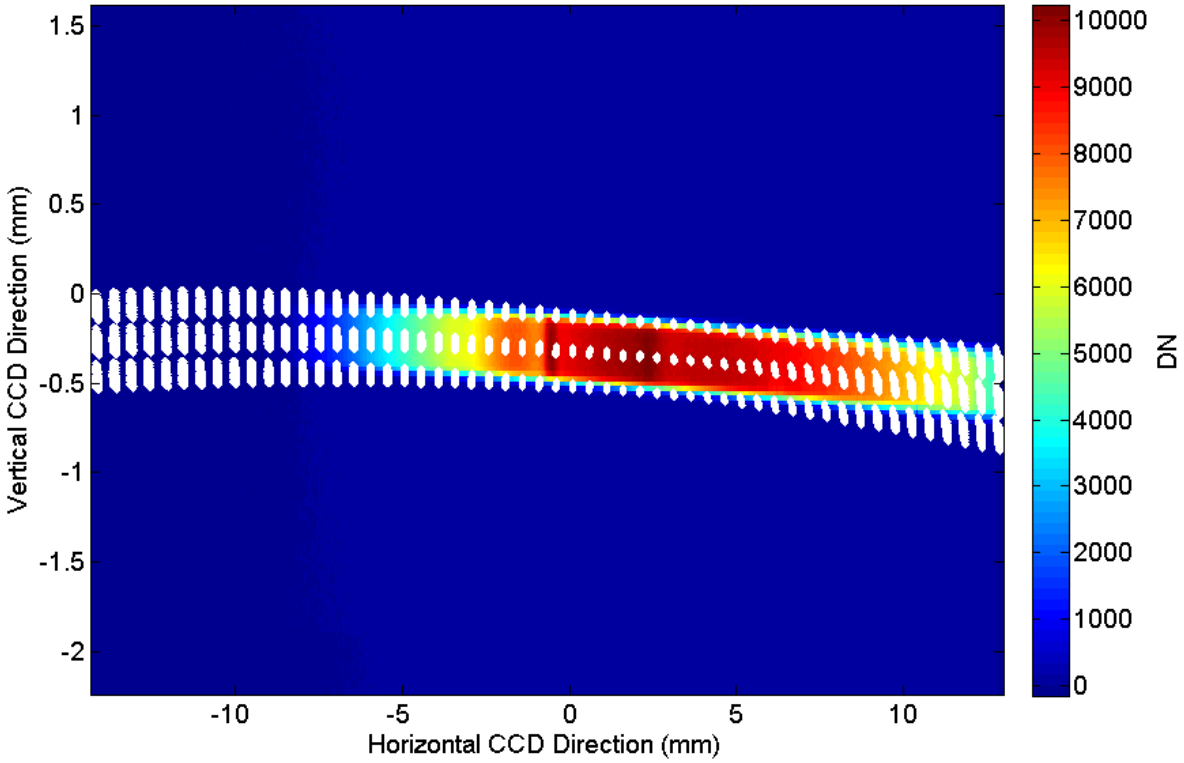

Figure 3.6: Ray trace modeled CCD positions of various wavelengths of OSIRIS-DM slit, shown in white, superimposed on Tungsten-Halogen spectrum measured with original OSIRIS-DM slit.

3.2 Discussion of Multi-Slit Design with Ray Tracing

As shown in the previous section, the objective mirror causes light entering the aperture of OSIRIS-DM to strike different regions on the slit plate. Therefore, if additional slits are added to the slit plate, multiple fields of view can be passed through the system. This is the basis for the CATS instrument.

3.2.1 New Slit Plate Revision 0

The design of the new slit plate started with the slit dimensions of the OSIRIS-FM, which are 90 µm × 3600 µm. This is larger than the original OSIRIS-DM slit plate, which had dimensions of 90 µm × 1200 µm. As a result of the larger slit length, the field of view of OSIRIS-FM is

larger than that of OSIRIS-DM. This also means that the total area illuminated on the CCD will be greater. This slit size illuminates a total of 44 pixel rows on the CCD. Figure 3.7 shows the ray trace simulation of light that would pass through the flight model slit projected onto the CCD.

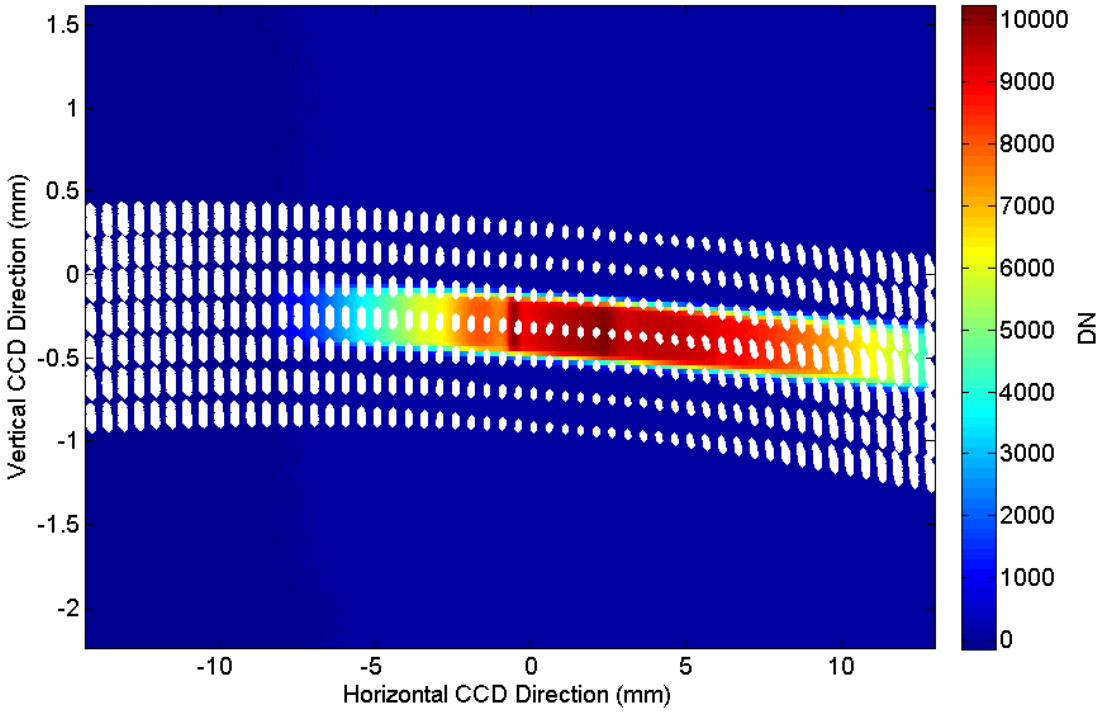

Figure 3.7: Ray trace modeled CCD positions of various wavelengths of OSIRIS-FM slit, shown in white, superimposed on Tungsten-Halogen spectrum measured with original OSIRIS-DM slit.

The first draft of the new slit plate consisted of 5 slits with dimensions of 18 µm × 500 µm. The slit heights were then adjusted to 90 µm, 72 µm, 36 µm, 18 µm and 18 µm as shown in Figure 3.8 to compensate for the variation in radiance corresponding to the variation in the angular fields of view on the atmospheric limb. In this figure, these five slits are shown with a detailed view included. Compared to the overall size of the slit plate, the slits are relatively small, hence Detail A is included to get a closer view of the slits themselves.

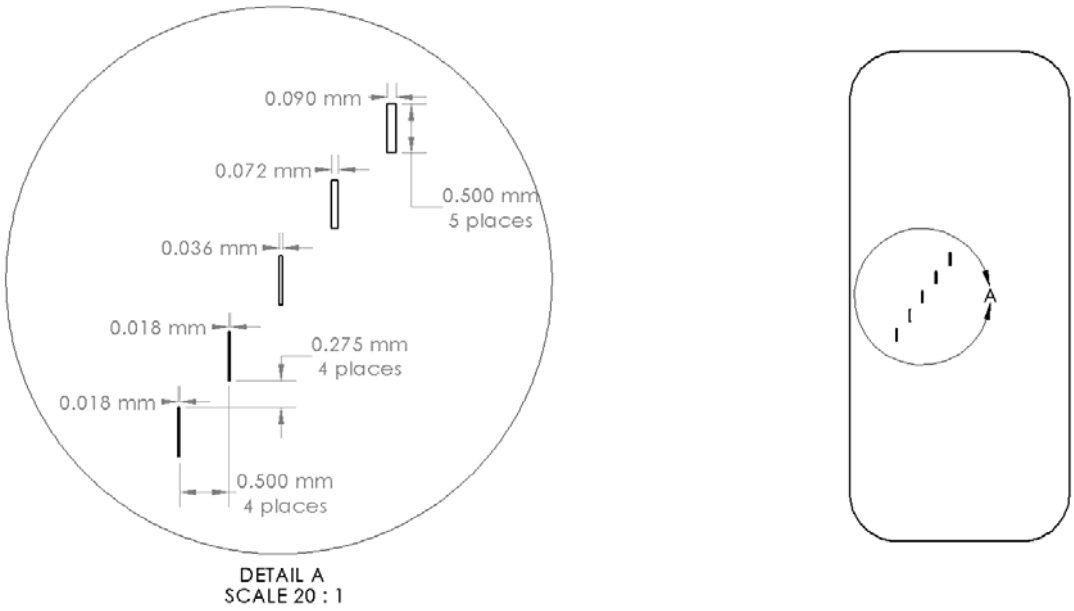

Figure 3.8: Mechanical CAD drawing of multi-slit plate rev 0.

Of the five slits in this configuration, the 90 μm slit captures light from the highest point in the atmosphere. This part of the atmosphere is dimmer than the points captured by the remaining slits, which are at lower altitudes. The variation in slit heights is designed to provide uniform illumination on the CCD when imaging various sections of the atmosphere, the radiance of which falls off with altitude roughly according to the exponentially decreasing atmospheric density. This will be addressed again in Section 3.4. The slits were separated by 275 μm in the direction aligned with the 500 μm side of the slits. This means the total size in this direction would match that of the slit in the OSIRIS-FM (500 μm × 5 + 275 μm × 4 = 3600 μm). When discussing the slit plate, the slit with the largest height will be denoted "Slit 1" and the remaining slits will follow in order of size ("Slit 2" will be the second largest height, and so on).

The diagonal pattern of the slits is very important for properly imaging different sections of the atmosphere. Figure 3.9a illustrates five slits that are arranged such that they span a large θ_y range. This is important because it is this dimension that dictates where the illuminated area from

the slits will land on the CCD. Recall that the flight model slit is 3x longer in this direction than the developmental model slit, and the flight model data covers 44 pixel rows on the CCD compared to the 18 rows covered by the developmental model. This is desirable because the slits must be separated on the CCD. The problem with this design however is that there is not much range in the θ_x direction, and thus all these slits would image the same altitude when projected onto the atmosphere. In Figure 3.9b, this has been adjusted so that the θ_x range is expanded, and thus multiple altitudes are measured, but now the θ_y dimension has been reduced. As a result of this, the image on the CCD would only cover a narrow band of pixel rows, and therefore all the data from the different altitudes would be mixed together within these rows. The solution to this issue is simply to put the slits on a diagonal, as shown in Figure 3.9c. This will allow imaging of different altitudes while keeping the illuminated areas separated on the CCD. The trade-off involved in this is that the wavelengths will have an offset in pixel columns on the CCD, which will be shown later. A more thorough discussion of the slit plate with respect to the projection area in the atmosphere will be provided in Section 3.4.

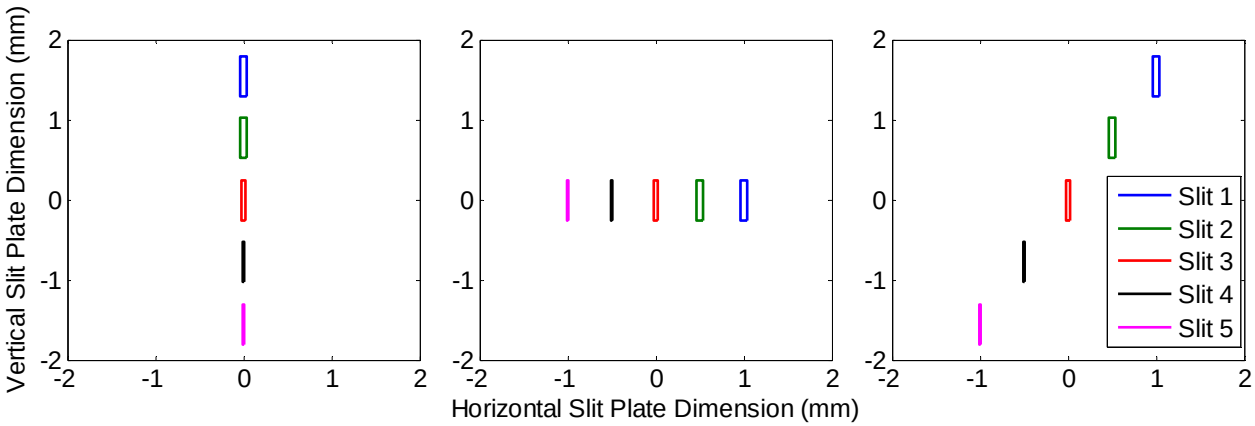

(a) (b) (c)

Figure 3.9: (a) Multi-slit plate drawn with appropriate vertical spacing. (b) Multi-slit plate drawn with appropriate horizontal spacing. (c) Multi-slit plate drawn with appropriate vertical and horizontal spacing.

The new slit plate is now analyzed. The first step is to define the new fields of view that each of these slits defined. This was once again done by determining the range of angles that would allow some portion of the ray bundles pass through the slit plate as they travel through the instrument. These fields of view are listed in Table 3.1

Table 3.1: Fields of view defined by multi-slit plate rev 0.

	Vertical Field of View	Horizontal Field of View
Slit 1	$0.210° \leq \theta_x \leq 0.230°$	$0.290° \leq \theta_y \leq 0.400°$
Slit 2	$0.100° \leq \theta_x \leq 0.120°$	$0.120° \leq \theta_y \leq 0.230°$
Slit 3	$-0.005° \leq \theta_x \leq 0.005°$	$-0.060° \leq \theta_y \leq 0.060°$
Slit 4	$-0.115° \leq \theta_x \leq -0.105°$	$-0.230° \leq \theta_y \leq -0.120°$
Slit 5	$-0.225° \leq \theta_x \leq -0.215°$	$-0.400° \leq \theta_y \leq -0.290°$

In Figure 3.10a, ray bundles from angles within the acceptance range for each slit are shown as they strike the slit plate. The ray bundles plotted represent the light entering the system at each extreme value that still allows light to pass through a certain slit. For example, the four ray bundles plotted in blue around Slit 1 represent the four combinations that are obtained by combining maximum and minimum θ_x and θ_y values for this slit. It is shown that the largest amounts of aberrations are present in the rays passing through Slits 1 and 5 because these are furthest from the optic axis. This is because the spot sizes for rays striking these slits are larger than those striking closer to the optic axis. These rays are then traced further through the system until they reach the CCD, where the respective spot sizes are shown in Figure 3.10b.

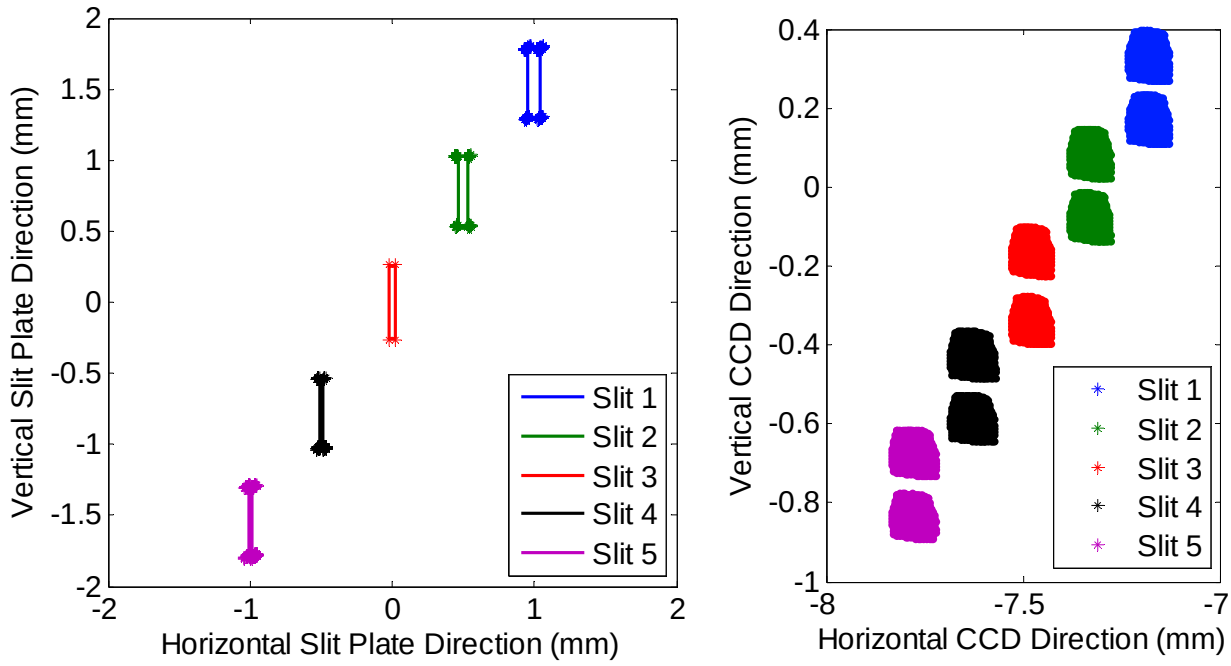

(a) (b)

Figure 3.10: (a) Ray bundle striking multi-slit plate rev 0. (b) Ray bundle striking CCD through multi-slit plate rev 0 at 400 nm.

In the Figure 3.10, only rays at 400 nm have been shown. The locations of ray bundles on the slit plate are only functions of input angle and have no dependence on wavelength, however the locations that the rays land on the CCD are dependent upon both. Note that for a single wavelength, the pixels are not stacked upon one another in a single pixel row, but rather experience an offset. This is due to the diagonal pattern of the slits. Now, multiple wavelengths striking the CCD are shown in Figure 3.11.

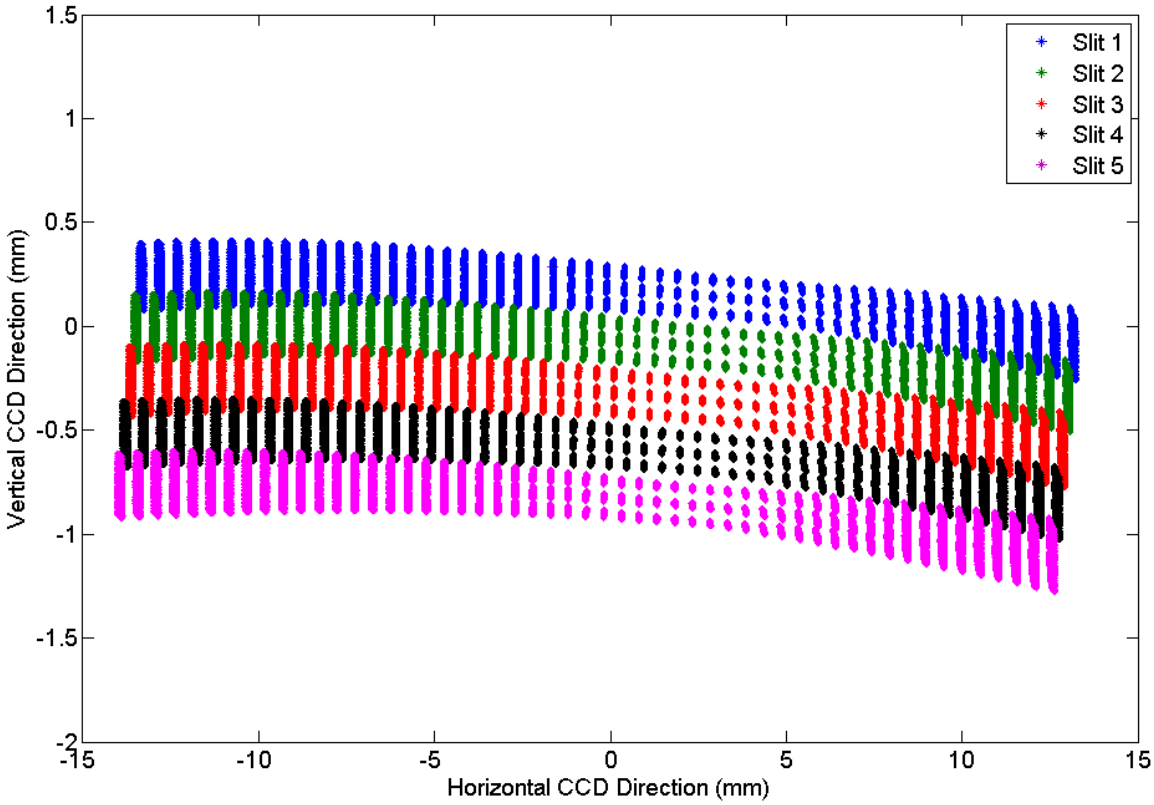

Figure 3.11: Ray trace model of various wavelengths passing through multi-slit plate rev 0.

As shown in Figure 3.11, the area on the CCD covered by the new slit pattern is similar to the area shown to be covered by the flight model slit in Figure 3.7. This is an expected feature because the full length of the flight model slit is equal to the sum of the lengths of all 5 slits in the multi-slit system plus the spacing between in this direction. There is however a definite overlap of light reaching the CCD coming from different slits on the high and low end of the collected spectrum, due to chromatic aberrations within the instrument. This is an undesirable result because the slits must be separated in order to determine which slit the light has passed through and hence, which direction the light was travelling.

As shown in Figure 3.4, the spacing in the horizontal direction on the CCD was determined by the spacing in the horizontal dimension of the slit plate. Therefore, in order to separate the spectra on the CCD, the spacing between the slits must be extended.

3.2.2 New Slit Plate Final Revision

The slit plate underwent revisions to accommodate the separation required on the slit plate. The first revision made was to extend the slits to have 1 mm spacing between the slits, which would provide a separation of approximately 5 pixels on the CCD. In this revision, the slits span 6.5mm.However, the aperture of the assembly that would hold the slit plate is 5.33 mm in the vertical direction and 6.35 mm in the horizontal direction. This means the slits would experience a clipping effect. The slit plate assembly is shown in Figure 3.12.

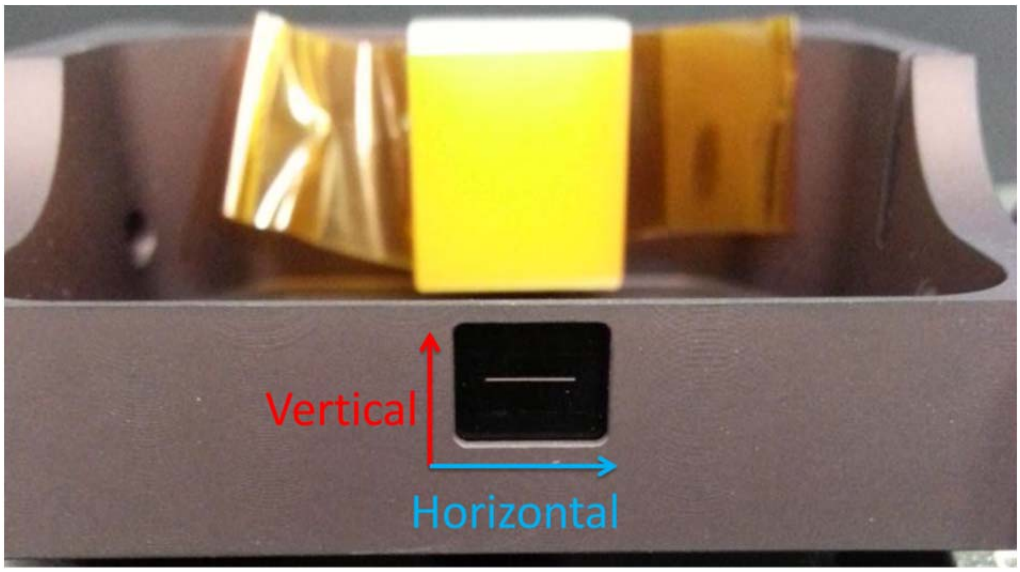

Figure 3.12: Slit plate assembly with open aperture measuring 5.33 mm by 6.35 mm.

A sample flight model slit plate is shown in Figure 3.12 installed in the slit assembly. This is the dark black rectangle with the white line across it. The slit plate is mounted to the reverse side of the slit assembly. As shown in the picture, only a rectangular section of the slit plate is visible

through the slit plate assembly, defined by the aperture mentioned. This rectangle in the assembly is the limiting factor on the multi-slit dimensions.

The two options presented to alleviate this problem were to either shorten each slit to 0.3 mm or to remove the second 18 μm slit. It was decided that the safest solution was to eliminate the slit all together but keep the rest of the sizing the same. The small repercussion associated with this decision is that there could no longer be a slit aligned along the optic axis, which results in additional vignetting associated with each slit due to defocussing of the spot size of rays as they strike the slit plate. This vignetting will play the most significant effect in light interacting with the slit plate furthest from the optic axis. The finalized slit plate design is shown in Figure 3.13, which is referred to as revision 2.

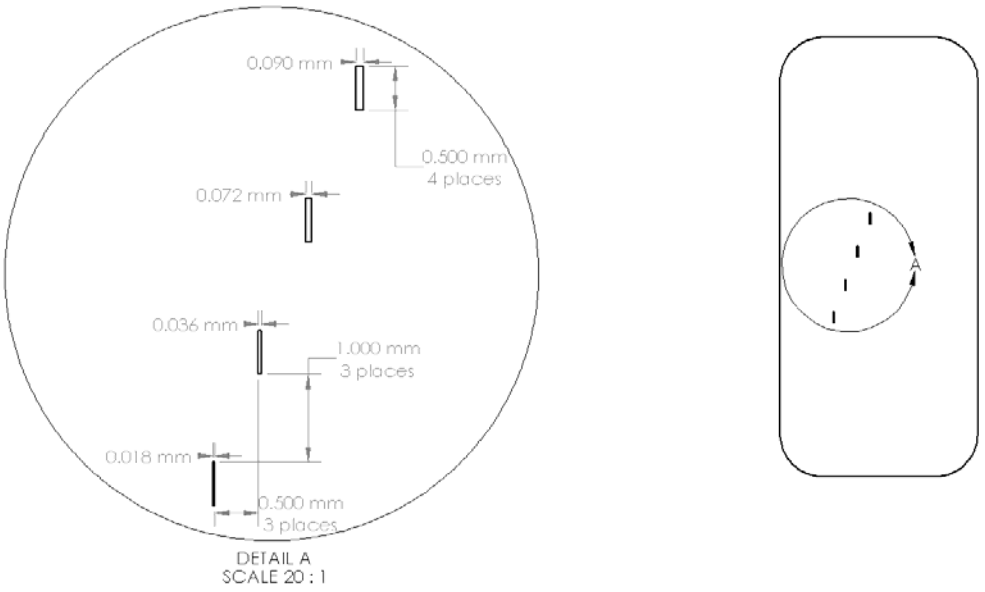

Figure 3.13: Mechanical CAD drawing of multi-slit plate rev 2.

As before, ray tracing was used to analyze the slit plate design to understand the fields of view defined by the slits, as well as their position on the detector. The fields of view for the slit plate are defined in Table 3.2.

Table 3.2: Fields of view defined by multi-slit plate rev 2.

	Vertical Field of View	Horizontal Field of View
Slit 1	$0.150° \leq \theta_x \leq 0.180°$	$0.444° \leq \theta_y \leq 0.564°$
Slit 2	$0.045° \leq \theta_x \leq 0.065°$	$0.110° \leq \theta_y \leq 0.226°$
Slit 3	$-0.061° \leq \theta_x \leq -0.049°$	$-0.226° \leq \theta_y \leq -0.110°$
Slit 4	$-0.172° \leq \theta_x \leq -0.158°$	$-0.564° \leq \theta_y \leq -0.443°$

When the slit plate is projected onto the CCD in Figure 3.14, there are distinct dark regions between the illuminated areas from each slit, as required. This will allow the analysis for light passing through each individual slit.

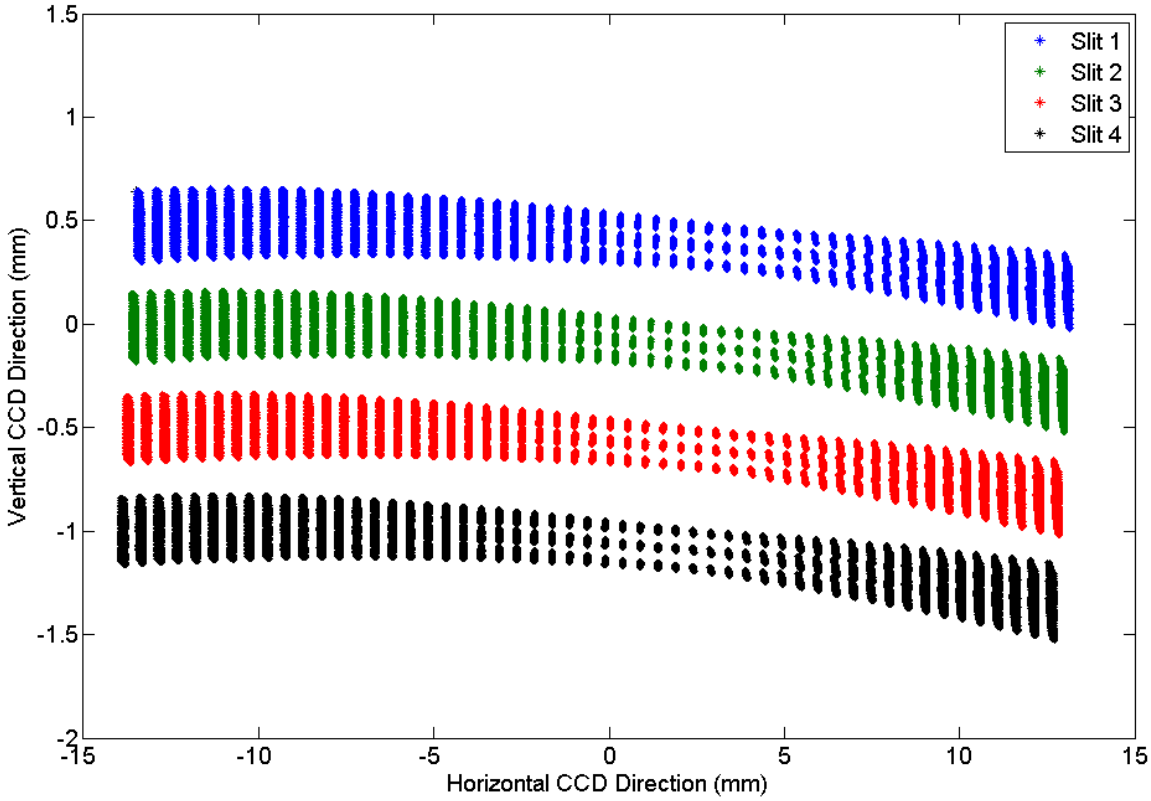

Figure 3.14: Ray trace model of various wavelengths passing through multi-slit plate rev 2.

3.3 Description of Multi-Slit Plate and Installation

Once the slit plate design was finalized, it was produced by Bob Weeks of Algonquin College. The machined slit plate is shown in Figure 3.15.

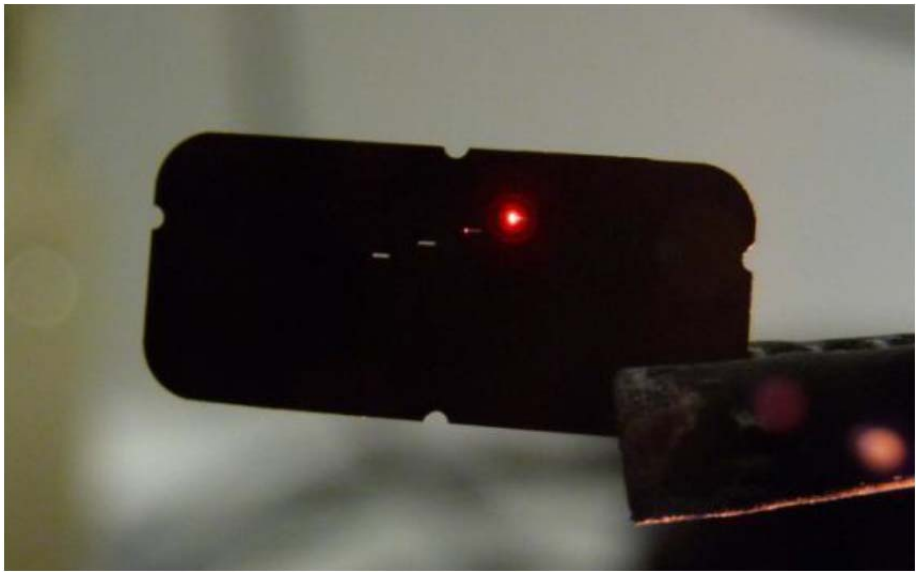

Figure 3.15: Machined multi-slit plate according to multi-slit plate rev 2 drawing.

The slit plate was inspected by Sandy Beaton of COM DEV to verify that it met the design specifications. Two methods were used to measure the slit plate. The first was to use a Dinolite Pro microscope with a calibrated scale. A sample image from this measurement technique is shown in Figure 3.16. Table 3.3 summarizes the sizes measured with this technique.

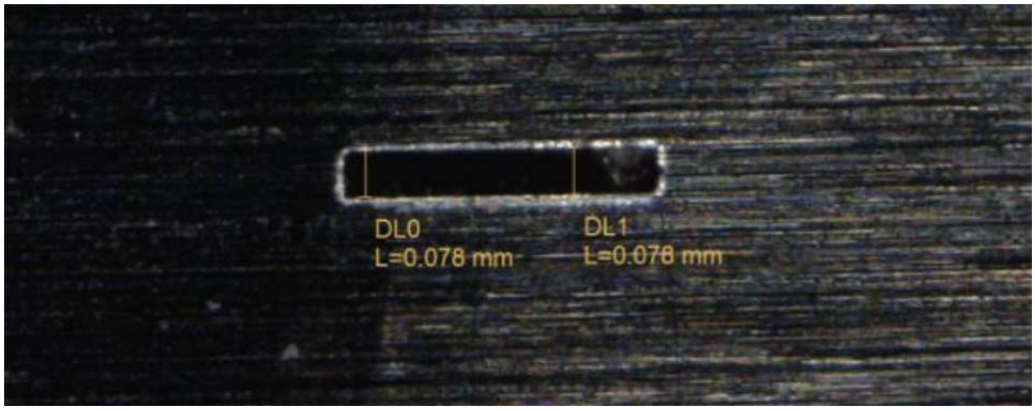

Figure 3.16: Microscopic view of Slit 1 in machined multi-slit plate with digital measurements.

Table 3.3: Slit sizes measured with digital microscope and diffraction techniques

	Height (μm)	Width (μm)
Diffraction Measurements		
Slit 1	78	518
Slit 2	61	549
Slit 3	21	506
Slit 4	13	532
Diffraction Measurements		
Slit 1	77	425
Slit 2	57	425
Slit 3	20	425
Slit 4	8	425

A diffraction technique was also used to measure the slits. A 632 nm laser was directed through each slit and imaged on a 0.25 in × 0.25 in grid paper placed 8.534 m away from the slits. The spot size of the laser was adjusted to ensure the entire slit was fully illuminated, and then aligned by monitoring the brightness of the diffraction pattern. The expected diffraction pattern for a rectangular aperture is:

$$I = a^2 sinc^2\left(\frac{a\pi sin\theta}{\lambda}\right) \quad \text{(Eq. 3.1)}$$

where a is the width of the slit, λ is the wavelength and θ is the angle between the incident wave ray and a point on the screen. The minima of this function are defined by:

$$\frac{a\pi sin\theta}{\lambda} = m\pi \quad \text{(Eq. 3.2)}$$

where m is the order of the minima. For the first case, $m = 1$, so

$$sin\theta = \frac{\lambda}{a} \quad \text{(Eq. 3.3)}$$

Now, let y be the distance from the central maximum of the diffraction pattern to the location of the first minimum on the detector, and L is the distance from the slit plate to the image, then

$$tan\theta = \frac{y}{L} \quad \text{(Eq. 3.4)}$$

Now, if $L>>a, \lambda$, then θ is small and

$$tan\theta \approx sin\theta \quad \text{(Eq. 3.5)}$$

Now, combining equations 3.3 and 3.4 to obtain

$$\frac{\lambda}{a} = \frac{y}{L} \quad \text{(Eq. 3.6)}$$

$$a = \frac{L\lambda}{y}$$

A sample image of this measurement technique is shown in Figure 3.17. The results of this measurement technique are shown in Table 3.3.

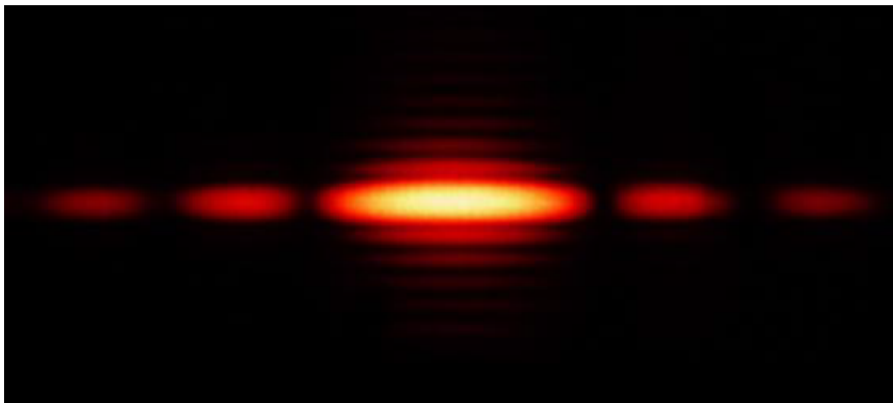

Figure 3.17: Diffraction pattern to measure slit sizes.

Comparing the two sets of measurements in Table 3.3 shows that there is a small discrepancy in the size of the slits based on these two sets of measurements, most significantly is the height of the Slit 4. These slit heights are also all smaller than the designed specifications. These sizes were however deemed acceptable by the University of Saskatchewan team and therefore the installation of the new slit plate proceeded.

In October of 2013, the OSIRIS-DM was transported to Kanata, Ontario to the COM DEV facility for its internal modification. With the extensive help of Sandy Beaton and supervision by Ashley McColgan and Craig Haley, the instrument was disassembled and the slit assembly was removed. The optical chain of OSIRIS-DM is shown in Figure 3.18, which resembles the ray trace model shown in Figure 3.1.The slit assembly is highlighted in Figure 3.19, as well as the original slit plate that will be replaced.

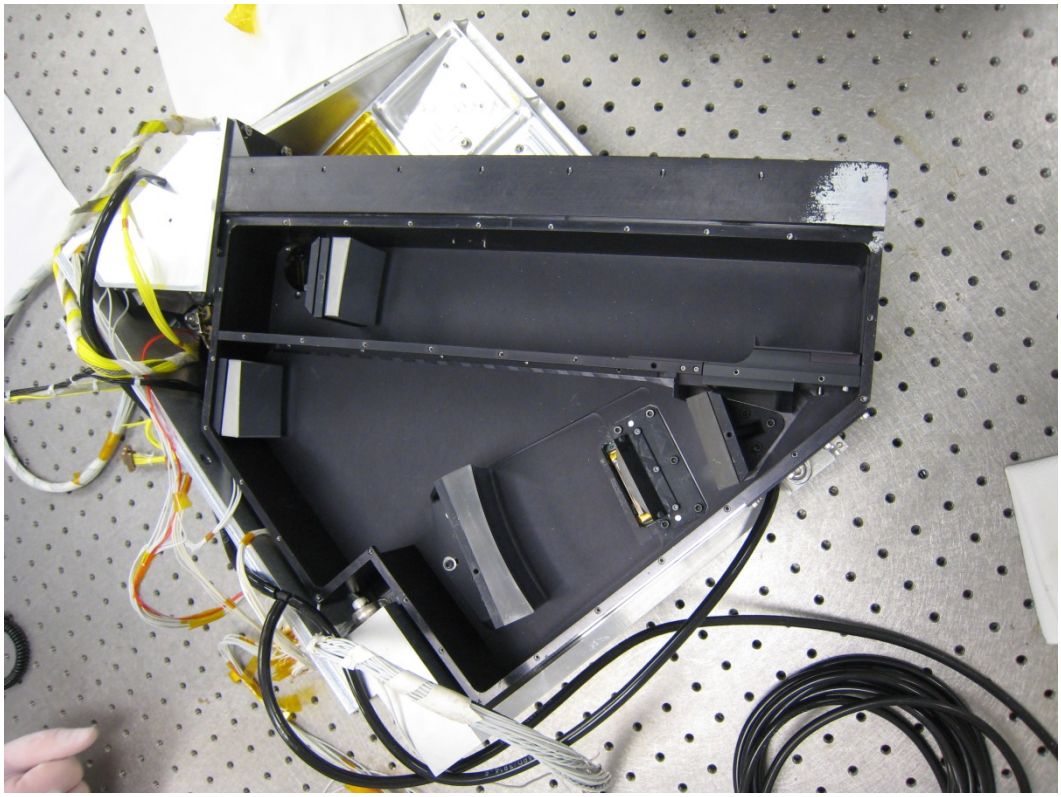

Figure 3.18: Exposed optical chain of OSIRIS-DM in preparation for slit plate replacement.

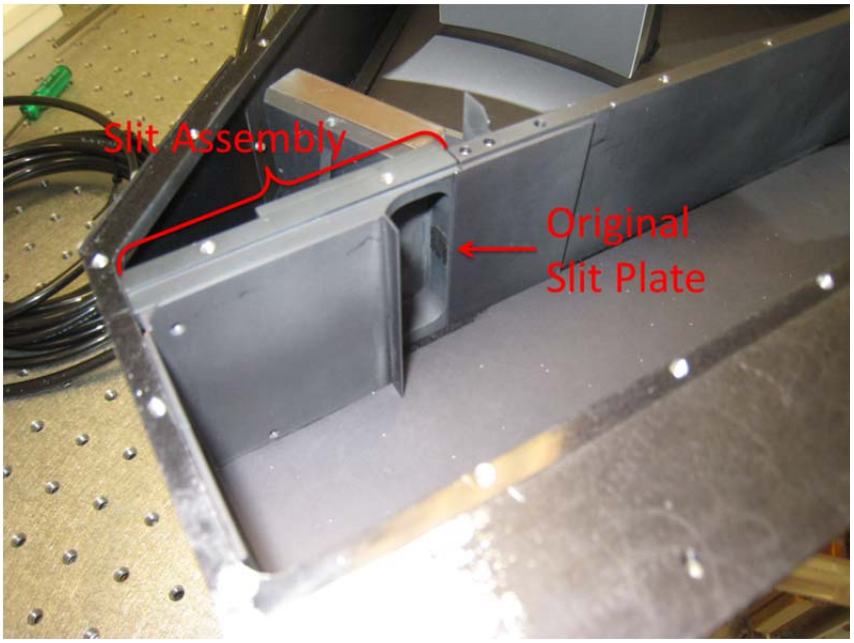

Figure 3.19: Close up of exposed optical chain of OSIRIS-DM with special attention drawn to slit plate location and slit plate assembly.

Figure 3.20: Slit plate assembly removed from optical chain of OSIRIS-DM. Red arrow indicates an unexpected aperture which will be addressed.

Figure 3.20 shows the slit assembly removed from the OSIRIS-DM. An arrow highlights an aperture that will be discussed shortly. Before removing the original slit from the slit assembly, the assembly was mounted above a digital microscope, and the location of the original slit plate was recorded and a digital outline was produced, as shown in Figure 3.21. It should be noted that the original slit plate within the OSIRIS-DM had three slits cut into it, and although it is not evident from Figure 3.21, the two slits on the outer edges were both masked with an adhesive tape so that no light could pass through.

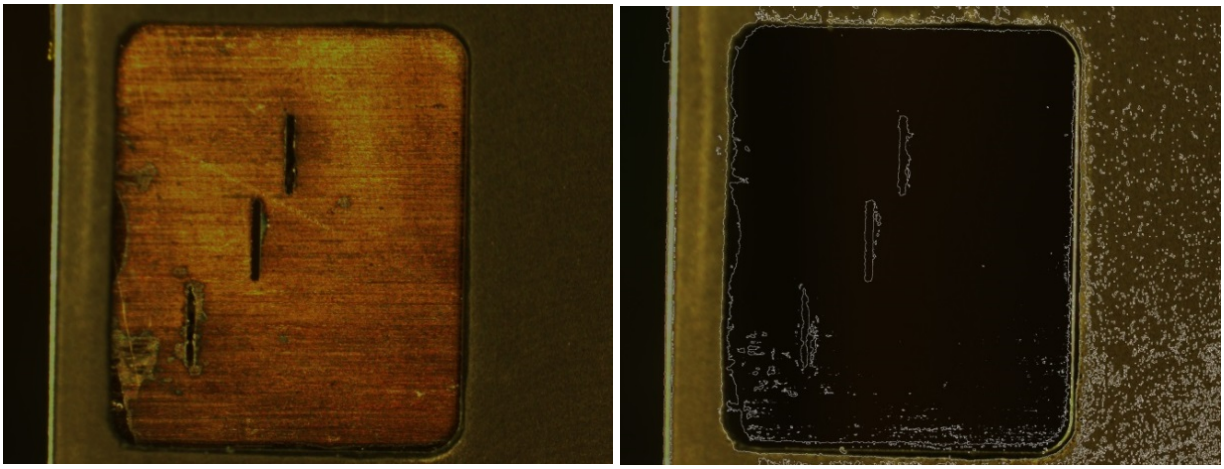

(a) (b)

Figure 3.21: (a) Microscopic image of original OSIRIS-DM slit plate. The outermost slits were both masked off to prevent light from passing through. (b) Digital overlay of original OSIRIS-DM slit plate.

It was found upon opening the OSIRIS-DM that the original slit plate did not have the shape expected from the CAD drawings of the instrument as shown in Figure 3.1. Figure 3.22 shows an image of the original slit plate.

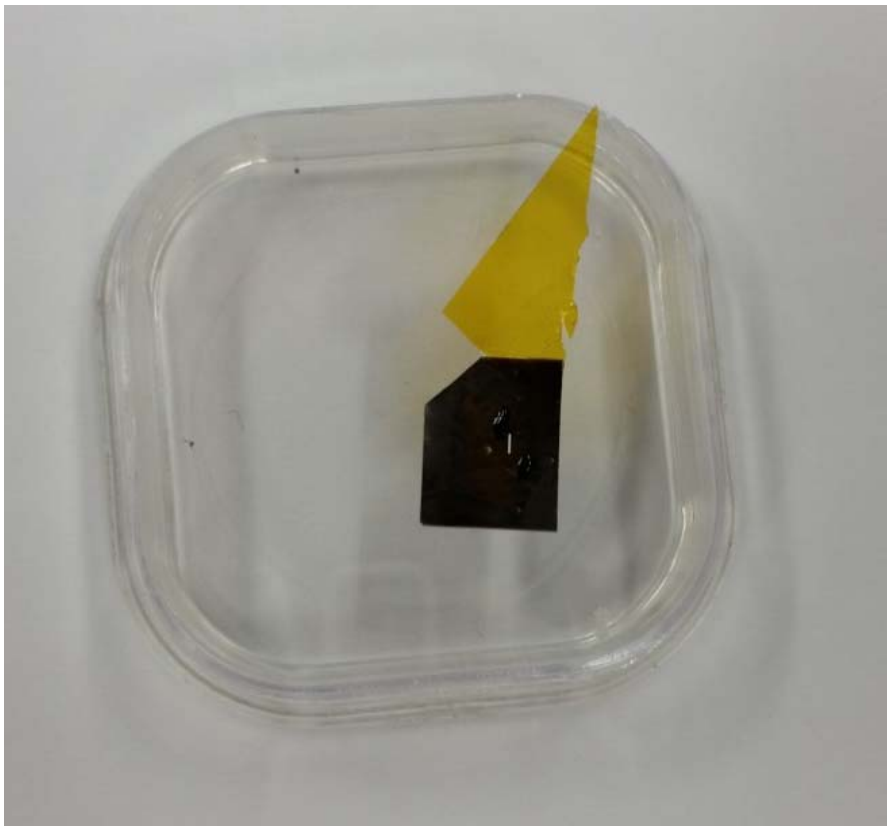

Figure 3.22: Original OSIRIS-DM slit plate after removal from slit assembly secured to sample holder with Kapton tape.

Because the original slit plate does not match the expected shape, it was would have been very difficult to align the original slit along the optic axis when it was first installed. In order to verify if the slit was aligned, a spare slit plate produced for the ORISIS-FM was inserted into the slit assembly. As seen in Figure 3.23, the slit from the flight model is about 3x longer than the slit for the OSIRIS-DM, and they do not overlap. To see this, pay close attention to the digital overlay of the original OSIRIS-DM slit plate that is superimposed over the OSIRIS-FM slit plate. This suggests that the original slit plate did not lie along the optic axis, as was assumed. The only repercussion this has on the analysis of the system is that the angles in the θ_x direction are all offset by some systematic value.

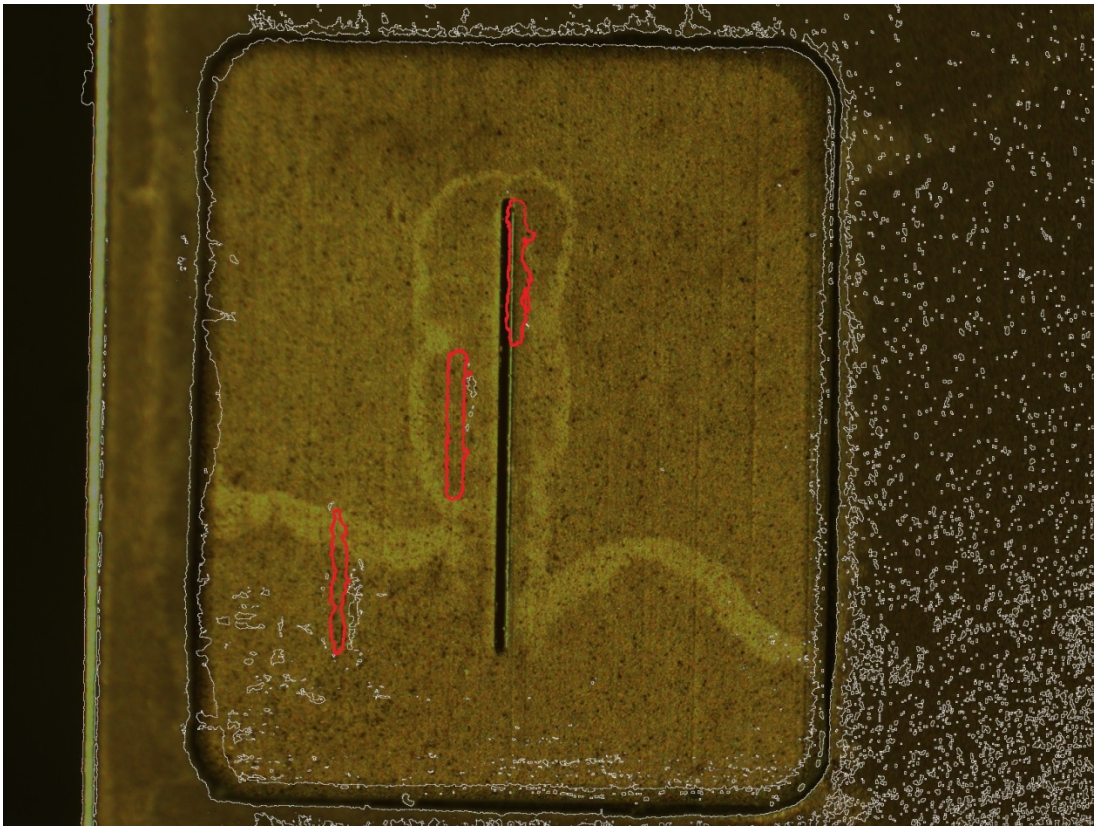

Figure 3.23: Spare OSIRIS-FM slit plate installed on slit assembly with original slit plate overlay highlighted in red.

Once the optic axis was more accurately defined, it was time to install the new slit plate. As explained previously, with only 4 slits, the optic axis would now have to lie between the inner two slits. The new slit plate was aligned with best effort to center it about the location defined by the flight model slit as the optic axis. The slit plate was initially secured to the slit assembly using Kapton k102 adhesive tape, and then more rigidly secured with Scotch-Weld 2216 adhesive. The new slit plate is shown in the slit assembly in Figure 3.24. Arrows are included to show the locations of the slits, as they are difficult to see even with the microscope.

After allowing the adhesive to sit for the required set time, the instrument was reassembled. The system was then tested using a Tungsten-Halogen bulb as was used for the single slit

analysis explained earlier. Figure 3.25 shows the measured spectrum for the new multi-slit system.

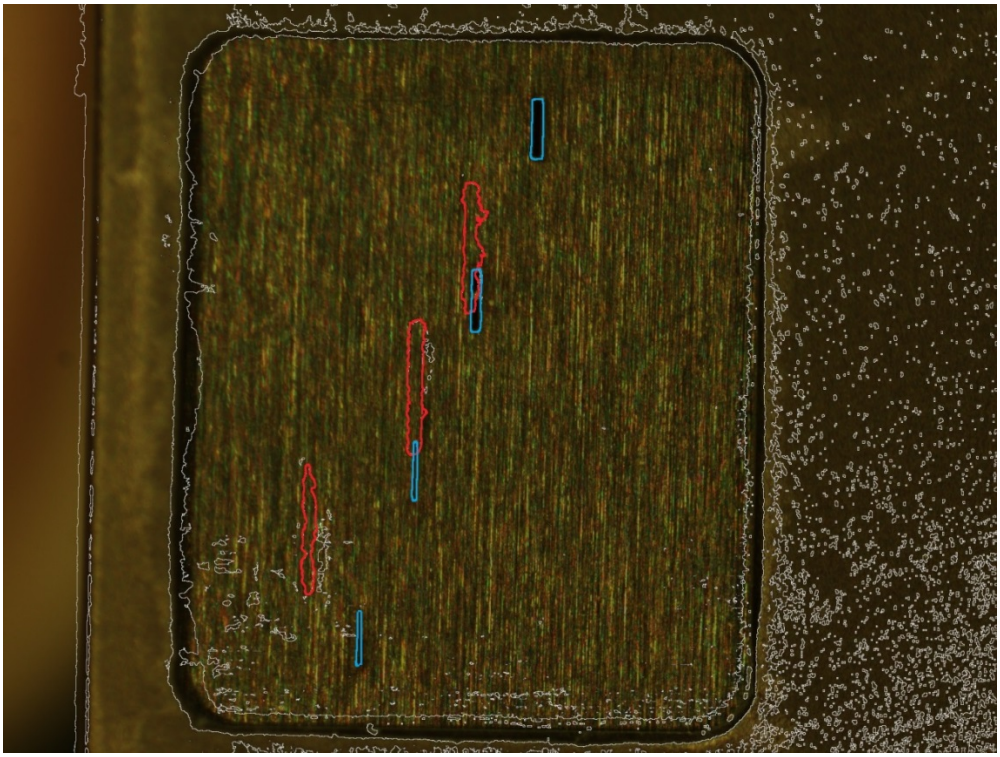

Figure 3.24: Multi-slit plate installed on slit assembly with original slit plate overlay. Red indicates the location of slits on original slit plate, blue indicates location of slits on new multi-slit plate.

From the images Figure 3.25, it was determined that the new multi-slit system was not operating as expected. To first order, the light entering the system can be considered uniform. It is therefore expected that the slit with the largest height (Slit 1) should measure the most signal, and the slit with the narrowest height (Slit 4) should measure the least. Upon first inspection, it appeared that Slits 2, 3 and 4 were working as expected, but there was an issue with Slit 1.In Figure 3.25a, Slit 1 is represented by the spectrum measured closest to the top of the CCD. Figure 3.25b shows a cross section of the CCD around 745 nm. This cross section represents the number of photons recorded in each illuminated region for approximately the same wavelength.

As shown, the detector picked up far fewer photons coming through Slit 1 than it did through Slit 2.

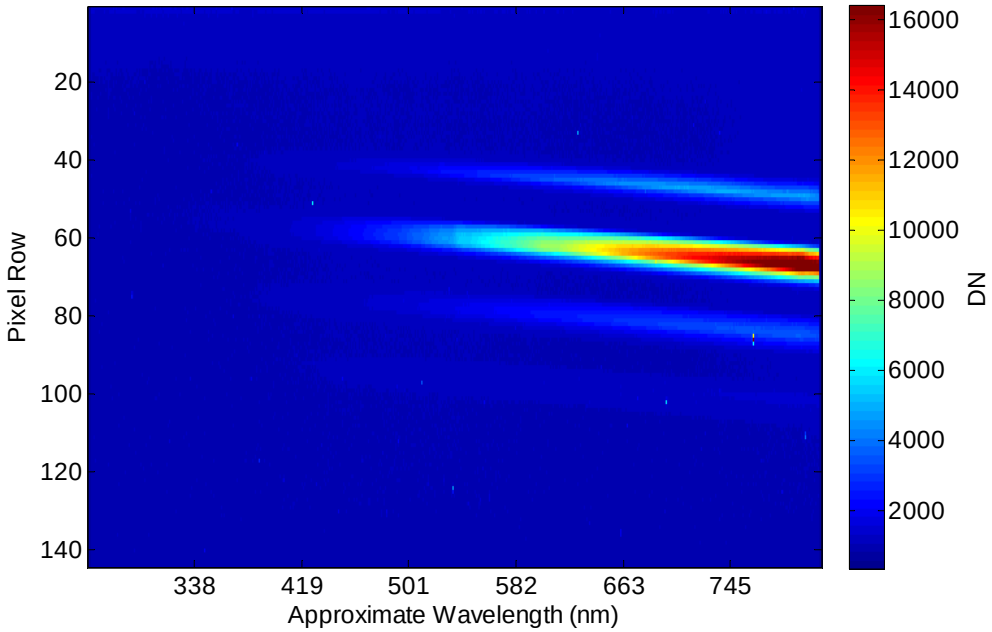

(a)

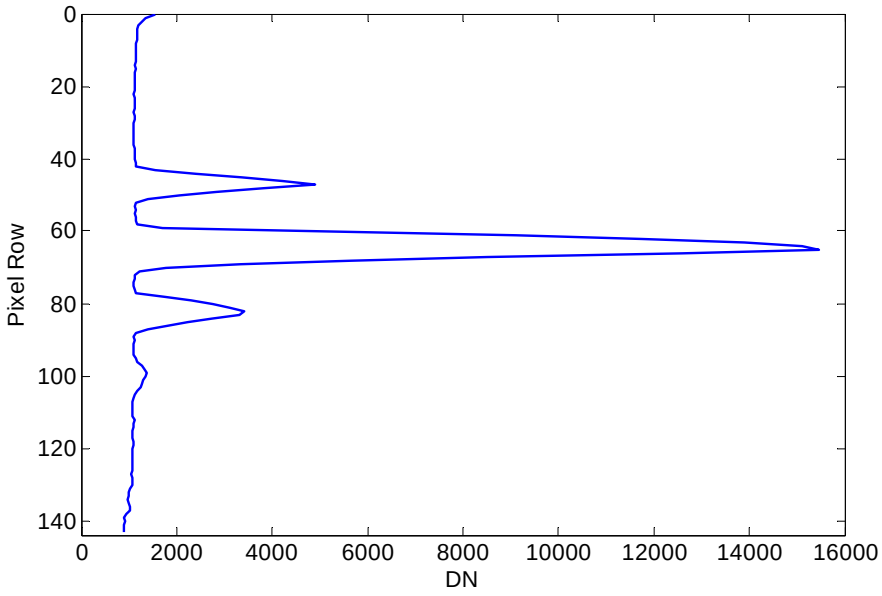

(b)

Figure 3.25: (a) Tungsten-Halogen spectrum measured through multi-slit plate. (b) Cross section of multi-slit CCD around 745 nm.

To diagnose this issue, the instrument was opened again to investigate why less light was making it through Slit 1 than originally expected. A small light source was placed in the optical chain before the slit plate, and a mobile microscope was used to image the slit plate from the reverse side. An image captured with the microscope is shown in Figure 3.26. In this image, the entrance aperture is located on the left hand side behind the slit assembly, and the CCD is located further to the right of this image.

Figure 3.26: Digital microscopic image of multi-slit plate showing evidence of clipping.

The expectation from this image is to see all four slits extending the same distance in the vertical direction. However, the observed result is a shortened Slit 1 and Slit 4 (located at the top and bottom of the slit plate, respectively). From this image, it is obvious that there is a clipping effect occurring on the largest slit. The clipping is also somewhat evident on the smallest slit. The cause of this clipping is an additional aperture located within instrument itself, which can be

seen in Figure 3.20. The aperture in question is the one highlighted by the arrow in that figure. This aperture is not part of the slit assembly, but does however rest right against the aperture to the assembly. With reference to Figure 3.1, this aperture is located directly behind element 4. This component was not known at the time of the design of the slit plate, and therefore went unaccounted for. This aperture is part of a support structure for the instrument, and therefore could not be removed. It was also not possible to make the aperture any wider without causing damage to the blackout coating within the instrument. It was decided that the easiest solution was to slide the slit plate in the horizontal direction until three slits were fully visible through the aperture and fully blocking the fourth slit. The slit plate was finally aligned so that only the 8 μm, 20 μm and 57 μm slits would allow light to pass through. Figure 3.27 shows the Tungsten-Halogen spectrum measured through the 3 slit system.

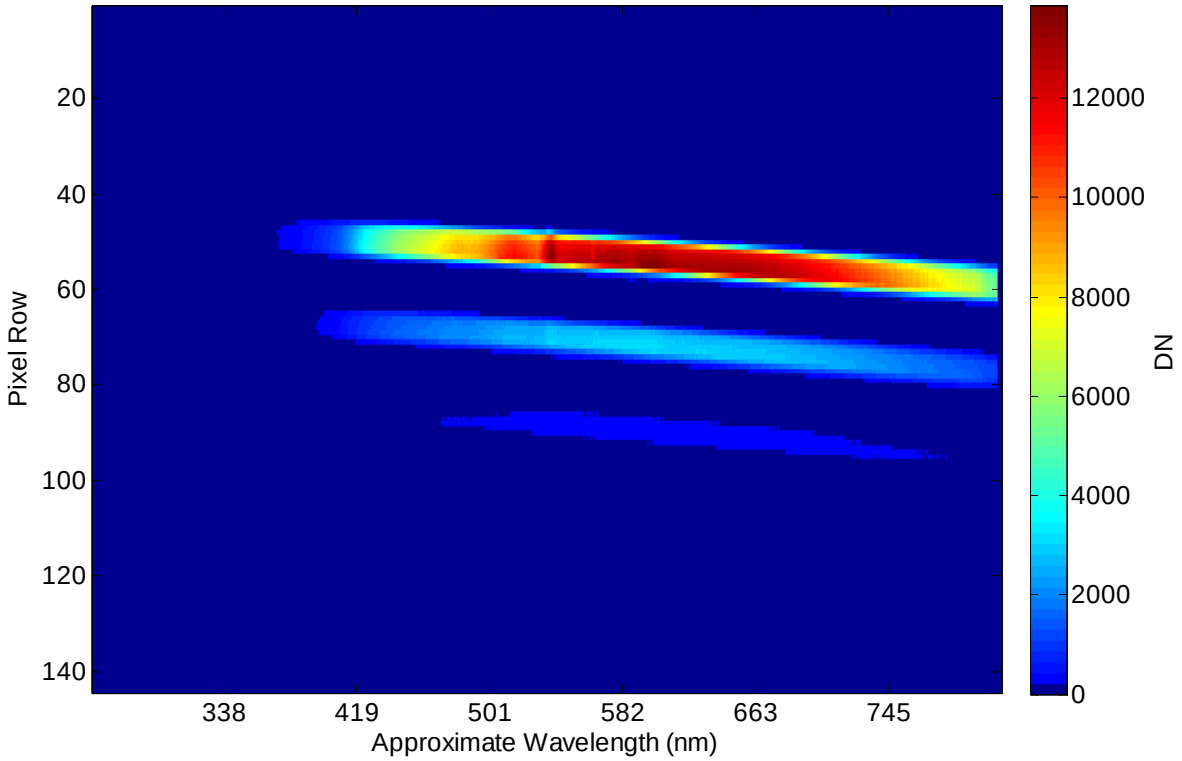

Figure 3.27: Tungsten-Halogen spectrum measured with finalized multi-slit plate configuration.

This figure is a representation of the raw data collected through the multi slit system. It is shown that three individual spectra are measured, and the photons measured drops as the slit size is reduced. Light passing through Slit1 strikes with the highest portion of the CCD and Slit 3 light strikes with the lowest portion. Once again, when viewing from a satellite platform, the different slit sizes account for the difference in radiance over the different altitudes viewed by each slit. This results in roughly uniform illumination of the CCD by all three slits from the satellite geometry.

3.3.1 Analysis of Installed Slit Plate

Ray tracing was again executed to verify the performance of the final product. To start with, the fields of view were redefined for the three slits using both sets of measurements provided by Beaton. These are summarized in Table 3.4. These fields of view were then used to determine the locations that light would strike the slit plate. These locations are then overlaid onto a measurement with the multi-slit system in Figure 3.28.

Table 3.4: Fields of view defined by two measurement techniques.

	Vertical Field of View	Horizontal Field of View
	Microscope Measurements	
Slit 1	$0.101° \leq \theta_x \leq 0.119°$	$0.273° \leq \theta_y \leq 0.399°$
Slit 2	$-0.002° \leq \theta_x \leq 0.002°$	$-0.056° \leq \theta_y \leq 0.056°$
Slit 3	$-0.114° \leq \theta_x \leq -0.106°$	$-0.397° \leq \theta_y \leq -0.274°$
	Diffraction Measurements	
Slit 1	$0.101° \leq \theta_x \leq 0.119°$	$0.287° \leq \theta_y \leq 0.385°$
Slit 2	$-0.002° \leq \theta_x \leq 0.002°$	$-0.047° \leq \theta_y \leq 0.047°$
Slit 3	$-0.114° \leq \theta_x \leq -0.107°$	$-0.385° \leq \theta_y \leq -0.286°$

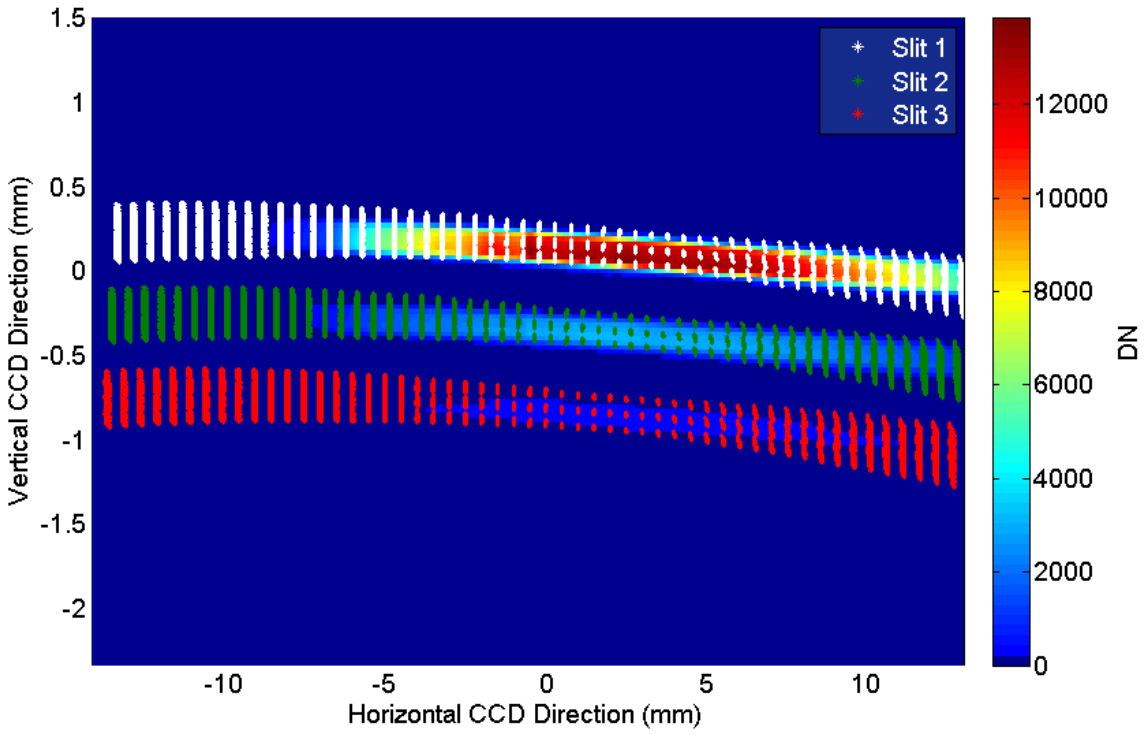

Figure 3.28: Ray trace modeled ray locations for multi-slit plate superimposed on Tungsten-Halogen spectrum measured with multi-slit plate.

From the Figure 3.28, it is evident that the ray trace agrees quite well with the measured data because the modeled data overlaps the illuminated area on the CCD. Once again, slight differences between the data sets can be seen, but this is still due to the over aspherization of the diffraction grating which was mentioned previously.

It is important to look at the intensities of the three slits relative to one another in this system. In an ideal system, without any aberration effects and if the slits could all be placed along the optic axis, then the ratio of measured radiance intensity from a uniform source between any two slits should be the ratio of the areas of the slits themselves. Based on this, the expected radiances normalized to Slit 2 are shown in Table 3.5. In addition to this, the measured normalized radiances are shown in this table. These will be examined later in this section.

Table 3.5: Normalized radiances for multi-slit system based on two measurement techniques and measured values.

	Slit 1	Slit 2	Slit 3
Microscope Measured Area	33489 μm^2	10626 μm^2	6916 μm^2
Expected Radiance Normalized to Slit 2	3.15	1	0.65
Diffraction Measured Area	24225 μm^2	8500 μm^2	3400 μm^2
Expected Radiance Normalized to Slit 2	2.85	1	0.4
Measured Radiance Normalized to Slit 2	4.21	1	0.12

These values could now be compared to measurements taken by the new multi-slit system. The data used to generate Figure 3.27 is used for this analysis. By isolating each illuminated region on the CCD, a single spectrum is obtained by binning the values in each pixel row and then averaging them based on the number of pixels used. This process is described in detail by *Taylor* (2015). In Figure 3.29a the single spectra collected by Slits 1 and 2 is shown, as well as the ratio between these two spectra. These spectra are a representation of the light entering the system through the defined slits for a set exposure time. The relative sensitivity of the instrument between the different slits can then be determined based on these measurements. The saw tooth pattern that is visible in the measurements is an effect of the binning method used to develop a single spectrum from the full width of the slit, described by *Taylor* (2015). Figure 3.29b then shows similar data, but in this case shows the spectra for Slits 3 and 2, as well as the ratio. It should be noted that when calculating the ratio, the offset in pixel column based on the wavelength shift noted in Figure 3.10b was accounted for based on the wavelength registration performed by *Taylor* (2015). In both of these cases, rather uniform results are shown for wavelengths greater than 450 nm, but very noisy results in the low end of the spectrum. This is because the illumination source used for this experiment does not provide sufficient signal in the ultraviolet region, and therefore this region is not included while calculating the average results for this test.

This analysis was performed on additional data sets to include various exposure times. The radiance ratios were then averaged across the entire illuminated spectrum to determine the radiance measured by each slit normalized to Slit 2. This was summarized in Table 3.5.

As shown, the measured radiances do not agree with the values predicted by the measured slit areas. It is important to recall that the radiances predicted were based on ideal optics within the system, with each slit being centered about the optic axis. In the real system, this is not the case, so some additional constraints need to be taken into consideration.

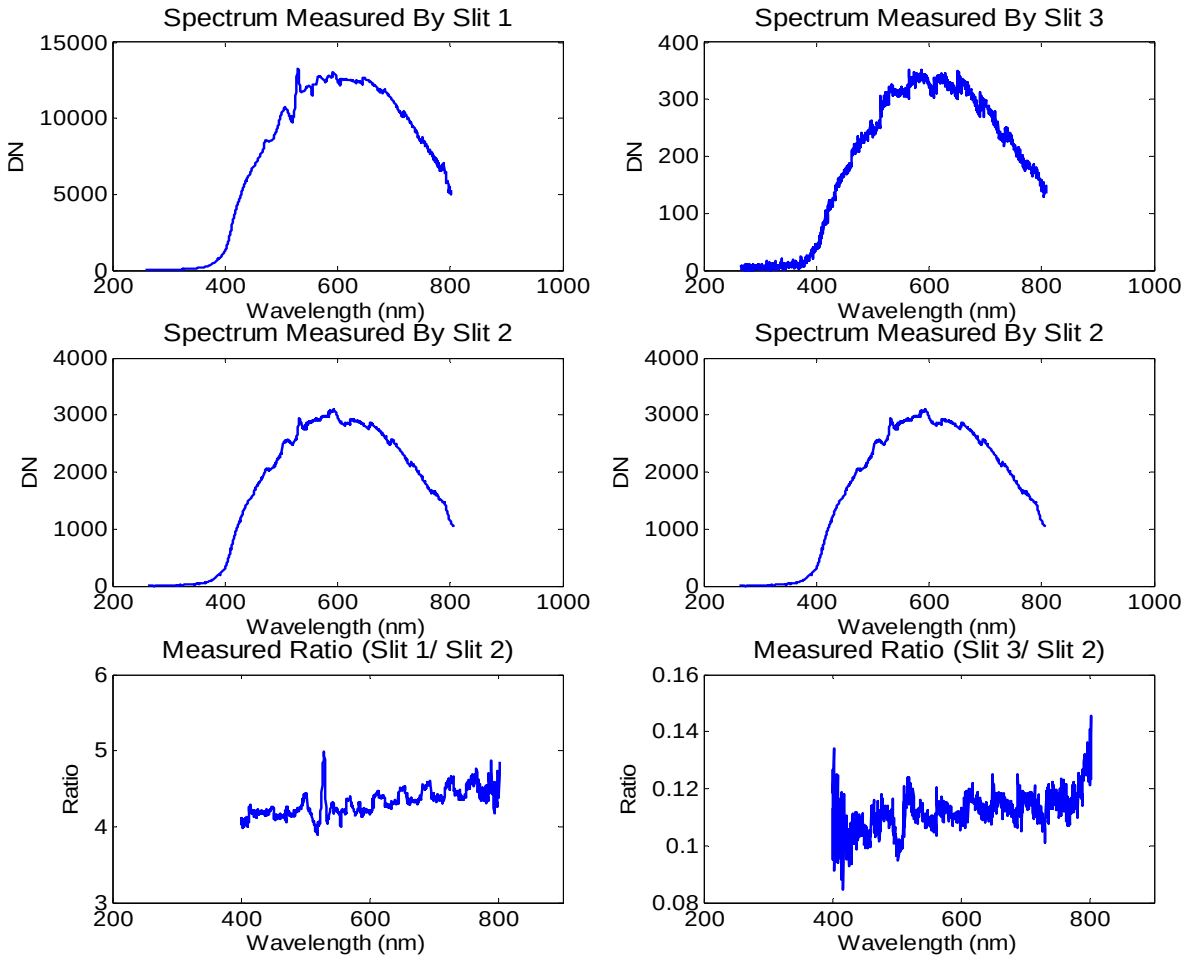

(a) (b)

Figure 3.29: (a) Slit 1 and 2 spectra to determine radiance ratios. (b) Slit 3 and 2 spectra to determine radiance ratios.

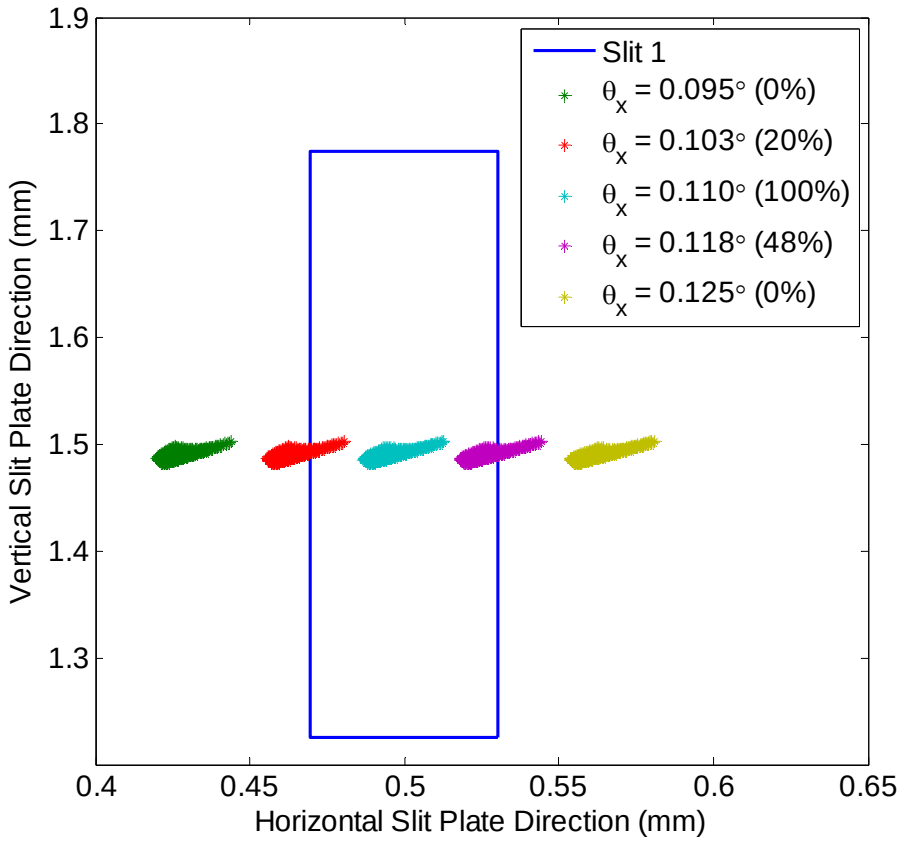

Figure 3.30: Slit 1 with various incoming angles to demonstrate vignetting effect.

As mentioned previously, off axis light will experience a level of vignetting that is not negligible compared to the size of the slits. In Figure 3.30, five sets of ray bundles are shown as they strike the slit plate, each coming from a different direction. The θ_y value was maintained for each of the ray bundles, while the θ_x value was changed. The figure shows that for θ_x values outside of the field of view defined in Table 3.4, shown here in dark green and yellow, none of the light entering through the aperture will pass through the Slit 1 as it is traced through the system. The figure also shows that for $\theta_x = 0.110°$, 100% of the rays entering through the aperture at this angle will pass through the slit. This is because this value lies comfortably within

the field of view, and this slit is wide enough to accommodate the whole ray bundle, even with aberrations. Finally, the figure shows that for input angles near the limits of the field of view, the aberrations cause only a certain number of rays entering the system to pass through the slit. In a system free from aberrations, the rays would be focused to a single point on the slit plate and the fields of view would be very well defined, but the aberrations cause a gradient to occur in the percentage of incoming rays to pass through the slit as a function of input angle. This is the vignetting effect caused by the slits. Classically, vignetting is the clipping of off axis rays by elements far from the aperture stop (*Fischer et al.*, 2008). In this case however, the apparent vignetting effect is a result of the separation of rays caused by aberrations in the system, which results in clipping at the plane of the slit plate. This effect is most significant for Slits 1 and 3. This is because these slits are the furthest from the optic axis, and thus the rays at these angles experience the greatest amounts of aberrations. This analysis was performed over the entire fields of view for each of the slits and is presented in Figure 3.31.

The resolution for both θx and θy in Figure 3.31 is 0.001°. This means that each pixel in the plots represents a field of view with solid angle of 3.046×10^{-10} sr. If it is assumed that uniform unit radiance is coming from the solid angle viewed by each of these pixels in the system, then summing the percentages in each plot gives a total incoming radiance for each slit with vignetting taken into account. To put this another way, if 1 unit of radiance entered the system from each direction defined by the pixels in Figure 3.31, then the radiance that would pass through the respective slits at that specific direction would be the vignette percentage, as indicated by the color of the pixel. Now, the total radiance passing through an individual slit is the sum of the vignetted percentages corresponding to the light exiting the slit. These values are

shown in Table 3.6 as the sum of unit radiance elements as well as the values normalized to the radiance passing through Slit 2.

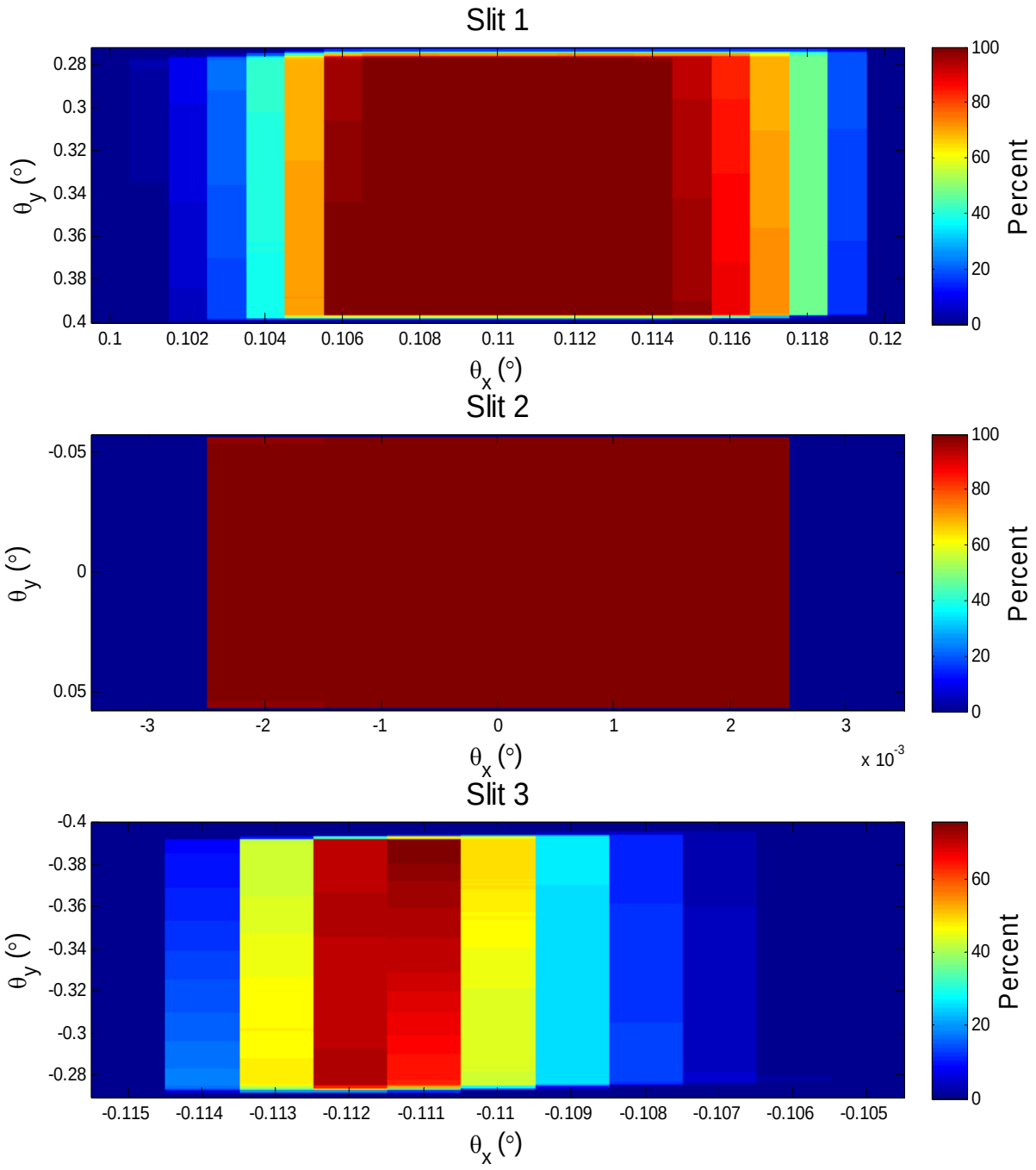

Figure 3.31: Vignetting effect on three slits as functions of vertical and horizontal incoming angles.

Table 3.6: Expected normalized radiances for multi-slit system accounting for vignetting effect.

	Slit 1	Slit 2	Slit 3
Incoming Radiance (With Vignetting)	1205.2	472.87	168.69
Normalized Incoming Radiance	2.55	1	0.36

These ratios still do not agree with the measured ratios of Table 3.5. They do however contribute to explaining why the measured results do not agree with the predicted results. Without taking the vignetting effect into account, the predictions in Table 3.5 are larger than expected. This suggests that in addition to the vignetting effect, there is still another factor contributing to this inconsistency.

Recall the measurement techniques performed by Beaton. The slit sizes provided a measurable diffraction pattern for 632 nm. This wavelength is within the range that is measured by OSIRIS-DM, indicating that the light passing through OSIRIS-DM is being diffracted by the slits. In Figure 3.32, the diffraction patterns of each slit are shown for wavelengths of 350 nm and 750 nm.

The diffraction patterns in Figure 3.32 are shown for incident monochromatic light interacting with slits defined by the diffraction measurement sizes listed in Table 3.3. As shown, the diffraction pattern has the greatest effect on long wavelengths travelling through the Slit 3, which is the narrowest. Now, these patterns only represent light that is striking the slit normal to the slit plate. In the case of OSIRIS-DM however, light is entering in a cone of angles because the objective mirror is focusing it. A very rough estimate of this effect in the instrument is discussed below.

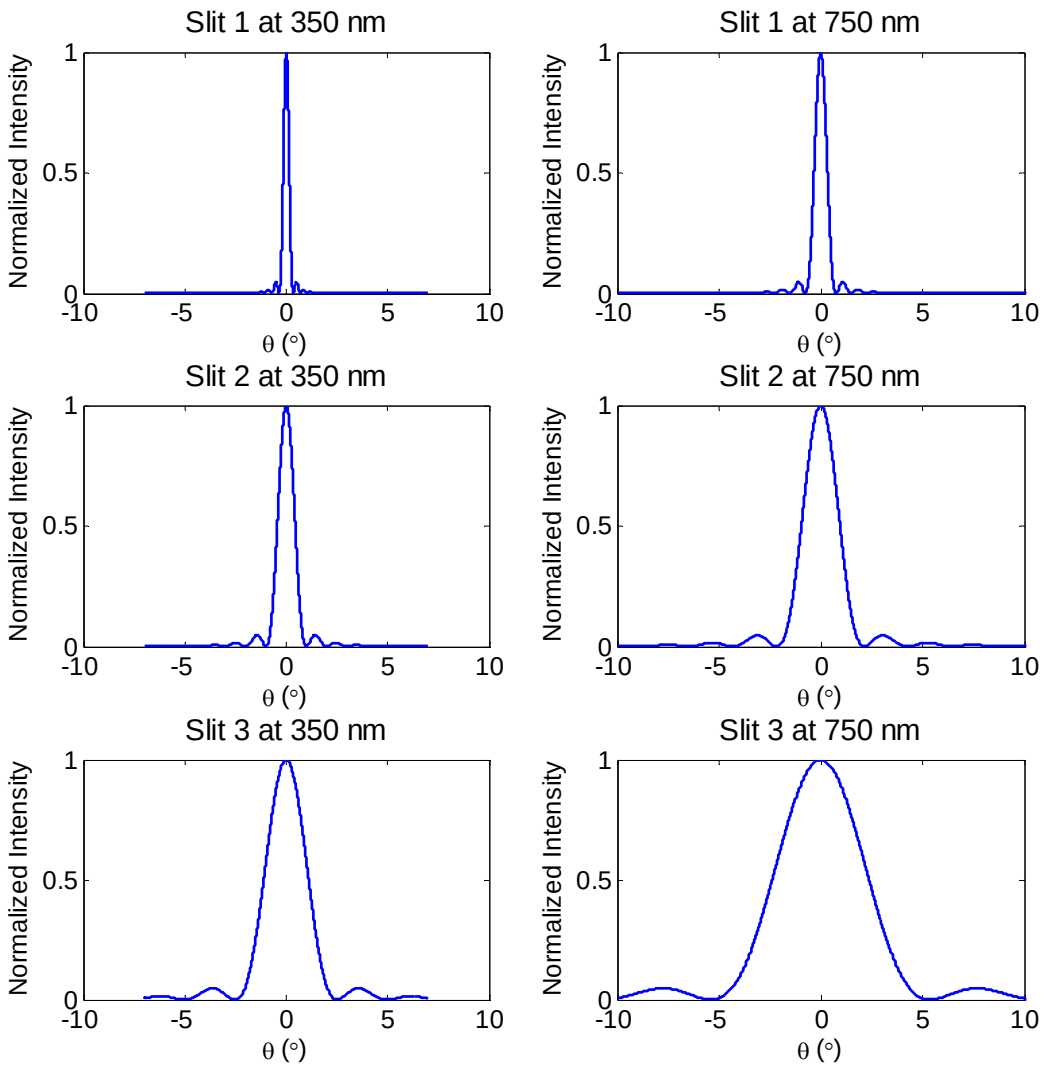

Figure 3.32: Diffraction patterns for various wavelengths over three slits.

For a very simplistic case study, it was assumed that the objective mirror is fully illuminated and the reflected light interacting with the slit plate is a plane wave. The range of angles associated with the focusing caused by the objective mirror was then determined. To do this, the distance between the objective mirror and the slit plate, along with the height of the objective mirror define the range of angles associated with this focusing effect. The diffraction pattern was then convolved with the range of angles seen by the slit plate for a single dimension. This is

shown in the left hand column of Figure 3.33 for the extreme case of 750 nm light interacting with Slit 3. The figure at in the top left corner is the diffraction pattern previously obtained, and the middle image then represents the step function defined by angles associated with the focusing caused by the objective mirror. The lower left corner finally shows the convolution of these two functions. This represents an idealistic view of how the light is dispersed as it exits the slit as a result of diffraction. This is carried up to the top right hand corner of the plot, with the associated area under the curve, which is 654 units^2. This area is a representation of the amount of light passing through the slit. The units here are arbitrary because it is a ratio of these areas that will be of interest. Now, if the light is traced as it travels away from the slit plate according to this convolution of diffraction patterns, it is possible to find what percentage of this light will reach the collimating mirror. This is shown in the right hand column of Figure 3.33.The middle figure on the right side represents the step function defining the angles required upon leaving the slit plate in order to interact with the collimating mirror. The final plot in the lower right hand corner represents the light that is reflected off the collimating mirror and is obtained by multiplying the convolution pattern with the step function defining the mirror. The area under this curve is 519 units^2, which indicates that approximately 20% of the light that passed through the slit was diffracted such that it does not interact with the collimating mirror and therefore does not make it through the rest of the system properly. Similar analysis was performed for Slit 2, and in this case, only 10% of the light passing through the slit plate missed the collimating mirror.

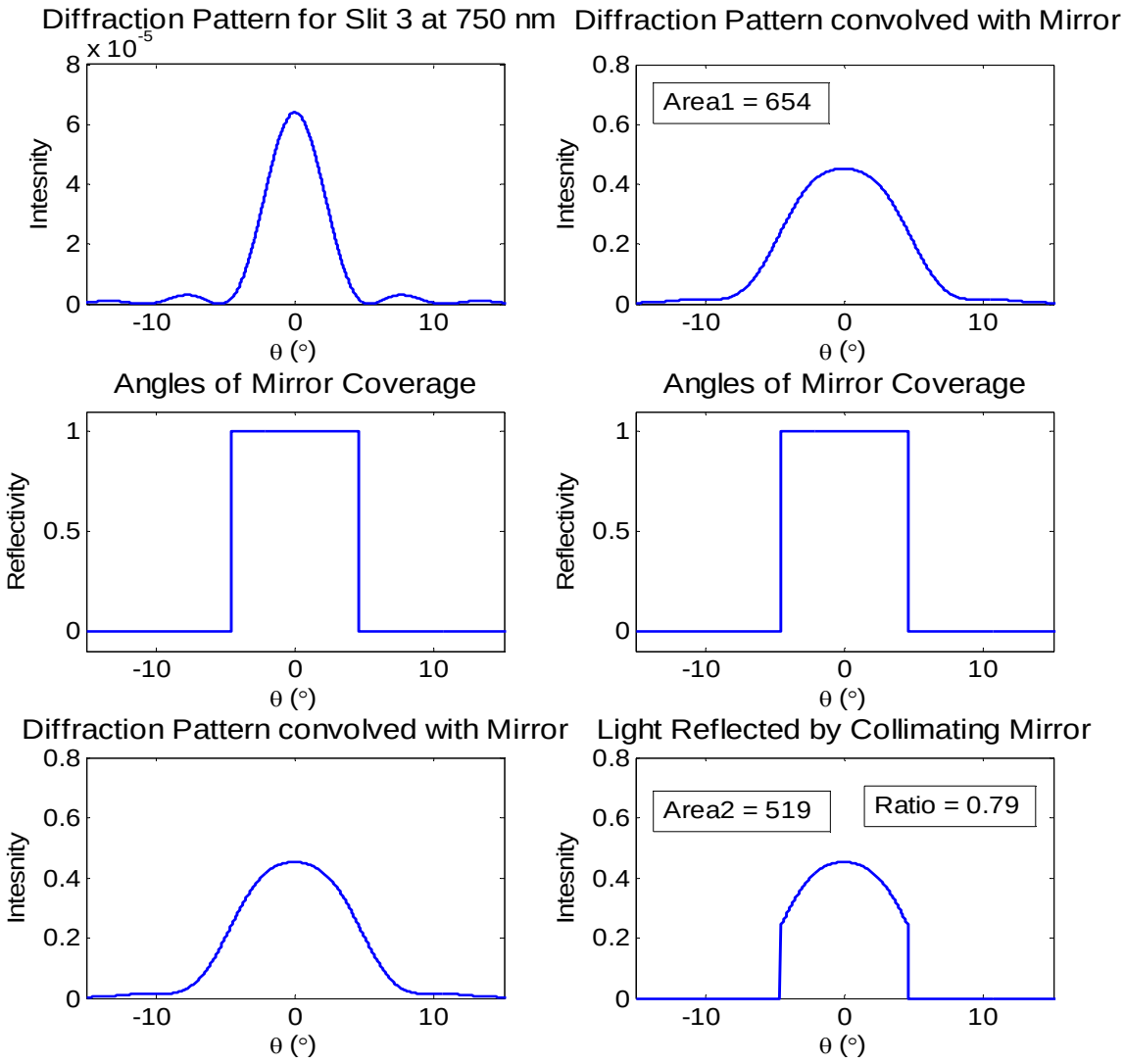

Figure 3.33: Diffraction pattern analysis.

As mentioned, this is an idealistic view of the possibility of diffraction through the system and therefore is not entirely accurate. It does however lend some insight to the possible reason for the discrepancies between measured and expected radiance ratios for the slits. A full analysis of this effect is beyond the scope of this work.

The analysis of the diffraction effects suggest the possibility that not all the light passing through the slits is necessarily being imaged at the correct location. The remaining light is still

passing through the instrument, but it could be interacting with the optical elements in an adverse manner. This is known as internal stray light. Therefore, there is a chance that the light is reaching the CCD through the slits in some process that is not dictated by the optical elements, and therefore would appear as stray light in the collected image. The instrument is now analyzed to investigate the stray light rejection of the new multi-slit system.

To start with, the original single slit system is investigated. For this analysis, a neon spectrum is investigated to look for any cases of stray light.

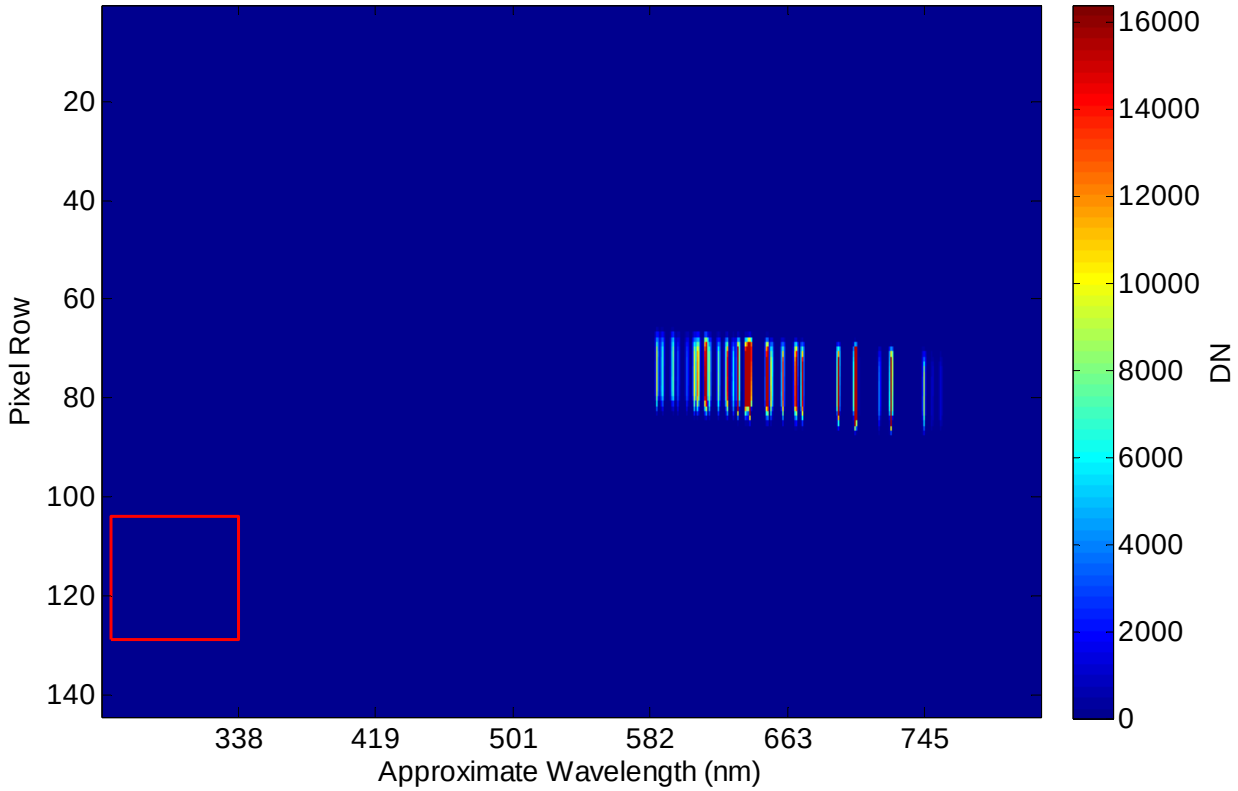

Figure 3.34: Neon spectrum measured with the original slit in OSIRIS-DM.

In Figure 3.34, the spectral lines associated with a neon spectrum are shown as measured by the original slit installed in OSIRIS-DM. As was the case for the Tungsten-Halogen spectrum measured in Figure 3.2, the original slit plate allows approximately 18 rows to be illuminated on

the CCD. The neon spectrum has its strongest peaks in the red end of the visible spectrum, so this is the reason why the region on the right side of the CCD appears to be illuminated. It should be noted that some of the pixels in this image have reached the saturation point of the CCD. The same measurement is shown in Figure 3.35, but the color scale has been shifted to enhance small scale features.

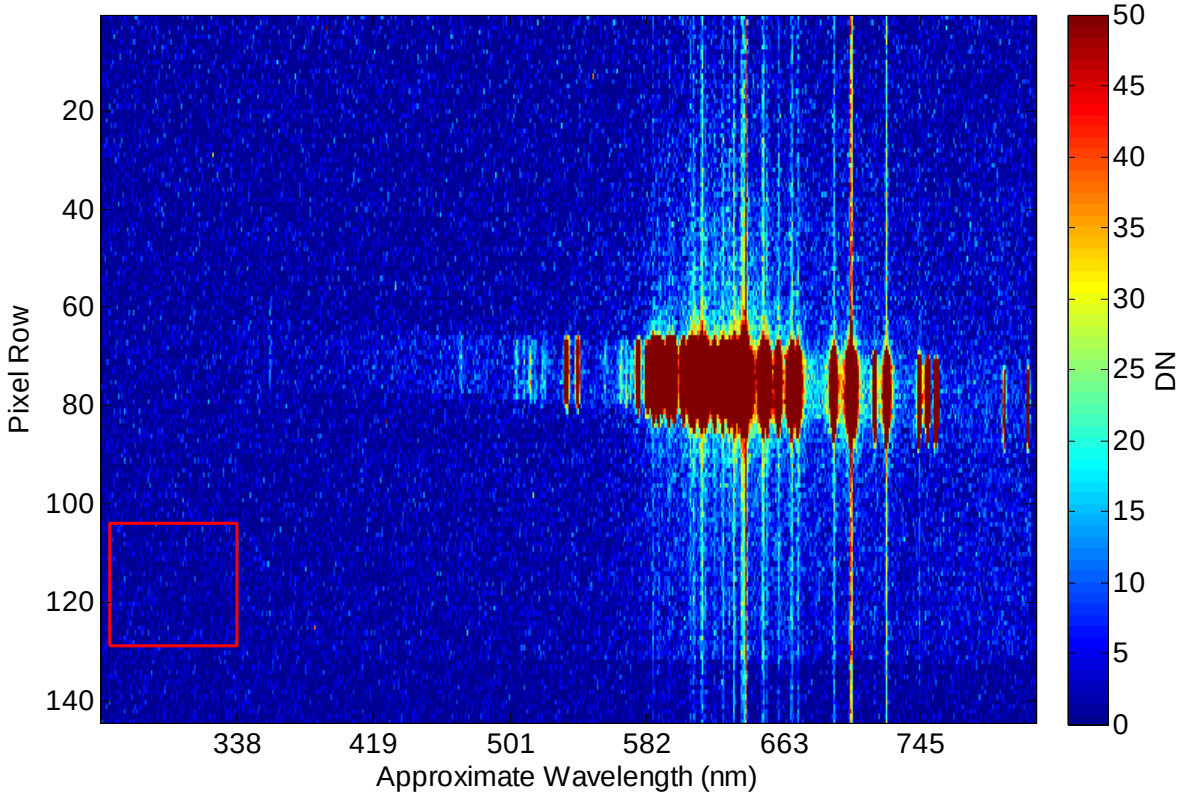

Figure 3.35: Neon Spectrum measured with the original slit in OSIRIS-DM with decreased color scale.

In Figure 3.35, the color of each pixel represents the CCD count in a range from 0 to 49, with all pixels at any higher count shown in dark red. This figure indicates that the neon spectrum has additional weak lines at lower wavelengths that were not visible in Figure 3.34. It also shows that there is a read out issue associated with the over saturated pixels, resulting in the vertical lines that are visible on the red end of the CCD in the region that should not be illuminated.

In Figures 3.34 and 3.35, a red box has been drawn in covering a region in the lower left corner of the CCD. This box surrounds 4836 pixels in a region that is not illuminated by the slit, and does not have any apparent contamination by any read out smearing of the CCD. This is the region that is analyzed for any stray light. This region could be made larger for the original single slit CCD images shown, however, for the analysis of the multi-slit system, this region is closer to the limit of the total size that could be used for this analysis.

The type of image seen in Figure 3.35 was generated by taking an illuminated image on the CCD and subtracting an unilluminated image that was collected shortly after the first. These are defined as corrected illuminated images. This method is described by *Taylor* (2015) as an effective way to remove dark current and the direct current (DC) bias from images in the lab environment. In addition to the image shown, a second type of image is also required for this analysis. A second unilluminated image was collected, and then the same first unilluminated image was subtracted from this image. These types of image will be called a corrected dark image, and are used to form a baseline for this analysis.

Histograms of the DN collected within the red box for three corrected illuminated images and three corrected dark images are shown in Figure 3.36.

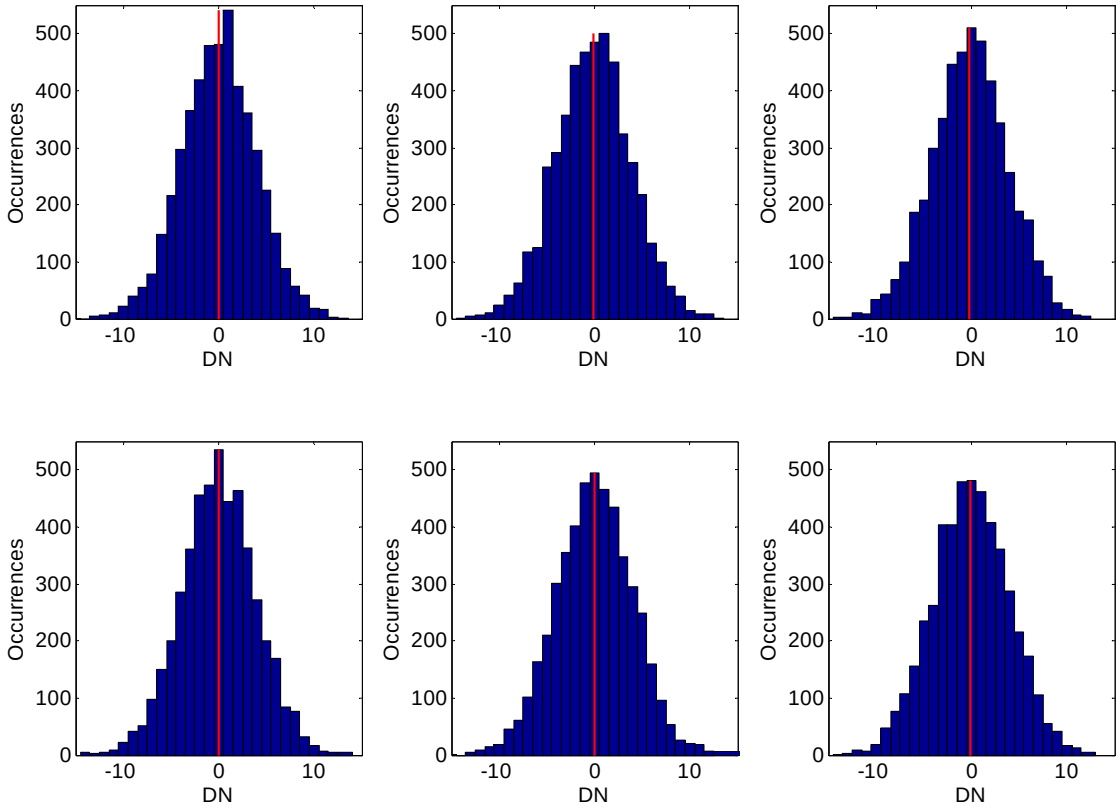

Figure 3.36: Histograms of DN counts for corrected illuminated images (top row) and corrected dark images (bottom row) with original OSIRIS-DM slit.

In Figure 3.36, the top row of histograms show examples of corrected illuminated images collected with the original slit plate, and the bottom row are examples of corrected dark images. To start with, the corrected dark images histograms were investigated.

The two measurements used to generate these histograms were both imaging a region in the absence of light. As a result, it is expected that the subtraction of these two images should result in zero, within the random error of the CCD, across all pixels. The statistical variation of analyzed pixel counts is centered about zero, as shown in the bottom row of histograms. For the corrected illuminated region, the same result is expected for the selected region because it is far from the region on the CCD that should be illuminated by light. However, if stray light is

causing an effect, the histogram should show some indication of this. In the case of the single slit system, the histograms are once again all centered nearly at zero. From the data sets measured, the absolute average of the offsets of the histogram centers was found to be 0.1077 DN. This means that, in an unilluminated region of the CCD, the average effect of stray light on a pixel is 0.1077 counts. Now, this value is only valid for the specific lab set up used to collect these images. For a broader understanding of the effects of stray light, it is important to consider the total amount of light that was entering the system in this specific image. The total number of counts on the CCD therefore must be determined. As was mentioned, some of the pixels were saturated in the images collected, so a scaling factor was used to account for this based on unsaturated images. It was found that the average total counts for the corrected illuminated images was 49,599,498 DN. So, for every 49,599,498 DN of measured light entering the system, 0.1077 DN on each pixel was a result of stray light in the system. Therefore, the stray light rejection value will be described as the ratio of these. For the single slit system with this simplistic definition, the stray light rejection value is 2.2×10^{-9} DN/DN.

Now, the new slit plate is investigated to analyze the stray light response associated. Figure 3.37 shows saturated neon spectra collected using the multi-slit OSIRSI-DM system. Once again, these images have been saturated past the limit of the CCD. In Figure 3.37a, the corrected illuminated image is shown with a color scale indicative of the full range of the CCD. Figure 3.37b shows the same image with a decreased color scale. The red box is once again included in the same position as those shown for the single slit images. As before, histograms are created for corrected illuminated and corrected dark images with the multi-slit image.

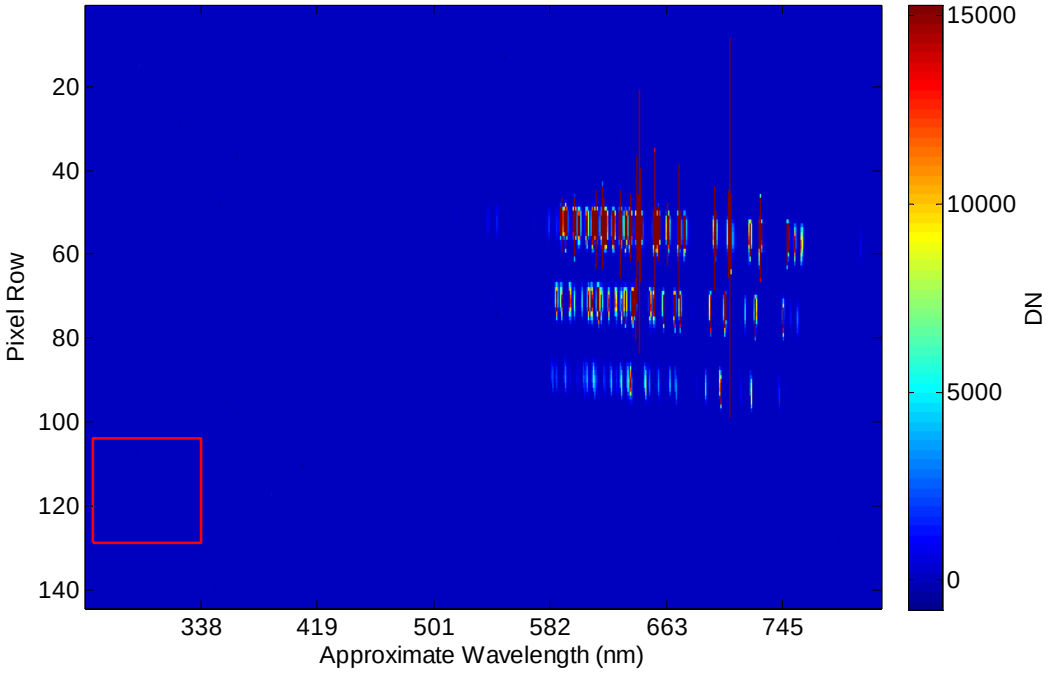

(a)

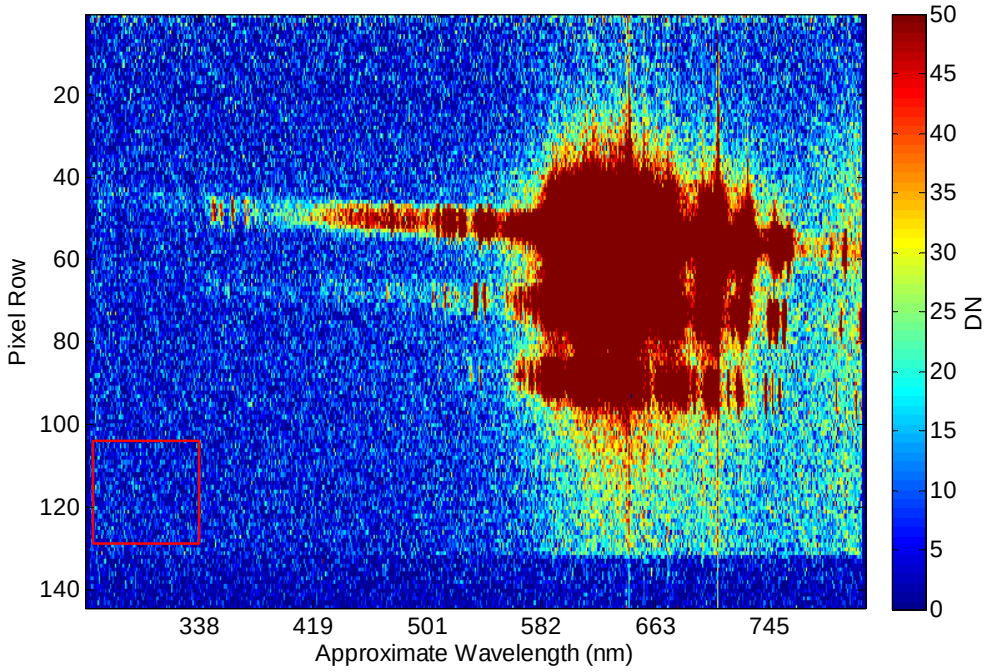

(b)

Figure 3.37: (a) Neon spectrum measured with the multi-slit OSIRIS-DM. (b) Neon spectrum measured with the multi-slit OSIRIS-DM with decreased color scale.

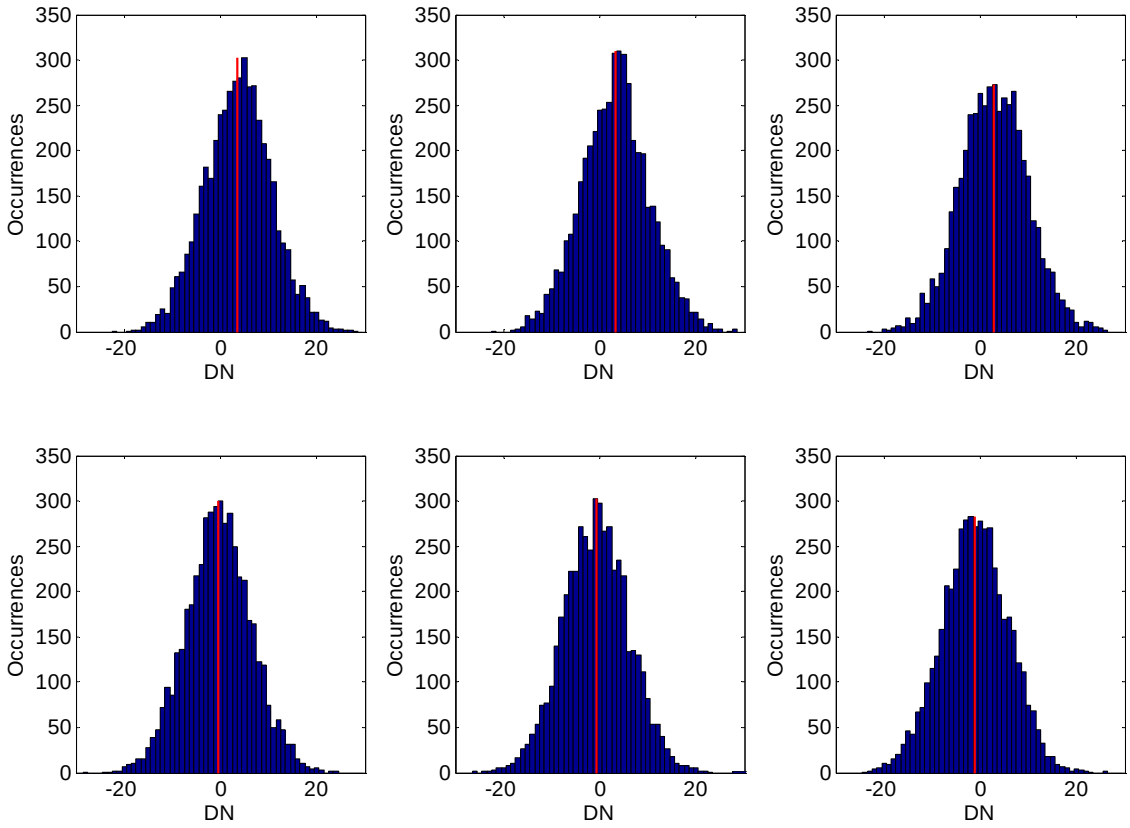

Figure 3.38: Histograms of DN counts for corrected illuminated images (top row) and corrected dark images (bottom row) with multi-slit OSIRIS-DM.

Figure 3.38 shows three examples of corrected illuminated image histograms in the top row, and three corrected dark image histograms in the bottom row. It is seen that the histograms created from the corrected dark images are all centered about zero. This is expected for the same reasons as before. Now however, it is evident that the centers of the histograms for the illuminated images are shifted away from zero. The average shift for the data collected is 3.166 DN. Once again, this means that for the image shown in Figure 3.37, an average of 3.166 DN of stray light was measured on each of the pixels on the CCD. To compare this to the previous case, the total number of counts collected must be calculated. For this case, the average total counts

was 51,252,815 DN. Therefore, the stray light rejection value for the multi-slit system with the previously defined definition is 6.2×10^{-8} DN/DN.

To put this into perspective, if an image was captured with completely uniform light across all wavelengths and varying intensity based on slit field of view such that the maximum count was achieved on each illuminated pixel, then the total DN entering through the three slits would be 214,043,895 DN. This is based on the total number of illuminated pixels on the CCD multiplied by the maximum count of 16,383 DN. This is the worst case scenario, because the DC bias has been assumed to be 0, and all three slits have imaged the same total amount of light. In this case, based on the stray light rejection value, 13.27 DN of stray light would be accumulated on each pixel. This suggests that 0.08% of the light measured would be the result of stray light. Although the multi-slit configuration has roughly increased the internal stray light by an order of magnitude, this is still a very small effect and therefore is an acceptable level of stray light rejection.

3.4 Slit Projections onto Atmospheric Limb

The fields of view define the directions from which light must enter the aperture to OSIRIS-DM in order to be imaged on the CCD. Each of the projection areas is a projection of the entrance aperture over the solid angle defined by the field of view for any given slit. It is however helpful to represent these solid angles as planar areas in which the light passes through. When the field of view is projected outward onto a planar area, this plane will be referred to as the object plane. This is easiest to understand in the case of lab based measurements when the instrument measured radiance from a screen or diffusing plate. In this case, the plane of the screen or plate represents the object plane.

If the slit plate had a single opening in the shape of an infinitesimally small hole lying along the optic axis, then the only light that would pass through the slit would perfectly collimated light entering the system along the optic axis. If the unidirectional light passing through the pinhole slit was projected outwards from the entrance aperture, it would have dimensions of 36 mm × 36 mm, as defined by the entrance aperture. This collimated projected light would travel outwards from the aperture towards the atmosphere. If a screen was placed anywhere within the line of sight defined by this field of view, then the slit projection would be a square on the screen also with dimensions of 36 mm × 36 mm.

For the case of rectangular openings in the slit plate, it has been shown that a range of angles have the opportunity to pass through the slit plate, defined in two directions. The aperture of the instrument must therefore be projected outwards for each combination of θ_x and θ_y that pass through any given slit. Then, depending on the environment that the instrument is imaging from, different projected areas will define where the light must be coming from to pass through the slits.

3.4.1 Lab Based Projections

For measurements made in the lab, the size of the projected area is dictated primarily by the size of the entrance aperture. A majority of the tests performed in the lab were images of either a screen with light reflecting off of it, or images of a diffusing plate with the source on the opposite side. In both of these cases, the imaged surface was uniformly illuminated by the source. The figures in this section show the size of the projected area for lab based measurements as the fields of view defined by the slits is projected outwards from the aperture.

Figure 3.39a shows the area captured by the field of view defined by the original slit plate is still relatively close to a square, which is a result of the square aperture. It is easy to see however

that the area stretches slightly further in the horizontal direction than it does in the vertical. This is due to the fact that the field of view is larger in the horizontal dimension than it is in the vertical. The angles defining the field of view are relatively small, so over a distance of 2 m, they have not had much of an effect on the projection of the slit.

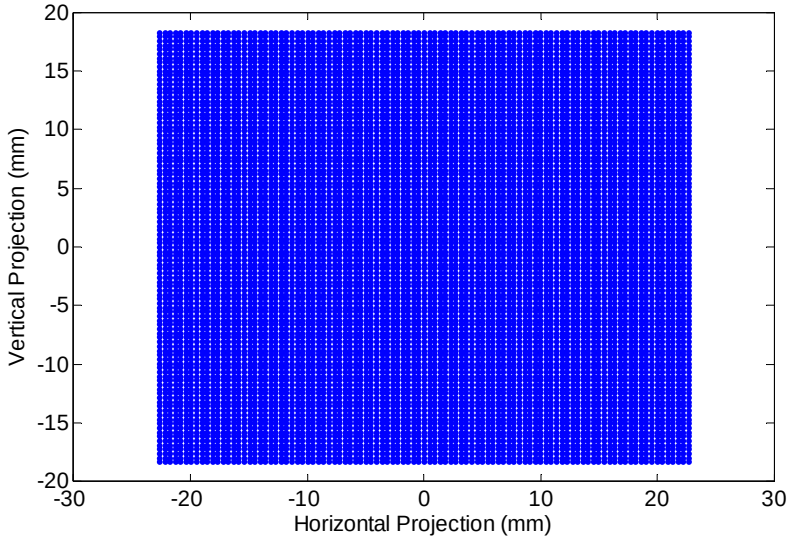

(a)

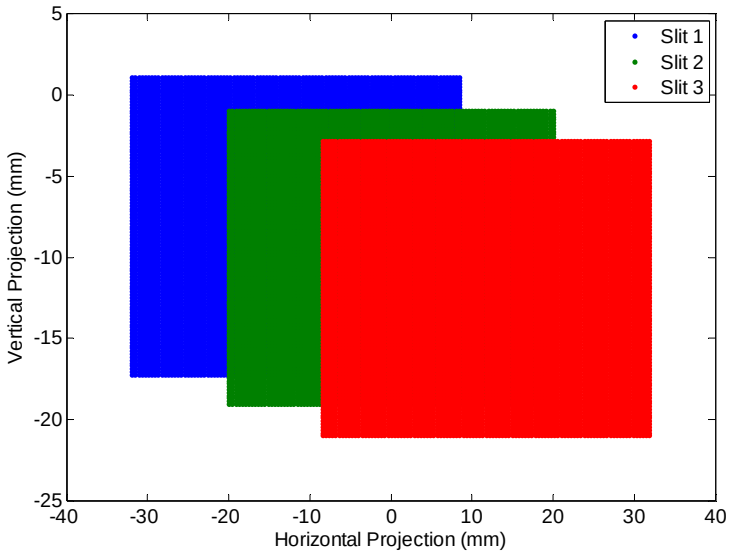

(b)

Figure 3.39: (a) Original OSIRIS-DM slit plate with object plane 2 m from aperture. (b) Multi-slit plate with object plane 2 m from aperture.

In Figure 3.39b areas defined by the three fields of view of the installed multi-slit plate are shown. It is shown that there is an overlap in the light entering the system from 2 meters away. This once again is a result of the small field of view angles and the short distance between the instrument and the plane being imaged. This means that for the lab based measurements with a uniformly illuminated object plane, each of the slits was viewing effectively the same radiance.

3.4.2 Satellite Based Projections

Recall that the optical element sizes in OSIRIS-DM match those in the OSIRIS-FM. Therefore, they are designed for viewing the atmosphere from a satellite platform. In the case of atmospheric measurements, the object plane is representative of a section of the atmospheric limb, as shown in Figure 3.40.

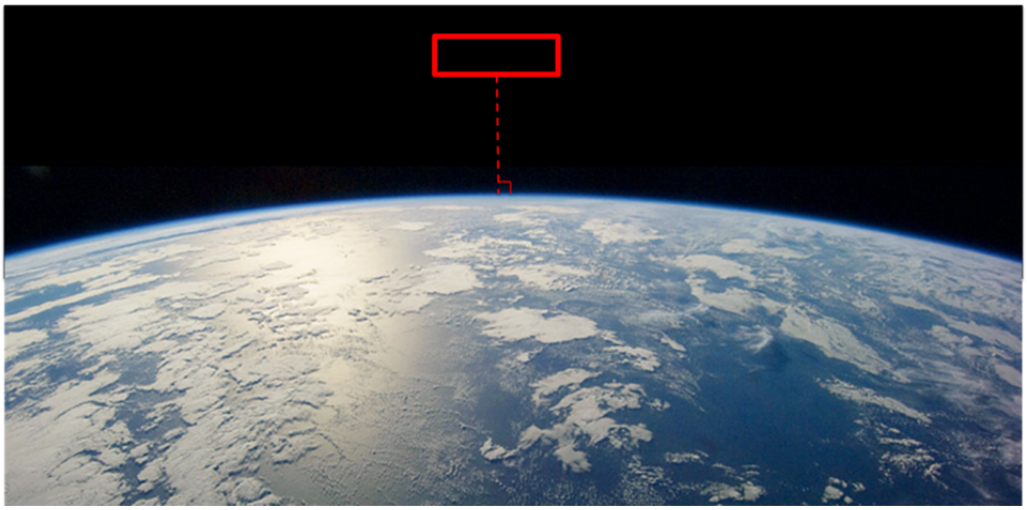

Figure 3.40: Conceptual slit projected into atmosphere from satellite borne instrument (not to scale).Adapted from *Riebeek* (2010). Image courtesy of the Earth Science and Remote Sensing Unit, NASA Johnson Space Center (ISS022-E-6674).

Figure 3.40 is meant for illustrative purposes only, with the approximate size of the slit projection significantly larger than what is defined by the field of view of the instrument. The altitude at which this projection is shown is also greatly exaggerated. For these types of

measurements, the distance between the aperture and the object plane area changes depending on the tangent altitude that is observed, based on the look direction of the instrument. This concept will be discussed further in Chapter 4. The important aspect to understand now however is that when the instrument images from above the ground, the object plane area increases with greater instrument heights and lower tangent altitudes.

For an instrument height of 600 km above the Earth and a line of sight defining a tangent height of 20 km, the object planes captured by the fields of view are shown in Figure 3.41.

Figure 3.41a illustrates that the fields of view of the original OSIRIS-DM slit and the OSIRIS-FM slit have a significant effect on the size of the projection area. Both of these slits had the same height and therefore the same horizontal field of view, so the projection areas both have a vertical height of approximately 1 km. In the vertical direction however, the flight model slit is roughly 3x larger, so the larger field of view results in a horizontal length of roughly 40 km compared to the 12 km imaged by the developmental model slit.

When looking at the multi-slit configuration for satellite-based measurements in Figure 3.41b, it is shown that the slits are separated by roughly 5 vertical kilometers, as designed. It is also evident that the size of the object planes defined by the slits varies for all three. As expected, Slit 1 which is the largest and has the largest field of view, images the highest altitude where it is expected that to receive the least signal. It also has the largest projected area based on its dimensions. Slit 3 on the other hand has the smallest area, but the area it collects light from is larger than that of Slit 2 due to the larger acceptance angle associated. The acceptance angle is only larger as a result of the aberrations associated with realistic optics, and is not a result of the physical size of the slits. It is important to recall the vignetting effect that was highly prevalent in

this slit shown in Figure 3.31. As a result of this effect, less light is collected from this area. This is once again designed for because the lower altitudes have the greatest radiance.

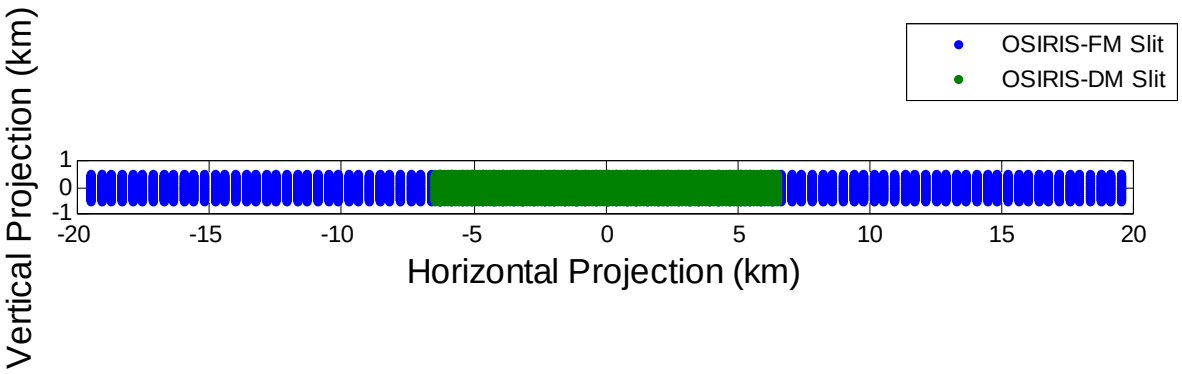

(a)

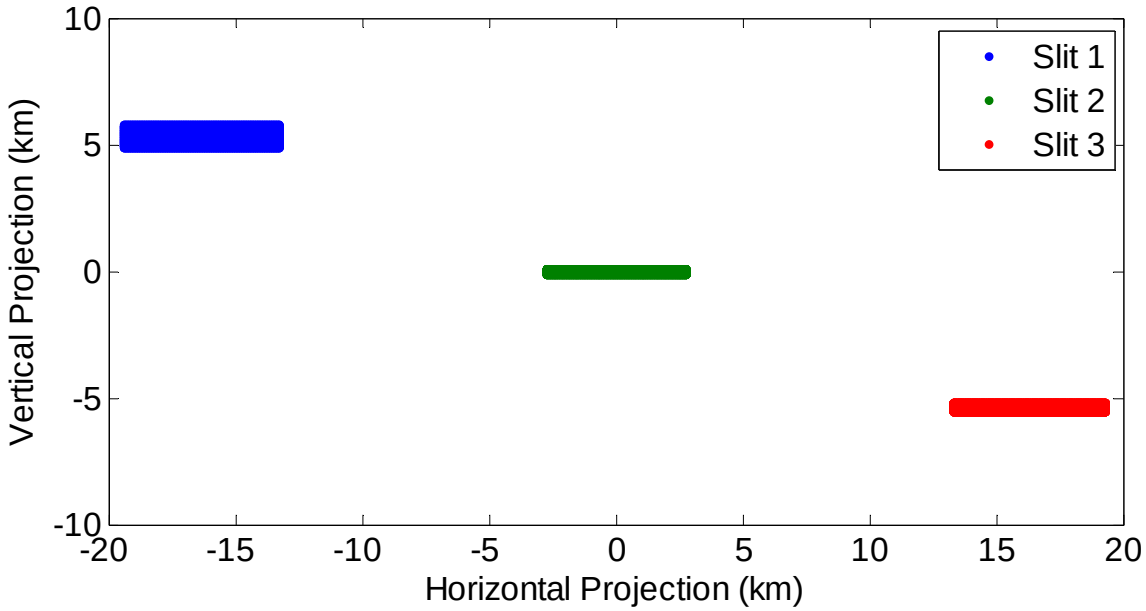

(b)

Figure 3.41: (a) Original OSIRIS-DM slit plate and OSIRIS-FM slit plate with the object plane 2784 km from aperture. (b) Multi-slit plate with object plane 2784 km from aperture.

3.4.3 Balloon Based Projections

Finally, the projection area for a balloon-based instrument is investigated. This is the environment that was used to make atmospheric measurements with the multi-slit OSIRIS-DM. For this analysis, the instrument was placed at an altitude of 36 km and viewing a tangent altitude of 20 km.

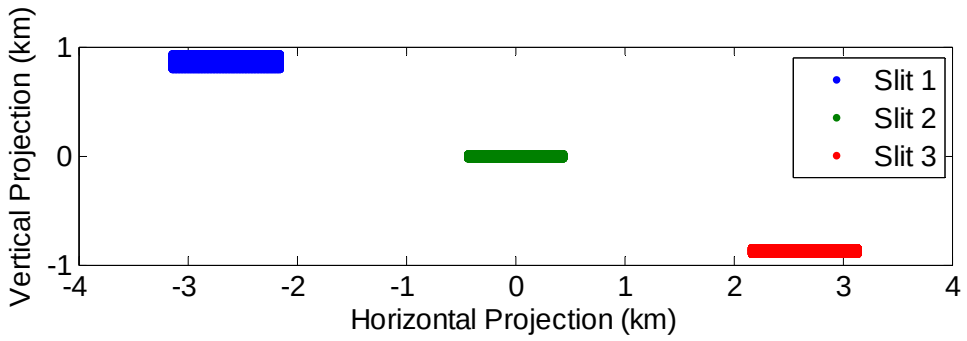

Figure 3.42: Multi-slit plate projection area at 452 km from aperture.

Figure 3.42 shows that for this viewing geometry, the projection areas are only separated by less than 1 vertical kilometer. This means that the radiances measured in the atmosphere will not vary significantly in the three fields of view. This effect will be examined closer in Chapter 5. It is also important to note that as the tangent altitude nears 36 km for this viewing geometry, the spacing between the projection areas approaches zero, and as the tangent altitude nears 0 km, the areas spread further apart. This effect is less prevalent in the two previous cases for geometric reasons. In the case of the lab-based measurements, the object plane is located too close to the aperture to allow for much angular spread for the three slits. In the case of the satellite-based geometry, the tangent altitudes are all much less than the height of the instrument and as a result the object plane is located very far from the entrance aperture. The balloon-based geometry

however merges these two situations, resulting in this interesting effect. The extent of this effect is shown in Figure 3.43.

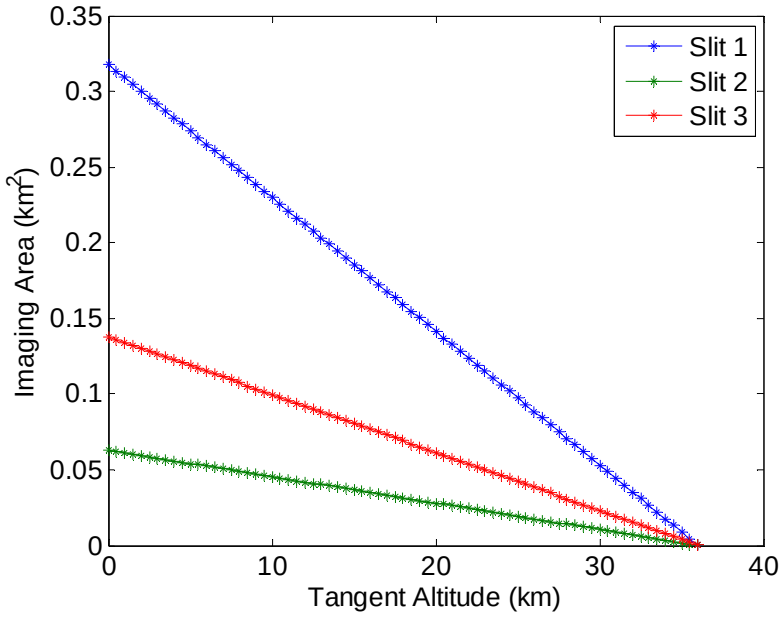

(a)

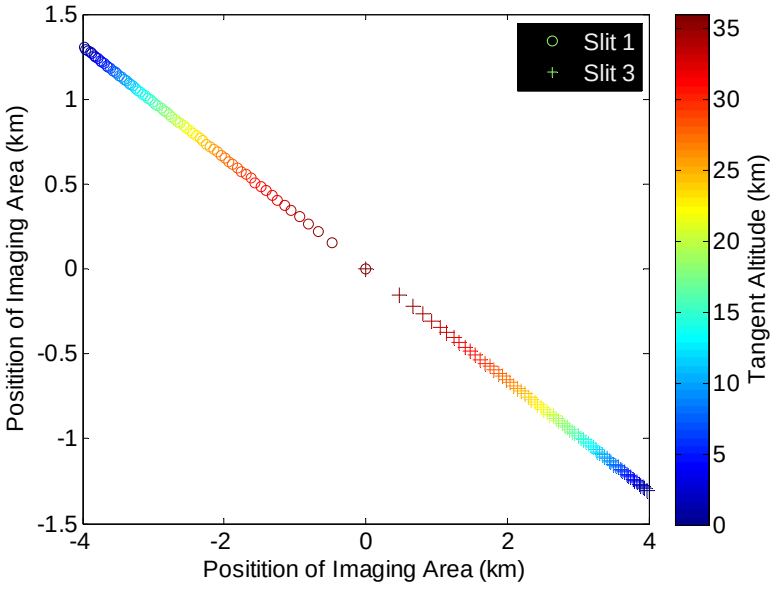

(b)

Figure 3.43: (a) Projection area for Multi-slit plate as function of tangent altitude measured from balloon-borne geometry. (b) Projection area location with respect to Slit 2 for Multi-slit plate as function of tangent altitude measured from balloon-borne geometry.

As shown in Figure 3.43, the projection areas decrease as the tangent altitude increases, and the areas imaged by Slits 1 and 3 move closer to the location of Slit 2 as the tangent altitude increases. In Figure 3.43b, the location of the projection area for Slit 2 is always located at (0, 0) km and the other slits are referenced to this. This is an effect that cannot be avoided in the balloon geometry, and therefore must be kept in mind while analyzing flight data.

The new multi-slit plate installed in OSIRIS-DM has been demonstrated to operate in an acceptable manner. Although the slit plate did not operate exactly as designed, it still demonstrates the ability to image light coming from different directions, which translates into imaging capabilities from different tangent altitudes in the atmosphere when positioned in the limb scatter geometry. The next step investigates the modifications required to convert lab-based instrument into a system that operates on a stratospheric balloon platform.

4. BALLOON-BORNE OSIRIS-DM SCAN MIRROR SYSTEM

It was desirable to perform a low cost satellite simulation of the new multi-slit instrument performance. Launching the instrument on a stratospheric balloon was a way to investigate the capabilities of the instrument in the limb scattering geometry, with significantly less cost than a satellite mission. As mentioned previously, the CSA and CNES opened a stratospheric balloon launch facility in Timmins, Ontario, which provided an ideal test scenario for this project under the FAST program.

The instrument was slated for launch in September of 2014. The flight requirements were set to reach an altitude ranging from 30-40 km for a period of at least four hours of sunlight measurements. The instrument was mounted on a gondola called CARMEN, which is controlled by CNES. The name CARMEN was chosen by the French design team, which synthesizes the qualities they strived for while designing the gondola (*Centre national d'études spatiales*). Along with OSIRIS-DM, four other instruments were also mounted on the gondola, so pointing of the gondola was standardized for all instruments involved.

4.1 Problem Description

In Chapter 3, the field of view was analyzed. Although there are three slits, and three separate fields of view, they are all fixed with respect to one another. Therefore for the purpose of this discussion, a single line of sight can be considered that is representative of these three fields of view. This line of sight is fixed with respect to the OSIRIS-DM instrument itself, and is directed along the optical axis that enters through the center of the entrance aperture. For the balloon-borne experiment, the instrument had to be rigidly secured to the gondola. As a result of this, the direction of the line of sight was defined only by the gondola pointing system, which as mentioned was fixed to accommodate all the instruments involved in the mission. Thus,

independent instrument level control of the line of sight was desirable in order to develop scanned vertical profiles for specific locations throughout the mission.

This requirement was split into two objectives. The primary concern was to have a system that was capable of scanning in the zenith direction from the balloon platform. This would allow the instrument to make measurements at varying tangent altitudes throughout the mission. The secondary concern was to have control over the azimuth pointing of the system. Additionally, the multi-slit plate has introduced a smearing effect on the CCD, which will be discussed in a coming section. As a result of this, a shutter was required to control the imaging and reduce this smearing. The final major constraint was that exposure times of approximately 0.5 second were desired, which must be sufficiently long with respect to the opening and closing times associated with a shutter system so that these are considered negligible. The instrument was designed to accommodate this with respect to the dynamic range of the limb signal.

The goal of this part of the thesis work was to build an optical system to interface to the multi-slit OSIRIS-DM, which redirects the instrument's line of sight, attenuates light for long exposures, and implements a shutter to reduce image smear. The optical system must effectively modify a system designed for a satellite based environment to operate on a balloon-borne platform.

4.2 Dual Axis Pointing System

The first step in building a system to meet the stated goal was to come up with an optical design to meet the requirements. Once the optics have been confirmed, a mechanical design was developed that would accommodate the optical design.

4.2.1 Single Mirror Pointing System

The most important aspect to bear in mind during the design of a pointing system was to maintain the orientation of the slits when they are projected into the atmosphere. This begins

with considering the orientation of the instrument with respect to the gondola platform. For a preliminary design, the instrument was oriented as shown in Figure 4.1.

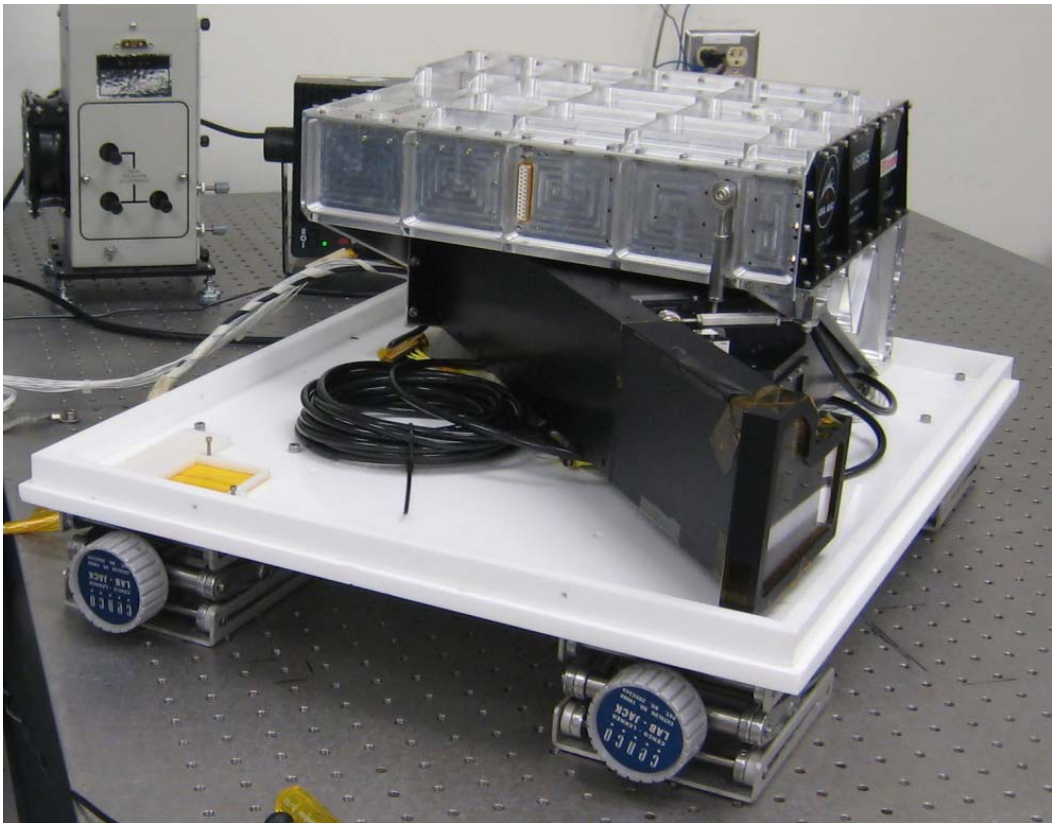

Figure 4.1: OSIRIS-DM dual axis mirror pointing system orientation.

In this configuration, the slit plate is rotated 90° with respect to the required orientation. This means that as the instrument sits right now, it would measure vertical columns of light in the atmosphere instead of horizontal rows as described in Section 3.4. This means that the pointing system installed on the instrument needs to account for this rotation.

The simplest system to add to this instrument was to place a mirror in front of the aperture that has the ability to be rotated in two dimensions. An example of this is shown in Figure 4.2.

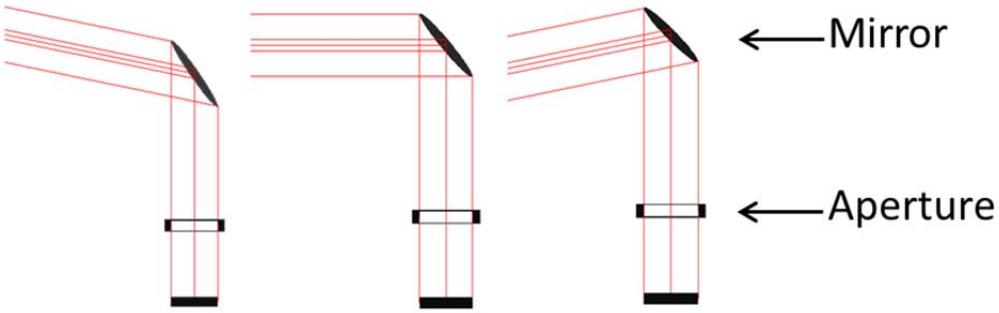

Figure 4.2: Top view of OSIRIS-DM aperture with single mirror in front. Three azimuth look directions are shown.

In this figure, the mirror has been rotated about the axis normal to the page. This represents the axis that would be normal to the base of the instrument if referenced to Figure 4.1. This figure shows that as the mirror is rotated about this axis, the azimuth look direction is altered for the instrument. Similarly, if the mirror is rotated about the axis lying in the plane of the page and parallel to the drawn mirror, then the line of sight will shift in the zenith direction. This suggests that a dual axis controlled mirror would meet the pointing requirements. It is important however to investigate the orientation of the slit as it is projected into the atmosphere. This is shown in Figure 4.3.

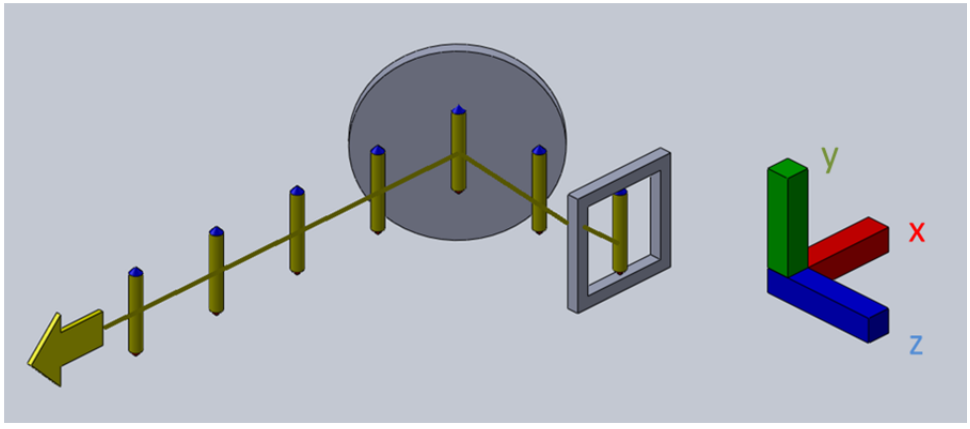

Figure 4.3: Slit indicator from aperture out into atmosphere with single dual axis mirror.

In this figure, the fields of view from all the slits are represented by a single element with an orientation representative of the orientation of the slit projection. This element is the yellow bar with colored caps. It will be referred to as the slit indicator, because it has a similar shape to the projection of the slit as it is mapped to the atmosphere in the limb scattering geometry. The slit indicator starts in the square aperture of the OSIRIS-DM, and is projected outwards towards the mirror, which then reflects it outward towards the atmosphere. For the slit indicator to be in the required orientation when it reaches the atmosphere, should lie along the x-axis defined in the figure. It is evident from this image that the slit indicator is not oriented correctly, so additional optical elements are required to correct for this.

4.2.2 Three Mirror Pointing System

A solution to this orientation problem was to add additional mirrors to accommodate the change in orientation of the slit indicator. This was achieved by reflecting the light over top of the instrument using three mirrors. This configuration is shown in Figure 4.4.

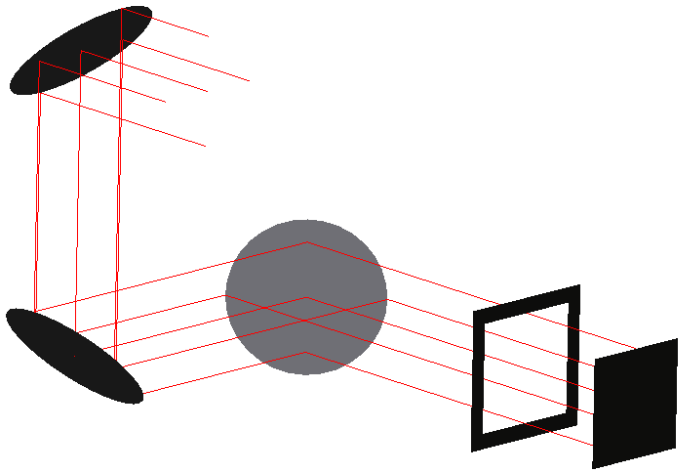

Figure 4.4: Three mirror pointing system with dual axis mirror.

In this orientation, the mirror furthest from the aperture was the mirror that could be rotated in two directions, and thus provided both pointing requirements requested. This mirror will be referred to as the scan mirror. The other two mirrors are each stationary and are only required for orientation correction. In Figure 4.5, the indicator is once again traced along the optical axis to verify that the correct orientation is achieved.

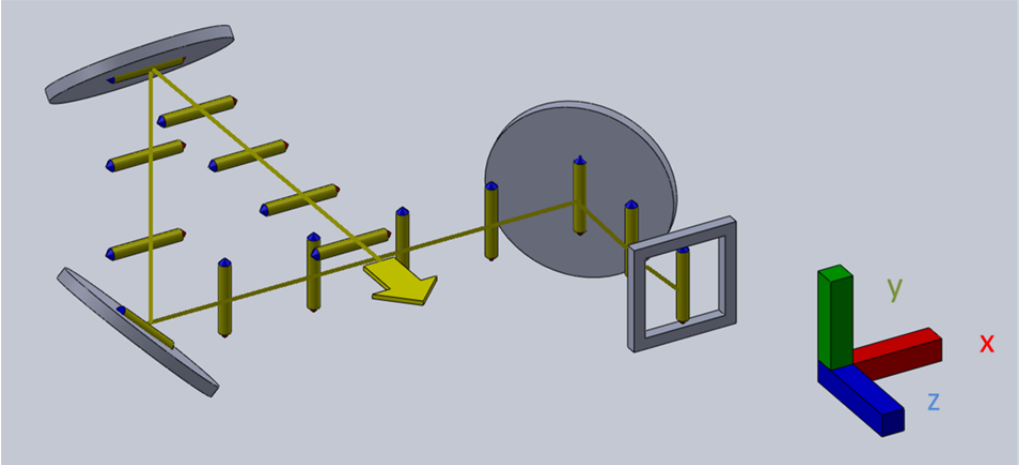

Figure 4.5: Slit indicator from aperture out into atmosphere with three mirror dual axis system.

In this orientation, the line of sight was directed over top of the OSIRIS-DM instrument itself, and the light that is captured originates from the opposite direction that the aperture faces. Not only was this preferred for the orientation of the slit indicator, as evidenced by the indicator aligning with the x-axis, but it also allowed for a more compact instrument to be built when a baffle was added to reduce external stray light. This will be explained in further detail later, but it is important to recognize the secondary benefit of this configuration.

Now, it is also interesting to address the fact that the orientation issue has been resolved simply by changing the direction from which the light is entering the system. Considering the goal of this system is also to change the direction from which light enters the system, it points

out a flaw in this simple design. To illustrate this point, the two objectives that have set out for the pointing system will be investigated to see if either of these causes an issue with the system.

First of all, the scan mirror will be rotated to image a different zenith angle. With reference to Figure 4.5, the mirror in Figure 4.6 has been rotated such that the line of sight is now at an angle θ with respect to the original position.

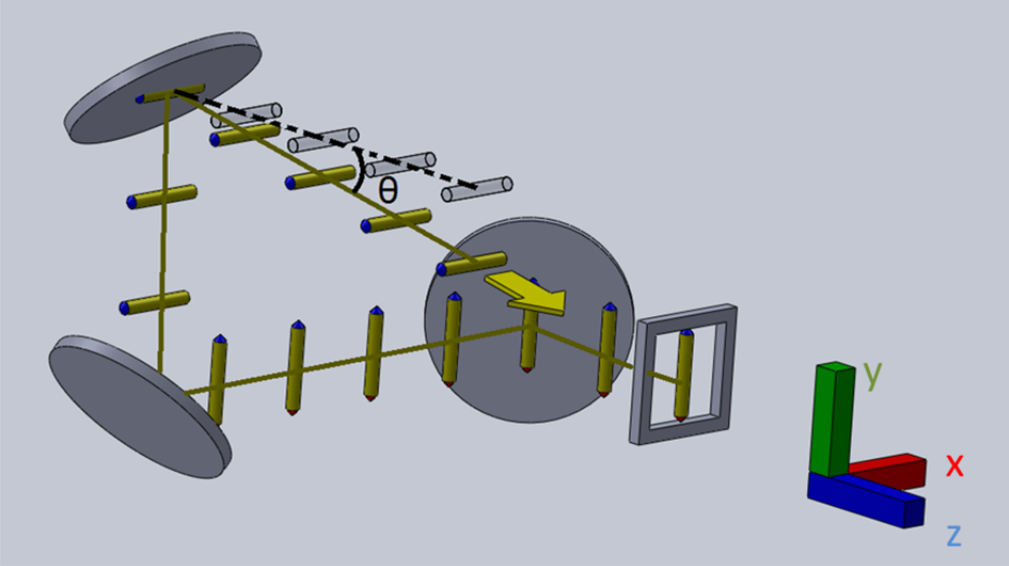

Figure 4.6: Slit indicator from aperture out into atmosphere with three-mirror dual axis system performing zenith scan.

When the scan mirror performs a zenith scan in this configuration, the slit indicator remains in the preferred orientation. The line of sight however is now pointed further downward (in the –y direction) than it was in the previous case. Now, if the scan mirror performs an azimuth scan, Figure 4.7 shows how the indicator is affected.

In Figure 4.7, the mirror has first been rotated in the azimuth direction by an angle φ, and then rotated in the zenith direction by θ. From this image, it is obvious that the orientation of the slit indicator no longer meets the requirements, which was foreshadowed by the original single mirror configuration. This means that when the scan mirror rotates in the azimuth direction, the

orientation of the slit indicator rotates as well. This effect is unacceptable because the light entering the system must come from a horizontal strip in the atmosphere in order to produce a valid radiance profile. Based on the orientation of the slit indicator, the instrument would capture a diagonal section of the atmosphere with respect to the Earth if it were placed on a limb scattering geometry platform. It appears that moving to a three-mirror system has not solved the image rotation problem that ruled out the single mirror configuration, although structurally this was still preferred over the first option.

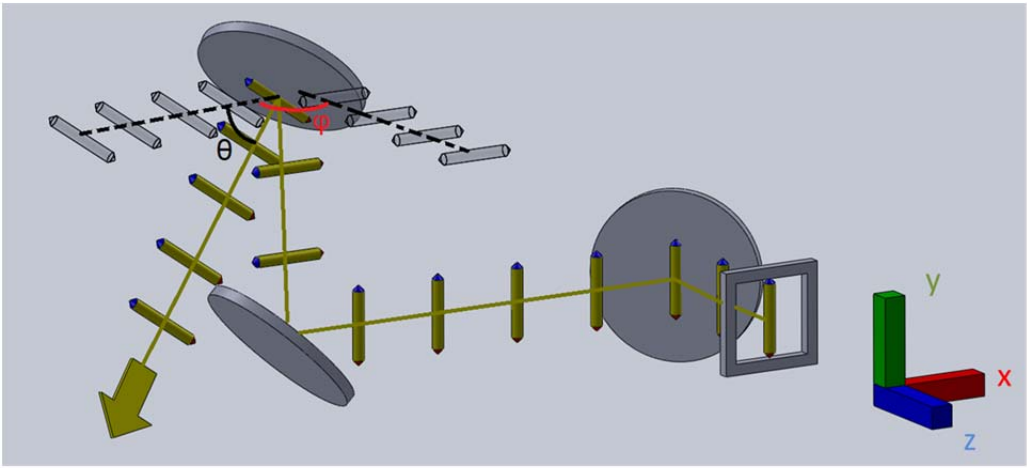

Figure 4.7: Slit indicator from aperture out into atmosphere with three-mirror dual axis system performing azimuth and zenith scan.

An optical solution to this problem was to use an element called a dove prism. A dove prism is a truncated right angle prism that utilizes total internal reflection which introduces two interesting characteristics to the transmitted light. The first of these characteristics is that the light that has traveled through the element will be mirrored about one axis. This characteristic has no undesirable effects on this system because the prism would be oriented in such a way that the mirroring effect will occur in the direction that maps to the wavelength distribution on the

CCD as the light passes through the entire system. The second and much more important characteristic of a dove prism is that a rotation of θ about the longest axis of the prism will result in a rotation of 2θ of the light passing through it. This property is easiest to see with the aid of an illustration:

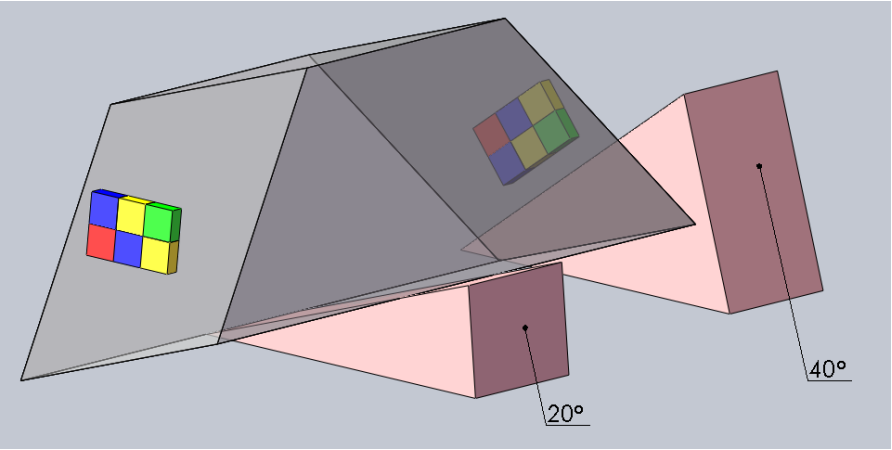

Figure 4.8: Dove prism displaying rotation of transmitted image.

In Figure 4.8, it is shown that the dove prism is rotated 20° with respect to the orientation of the base of the quad-colored object on the left side. The transmitted image on the right hand side displays both properties indicated earlier. Firstly, the transmitted image has been mirrored, and secondly the image is rotated by 40°. This shows that the addition of a dove prism to the optical chain could counteract the rotation caused by the azimuth-scanning feature of the scan mirror, as long as these are rotated in a corresponding 1:2 ratio. One constraint involved with adding a dove prism to the system is that there is a size limitation on available prisms. As a result of this, additional optics will be required to ensure that all the light required to fill the aperture of the instrument is properly rotated. This will be discussed in greater detail shortly. The final optical component required is a stray light baffle affixed to the front end of the pointing system. Although this is technically an optical component, it will be customized for this instrument and

therefore a full mechanical design will be required. For this reason, the design process will be discussed in Section 4.5.

4.2.3 Three Mirror Mechanical Design

As mentioned, the instrument was scheduled for launch in the late summer of 2014. For the two years leading up to this, it was important to keep in contact with the flight managers from the CSA as well as CNES to ensure smooth integration of the system onto the gondola. One of their requirements was to consistently provide updates on the mechanical structure of the instrument. Although the optical design was nearing completion, a very important design step revolving around the dove prism was yet to be completed. The CSA however required a structural update, so a first draft of the mechanical design was drawn with SolidWorks. The following illustration is helpful to get an overall feel for the development of the pointing system as a whole.

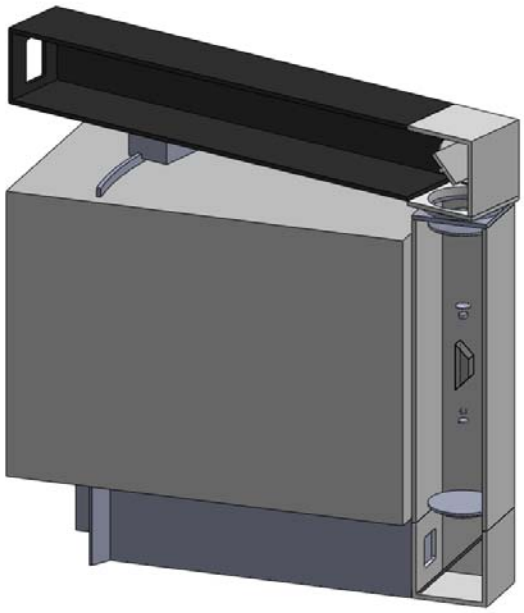

Figure 4.9: First draft of OSIRIS-DM pointing system for stratospheric balloon launch.

Figure 4.9 shows one of the early stages of the mechanical design of the pointing system added to OSIRIS-DM. In the figure, OSIRIS-DM is the dark grey box at the very bottom of the stack. Above it, the light grey box is a dummy region that was originally intended to hold the new power supply and computer boxes that control OSIRIS-DM and its pointing system. These components will not be described in this work, so a simple box will suffice as a placeholder in design images. In this image, the two stationary mirrors were modeled as a single mirror at the bottom of the optical chain, and a simple lens series is added to symbolize the additional rotation optics required for the dove prism to operate. It is apparent that the length of the optical chain of the rotation optics would primarily dictate the overall height of the pointing system. Although they are not shown in this image, rotation stages are required to rotate both the dove prism and the scan mirror/baffle region. These items had not been finalized so they were not included in the preliminary drawings. It is shown also that the baffle has yet to be completed, because it required the rest of the design to be finalized before it could be constructed. A dummy baffle has been included to show that it will slide along a curved track in order to be redirected in the direction chosen by the scan mirror.

As was mentioned previously, the three mirror system is structurally preferred primarily because it allows the baffle to rest upon the instrument. If a front end baffle were added to the single mirror system, it would be required to rotate on the base plate, which would mean that there would be a large amount of wasted space in the volume of the designed pointing system.

4.2.4 Rotation Optics

The task at hand that needed to be solved by the rotation optics was to rotate the light collected from azimuth scanned measurements to the correct orientation without disrupting the relative input angles or size of the beam as it reached the entrance aperture of OSIRIS-DM. As mentioned earlier, dove prisms are only commercially available in a limited size, typically less

than 15 mm × 15 mm. Recall from Chapter 3 that the entrance aperture is 36 mm × 36 mm. This means that the diagonal of the aperture is 50.9 mm. Considering the rotation effect can rotate the image by up to 90°, the entire diagonal length of the aperture must be able to pass through the smallest part of the dove prism, which is 15 mm. Available dove prisms do not meet the requirements alone, so condensing and expanding optics were required on either end of the dove prism. This is demonstrated in Figure 4.10.

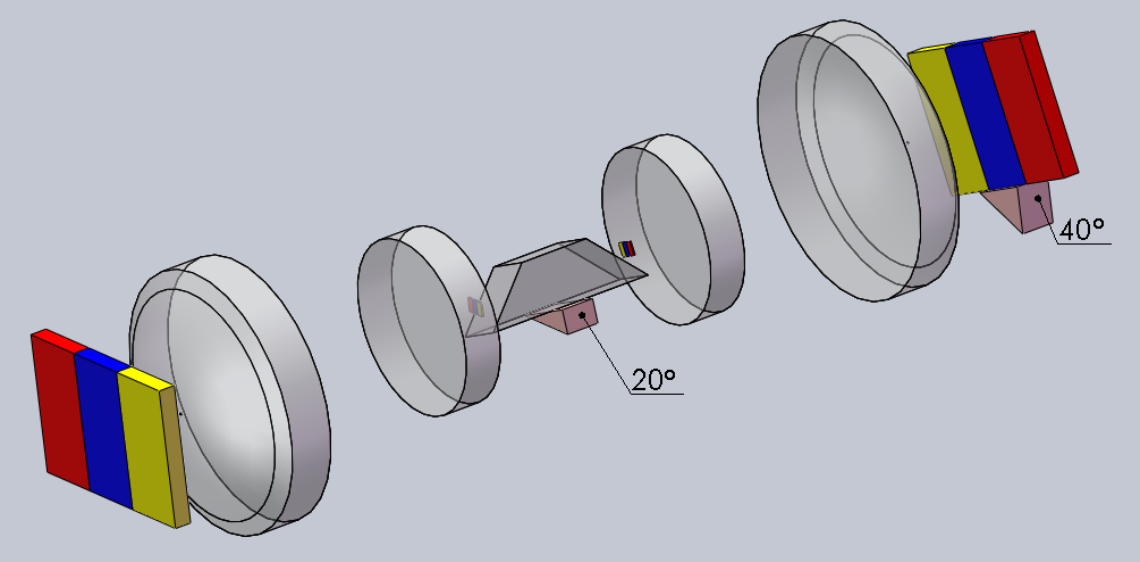

Figure 4.10: Rotation optics with sample image passing through.

Figure 4.10 demonstrates that the original size of the object has been maintained but the orientation of the image has been rotated. Figure 4.10 shows a simple two lens system used to condense the incoming light, and then the same system in reverse is used to expand the light back to its original size. A lens with this property is known as an afocal lens, but combinations of lenses can also be used to produce this characteristic.

With an afocal lens series, rays entering the lens parallel to the optic axis will also leave the lens parallel to the optic axis (*Bass et al.*, 2010). The heights of the rays will change however. This is shown in Figure 4.11.

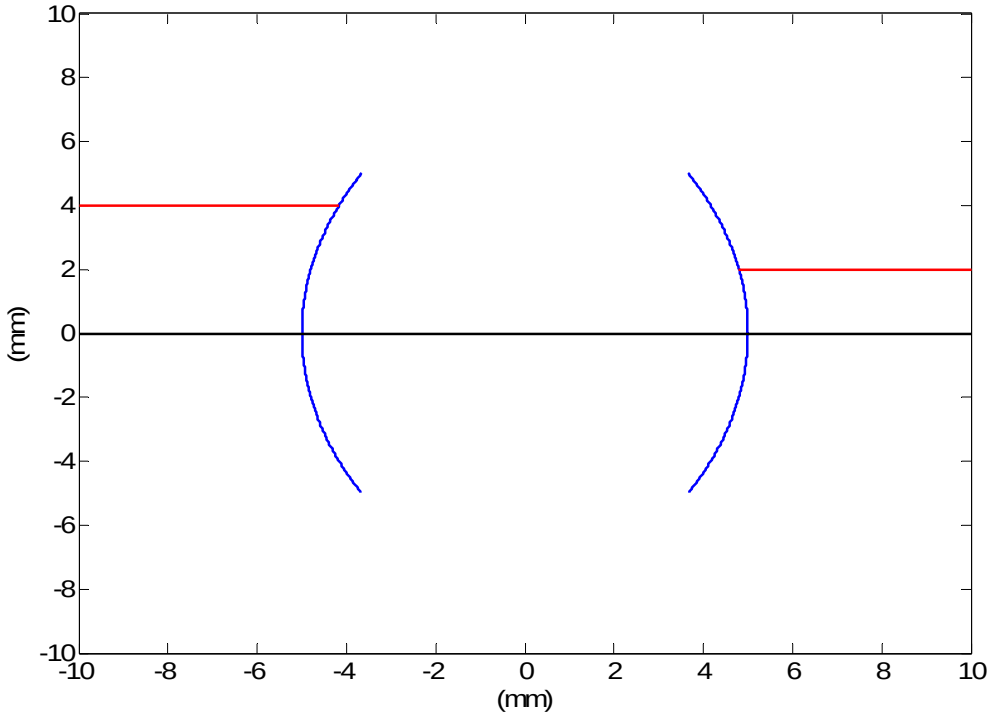

Figure 4.11: Arbitrary afocal lens with parallel paraxial rays, adapted from *Bass et al.* (2010).

In this example, rays coming in have a height of 4 mm, and the rays exiting the lens have a height of 2 mm. The ratio of the heights of the incoming and outgoing rays defines the transverse magnification, *m*. This value is constant for an afocal lens system. In the afocal lens sketch, the magnification is 1/2. This is an arbitrary lens and does not represent a real system. For the optical sizes in the pointing system being designed, the transverse magnification of the afocal lens system must be less than 0.3.

Afocal lenses also have an associated angular magnification, which is the ratio of angles of incoming and outgoing rays. This value is also constant for an afocal system. The relationship between the angular magnification and the transverse magnification is defined by:

$$m_\alpha = \frac{n}{n'}\frac{1}{m} \qquad \text{(Eq. 4.1)}$$

Where m_α is the angular magnification and n and n' are the refractive indices of the object and image spaces. In this case, the refractive indices are the same so the angular magnification is equal to the inverse of the transverse magnification. The angular response of an afocal system is shown in Figure 4.12.

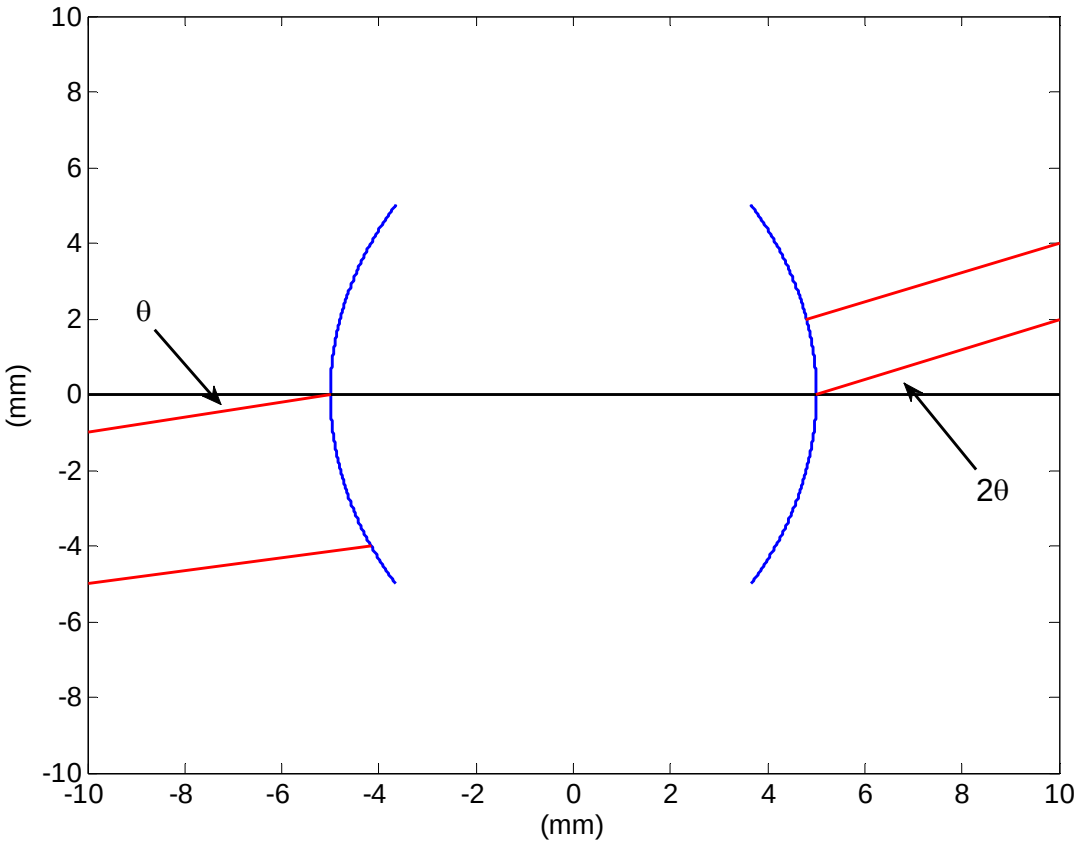

Figure 4.12: Arbitrary afocal lens with off-axis rays, adapted from *Bass et al.* (2010).

The lens in Figure 4.12 uses the same magnification constants as those used in Figure 4.11. Therefore, rays entering the system at an angle θ to the optic axis will leave the system at an angle 2θ as shown because the angular magnification is 2.

These characteristics caused a large problem for the rotation optics system that was in the design phase. The fields of view of OSIRIS-DM had to be maintained, but with these afocal systems in front and behind the dove prism, it was unlikely that light from the entire field of view would pass through the dove prism and be maintained by the time it reached the expanding optics. Although this design was not pursued further, this work has been documented for future work by the OSIRIS research group.

4.3 Three Mirror Single Axis Pointing System

By late summer of 2013, it was decided that the two-axis scan mirror system was too ambitious to complete and test before the expected launch date. As mentioned, the azimuth scan was only a secondary objective, but was not entirely necessary to meet the primary goal of obtaining radiance profiles from the atmosphere. The previous work however was not done in vain, because it gave a fuller understanding of the design problem and insight into the structure that should be aimed towards for the single axis scanning system.

The starting point for the new system was to maintain the three-mirror system described earlier. It was already shown in Figures 4.5 and 4.6 that scanning the mirror in the zenith direction for this orientation maintained the required orientation of the slit indicator.

It was now important to define the pointing requirements for the zenith scan mirror. A simplified sketch is shown in Figure 4.13 to better understand the geometry associated with the balloon flight.

In Figure 4.13, the horizontal line of sight is set as the look direction defined by the instrument looking out parallel to its base plate. The look direction is then shifted by angle θ to achieve differing tangent altitude measurements. A tangent altitude is defined as the altitude at which the line of sight is tangential to the surface of the Earth directly below. In Figure 4.13, it is shown that tangent altitudes near the instrument height are defined close to the instrument, whereas tangent altitudes that are small are defined further away from the instrument. It is also shown that for tangent altitudes near the instrument height, the angle is very small, whereas for smaller tangent altitudes the angle grows. It is important therefore to define the maximum angle that will be required for viewing in order to start selecting parts for this design.

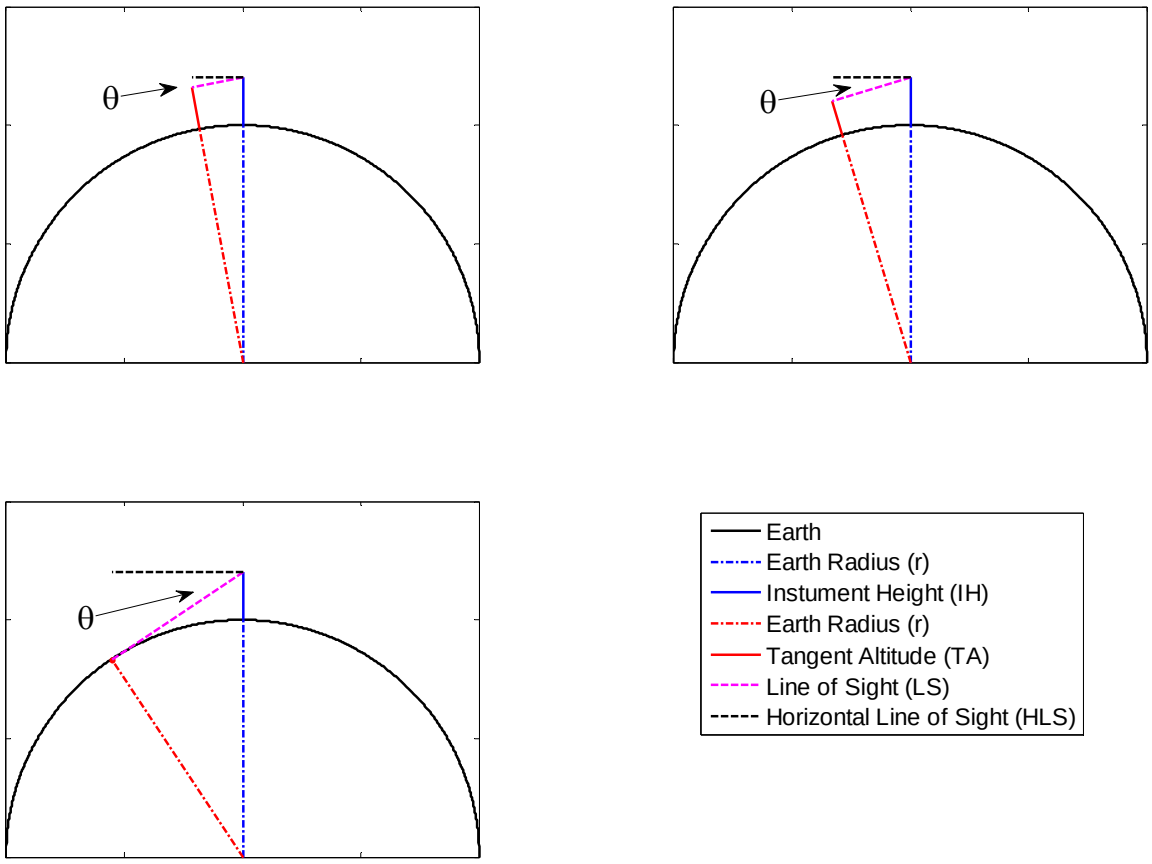

Figure 4.13: Balloon-Borne instrument geometry for various tangent altitudes.

Based on the geometry described, it can be shown that the angle for a given tangent altitude is defined by:

$$\sin(90 - \theta) = (\frac{TA + r}{IH + r}) \quad \text{(Eq. 4.2)}$$

For the balloon geometry that will be utilized in this mission, the instrument height (IH) will be around 35 km, the radius of the Earth (r) is 6371 km, and the tangent altitude will range from 0 km to 35 km. Figure 4.14 shows the relationship between tangent altitude and look direction angle.

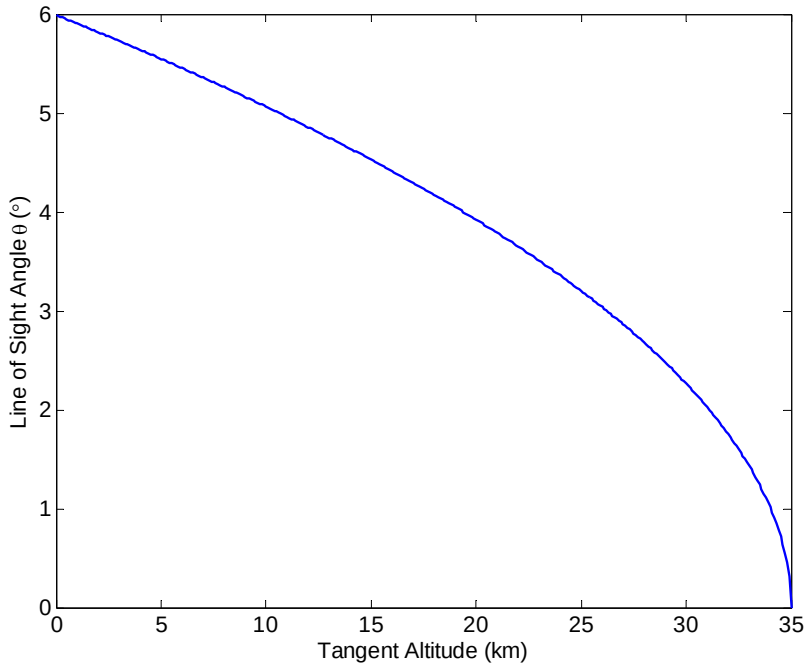

Figure 4.14: Relationship between tangent altitude and line of sight angle for balloon geometry.

It is shown that the line of sight angle will range from 0° to 6°. Based on the properties of a mirror, the reflection angle is equal to the incident angle. This meant that the mirror needed a range of 0° to 3° of mobility.

Once again, the CSA was requiring an update on the footprint of the instrument, so a rough SolidWorks sketch was provided, as shown in Figure 4.15.

This figure shows that the three mirrors have been mounted in front of the aperture to OSIRIS-DM, and a baffle has been added to the front end. The total field of view defined by the 6° line of sight angle has also been included. This drawing also includes a 3° wedge that the instrument is sitting upon. The pointing system was defined such that on the lab bench, the field of view represents ±3° from horizontal, so this wedge adjusts that by the required 3° in order to view only downward directions from the horizontal when the instrument is mounted on the gondola of the balloon. The mirror mounts selected for this design were purchased, and will be discussed further in a following section.

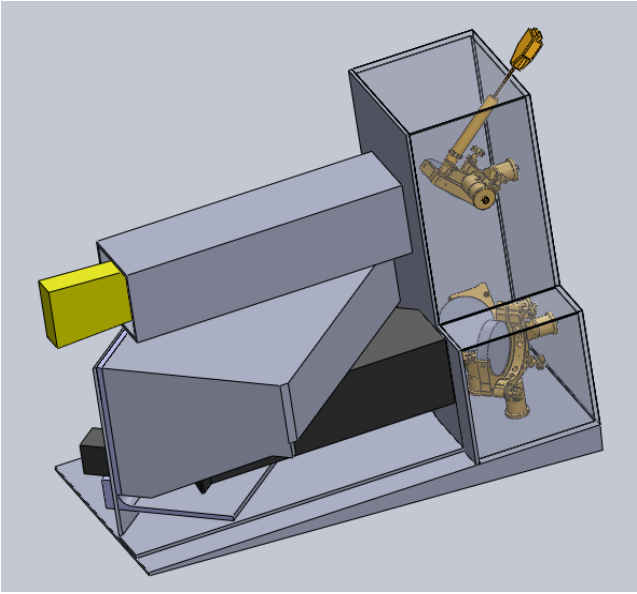

Figure 4.15: Draft of three mirror single axis pointing system for stratospheric balloon launch. The second stationary mirror is partially hidden behind the first, which is positioned directly in front of the OSIRIS-DM aperture.

4.4 One Mirror Single Axis Pointing System

Around the time that this current design was being finalized, the instrument was transported to Kanata, Ontario for modifications to the slit plate described in Chapter 3. While at COM DEV, a discussion was held with the original team that built the OSIRIS-DM about the structure of the instrument. It was determined that the brace used to hold OSIRIS-DM was produced only to ease lab based measurements, and did not dictate any preferred orientation of the instrument. With this information, new design opportunities were opened up that allowed for the instrument to be rotated in orientation. This meant that the instrument could be mounted in any orientation that may be preferred by a specific optical design. This would reduce the number of reflecting surfaces required in front of the aperture. This also meant it was back to the drawing board one last time to come up with a simplified single axis pointing system.

4.4.1 Ray Tracing

OSIRIS-DM comes equipped with two legs extending from the rear of the instrument that are designed to be heat sinks for the detectors within. These legs are designed to be mounted to a radiator plate which is utilized on OSIRIS-FM. OSIRIS-DM also had a radiator plate produced, which was available for this project. It was determined that by placing the radiator plate flat on the lab bench, the instrument was very sturdy. Figure 4.16a demonstrates the instrument standing on these two legs to indicate the preferred orientation of the instrument, which acts as a reference for the optical path that the light now follows through the instrument.

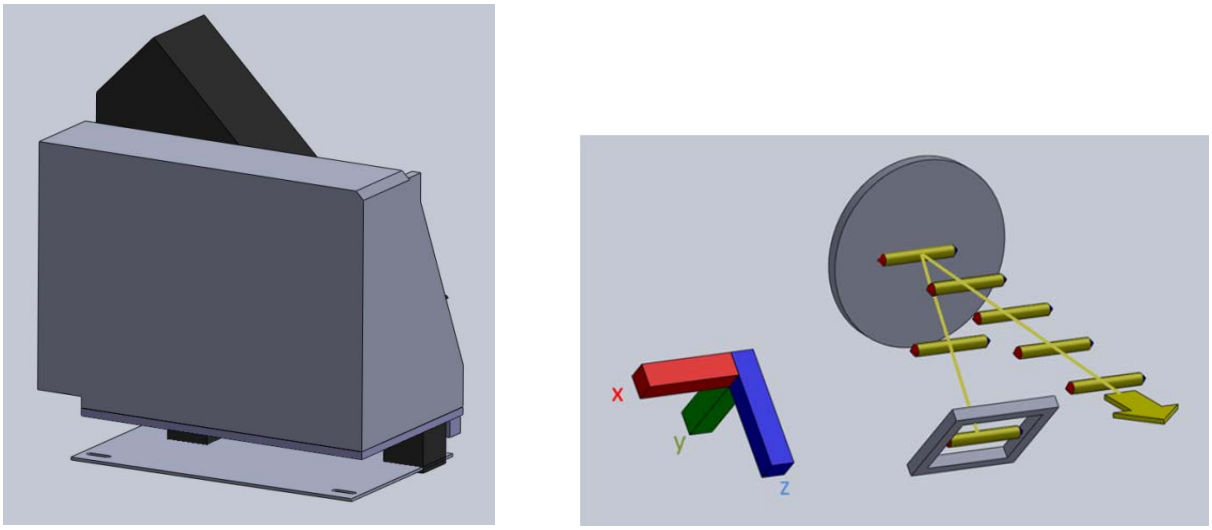

(a) (b)

Figure 4.16: (a) OSIRIS-DM standing on heat sink supports mounted on radiator plate. (b) Slit indicator from aperture out into atmosphere with single axis one mirror system.

In this orientation, only a single mirror was required to perform the zenith scan as shown in Figure 4.16b. This mirror was capable of performing a zenith scan while retaining the slit indicator orientation. This option was analyzed with ray tracing, as shown in Figure 4.17.

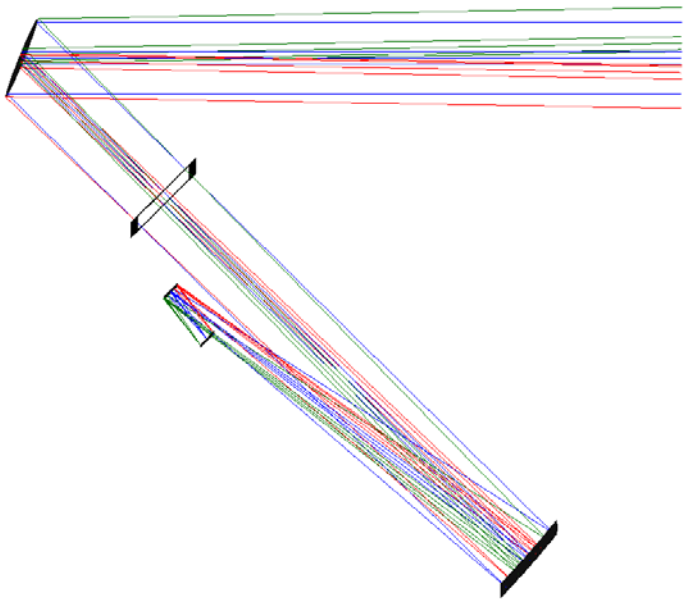

Figure 4.17: Single axis single mirror pointing system with 3 directions of incoming light.

Figure 4.17 shows light entering the system from three different directions with a single mirror position. The rays in these images are traced from the atmosphere until they reach the slit plate to demonstrate the where they will strike it. Recall Figure 3.26. In this image, it was shown that the slits are aligned such that the largest slit is on the side of the slit assembly that is closest to the CCD, and the narrowest slit is closest to the objective mirror. Bearing in mind that the largest slit is designed to view the highest altitude and the narrowest slit should view the lowest altitude, then it is shown in Figure 4.17 that this system meets these requirements. The red rays are coming from the lowest altitude, and they strike the slit plate on the side closer to the objective mirror. The blue rays come in from a mid-altitude, and they the center of the slit plate, and finally the green rays coming from the highest altitude strike the slit plate on the side that is closest to the CCD. It is important to note that for each of these three situations, the mirror has not moved, meaning only a single line of sight has been defined. This optical design became the finalized design for this project.

4.4.2 Parts Description

Now that the optical design was finalized, it was now time to start selecting parts for the mechanical design. The selected parts are detailed below.

Mirror

The first item to be selected for the pointing system was the mirror. The starting point for this selection was first to determine the sizing requirement of the mirror. Based on the geometry of OSIRIS-DM as it stands on the heat sink posts, optic axis from the aperture to the objective mirror is elevated 45° from the horizon. Therefore, if rays parallel to the horizon are required to be directed towards the aperture, the mirror must be positioned 22.5° with respect to the aperture. This is the case shown for the blue rays in Figure 4.17. The mirror will then rotate a maximum of 3° from this position in order to scan the required 6°. With this geometry, it was now possible to

determine the spot size required on the mirror to fully illuminate the 36 mm × 36 mm aperture. This is shown in Figure 4.18.

Figure 4.18 shows the full range of the aperture spot size on the mirror, taking the ±1.5° rotation into account. This was calculated simply based on the geometry of the system. The region outlined is therefore the maximum reaches of the spot size for any mirror angle. The figure shows that the minimum mirror diameter for this geometry is 53.7 mm. Therefore, a mirror had to be selected with a usable diameter greater than this value. Standard mirror diameters are typically in half-inch denominations, so a 3-inch mirror with 80% usable diameter would meet the mirror requirements. Although the full surface of mirrors are covered with a reflecting coating, it is typically suggested that only the central portion is used to reduce imaging flaws caused by edge effects of the mirror, therefore a usable diameter is suggested.

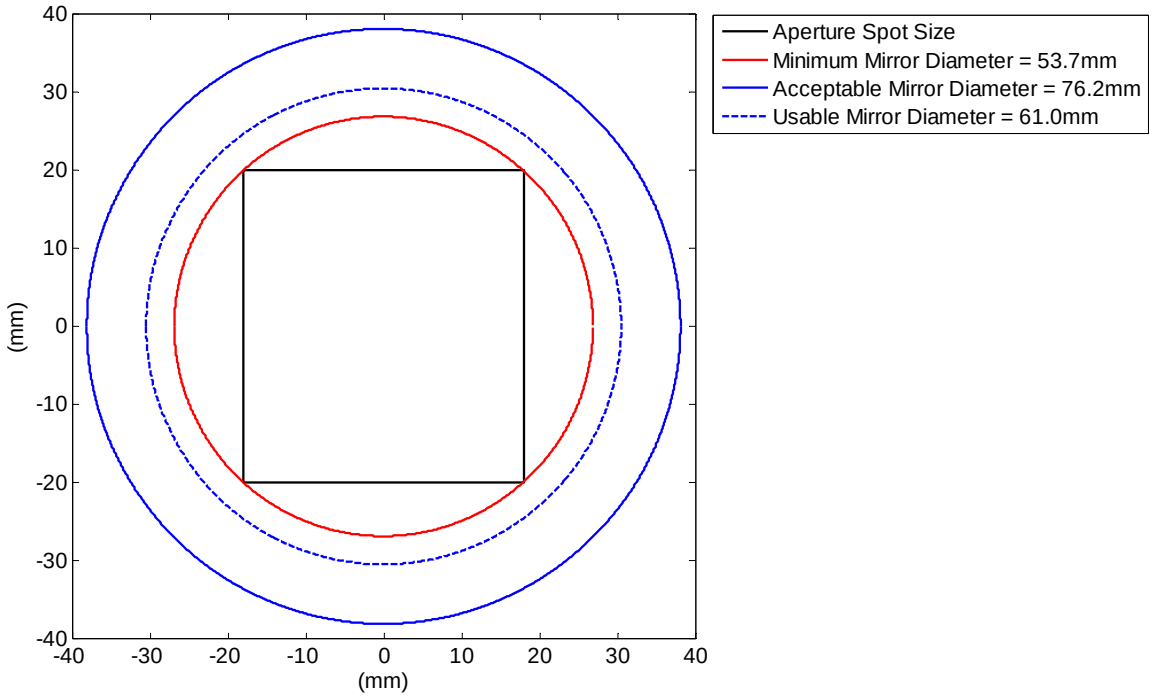

Figure 4.18: Aperture spot size on scan mirror with acceptable mirror dimensions.

Now that the sizing requirements were finalized, the next step was to decide upon the substrate and surface coating for the mirror. The mirror should be a first surface optical mirror to reduce any refraction effects that would be caused by the light travelling through the substrate of a second surface mirror. The mirrors in OSIRIS-DM are made of fused silica with a protected, unenhanced aluminum coating (*Warshaw et al.*, 1996). The scan mirror therefore was chosen to match these mirrors. Mirrors of this variety were available from Space Optics Research Laboratories, who produced the mirrors in OSIRIS-DM, but they were beyond the budget of this project. The mirror selected for this project was made by Advanced Optics Inc. It has a diameter of 76.2 mm and 85% usable diameter.

Mirror Mount

Now that the mirror was selected, an appropriate mount was required. The main requirement on the mirror mount was the flexibility to rotate the mirror up to 3°. Solutions to this are easily accessible from numerous optics companies. The mount that was selected was an Ultima U300-A3K Clear Edge Mirror Mount from Newport Corporation. This mount comes equipped with three micrometers for adjustments in three dimensions of up to ±3.5° and is spring loaded to offer long term stability. The mount is designed such that the micrometers can be removed and replaced by adjustable screws or motorized actuators, which was ideal for this project.

Actuator

To control the mirror position, a TRA12PPV6 Miniature Motorized Actuator was also purchased from Newport Corporation. This actuator offers 12 mm of linear travel and is designed to interface with the Ultima series of mirror mounts. The actuator is vacuum compatible, meaning it does not contain any outgassing oils that would contaminate the surface

of the mirror in a low-pressure environment. In Figure 4.19, the actuator is shown interfaced with the mirror mount.

Figure 4.19: Mirror mount with interfaced actuator. The actuator is the long tube extending from the back of the mirror mount.

In Figure 4.19, the actuator is shown extending from the back side of the mirror mount. It is the long tube-like structure with white cables coming out of it. The actuator arm has been extended to rotate the mirror mount. This is the reason that the front of the mirror mount does not lie parallel to the back of the mount. This figure demonstrates how the actuator can rotate the mirror when it is mounted in this mirror mount.

The actuator is controlled by a SMC100PP Single-axis stepper motor controller/driver, also available from Newport Corporation. This controller is not vacuum compatible as available off the shelf, so modifications were required for balloon flight. The main alteration that was performed was to replace the electrolytic capacitor with tantalum capacitors. Electrolytic

capacitors have a sealed compartment, which would burst in low pressure, so the electrolyte within would leak out and render the capacitor useless.

Shutter

As mentioned previously, the multi-slit plate introduces a smearing effect on the CCD. Without a shutter, the CCD is constantly illuminated by light passing through the three slits. This means that when an image is captured, in order to be clocked out, the pixels must move through all three illuminated rows. The same effect is also prevalent before the exposure is started because the CCD operates by continuously clocking out the pixels between exposures. This causes a problem because it means the pixels would measure some portion of light from all three slits, which is undesirable. This effect was shown in Figure 3.37b. In order to combat this, a shutter can be used. The shutter must be closed whenever the pixels are being clocked through the CCD, whether that is before or after an exposure. Recall also that the open and close times of the shutter are required to be much less than 0.5 s.

The shutter selected for this project was a CS65 65 mm Uni-stable Shutter by Uniblitz Shutter Systems. The aperture of this shutter was large enough to allow all the required light for the system to travel through unimpeded when opened and it met the timing requirements set forth, which will be examined shortly. The shutter was driven by a D880C Open Frame Uni-stable driver. This shutter operated using only one input voltage to either open or close the shutter. This driver also required similar modifications to the ones described for the actuator driver. The shutter and driver are shown in Figure 4.20.

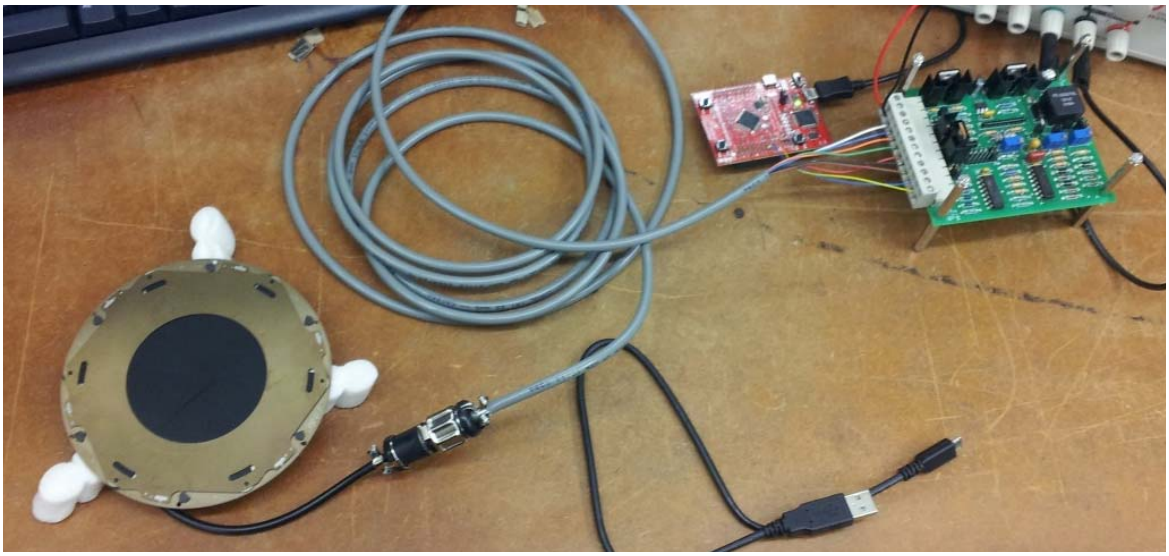

Figure 4.20: Shutter (bottom left) and shutter driver (top right).

Mechanical Enclosure

The mechanical enclosure for the pointing system was made primarily of two types of components. The first of these are Aluminum T-Slotted Framing Extrusions, and the second are Aluminum panels. Figure 4.21 shows an example of most of the pieces used to build the enclosure.

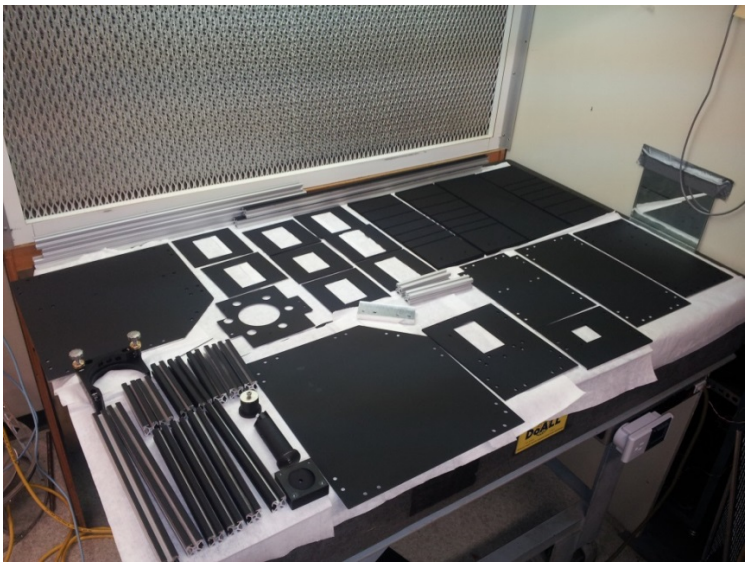

Figure 4.21: Aluminum extrusions and panels used to build pointing system enclosure.

The Aluminum extrusions are the posts shown in the lower left corner of Figure 4.21. These were purchased from McMaster-Carr and cut to the appropriate lengths by technicians at the Physics Machine Shop at the University of Saskatchewan. The Aluminum panels and additional mounting pieces were designed using SolidWorks and were also produced by these technicians. Further details of this design will be shown in Section 4.6.

4.4.3 Shutter Analysis

An important first step when configuring the system was to determine the minimum exposure time that the shutter could provide. As was briefly mentioned earlier, the shutter driver requires only a single input. When the voltage at this input is high, the shutter opens, and when it is low, the shutter closes. Therefore, an exposure time is defined as the time in which the pulse is high. There is of course a finite time that the shutter requires to open its blades, as well as to close them. These transition periods were addressed by measuring the radiance measured by OSIRIS-DM with exposure times that ranged from those that were too short for the shutter to fully open to those that were sufficient for the shutter to open completely before closing once more. The expectation is that after a certain exposure time that defines the minimum exposure, the shutter will be fully opened and pixel counts should increase linearly with exposure time. Before this point however, an unpredictable pattern should be noticed that is defined by the extent to which the shutter can open within the exposure time. The results of this test are shown in Figure 4.22.

This figure shows 5 test pixels selected arbitrarily from the illuminated area of the CCD to determine the minimum exposure time of the CCD. An exposure time also had to be set on the CCD, so it was selected to be much longer than the shutter exposure times. The number of counts on each of these test pixels was then plotted as a function of shutter exposure times. From this figure, it is shown that the transition point between the two cases described earlier is in the

70 ms range. For exposure times shorter than this, an unpredictable pattern is observed. However, for exposure times longer than 70 ms, the photon counts picked up by each pixel of the CCD increases approximately linearly with time. From this it was determined that a safe minimum exposure time the system would use was 100ms.

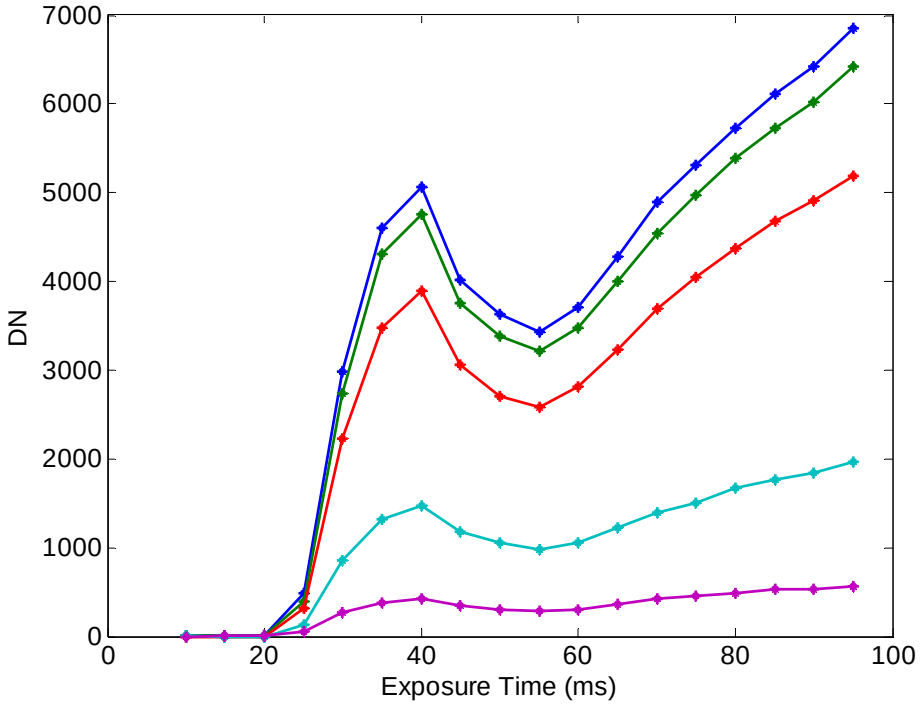

Figure 4.22: Exposure time tests to determine minimum exposure time for installed shutter. Arbitrary pixels were chosen within illuminated region of CCD.

4.4.4 Exposure Time Analysis

It was now important to verify that the OSIRIS-DM with pointing system would be versatile enough to operate on the balloon with regards to exposure times. The shutter has defined a minimum exposure time of 100 ms, and the OSIRIS-DM electronics system defines the maximum exposure time to be 10 s. It was decided that the ideal exposure time for low altitude measurements was 0.5 s. This gives the freedom to adjust the exposure time up to 20x higher or 5x lower and still be in the accepted operating range.

It was likely that a reduction in sensitivity would be required in order to meet these requirements. The following method was performed to investigate if any alterations needed to be made to the instrument.

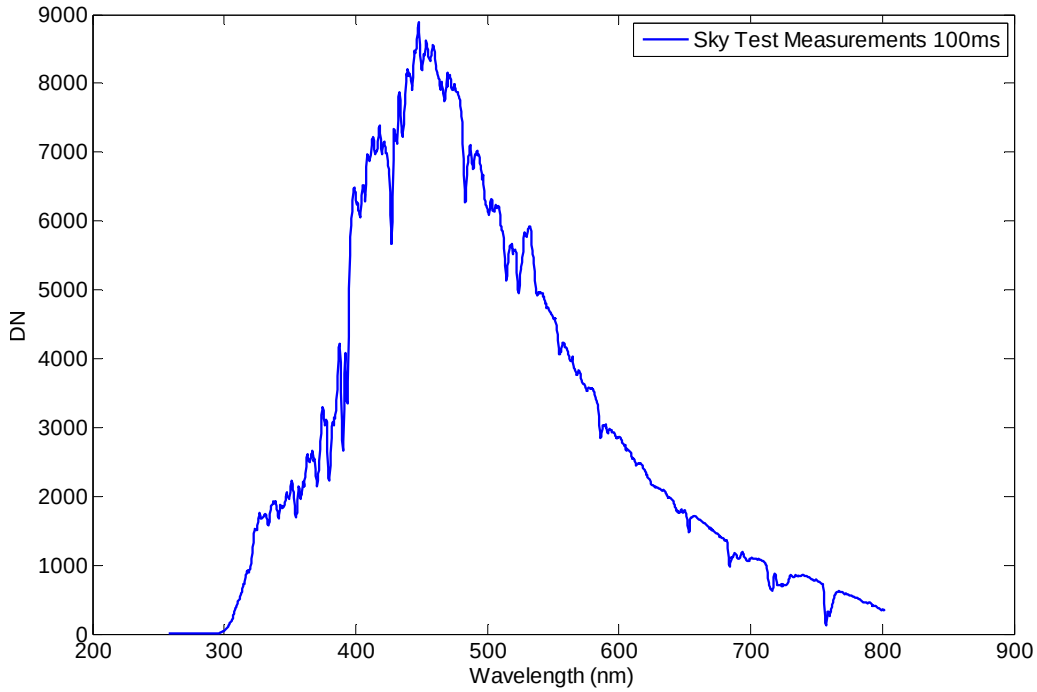

Figure 4.23: Raw sky test measurement from Slit 1 with 100ms exposure time.

Figure 4.23 shows the data that was measured on the roof of the Physics building at the University of Saskatchewan on June 24, 2014. This image was collected with the pointing system attached to OSIRIS-DM with an exposure time of 100 ms through Slit 1. This data was scaled to meet the expected conditions for a balloon launch in September 2014.

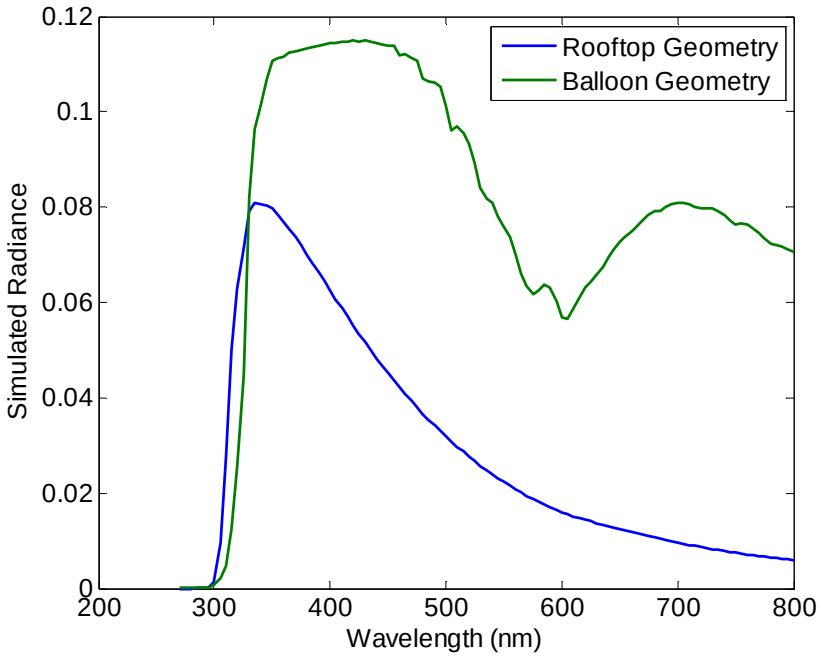

(a)

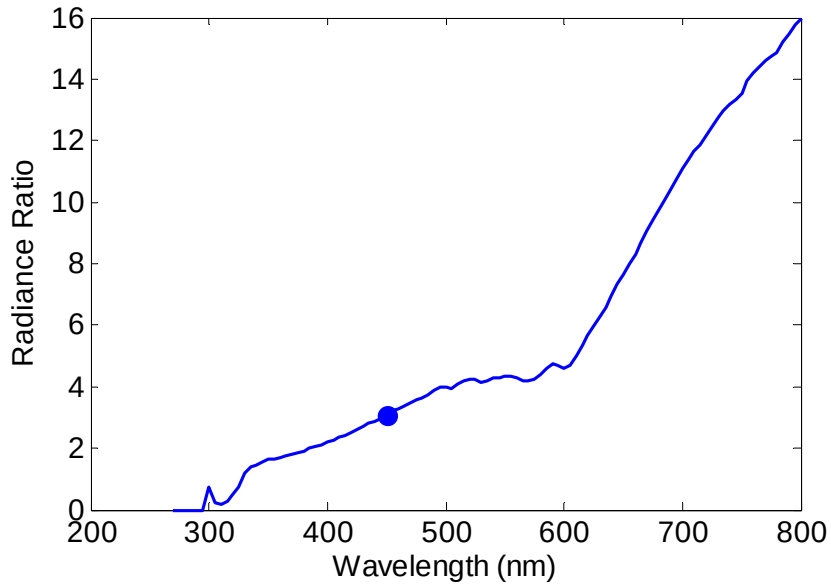

(b)

Figure 4.24: (a) SASKTRAN radiance simulation for rooftop geometry on June 24, 2014 and SASKTRAN radiance simulation of balloon geometry on September 9, 2014. (b) Ratio of SASKTRAN radiance simulations.

Figure 4.24a utilizes SASKTRAN to estimate the differences in radiance for the rooftop viewing geometry measured at the University of Saskatchewan and the expected radiance measured from a balloon located over Timmins, Ontario on a date close to the expected launch date. The units on these, which are radiance per unit solar irradiance, differ from the radiance directly measured with the instrument, but they will be used as a ratio so the units will not play a factor in the final result. This second spectrum was simulated for the lowest look angle from the balloon, which should see the brightest part of the atmosphere. All other look angles would see dimmer sections of the atmosphere, and therefore the exposure times would need to be increased. This would not be a problem because it was stated earlier that the exposure times could be increased by up to 20x with the OSIRIS-DM specifications. The ratio between these two radiance spectra is then shown in Figure 4.24b. In this final plot, the point at 448 nm is highlighted. This is the wavelength that the highest radiance for the sky measurements in Figure 4.23, and therefore was the point used to scale the spectrum. The ratio between SASKTRAN simulations for this wavelength was approximately 3.

With this ratio, the rooftop measurement was scaled by 3 to find the expected radiance for a 100 ms exposure from the balloon geometry. This is shown in Figure 4.25.

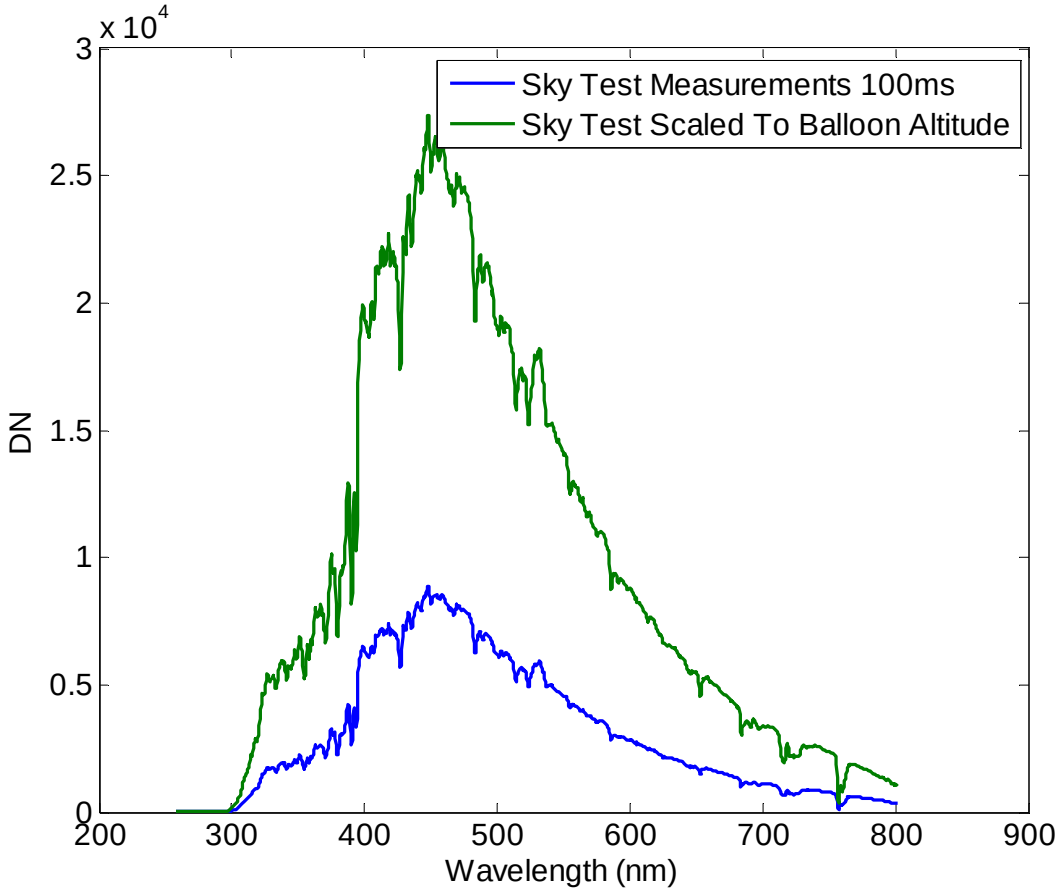

Figure 4.25: Sky test measurement scaled to expected balloon geometry.

It was now important to take the exposure time requirements into account. Recall that the desired exposure time was 0.5 s. In order to do this, a simple test was run with various exposure times and a constant radiance source imaged in front of the system.

Figure 4.26a shows a tungsten spectrum measured at varying exposure times. In this figure, the 448 nm measurements are highlighted once again. These points are then plotted as a function of exposure time in Figure 4.26b and then a least squares fit method is utilized to determine the equation relating the DN count to the exposure time. It was now possible to determine the ratio between a 0.5 s exposure and the 100 ms exposure shown previously from this equation.

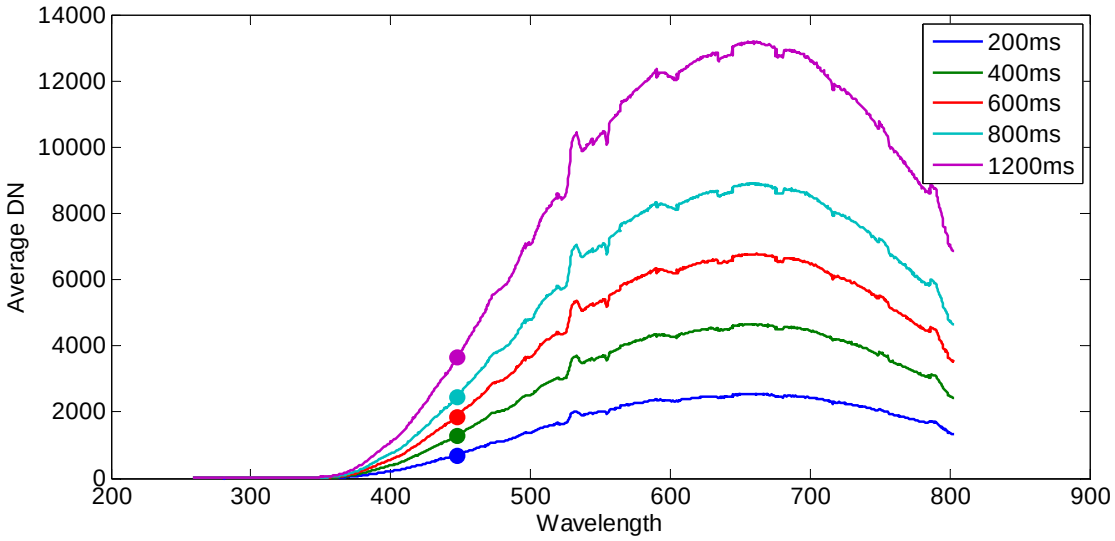

(a)

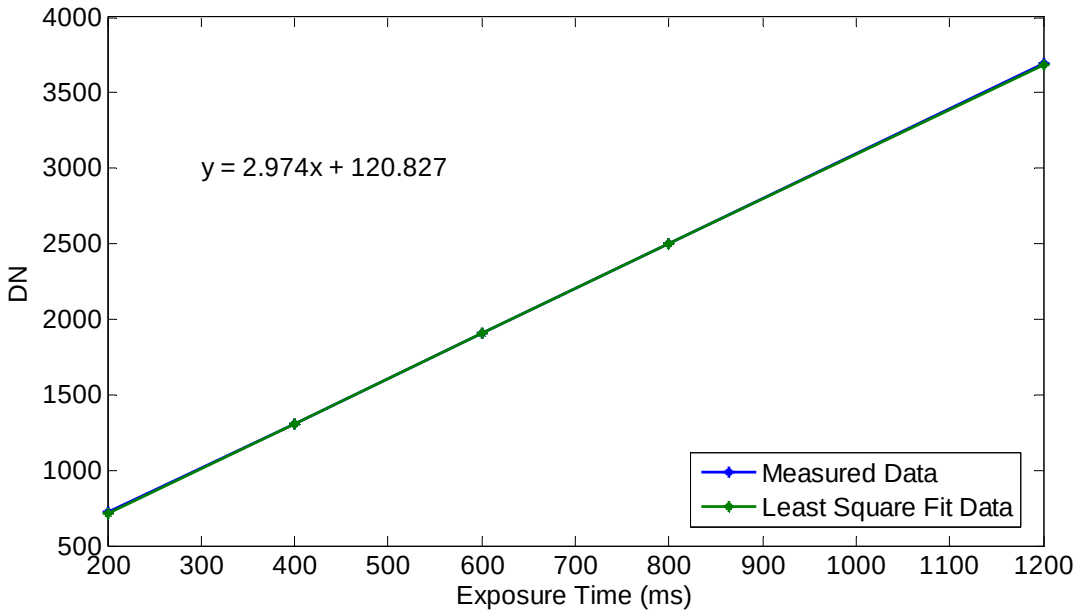

(b)

Figure 4.26: (a) Constant radiance source imaged at various exposure times. (b) Linear equation relating expected DN counts as a function of time for 448 nm.

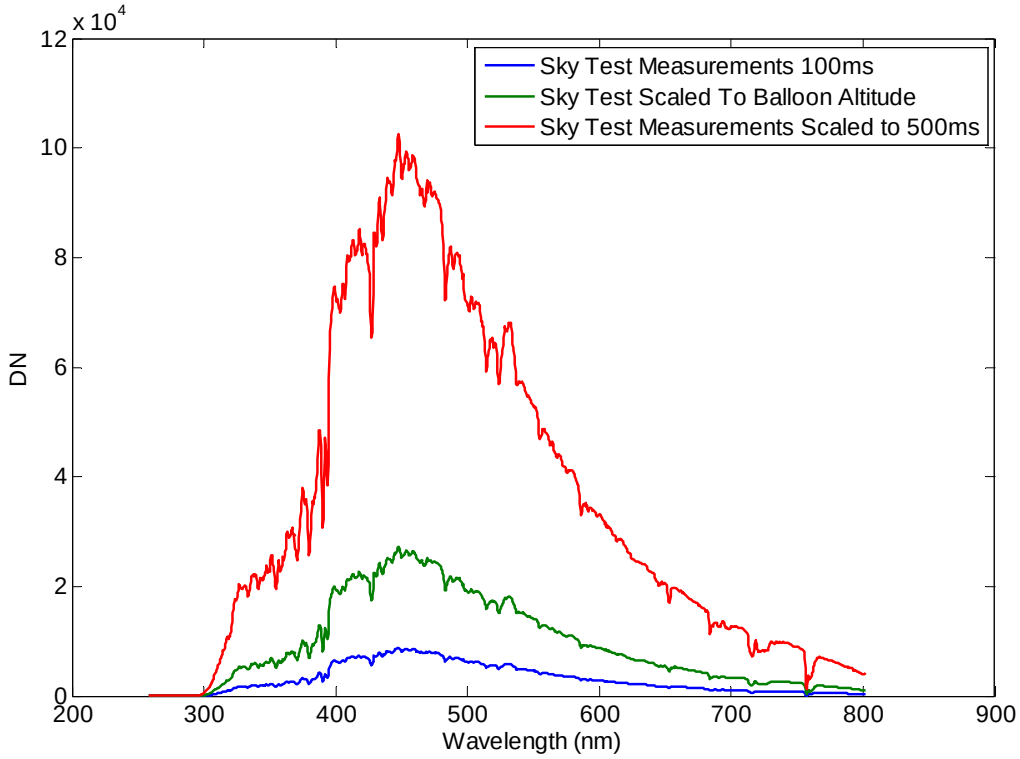

Figure 4.27: Balloon measurement scaled from 100 ms to 500 ms.

The ratio between the two exposure times was calculated to be 3.844. The balloon measurement from Figure 4.25 was now scaled by this factor and plotted in Figure 4.27. This shows that with the current system, a 0.5 s exposure would result in 102500 DN counts on the detector. This is significantly higher than the limit on the CCD in OSIRIS-DM, which has a maximum of 16383. If the CCD well was desired to be to be only 3/4 full for an ideal measurement, then 12287 counts was optimal. The predicted 0.5s exposure value could then be used along with this to find the attenuation factor that must be applied to the predicted measurements in order to obtain an ideal measurement. This scaling factor is 0.120. The effect of this scaling factor is shown in Figure 4.28.

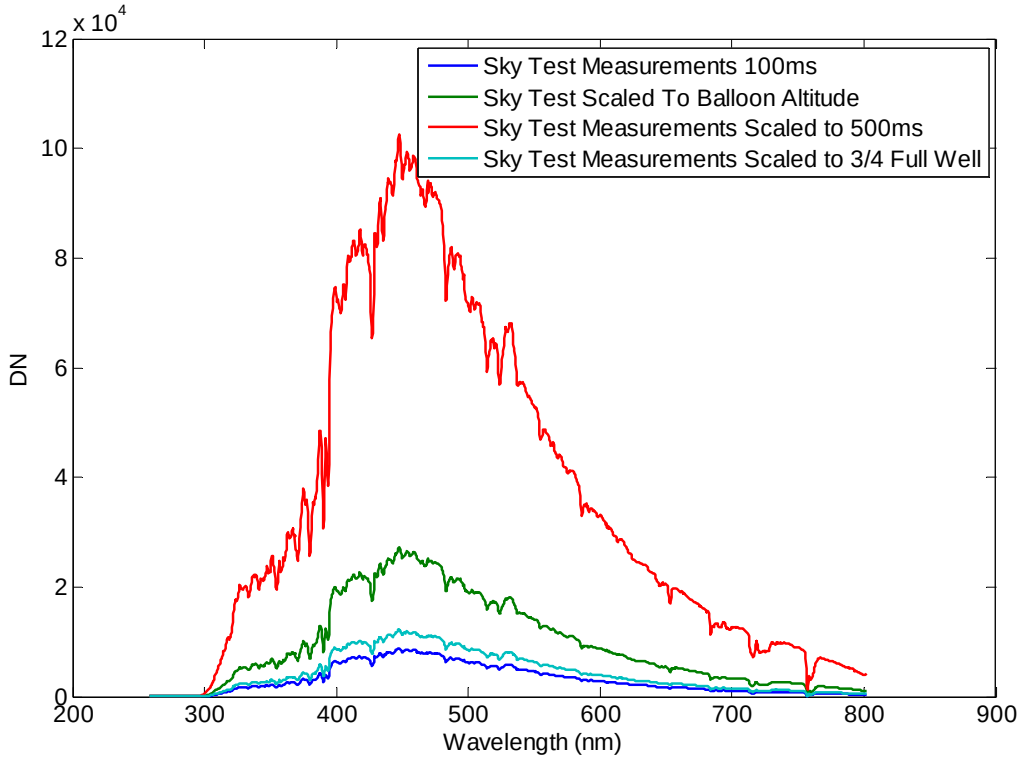

Figure 4.28: 500 ms balloon measurement scaled to ideal measurement.

This analysis has shown that to meet the exposure time requirements for a balloon borne system, the light must be attenuated by a factor of 0.88.

Neutral Density Filter Solution

One solution to attenuate the light was to install a neutral density filter. The optical depth of the filter would determine what percent of the incoming light would be transmitted through the filter. Neutral density filters are designed to operate uniformly over a broad band of wavelength.

The relationship between transmission percentage and optical depth is defined by:

$$T = 10^{-OD} \qquad \text{(Eq. 4.3)}$$

where T is the transmission percentage and OD is the optical depth of the filter. For the case of the OSIRIS-DM pointing system, the transmission percentage is known, so the optical depth can be calculated by:

$$OD = -\log(T) \quad \text{(Eq. 4.4)}$$

Based on the required 12% transmission calculated earlier, the optical depth required was found to be 0.92. Neutral density filters are available commercially with optical depths of 0.9.

The neutral density filter selected was produced by CVI laser optics. The filter is 50.8 mm × 50.8 mm, so it is large enough to cover the entire 36 mm × 36 mm aperture of OSIRIS-DM. It is made of a fused silica substrate and filters wavelengths from 250 nm to 2500 nm. Although it was mentioned that neutral density filters with an optical depth of 0.9 are commercially available, at the time of purchase of the filter, these were on back order and would require a lead-time of 2-4 weeks. The launch date was nearing, so it was decided that an optical depth of 0.8 would suffice. This would let through slightly more light, which is shown in Figure 4.29.

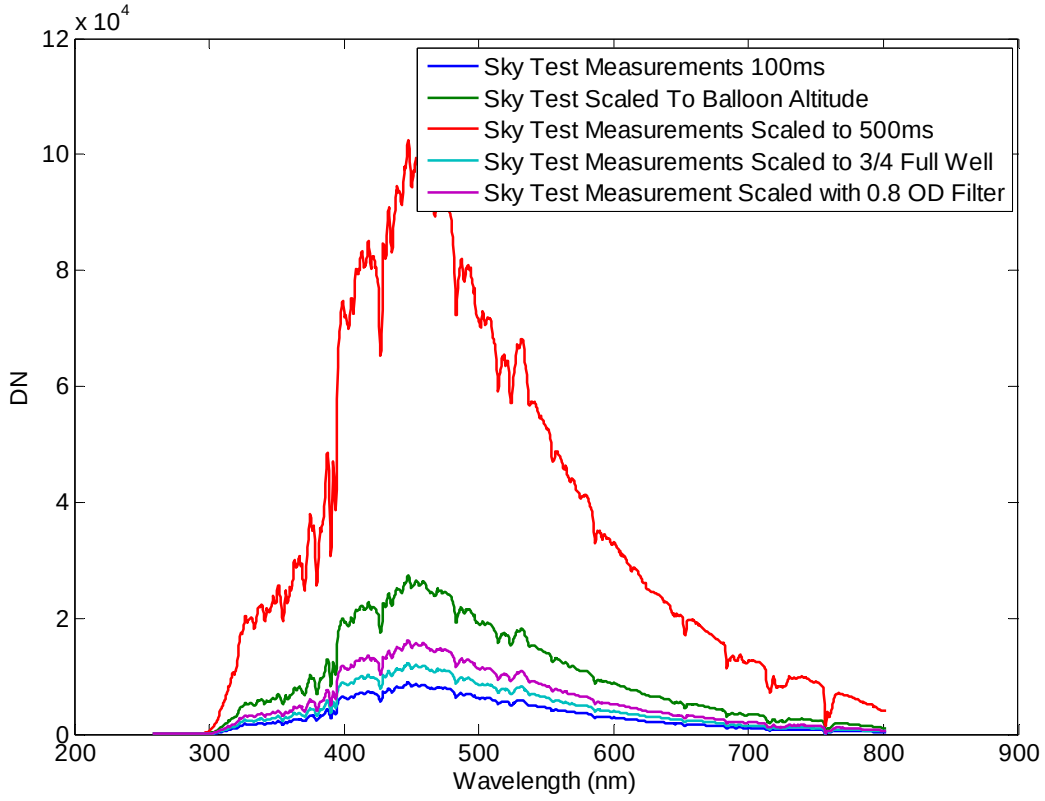

Figure 4.29: 500 ms balloon measurement scaled by neutral density filter with optical depth of 0.8.

When the neutral density filter was received, it was epoxied onto the Aluminum plate that connects the pointing system to OSIRIS-DM. This is shown in Figure 4.30.

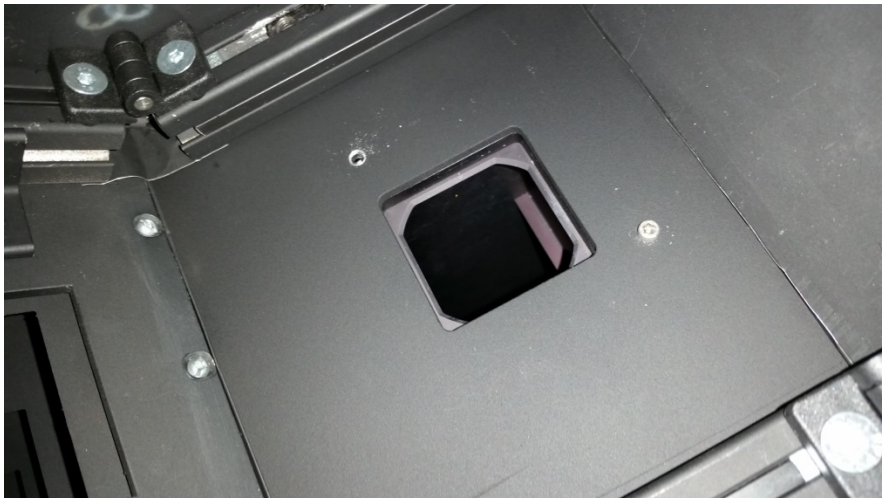

(a)

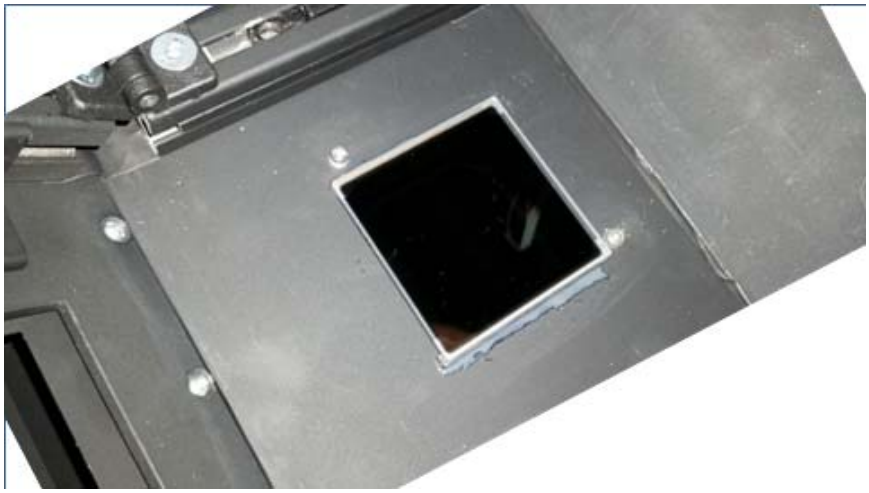

(b)

Figure 4.30: (a) Original Aperture of OSIRIS-DM in pointing system. (b) Neutral density filter installed in OSIRIS-DM pointing system.

When testing the system with the newly installed neutral density filter, the performance was just as expected.

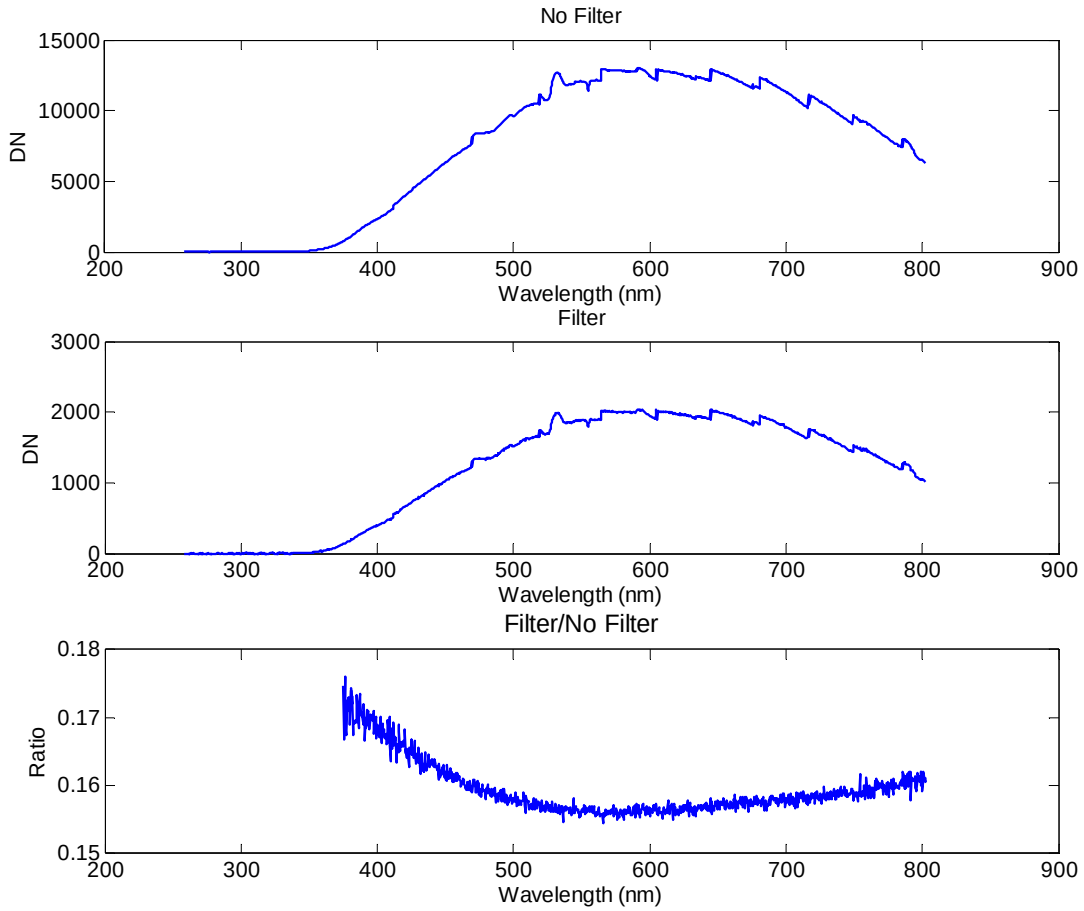

Figure 4.31: Tungsten spectrum measured with and without neutral density filter and ratio of measurements.

Figure 4.31 shows the results of obtained by imaging a tungsten source with a set exposure time both with and without the neutral density filter in place. The ratio of these two measured spectra was found to validate the performance of the neutral density filter. As stated, the filter worked as expected. This is shown by the relatively constant ratio for the illuminated region of the spectra, specifically for wavelengths longer than 375 nm. This figure only shows the measurement for the Slit 1, but similar results were obtained for the remaining slits. However, when measurements were made of a source with discrete spectral lines (in this case a neon

source), it became apparent that the addition of the neutral density filter caused reflections within the system. This is shown in Figure 4.32.

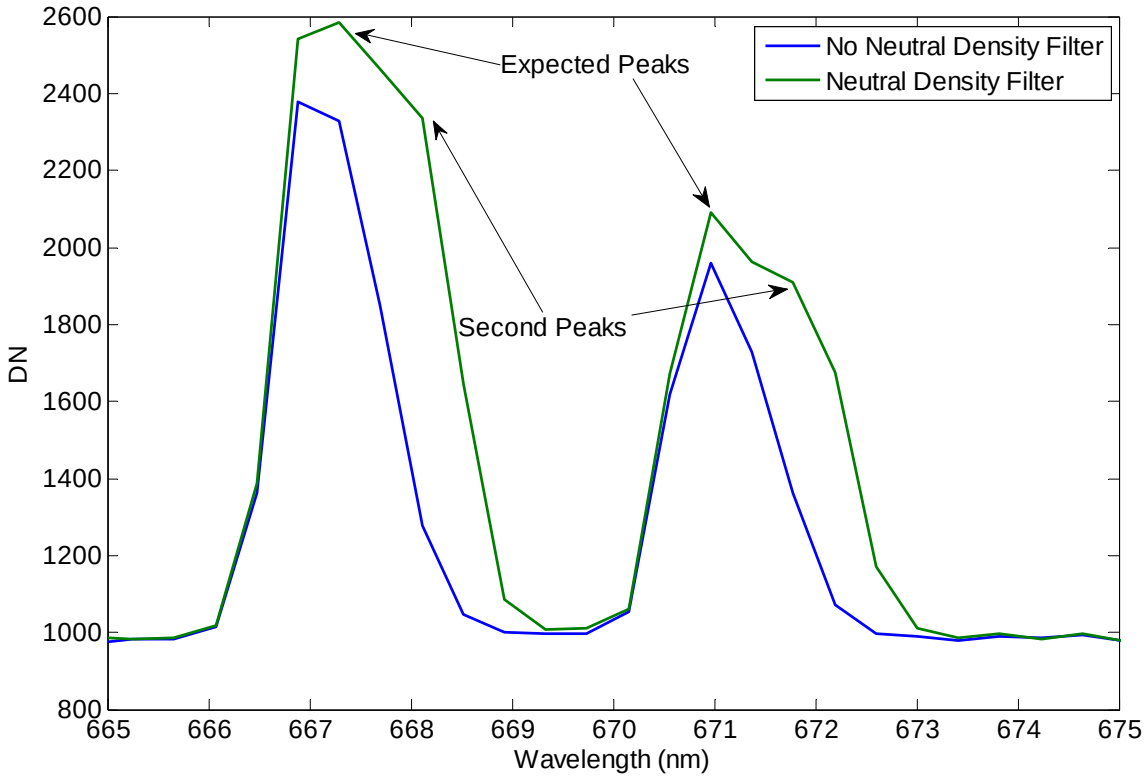

Figure 4.32: Neon spectral lines measured with and without neutral density filter.

Notice in Figure 4.32 that single peaks are visible at wavelengths 667.6 nm, and 671.3 nm for the unfiltered case, as expected from a neon source. Now, when looking at the filtered data set, it is apparent that a secondary peak has appeared. The second peak is registering at a slightly longer wavelength, and has a slightly smaller signal than the expected peak. The expected and secondary peaks are indicated in the figure. This suggests that the CCD is imaging secondary corrupt light. It was determined that the source of this was light reflecting off of the filter, then reflecting off the mirror and interacting off of the baffle. Even with much effort, this problem

could not be eliminated. It was decided that the neutral density filter option had to be abandoned due to the greatly increased stray light in the system.

Reduced Aperture Solution

A second solution to attenuate the light entering the system was to reduce the size of the entrance aperture. This was not the preferred solution because it means that the fields of view will be altered slightly due to imperfections in the optics within OSIRIS-DM.

First, the reason why the field of view is changed is investigated. Figure 4.33 and 4.34 will help illustrate this point. These figures are strictly for illustrative purposes only and do not represent numerical ray traces of lenses.

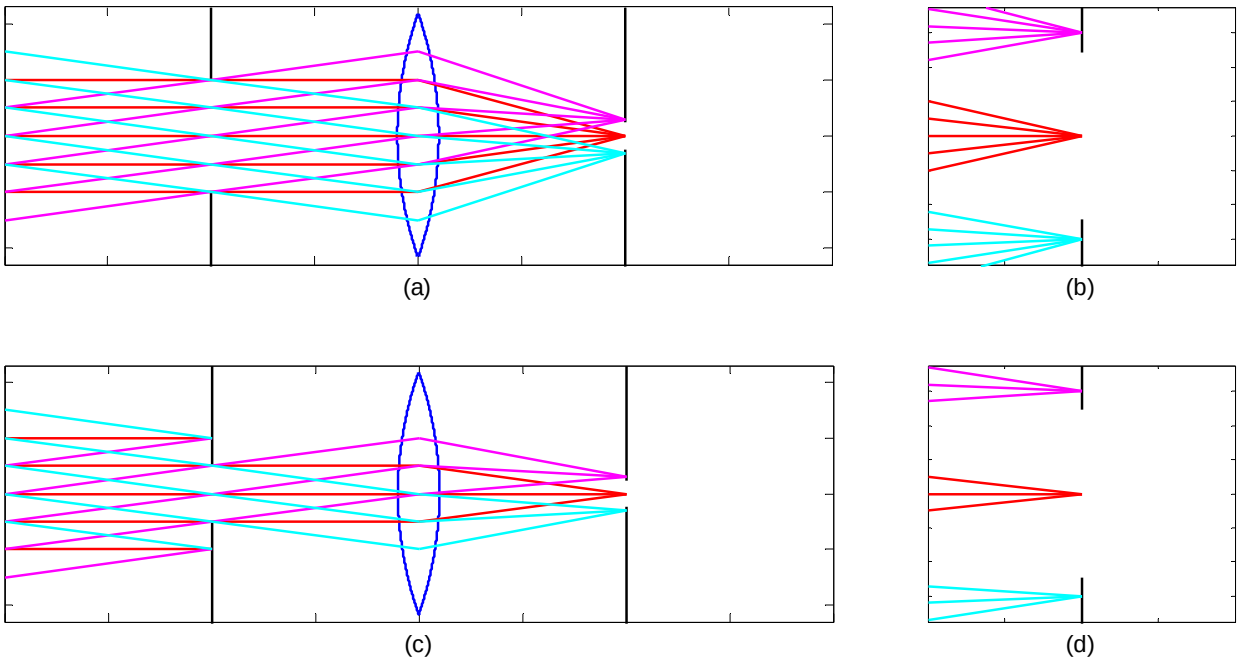

Figure 4.33: (a) Ideal lens with large aperture. (b) Ideal lens with large aperture zoomed in on slit plate. (c) Ideal lens with small aperture. (d) Ideal lens with small aperture zoomed in on slit plate.

Figure 4.33 demonstrates rays entering a system from three different directions. Two cases are shown, one with a large aperture size and one with a reduced aperture size. In both cases, an

ideal lens is used. The lens represents the objective mirror in the OSIRIS-DM system. With an ideal lens, no aberrations are present, and the rays are perfectly focused on the slit plate, which is located on the focal plane. It is shown that the incoming ray directions dictate the location that the rays are focused. In both cases, the rays coming in normal to the entrance aperture are focused at the middle of the slit on the slit plate. The two extreme sets of rays however are focused slightly outside of the area of the slit. This means that in both cases, no portion of either the magenta or the cyan rays would make it past the slit plate. This suggests that by reducing the size of the aperture in a system with ideal optics, the only effect is a reduction in the number of photons passing through the system. The aperture size therefore has no effect on the field of view for such a system.

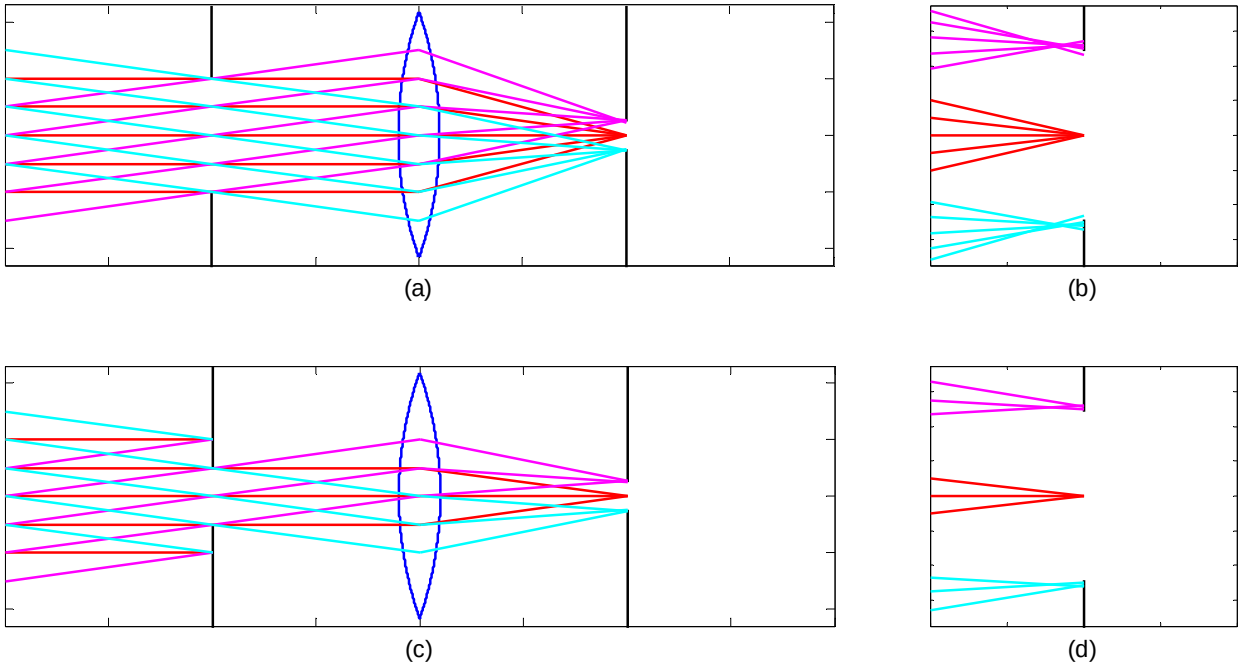

Figure 4.34: (a) Realistic lens with large aperture. (b) Realistic lens with large aperture zoomed in on slit plate. (c) Realistic lens with small aperture. (d) Realistic lens with small aperture zoomed in on slit plate.

Now in Figure 4.34, a realistic lens is used, which introduces aberrations to the system. It is shown that a realistic lens refracts rays interacting with regions furthest from the optic axis the most. Focusing on Figure 4.34b, it is apparent that these aberrations play a strong enough effect to actually refract some of the incoming light through the aperture. For the magenta ray bundle, it is shown that the ray entering though the very top of the aperture is affected by the aberration the greatest and therefore makes it through the slit, and similarly the cyan ray entering through the bottom of the aperture makes it through the slit. Now, in Figure 4.34d, there are no longer any rays passing through the slit. This is because the rays that made it through with the larger aperture have now been blocked when the aperture size was reduced. This suggests that the vignetting described in detail in Chapter 3 will not be as significant when the aperture stop size is reduced.

As mentioned, when the aperture size is reduced with ideal optics, the only effect is a reduction in the number of photons entering the system. This theory can be used to determine the required reduction of the aperture. The area of the original aperture is 1296 mm^2. As tested, the transmission through the neutral density filter with an optical depth of 0.8 was acceptable, so it was attempted to replicate this effect with the reduced aperture size. This means that approximately 15% of light needs to be transmitted, which requires an aperture sized roughly 14 mm × 14 mm. The vignetting effect of this aperture size is now modeled.

In Figure 4.35, the left hand column is a duplication Figure 3.31. This is the vignetting effect that was expected for the original 36 mm × 36 mm aperture size. In the right hand column, the ray trace analysis has been run again, but this time the aperture size is changed to 14 mm × 14 mm. The first thing to note for slits 1 and 2 is that the signal has been reduced to nearly 15% as expected. The second thing to notice in Slit 1 and 3, the vignetting effect has been reduced

significantly. This agrees with the concept described earlier about realistic optics and vignetting effects. This suggests that decreasing the size of the aperture will reduce the point-spread function of a single wavelength on the CCD, which is analyzed by *Taylor* (2015).

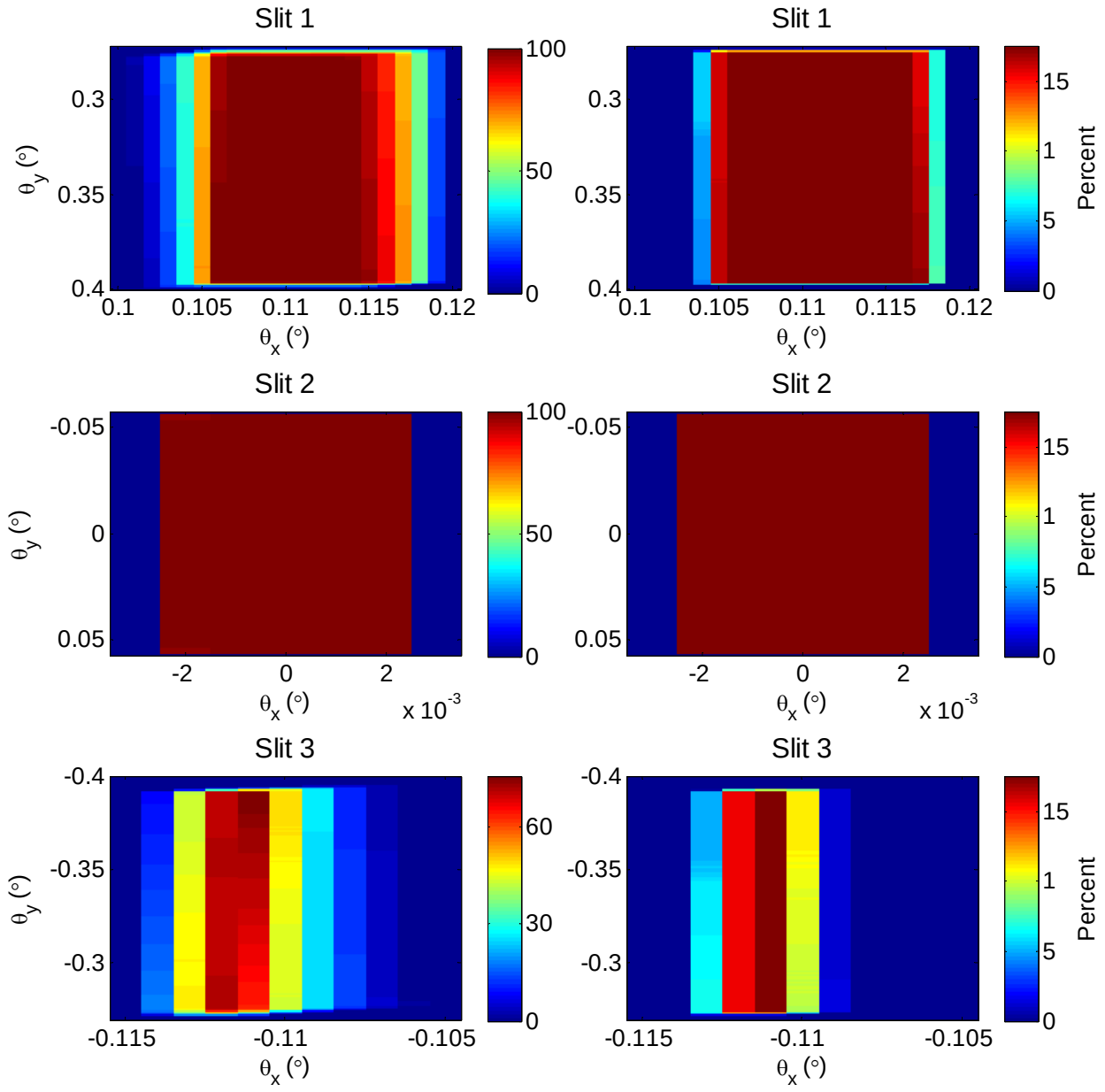

Figure 4.35: Vignetting effect in multi-slit system with original aperture size and reduced aperture size.

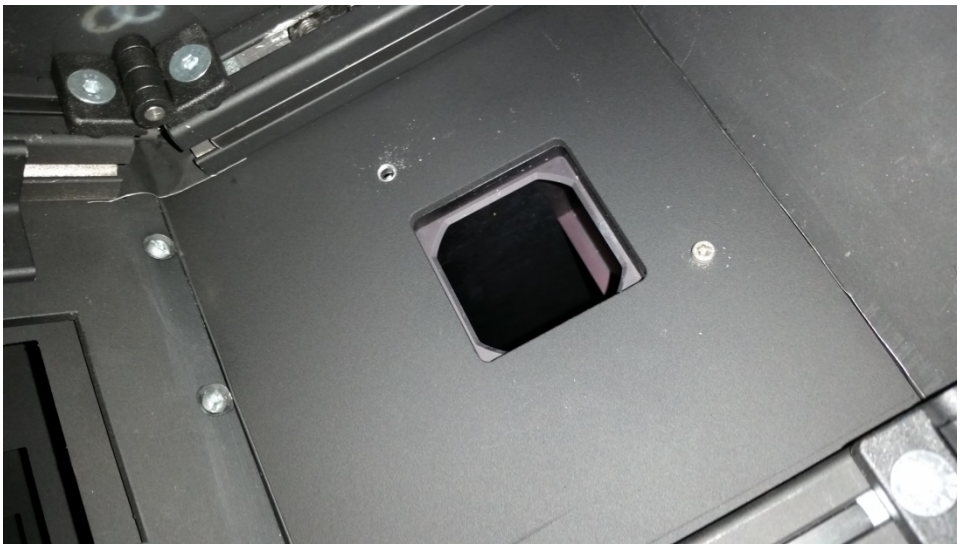

(a)

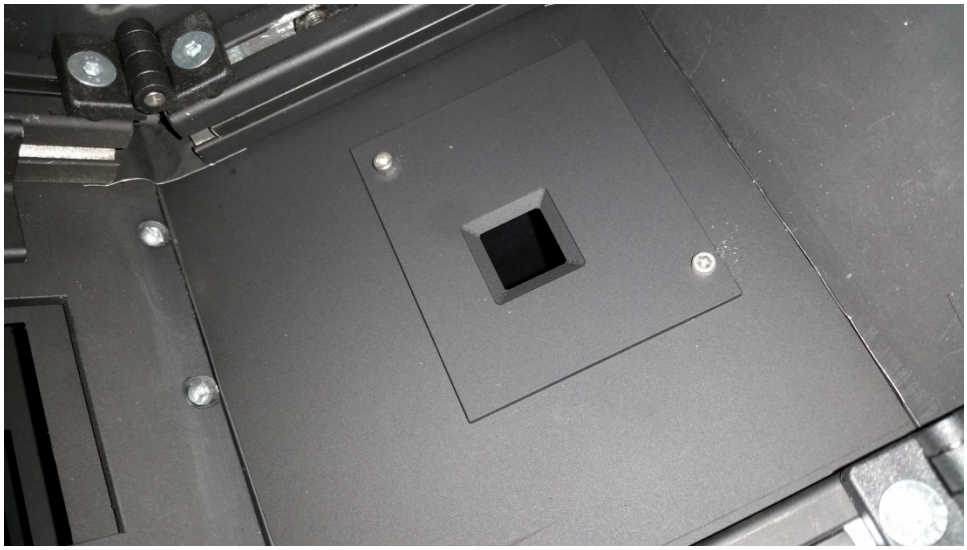

(b)

Figure 4.36: (a) Original Aperture of OSIRIS-DM in pointing system. (b) Reduced aperture installed in OSIRIS-DM pointing system.

The reduced aperture was installed in the pointing system as shown in Figure 4.36 and was once again tested with a tungsten source to analyze the attenuation. This is shown in Figure 4.37.

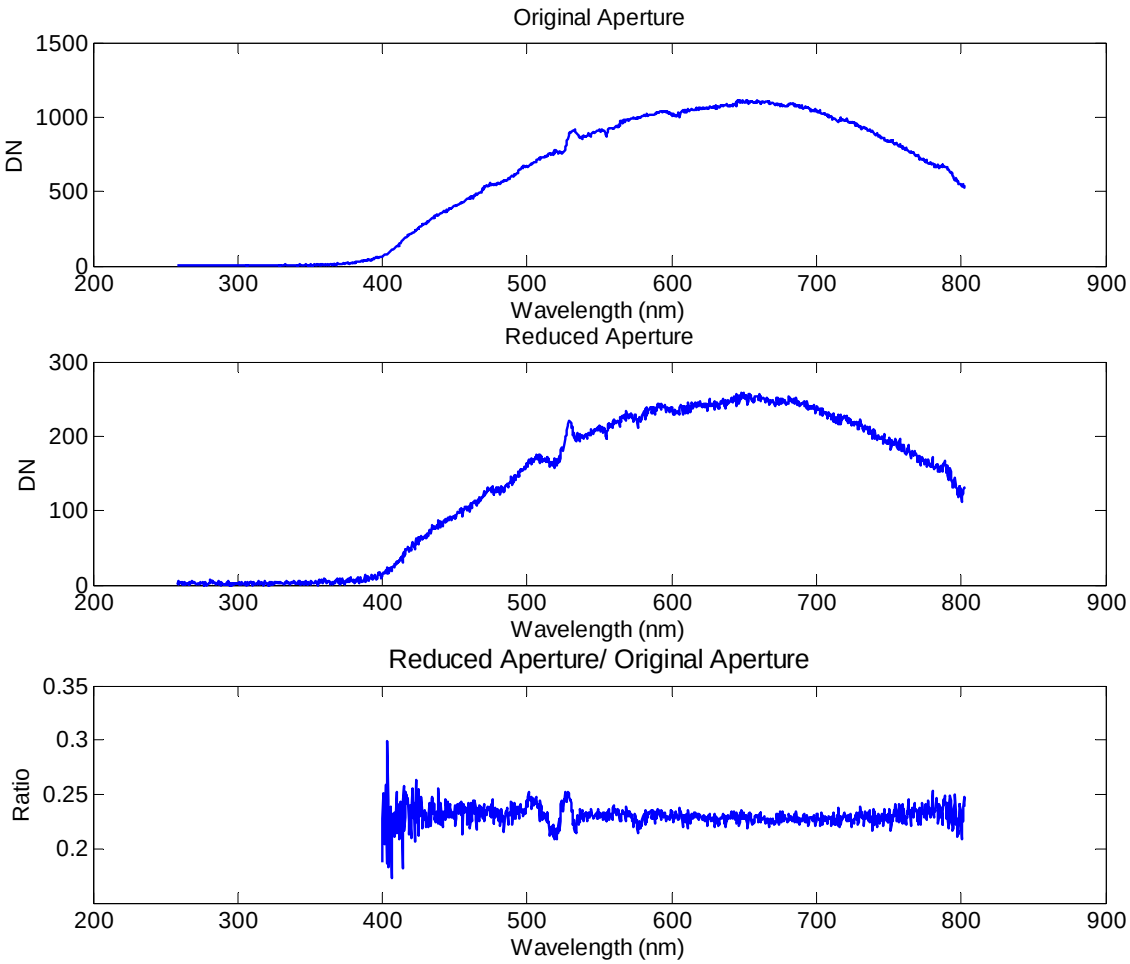

Figure 4.37: Tungsten spectrum measured with and without reduced aperture in place and ratio of measurements.

In this figure, the large aperture size measurement is shown on the top and the reduced aperture size measurement is shown in the middle panel of the figure. These measurements were made using a constant radiance source and a set exposure time. In this figure, it is apparent that the reduced aperture size has reduced the signal passing through the system. It did not however reduce it to the extent expected. With the new aperture stop in place, the signal has dropped to about 23% of its original strength through the original aperture, as shown by the ratio of the measurements. Once again, the design size of the new aperture was based on an instrument with

ideal optics. For similar reasons to the slit sizing vs. intensity issue explained in Chapter 3, it is once again observed that the reduction of aperture size does not relate directly to the intensity of light passing through the system. However, the reduced aperture size does an acceptable job in reducing the radiance entering the system, and therefore will be used for the balloon flight.

One issue that did arise as a result of reducing the aperture size is a fringing effect observed on the higher wavelength end of the spectrum measured by Slit 1. This is shown in Figure 4.38.

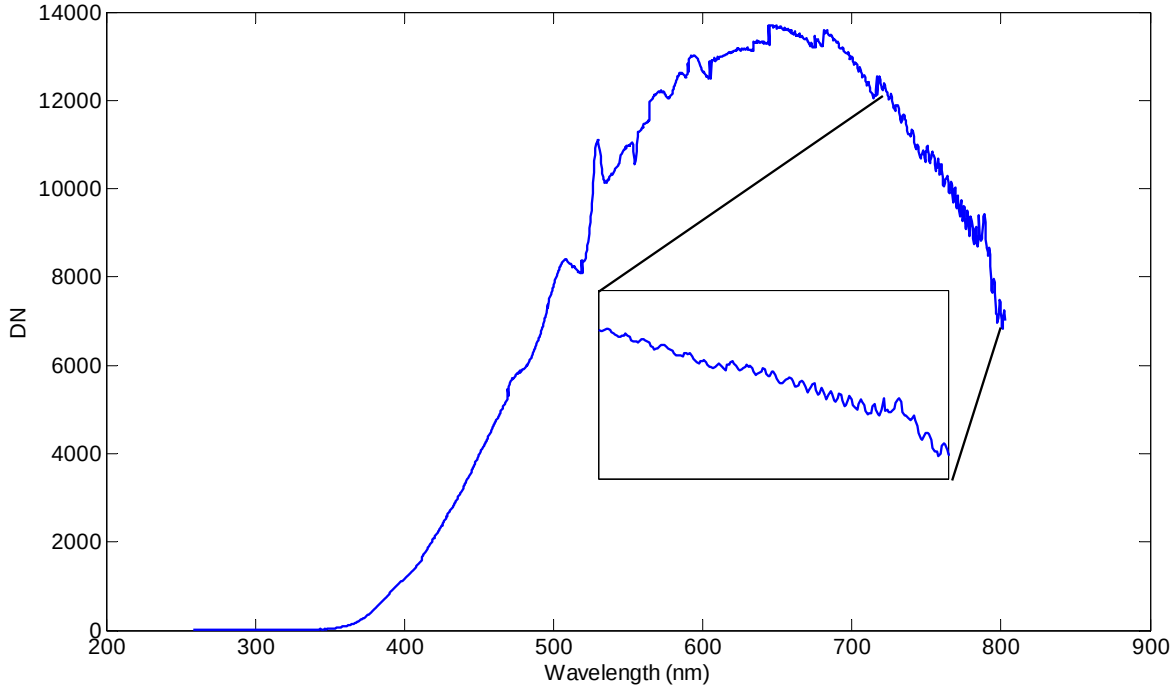

Figure 4.38: Tungsten spectrum measured with reduced aperture with inset magnifying fringing effect.

It is shown that for wavelengths greater than approximately 720 nm, a fringe pattern is apparent that had not been observed until this point. Fringing is not uncommon for CCD imaging, especially when measuring light on the red end of the visible spectrum. The fringes are caused by constructive and deconstructive interference in the multiple reflections that occur within in the coating on the surface of the CCD (*Howell*, 2006). It is likely that with the original

aperture size, the fringing was washed out by the extended range of angles incident on the CCD, but once this was narrowed it became apparent. This effect is not noticeable in Slits 2 or 3.

4.4.5 System Testing

Environmental Testing

The environmental aspects of the balloon-borne test had two significant differences from the lab environment. These differences are temperature and pressure. From the information received from the CSA, it was expected that the temperature of the gondola at its float altitude could be as low as -40 °C. The pressure at this altitude is expected to be roughly 5 Torr, which is 150x less than atmospheric pressure at the ground, which is typically around 760 Torr. To prepare for this, it was desirable to test as many components as possible in simulated environments.

The first environmental test performed was a low-pressure test. For this, a vacuum tank in the Physics department at the University of Saskatchewan was used. The tank was not large enough to accommodate the entire OSIRIS-DM pointing system in it, so only the shutter, actuator and control hardware were tested. This is acceptable however because the components used for the instrument itself are the same as those on the OSIRIS-FM, which operates in an even lower pressure system without any problems. As mentioned, modifications were made to the drivers for the shutter and actuator to accommodate low pressures. The vacuum tank was brought down to a pressure of 3 Torr, which surpasses the requirements of the balloon flight. The components used in the design operated well in this environment. Extreme measures were taken to stress the components, including a power on scenario at low pressure, which had no negative effects on the components. The timing of the shutter was also analyzed, and appeared to perform as expected.

The second environmental test performed was to place the instrument in a cooler located in the Biology building at the University of Saskatchewan. For this test, operation was not the only concern, but also performance of the optics due to thermal contraction. Therefore, the entire

system had to be placed in the cooler. Because of the size of the instrument, it was difficult to find a freezer large enough that would provide the desired temperature. The best effort that could be made was to get the cooler down to 4 °C. The shutter and actuator both performed well through this test and showed no sign of failure at this temperature. It should also be mentioned that the power budget on the gondola did not leave much room for additional heaters to be used, so there was no option to add a thermal control unit to the system.

Mirror Position Feedback

As mentioned previously, a driver unit designed for the actuator controls the component. This driver has the ability to provide feedback to the user on the position of the actuator. However, considering the system was not tested in an extreme temperature condition, it was desired to have a secondary feedback system to verify that the mirror position was in fact changing. The system chosen for this feedback was a simple linear potentiometer used as a voltage divider. This is a low power option that is very simple to implement. The potentiometer was affixed to the mirror mount such that as the actuator arm is extended, the potentiometer arm also gets extended. The voltage dropped across the potentiometer was therefore a function of the distance that the actuator was extended. A data set was collected in the lab for various mirror positions to develop the relationship between the mirror position and the potentiometer reading. This is shown in Figure 4.39.

In this figure, the data set collected for varying mirror positions is shown. A least squares fitting method was then used to determine the equation of a line fit to this data. This equation describes the potentiometer reading in volts as a function of mirror position in degrees. The equation can also predict the reverse, which will be used to track the mirror position during flight.

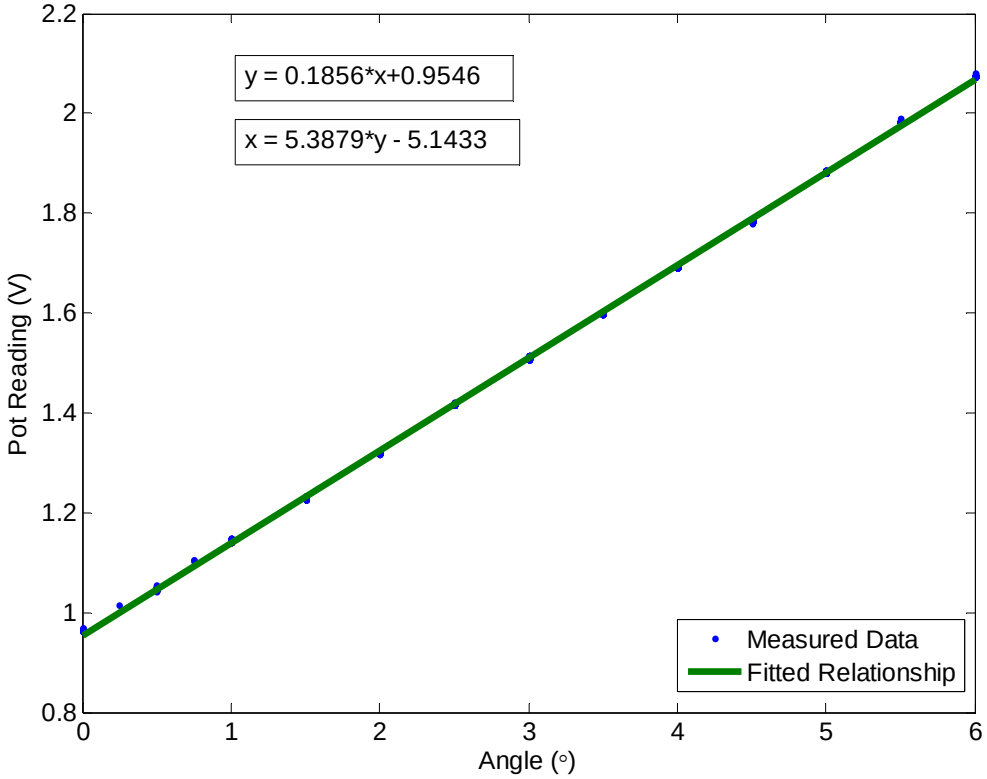

Figure 4.39: Potentiometer response to mirror position.

The potentiometer could not be used for fine position measurements because such systems are highly susceptible to noise. There was no way to test the OSIRIS-DM pointing system with the batteries used on the gondola until it arrived in Timmins, and along with that, the cable lengths specified for the instrument were 3.5 m, so there was too much variability involved to put any effort into fine tuning the potentiometer. It could however easily determine the position of the mirror to within 0.25°, so the system was used to verify rough pointing of the mirror.

4.5 Baffle

4.5.1 Baffle Design

A baffle was desired on the front end of the system to reduce external stray light from entering the system. The purpose of the baffle was to limit the directions from which it was possible for light to strike the scan mirror. The baffle is required to only block light that is outside of the field of view, but to not impede any rays that would pass directly through at an acceptable angle into the instrument. The design of the baffle follows steps outlined by *Fischer et al* (2008).

The technique described utilizes the "Three Bounce Rule." This rule states that the intensity of light drops approximately two orders of magnitude when it reflects off of a surface within the baffle. Therefore, if undesirable light can be made to reflect a minimum of three times, then its optical energy is diminished to 1 one-millionth of its original energy, and therefore is effectively negligible within the optical system. With very few steps, a baffle can be designed to maximize the number of scattering surfaces the unwanted light must interact with before entering the optical system.

The starting point for a baffle design requires a few set parameters, namely the length of the baffle, the height of the baffle, the height of the aperture and the field of view. During the design process for this system, a few iterations were required with the design of the rest of the enclosure in order to determine the dimensions that would allow all the pieces to interface together. The finalized input parameters are defined in Table 4.1

With these parameters, the outline of the baffle can be drawn, as shown in Figure 4.40. Figure 4.40a shows the main structure of the baffle. In this figure, the exit aperture is located at Length = 0 mm. The baffle is symmetric about the axis defined by Height = 0 mm in this figure. The baffle vanes defining the exit aperture are drawn in to extend from half of the exit aperture

size to the half the height of the baffle. The top and bottom casings are then extended the length required. The first vane, which for this system will be the critical baffle vane, is then drawn in at the full reach of the baffle, with its aperture being defined by the size of the exit aperture and the required field of view. Red lines are drawn in showing the field of view defined by this baffle outline.

Table 4.1: Physical parameters for baffle design.

Parameter	Value
Baffle Length	238 mm
Baffle Height	118 mm
Exit Aperture Height	66 mm
Field of View	±3°

The next step is to define mechanical tolerances to which the baffle can be built, shown in Figure 4.40b. Based on the equipment available in in the machine shop in the Physics Department at the University of Saskatchewan, these tolerances were set to 0.5 mm. The mechanical tolerance guidelines offset the field of view by the tolerance. The purpose of this step is to verify that the vanes manufactured do not become the critical baffle if they are built slightly too tall.

The next step is to add an indicator line drawn from the edge of the critical baffle to the plane of the exit aperture, as shown in Figure 4.40c. Indicator lines will be drawn to systematically place baffles from the back to front to suppress scattering.

The intersection of the indicator line and the mechanical tolerance line defines the location of the first baffle vane, as seen in Figure 4.40d. This vane will now be used to determine the location of the next baffle vane.

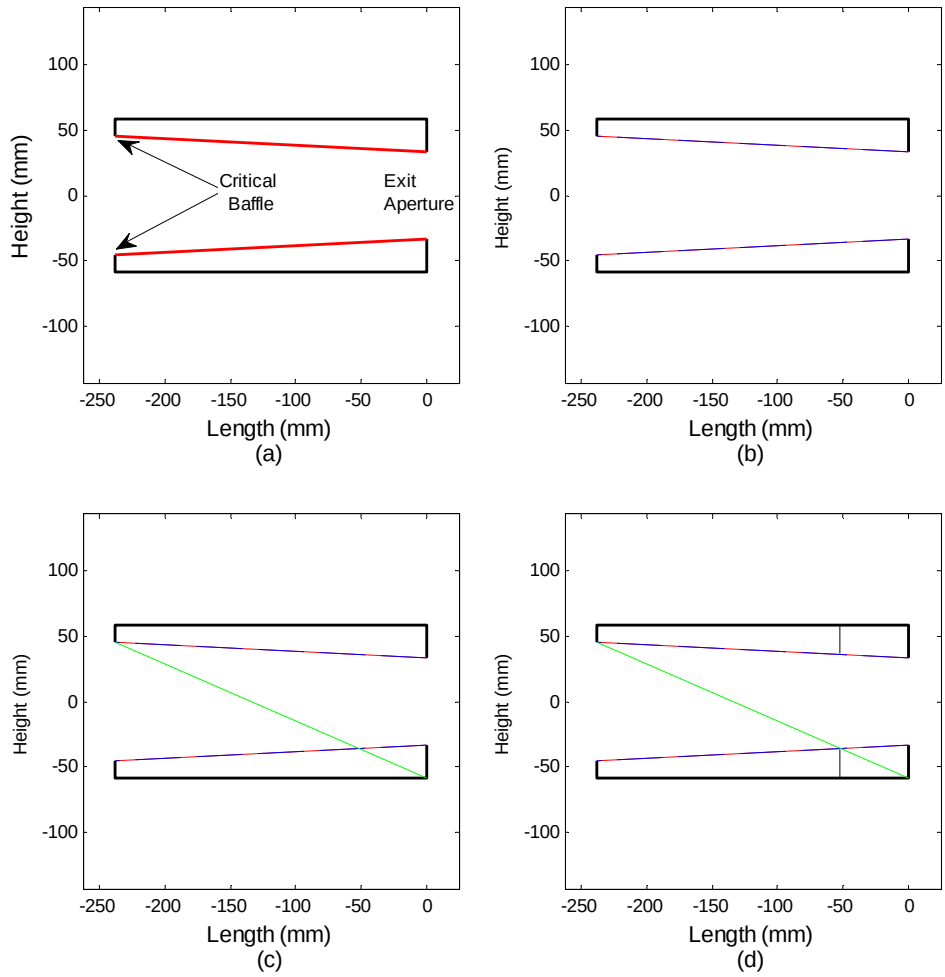

Figure 4.40: (a) Baffle outline. (b) Baffle with mechanical tolerance guidelines. (c) First baffle vane indicator line added to outline. (d) First baffle vane.

The second indicator line is draw in by first finding the location that a ray would begin if it were to start at the top of the baffle, graze the first baffle vane and then strikes the exit aperture plane at the bottom of the baffle. This is seen in Figure 4.41a. This point is then extended to the lower edge of the critical baffle.

The second baffle vane is now added in Figure 4.41b, at the location that the second indicator line intersects the mechanical tolerance line. Now this method is iterated to define the positions and heights for the remaining baffle vanes, shown in Figure 4.41c.

At some point near the entrance to the baffle, the indicator lines can no longer be drawn in using the described method. At this point, the baffle is can be considered complete. It can however be desirable to add one additional vane to the front end of the baffle.

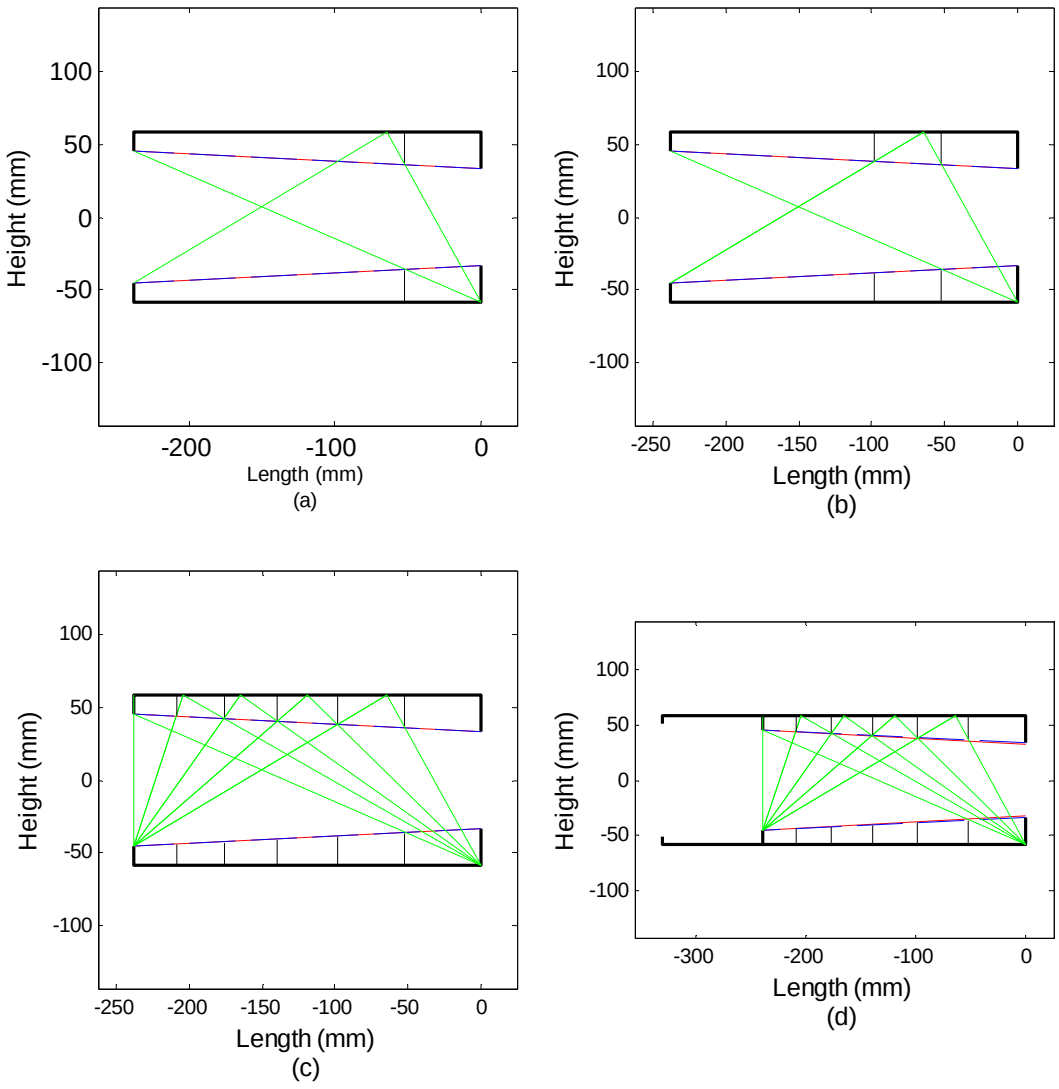

Figure 4.41: (a) Second baffle indicator line is added. (b) Second baffle vane. (c) Additional baffle vanes added. (d) External baffle vane added.

An external baffle vane is drawn based on the tolerance lines rather than the actual field of view of the baffle at any selected distance from the critical baffle, as in Figure 4.41d. This external vane greatly reduces the incoming angles of light that can make direct contact with the critical baffle edges. Because the critical baffle edges were drawn according to the field of view, they have an increased chance of glinting through the exit aperture, which should be avoided.

It should be noted that an entirely different set of baffle vanes would be calculated for the angle of the second field of view of the instrument, which extends in the horizontal direction. For this system however, the field of view in this second direction is much smaller than the first, and therefore offers less possibilities for undesirable light to enter the system. Therefore, the vane dimensions for this second dimension are determined solely by the locations of the first set of baffle vanes along the length axis, and the field of view in the second direction.

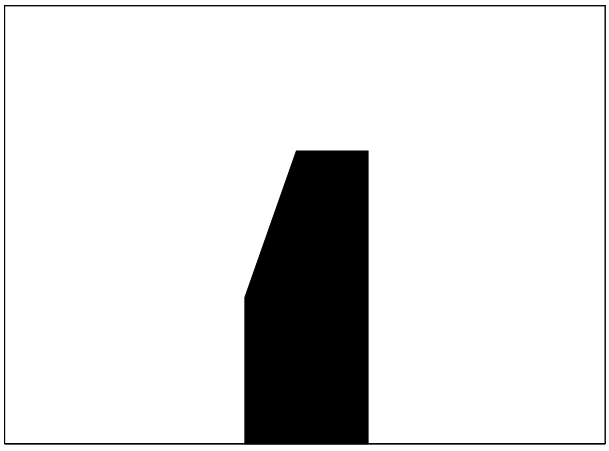

Figure 4.42: Typical baffle profile.

Now that the parameters of the baffle were settled, SolidWorks was used to develop a mechanical design. The case for the baffle was made of 6.35 mm aluminum to allow sufficient room for fasteners to be placed within the walls. This also provides sufficient room for the vanes to be inserted into grooves in the casing sides in order to secure them without requiring any

additional adhesives. The vanes were made of 2.38 mm aluminum. Because mechanical baffle vanes require a finite width, *Fisher et al*. recommend chamfering the vane edges at 30°. This means to shave the right angle down on the incoming side at a constant slope of 30° with respect to the vertical face. This helps to reflect unwanted light back towards the entrance to the baffle or towards other baffle vanes. This is shown in Figure 4.42.

The CAD model produced with SolidWorks for the baffle designed is shown in Figure 4.43a.

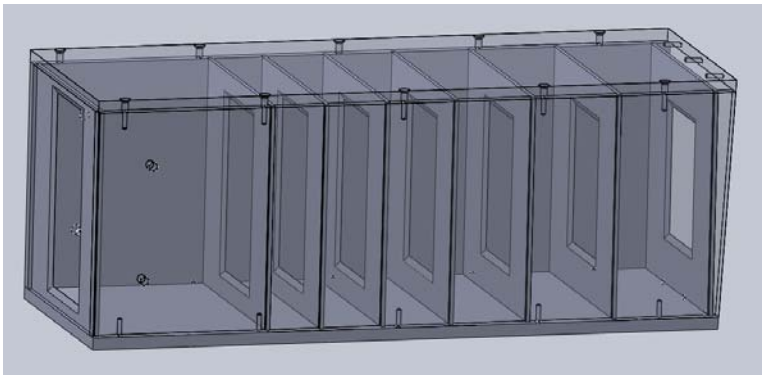

(a)

(b)

Figure 4.43: (a) CAD model of baffle. (b) Constructed baffle.

The CAD model shown has a semi-transparent top and side case to show the internal baffle vanes. Note also the diagonal edge cut on the right side, closest to the exit aperture vane. This side is cut at a 3° angle. This means that the baffle, which is designed to view ±3° to the horizon will now view 0° to -6° with respect to the horizon when mounted on a vertical face. This will accommodate the 6° declination that was calculated in Section 4.3. The baffle was then painted with a matte black paint in order to absorb light that interacts with any faces. The constructed baffle is shown in Figure 4.43b.

4.5.2 Baffle Analysis

As mentioned previously, the baffle is designed to utilize the Three Bounce Rule. Now that the baffle is fully designed, it is easier to depict this rule in an illustration.

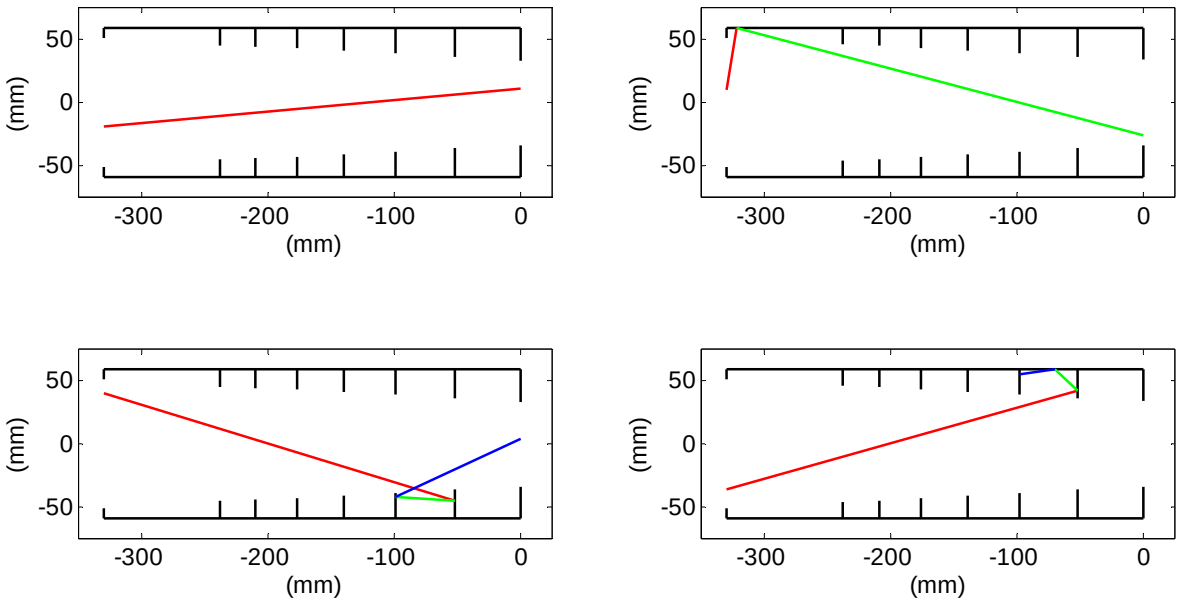

Figure 4.44: Designed baffle illustrating different ray bounce scenarios.

In Figure 4.44, the four different scenarios for ray interactions with the baffle are shown. For this analysis, the surfaces of the baffle are considered to be rough, implying that the reflection off a surface has the chance to be redirected at any angle, and will not necessarily leave the surface

at an outgoing angle equal to the incoming one. In the top left plot, a ray passes through the baffle without any interactions, so this is the 0 bounce case. In the top right plot, the 1 bounce case is shown because the ray enters the baffle, bounces a single time, and then passes through the exit aperture. In the lower left, the 2 bounce case is shown, with the ray bouncing off of two surfaces before exiting the baffle. Finally, the 3 bounce case is shown where the baffle has suppressed the ray enough that it is now considered negligible even if it happens to pass through the entrance aperture.

The MATLAB script used to produce these images was then modified to have a selectable input angle. Input angles were selected between -90° and 90° and 100000 rays were then put into the system at each of these angles. The success rate of rays making it through the exit aperture at each angle was then recorded. Figure 4.45 shows a breakdown of the percentage of rays that passed through the baffle system based on the number of bounces as a function of input angle.

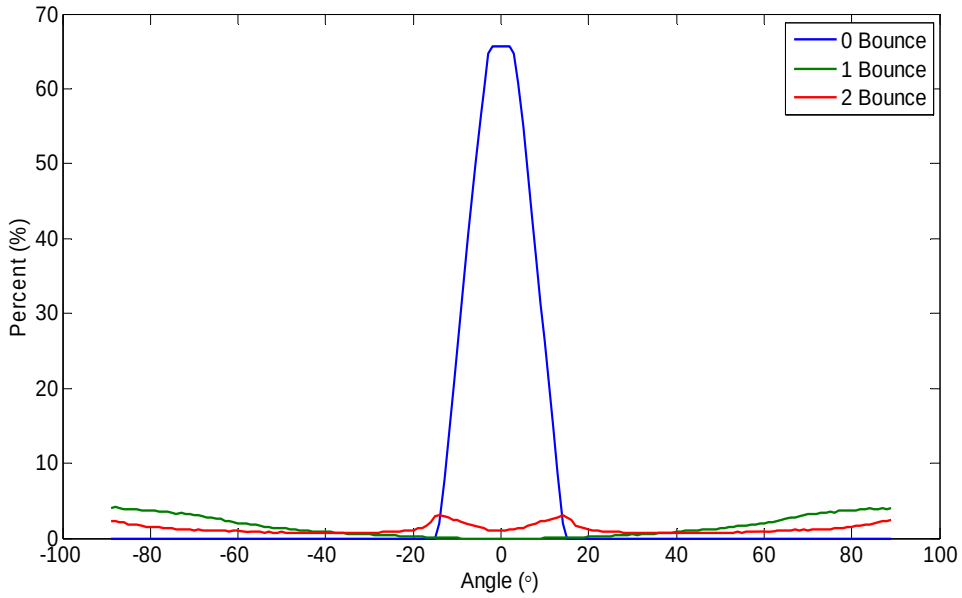

Figure 4.45: Baffle efficiency as function of input angle.

This plot shows that the baffle is very effective at limiting the direct light coming from angles outside the ±3° range, as it was designed. The flat area near the center represents the 6° that is desired to pass through the baffle, with degraded performance further past this point. This specified range has a nice uniform distribution of 0 bounce rays passing through, while the percentage drops as the angle moves further away from 0°. The plot shows that at angles nearing the extreme values, the number of rays passing through the system is steadily growing for the 1 and 2 bounce cases. It is also evident that the range between ±15° allows a noticeable percentage of 2 bounce rays to pass through. It is important to keep in mind however that the power of these rays is diminished to 0.01x and 0.0001x respectively. Also, although these rays pass through the baffle, they are still coming in at inappropriate angles to pass through the slit plate. Imperfections in mirror reflectance are the only way that these rays can pass through the slit, but they are not very significant due to their diminished power.

4.6 Full System

Now that all the components of the system have been described and analyzed, it is time to put them all together into one finalized system. As mentioned, the pointing system was designed primarily with SolidWorks. The starting point for the design was positioning the mirror and mirror mount along the optic axis of OSIRIS-DM at a 22.5°. In order to do this, a custom mounting bracket was designed, and then manufactured by the machinists responsible for producing most of the parts. The mirror and mounting assembly is shown in Figure 4.46.

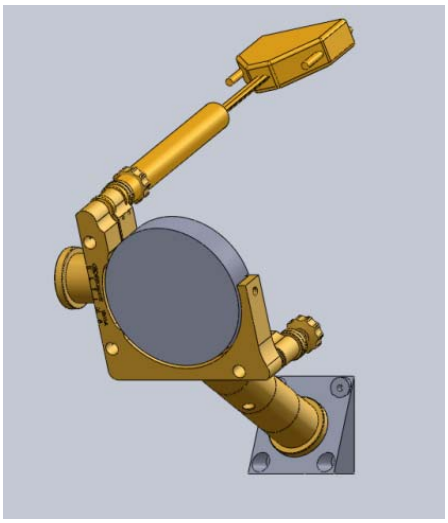

Figure 4.46: Scan mirror with required mounting pieces and actuator.

An enclosure then had to be built around this piece. The enclosure had to interface to the OSIRIS-DM as well as to the baffle. The main enclosure chamber is shown in Figure 4.47.

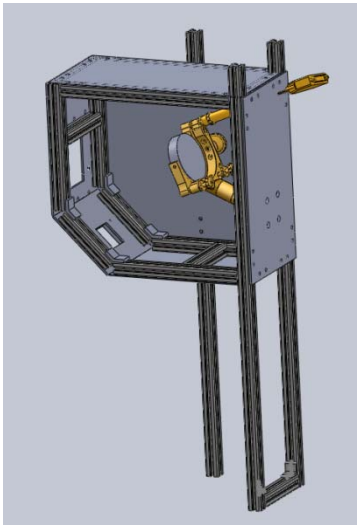

Figure 4.47: Scan mirror in mirror chamber.

In Figure 4.47, one panel has been hidden to show the inside of the mirror chamber. The figure shows two holes in the enclosure. The one nearer to the bottom of the enclosure is the

region that interfaces to the OSIRIS-DM aperture. The higher hole is where the baffle will attach.

The next piece required was a plate to attach the shutter to. The shutter was required to go between the mirror and the OSIRIS-DM aperture. Figure 4.48 shows the shutter is shown attached to the shutter plate designed, and it is also shown installed in the enclosure.

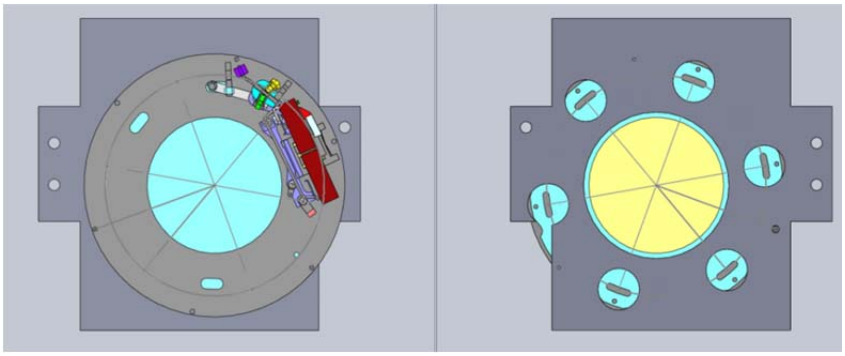

(a)

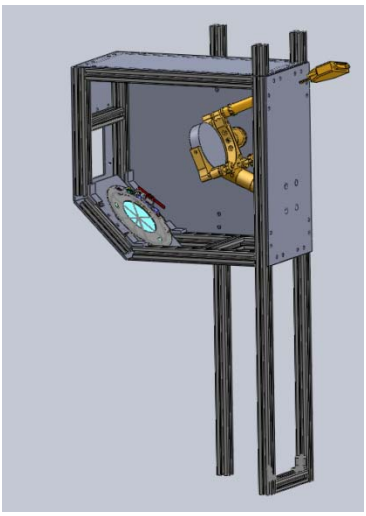

(b)

Figure 4.48: (a) Front and back view of shutter on shutter plate. (b) Shutter installed in enclosure.

Finally, the baffle can be attached to the front end of the pointing system, in Figure 4.49.

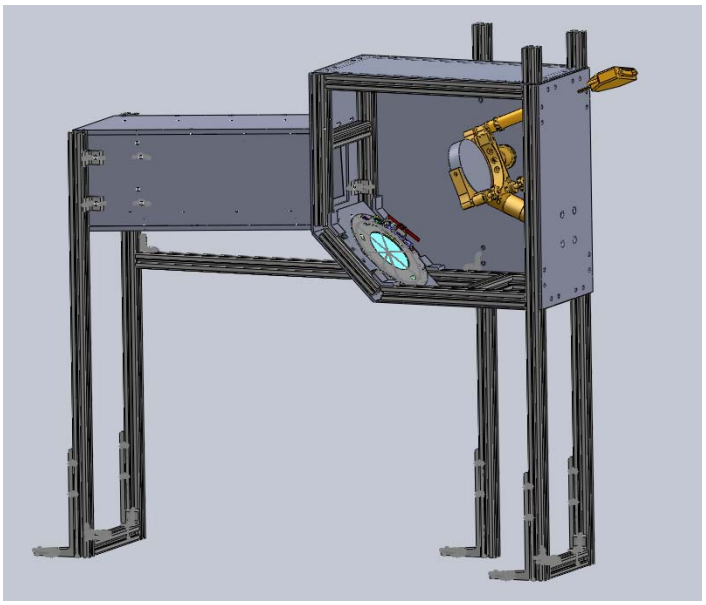

Figure 4.49: CAD drawing of optical enclosure for OSIRIS-DM pointing system.

This was the first group of pieces that was manufactured by the machine shop. Once the pieces were acquired, the system was assembled, as shown in Figure 4.50a.

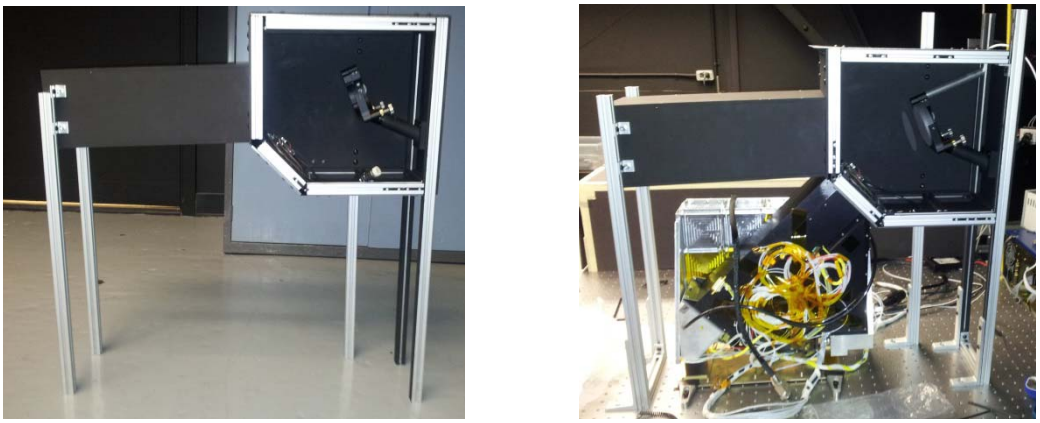

(a) (b)

Figure 4.50: (a) Assembled optical enclosure for OSIRIS-DM pointing system. (b) Assembled optical enclosure for OSIRIS-DM pointing system interfaced to OSIRIS-DM.

At this point, the pointing system could be interfaced to the OSIRIS-DM. This is shown in Figure 4.50b.

Finally, the baseplate and side panels were designed and assembled. The based plate is required to interface to the radiator plate on OSISIRIS-DM, to the legs of the pointing system enclose, and to the CARMEN gondola. The side panels were added for structural rigidity of the system. The final OSIRIS-DM pointing system is shown in Figure 4.51.

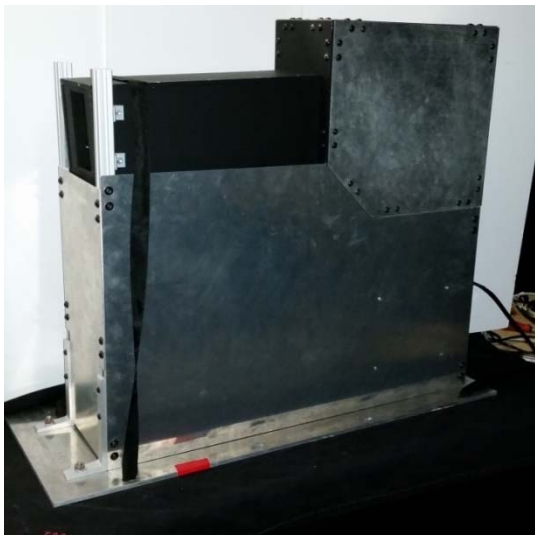

Figure 4.51: Final OSIRIS-DM pointing system.

With a completed optical pointing system designed and built, the system was ready to be launched on a stratospheric balloon. The system was tested in the lab and calibration of the system was performed by *Taylor* (2015). This balloon mission would give not only give feedback on the state of the atmosphere, but also on how well certain aspects of the system perform, which could not be tested in the lab. These aspects include baffle performance and the reliability of the system to image the atmosphere within the required exposure times indicated previously. The system worked effectively for all lab based tests, providing confidence that the system will operate well when viewing the atmospheric limb from the stratosphere.

5. STRATOSPHERIC BALLOON MISSION

The "Strato" Science 2014 Campaign in Timmins, Ontario took place in the late summer of 2014. Balloon launches took place between August 21st and September 19th. In this time, teams made up of CSA and CNES employees and scientific researchers launched 7 balloon missions into the stratosphere. OSIRIS-DM would fly on the final mission of the collaborative campaign.

5.1 Campaign Overview

The campaign for OSIRIS-DM started in the week of August 18th, 2014. Final flight tests were completed in this week at the University of Saskatchewan, and the instrument was packed for travel. On August 22nd, a van was loaded with the instrument and test equipment to be transported over land to Timmins, Ontario.

The Timmins Stratospheric Balloon Base (SBB) is located at the Timmins Victor M. Power Airport which is 11 km North-West of Timmins. The instrument arrived at Timmins SBB on August 25th, 2014 to begin a two week integration phase. Immediately following the integration phase came the flight window, which was set for September 8th to September 18th. Following this date, an additional flight window was scheduled for any gondola payloads that may have missed their original windows.

This integration phase included integration of each of the five scientific payloads onto CARMEN, the gondola to be used for the mission. Four of the five scientific payloads came from Canadian research groups, with two of these originating at the University of Saskatchewan. However, before installing OSIRIS-DM onto CARMEN, a verification test was required to ensure the instrument was not damaged through travel. The instrument was set up in the Payload Integration Bay at Timmins SBB to perform the verification test as shown in Figure 5.1.

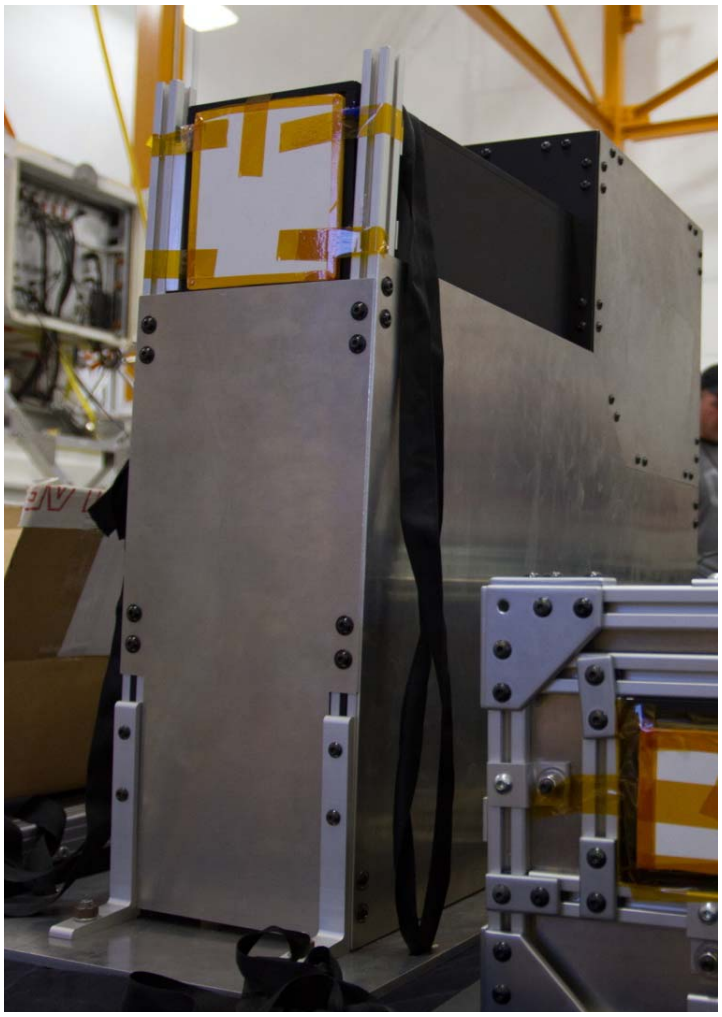

Figure 5.1: OSIRIS-DM upon arrival at Timmins SBB.

OSIRIS-DM passed the validation tests, which suggested that the instrument was not negatively affected by the transport. The tests ran validated the wavelength registration and overall CCD performance of the instrument. Before the instrument could be integrated onto CARMEN, a thermal enclosure was built out of insulating foam to surround the instrument. This structure is shown around the instrument after the instrument was installed on CARMEN in Figure 5.2.

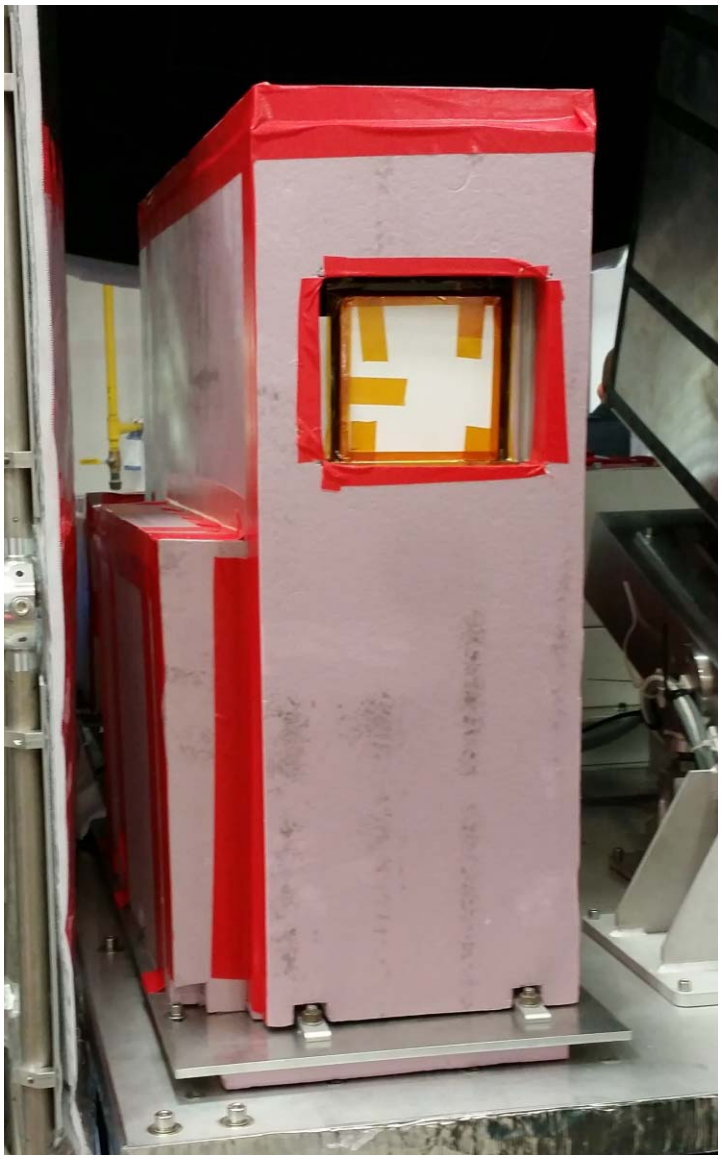

Figure 5.2: OSIRIS-DM beneath thermal insulation.

The next step for flight preparation was to build a thermal blanket to surround the instrument. It was important to cover the instrument where ever direct sunlight may strike it in order to regulate the temperature. The instrument is now shown with this blanket in Figure 5.3.

Figure 5.3: OSIRIS-DM with thermal blanket in preparation for launch.

With the OSIRIS-DM integrated onto CARMEN, integration tests took place that were designed to verify that all systems on CARMEN could operate as expected. Specific tests were run to test power consumption, telemetry rates, individual instrument performance and gondola pointing.

The flight plan was established through collaboration of the research teams associated with the five instruments on the gondola. The gondola would be launched a few hours before sunrise so it would achieve float altitude as the sun was edging over the horizon. The gondola would

then be oriented such that OSIRIS-DM was pointed 90° to the sun for a minimum of four hours. The gondola would then be rotated in 5° increments in order to allow the other instruments to obtain measurements at other solar scattering angles. The gondola would be rotated 40° with respect to its original orientation. At this point, OSIRIS-DM would be turned off for the remainder of the flight, which was dedicated specifically to allow other instruments on CARMEN to make measurements.

Once all the instruments were integrated onto the gondola, full system tests were performed. The Payload Integration Bay at Timmins SBB had a crane located in the center of the bay, which allows the gondola to be hoisted in order to test the pointing system. This is shown in Figure 5.4.

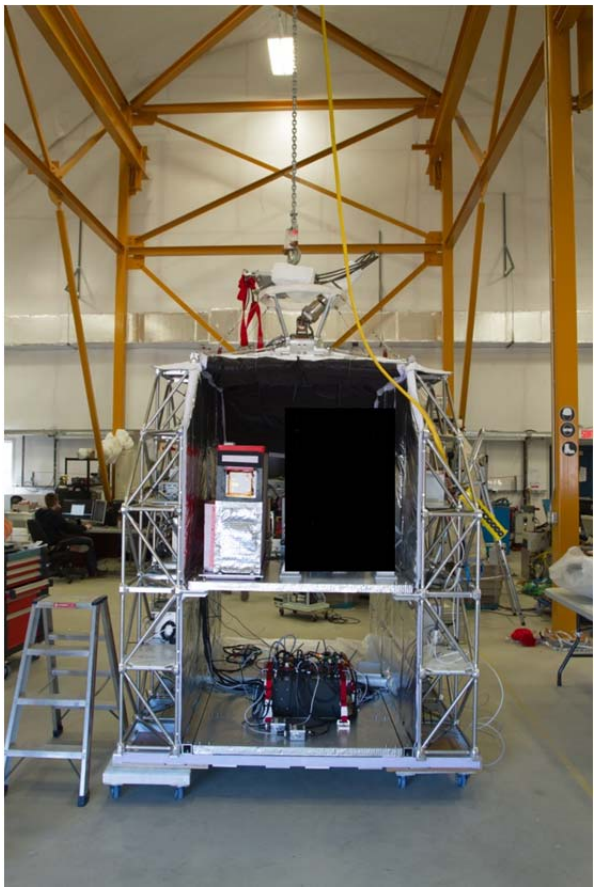

Figure 5.4: Pointing tests performed on CARMEN. Black box is used to mask a confidential instrument.

The integration period for CARMEN was delayed as a result of other flights that were scheduled during the integration period. The first two flights from Timmins SBB had the misfortune of landing in water, so the telemetry systems on board these two flight chains were unusable by subsequent missions. This resulted in delays for testing of the CARMEN gondola. In addition to this, poor weather conditions pushed many of the flights to the limits of their launch windows.

The flight window for CARMEN was quickly disappearing, and weather conditions were not improving. On September 18th, which was the last day of the original scheduled launch window, the gondola was prepared for flight but the conditions were still not favorable. However, all other missions had succeeded, so CARMEN was the priority for the window extension added to the end of the campaign. On September 18th, the U of S team got news that conditions were acceptable for launch on September 19th.

The team returned to Timmins SBB at 21:00 local time on September 18th for a meteorology meeting that said the flight was confirmed, and the launch was set for 01:30 on September 19th. The mission was officially labelled Nimbus 7. The nomenclature chosen for the Strato Science 2014 Campaign was to name the flights Nimbus x, where x indicates the launch number during the campaign. Hence, Nimbus 7 indicates that this was the 7th mission launched during the campaign.

After a final systems test before launch, the gondola was transported to the launch pad, which for Timmins SBB was one of the airport runways. The auxiliary balloons were inflated along with the main 400,000 m^3 balloon. The final mass of CARMEN was 673 kg, which nears the 700 kg maximum for this balloon size. The balloon is shown in Figure 5.5.

Figure 5.5: 400,000 m^3 balloon for Nimbus 7 mission.

Liftoff occurred at 01:35 on September 19th, 2014. The flight plan for the first period was to collect images with the shutter closed in order to perform a dark current analysis after the flight. This analysis was performed by *Taylor* (2015). During this time, the actuator was moved continuously and the shutter operated once a minute to prevent the components from freezing. As sunrise approached, the instrument was switched into science mode to start collecting images with the shutter controlling the exposures. At 05:33 local time, the instrument made its first measurement of light in the atmosphere.

The flight went according to plan. The gondola was stabilized with the instrument looking 90° to the sun for the required time before the azimuth scan was performed. At 13:23, the instrument was turned off in preparation for cut-down. The duration of the Nimbus 7 flight was 16 hours and 13 minutes. The gondola landed 70 km North East of Amos, Quebec. The flight trajectory is shown in Figure 5.6.

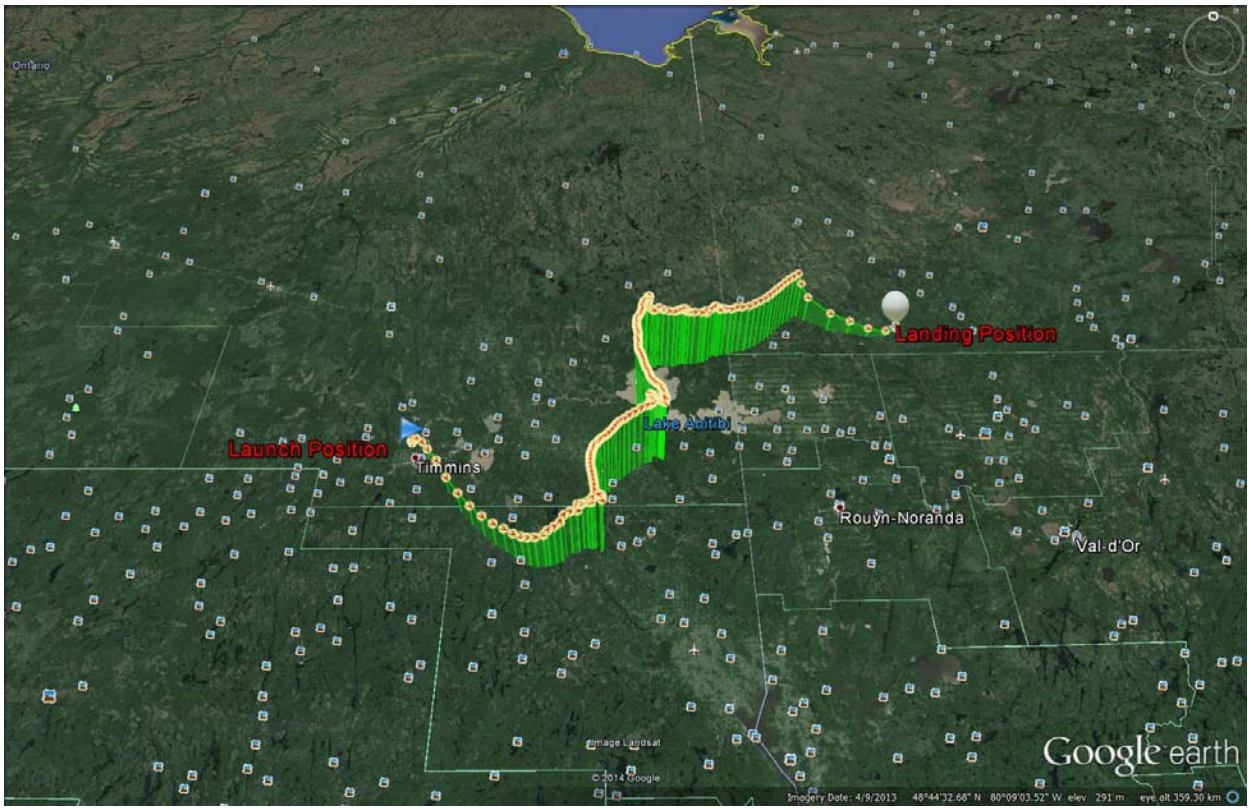

Figure 5.6: Flight trajectory of Nimbus 7.

5.2 Flight Data Analysis

5.2.1 Temperature Log

On board the OSIRIS-DM pointing system were a number of temperature sensors to monitor operating temperatures of many subsystems in the instrument. Of seven sensors installed on various locations within the instrument and the control electronics, two of these are important to look at for this project. These are shown in Figure 5.7.

These two temperature sensors give an estimated temperature distribution throughout the OSIRIS-DM pointing system. The temperature sensor that collected data shown in Figure 5.7a was located in the chamber that houses the scan mirror. This chamber had a direct opening to the atmosphere through the baffle, so it was expected that it would experience the greatest

temperature change. The second temperature record shown is from a sensor located within the region enclosed by the structural support panels. This sensor was placed as close to the CCD of OSIRIS-DM as possible, but this had to be on the outside of the optical chamber. This region was not directly open to the atmosphere, and had the actuator and shutter drivers in the vicinity that were expected to release some heat. For this reason, these temperatures did not drop as low as the first sensor mentioned.

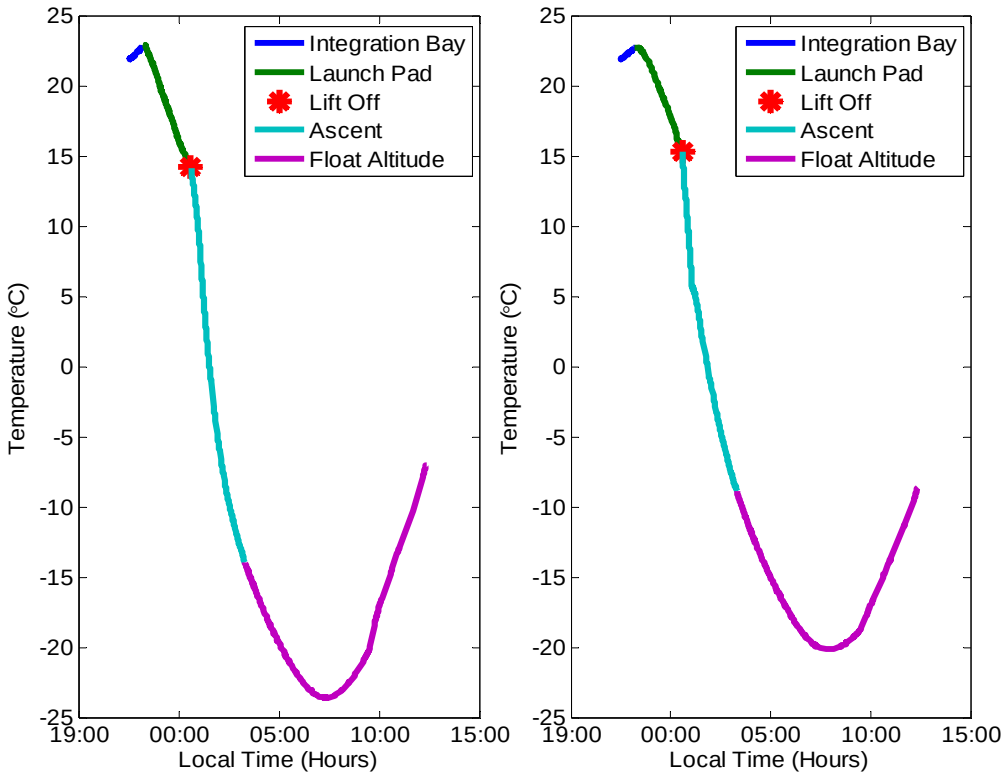

(a) (b)

Figure 5.7: (a) Flight temperature recorded in mirror chamber. (b) Flight temperature recorded in lower pointing system chamber.

In both plots of Figure 5.7, five different time periods are indicated. The first of these represents the time when the instrument was still in the Integration Bay. In this period, the instrument started around 22°C, and slowly increased as heat was generated by the system. The

gondola was then taken outside onto the launch pad where the temperature begins to drop, as indicated in the second region. Both figures show a knee occurring at the point of lift off. The temperatures each drop for the period when the instrument is moving up through the troposphere and into the stratosphere, which is expected because the temperature drops as the altitude is increased for most of this region. The final section shown is when the instrument had reached its float altitude. In this area, the temperature continues to drop for a while, until the sun rises and then begins to finally heat the system.

As shown in this figure, the operating temperatures at float altitude all stayed below -10°C. This was past the threshold of the environmental tests performed on the instrument prior to the flight. Both the actuator and the shutter continued to operate as expected even though these environments had not been tested. The shutter's operation was verified by the fact that it continued to open and close when required by the system. The actuator's operation was verified by the following analysis.

5.2.2 Mirror Position Feedback

As discussed in Chapter 4, a potentiometer was used to verify the positioning of the balloon during the flight. During the flight, the potentiometer reading was downlinked with the images collected. This allowed for real time analysis to verify that the mirror was moving to the correct position for each measurement. As mentioned, the potentiometer does not allow for fine tuning of the measurements, but it does provide confidence that the actuator has not failed.

In Figure 5.8, the relationship developed in Chapter 4 has been plotted to determine the mirror position from a measured potentiometer value. The expected mirror position is plotted against the recorded potentiometer value. There is good correlation between the flight data and the predicted relationship. There is a slight offset, which can be accounted for by the fact that resistance is a function of temperature, and therefore a change in resistance in the voltage divider

would have an effect on the measured value. This figure also shows an oversampling occurring in the range around 3° to 4°. This was the region that the mirror was designed to move through during the ascent in case the mirror stopped operating. If this scenario occurred, the most valuable data would be obtained from the region defined by this look direction and therefore it was desirable to have the mirror operate mostly in this region.

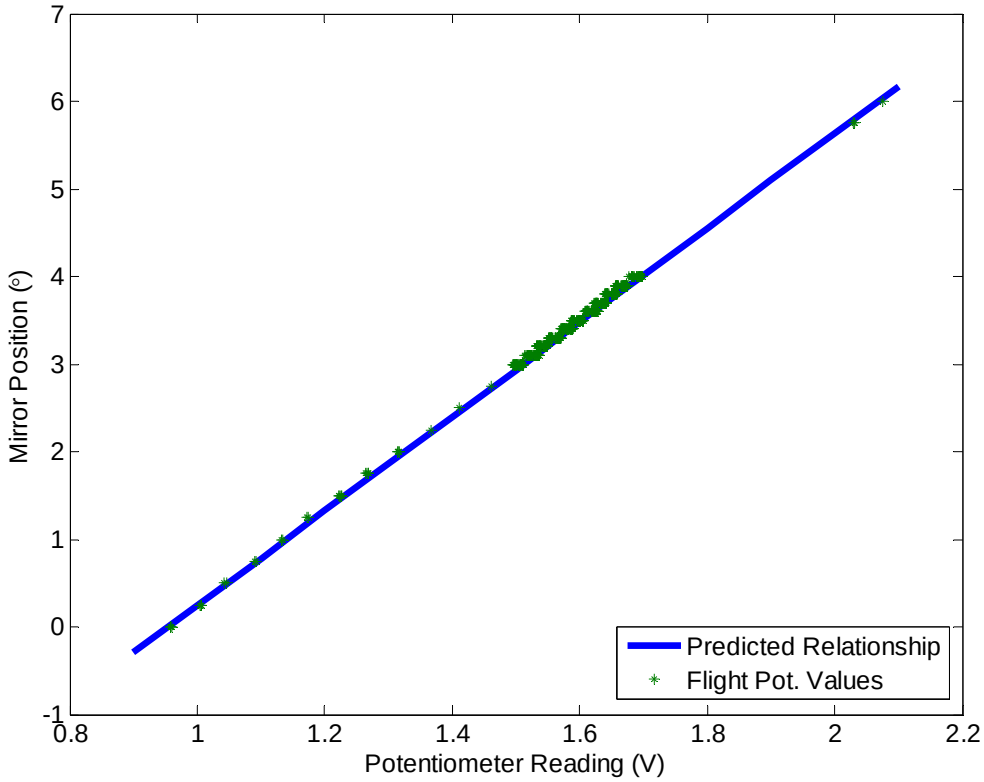

Figure 5.8: Predicted potentiometer relationship to mirror position with downlinked flight potentiometer readings.

5.2.3 Exposure Time Analysis

As explained in Chapter 4, modifications were made to the pointing system to ensure exposure times required for the balloon data were within the acceptable range of exposure times defined by both the shutter and the OSIRIS-DM electronics. Recall that the exposure times ranged from 0.1s to 10 s.

During the flight, zenith scans of the atmosphere were performed with the scan mirror system. During these scans, the exposure times were required to change depending on the tangent altitude in which the system was imaging. The range of exposure times required to obtain well defined data set throughout the mission ranged between 0.5 s and 8.9 s.

5.2.4 Zenith Scan Analysis

As stated in the original goals for the pointing system, it is desired to construct spectral profiles by scanning in the zenith direction through the atmosphere. During the flight, images were measured in half degree or quarter degree steps of the look direction angle to develop scan profiles. The look angle is related to the tangent altitude by the function shown in Figure 5.9. This relationship should be recognized as similar to that presented in Chapter 4, however this relationship takes into account the specific height of the instrument, and its position with respect to the Earth. From this point forward, the data presented will primarily be plotted for specific tangent altitudes, which were determined using this relation.

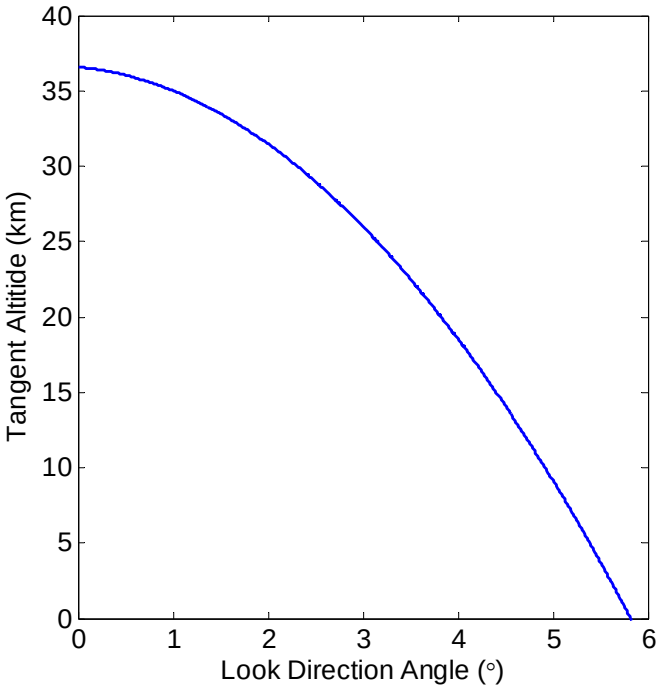

Figure 5.9: Look direction angle and tangent altitude relationship.

An example of one of a spectral profile scan is shown in Figure 5.10.

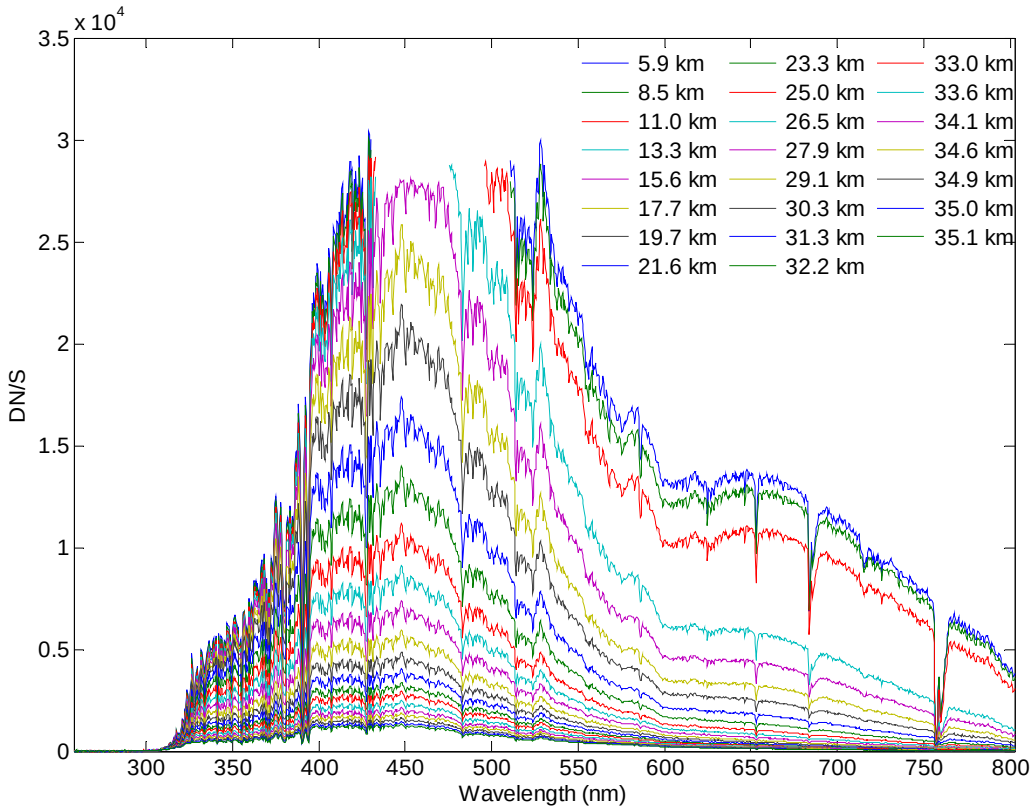

Figure 5.10: Spectra measured through Slit 1 of balloon-borne OSIRIS-DM. Tangent altitudes are indicated in legend.

The Figure 5.10 shows the spectra measured by Slit 1 of OSIRIS-DM on board CARMEN on September 19th, 2014. The data presented is in units of DN/s. This corrects for the fact that the individual spectra were all imaged at varying exposure times. These spectra have also had the DC bias removed, as explained by *Taylor* (2015).

In this figure, different intensity in DN/s corresponds to the tangent altitude at which the spectrum was measured. As stated earlier, lower altitudes in the atmosphere are expected to be brighter than higher altitudes. Although the colors in the legend are repeated, the descending order in the legend corresponds to descending order in measured spectra in the figure. One specific feature to note about this figure is that the spectra measured between 5.9 km to 13.3 km

all have saturated regions in the 430 nm – 510 nm regions. This means that the maximum DN counts were collected on the CCD and therefore the data is unusable because it is no longer representative of the measured light. These points have been excluded from the plot in Figure 5.10. This is important to keep in mind when further analyzing these spectra.

5.2.5 Modeling Radiance Profiles with SASKTRAN

It is of interest to look at discrete wavelengths from the measured spectra to construct radiance profiles and analyze the instrument performance. These profiles can then be modeled with SASKTRAN, where the atmospheric parameters can be altered to obtain better agreement. 30 orders of scatter are used in this simulation.

Figure 5.11 shows both balloon measurements and SASKTRAN simulated data. Although these two sets of data represent different quantities on their own and therefore cannot be directly compared, Figure 5.11 shows normalized radiances. The data sets have been normalized by the respective value at a tangent altitude of 29.1 km. When shown as ratios, these two data sets are directly comparable. Note also that in the 450 nm case, the final 4 measured data points are not included because these were saturated, as mentioned. The data sets shown here are only a small sample of the profiles that can be obtained from this data. Although those shown are typical, not all the wavelength profiles agree as well as the displayed sets, especially for shorter wavelengths in the measured spectrum.

In the SASKTRAN simulation shown in Figure 5.11, the model only predicts the effects of Rayleigh scattering by air molecules. No additional species have been added. It is apparent in the measured data that in the 650 nm and 750 nm profiles that there is a discontinuity located around the 11 km tangent altitude mark. The likely source of this is a high altitude cloud, which greatly enhances the scattering and will not be modeled in this work. This cloud is also the reason that the measurements were saturated when viewing low altitudes.

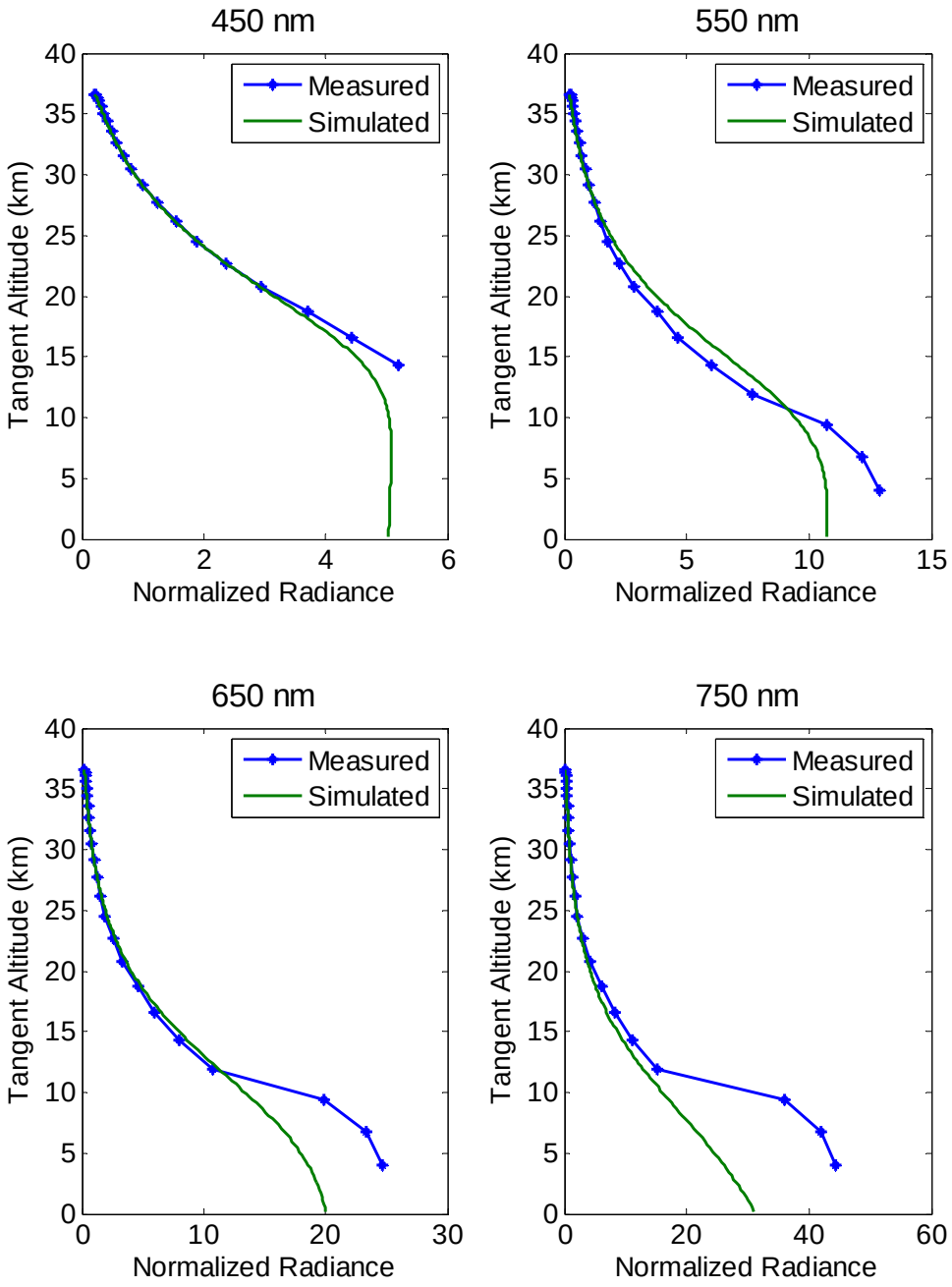

Figure 5.11: Normalized radiance profiles from balloon measurements and SASKTRAN simulations.

Select species can be added to the SASKTRAN model to obtain better agreement between the measured and simulated data. In Figure 5.12, a predefined, climatological, ozone profile is added to the SASKTRAN model.

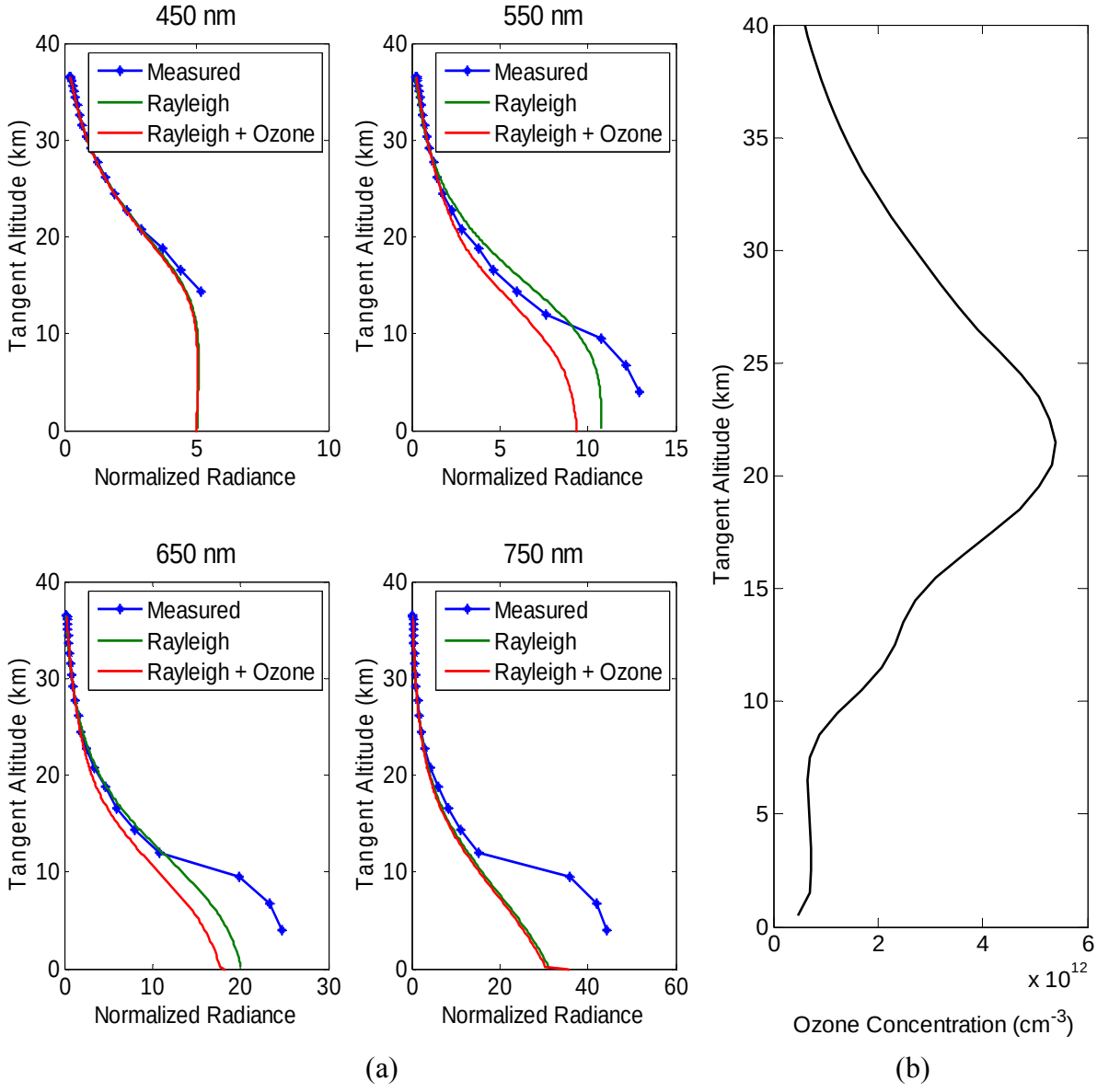

Figure 5.12: (a). Normalized radiance profiles from balloon data and SASKTRAN simulations with ozone added. (b) Ozone profile used in simulation.

Figure 5.12a shows that by adding ozone to the SASKTRAN model, the greatest effects are seen in the 550 nm and 650 nm profiles. The ozone profile added has its largest concentrations in the range of roughly 10 to 35 km, so this region is affected the most in the radiance profiles. The ozone profile added to the simulation is taken from a standard ozone climatology by *McPeters et al*. (1997). This profile is shown in Figure 5.12b. The SASKTRAN predicted radiance shows that there has been absorption of some wavelengths when ozone has been included in the model. This is due to the Chappuis absorption band of ozone, which covers the spectral range of approximately 500-700 nm. For the 550 and 650 nm cases, this has changed the predicted profiles by accounting for ozone absorption. Addition of ozone has not greatly affected the 450 nm or 750 nm profiles as these are outside of the absorption band. Because the profile used in the SASKTRAN simulation is an a priori profile from a standard climatology, it is not expected that the addition of this species will cause the modeled profiles to converge with the measured ones. The goal here is to show that by adding ozone to the model, the predicted profiles at select wavelengths will be altered due to absorption, while others remain relatively unaffected.

Figure 5.13 and Figure 5.14 show the same SASKTRAN modeled data as that from Figure 5.12, but in these cases, the measured data from Slits 2 and 3 are shown respectively. These figures show that the measurements also agree well with the SASKTRAN modelled data.

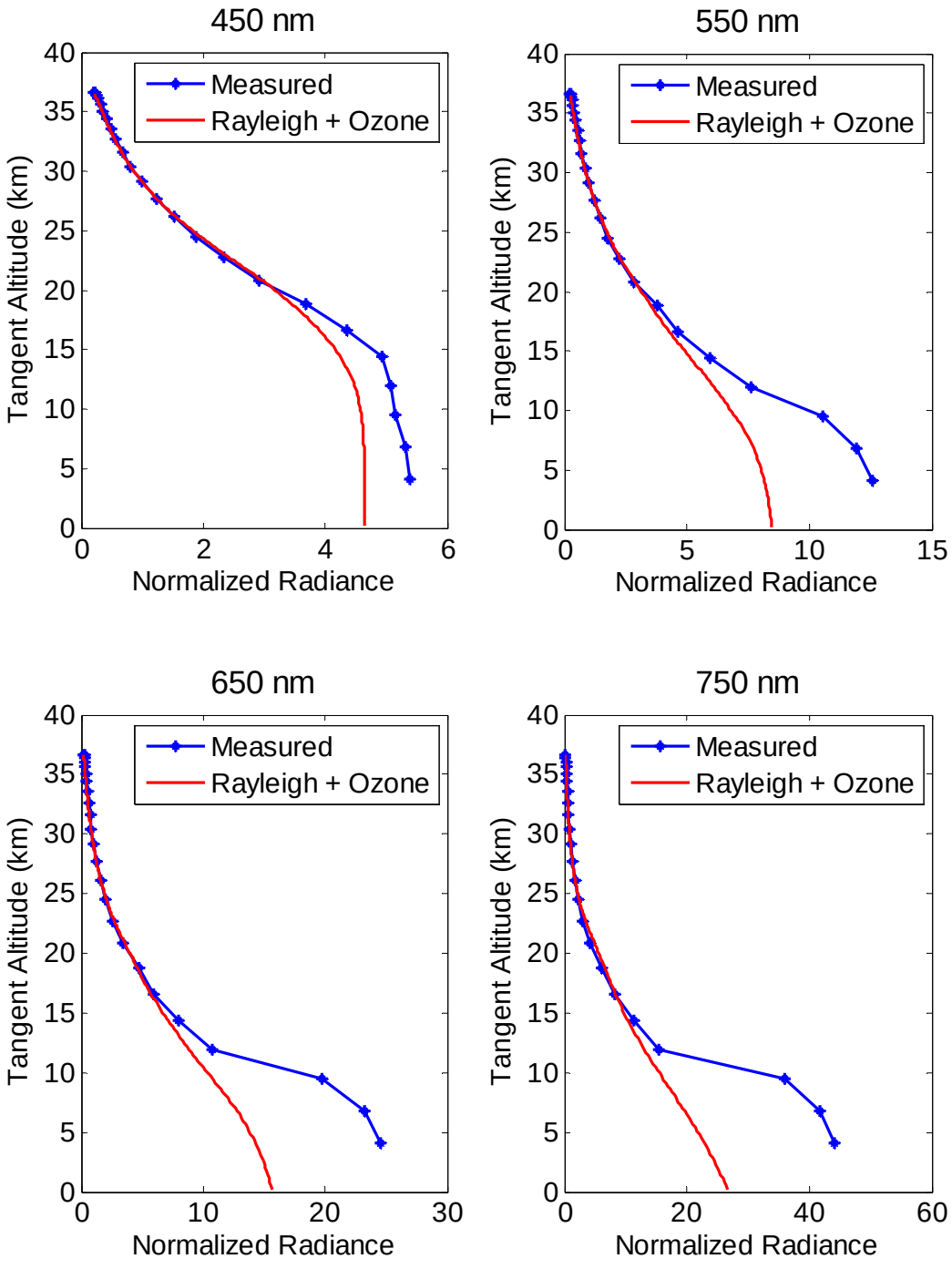

Figure 5.13: Normalized radiance profile from Slit 2 from balloon data and SASKTRAN simulations with ozone added.

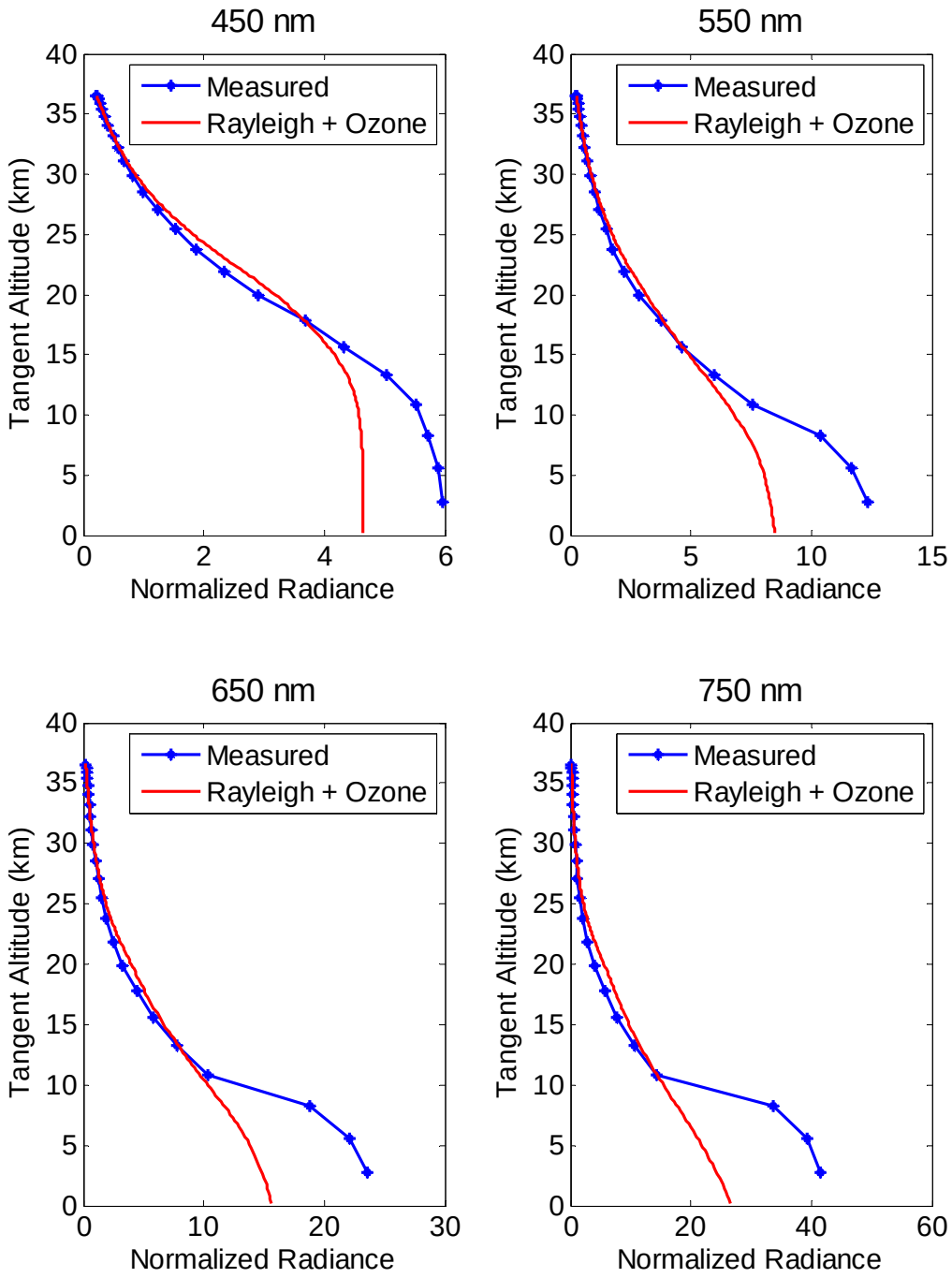

Figure 5.14: Normalized radiance profile from Slit 3 from balloon data and SASKTRAN simulations with ozone added.

5.2.6 Baffle Performance

To examine the baffle performance, external stray light rejection is observed. The baffle performance was already examined in Chapter 4, but now measured data can be observed to verify its performance. A baffle that performs well should limit light coming from angles outside of the field of view of the instrument.

For the limb scattering geometry, the Earth can be considered a radiating source that could potentially provide this stray light. The short wavelength end of the solar spectrum entering the atmosphere is strongly absorbed by the ozone layer, while mid to long wavelengths penetrate through and reach the Earth's surface. The albedo of the Earth then reflects large amounts of this light back into the atmosphere, which is the potential source of out-of-field stray light. The mid-range wavelengths measured by OSIRIS-DM correspond to the highest measured signal in the atmosphere, so effects of stray light tend to be small compared to the relatively larger signals measured in this region. However, on the red end of the spectrum, the optical depth of the atmosphere is lower, specifically at high altitudes, which means that the atmosphere is nearly transparent to the red end of the spectrum. This means that the light is not strongly scattered by atmosphere, resulting in a very low signal measured directly from the atmosphere.

Therefore, to look for stray light from the balloon measurements, long wavelengths should be investigated at the highest tangent altitudes.

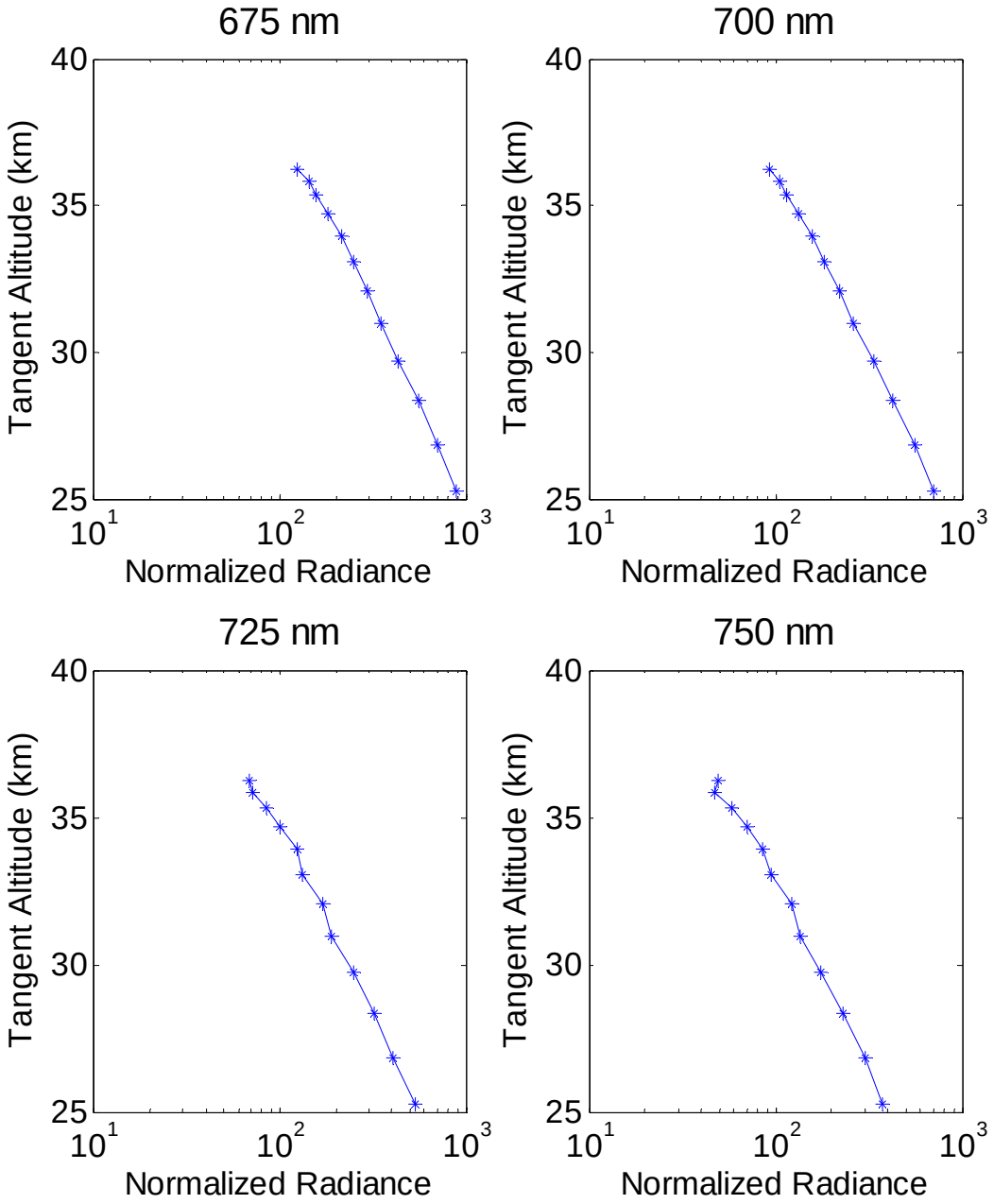

Figure 5.15: Measured radiance profiles at long wavelengths to investigate baffle performance.

Figure 5.15 shows the measured radiances profiles for 675, 700, 725 and 750 nm. The radiances are plotted on a logarithmic scale because limb signal is approximately exponential with altitude. These profiles all show a roughly constant decrease in radiance as the tangent

altitude increases. This indicates that external stray light has not had a very large effect on these measurements. If stray light were playing a large role, the radiance profiles would not show the linear decreasing trend with increasing altitude, but rather a constant or even increasing radiance from light reflecting from the Earth and entering the system at angles outside the field of view. This indicates that the baffle performed well from the balloon-borne environment.

5.2.7 Field Of View Verification

From the balloon data, the fields of view in the θ_x direction can be investigated. As mentioned in Section 3.4.1, in the lab environment, the projected area of the three slits is not widely separated. For this reason, all three fields of view effectively image the same radiance in the lab environment. However, this analysis also showed that from the balloon platform, the three fields of view have the opportunity to look at well separated regions in the atmosphere. In addition to this, the radiance in the atmosphere changes significantly as the look direction from the balloon is altered. The data from a zenith scan on the balloon can therefore be used to verify the angular slit separation as defined by ray tracing in Chapter 3.

Although the fields of view defined in the horizontal direction differ for each of the slits, the three separate columns measured and represented in a zenith scan are all relatively similar when comparing matching tangent altitudes. For this reason, it can be assumed that the three profiles measured should have the same radiance profiles when normalized. Therefore, it is expected that when plotted with the correct angular offset, the normalized profiles measured for specific wavelengths should overlap one another.

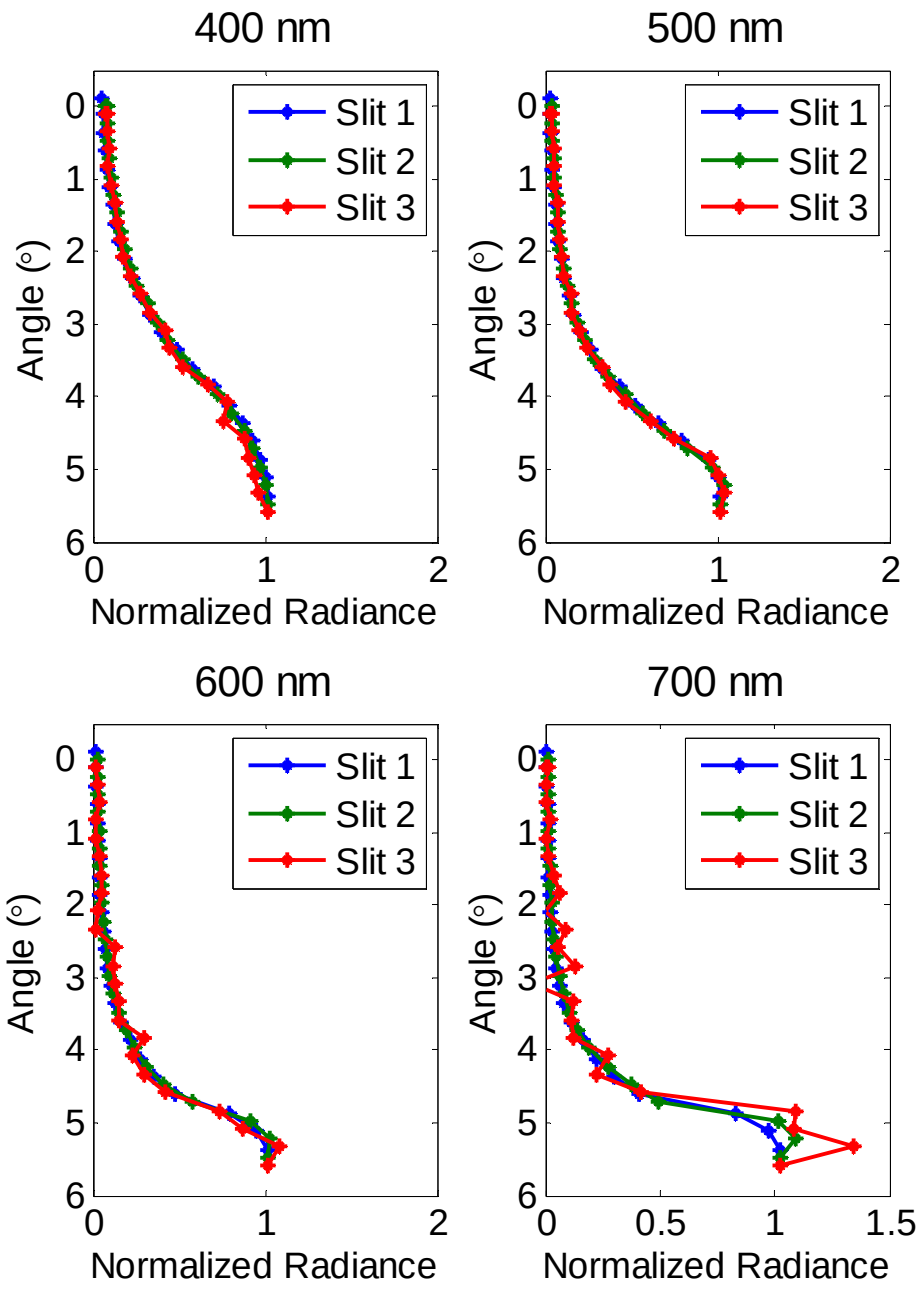

Figure 5.16: Normalized radiance profiles for three slits at select wavelengths with predicted offsets.

In Figure 5.16, four wavelengths have been sampled. The radiance profiles are plotted as functions of mirror angle. The mirror angle is plotted on the y axis because it relates to the tangent altitude, which has conventionally been plotted on this axis thus far. The radiance

profiles have each been normalized by measurement made at the lowest altitude. It is shown that for 600 and 700 nm, the data collected through Slit 3 appears to be subject to large amounts of noise due to low signal levels. The angles associated with each of the three profiles in a single plot differ only by the offsets defined by the fields of view from Chapter 3. As it was, Slit 1 looks at an angle 0.11° higher than Slit 2, and Slit 3 looks at an angle 0.11° lower than Slit 2. From the plots in Figure 5.16, it is shown that the normalized profiles agree quite well when the angles used have these offsets. This verifies the fields of view that were defined in Table 3.4.

5.3 Ozone Retrieval from Balloon-Borne Measurements

A proof of concept ozone retrieval was performed on data collected during the balloon experiment. This retrieval used a simplified version of the technique outlined by *Degenstein et al.* (2009).

5.3.1 Ozone Retrieval Method

Ozone profiles can be retrieved from normalized triplets of radiance measurements made by OSIRIS-DM. These triplets are formed by three wavelengths in and around the Chappuis band. Additionally, pairs of wavelengths can be selected from the Huggins band, but these wavelengths typically work best for higher tangent altitudes than those measured from the stratospheric balloon platform in this experiment.

To perform this ozone retrieval, a Multiplicative Algebraic Reconstruction Technique (MART) will be used, which is a direct implementation of a method described by *Degenstein et al.* (2009). The MART starts with an initial guess atmospheric state parameter, in this case the ozone density, and uses measured and modeled data to iterate to a more accurate prediction of the state parameter using a multiplicative update to the state parameter at each iteration.

The first step in this MART retrieval is to select appropriate wavelengths, defined by *Degenstein et al.* (2009). As mentioned, three wavelengths will be used, all located around the

Chappuis absorption band. Two of these wavelengths will be reference wavelengths, so they will be selected at weakly absorbed wavelengths on both the high and low end of the absorption band. The final wavelength will be selected near the peak of the absorption band. The wavelengths selected for this retrieval are 545, 602 and 678 nm. These are indicated in Figure 5.17.

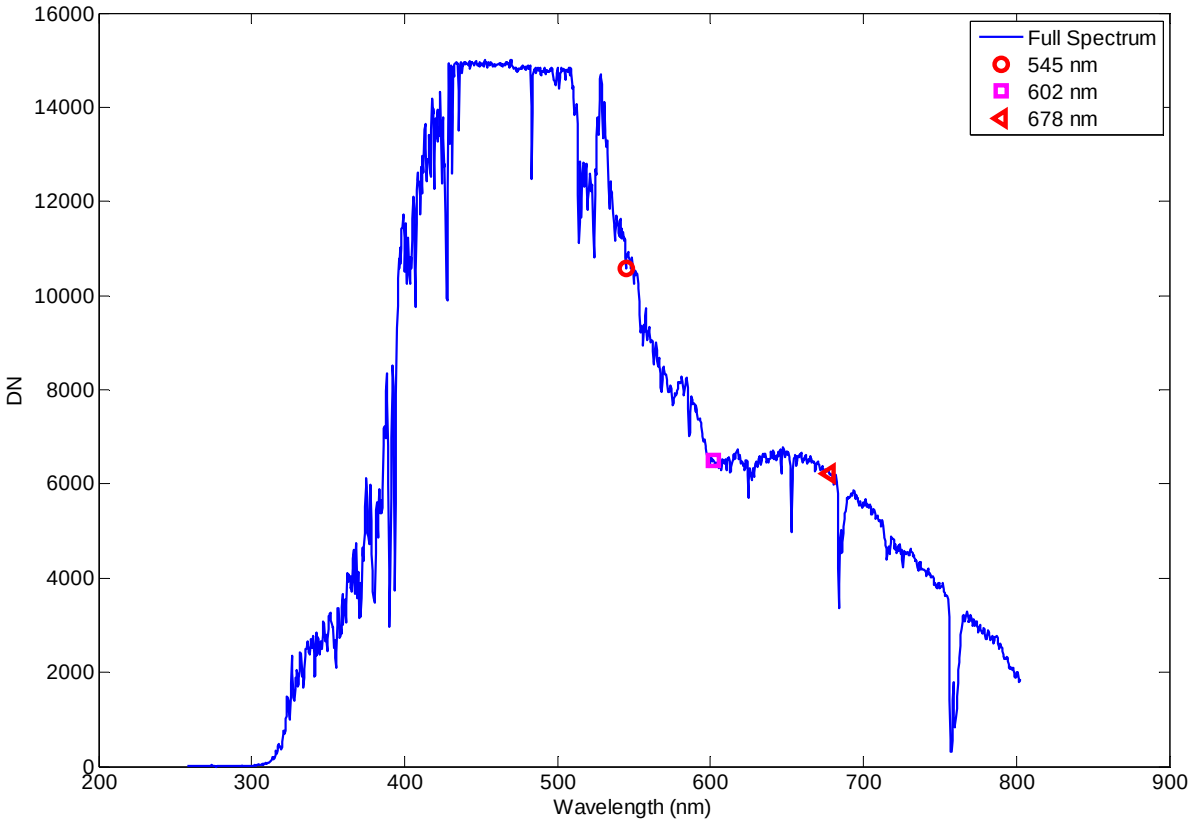

Figure 5.17: Measured spectrum with 3 wavelengths for ozone retrieval indicated.

At these select wavelengths, normalized radiance profiles are calculated. These profiles, *I*, are composed of 5 point radiance averages centered about the selected wavelengths for each tangent altitude measured. The three radiance profiles will be denoted $I(i,\lambda_{ref1})$, $I(i,\lambda_{ref2})$, and $I(i,\lambda_{abs})$. In this case, *i* signifies the tangent altitude at which the radiance profile is measured.

From these radiance profiles, measurement vectors are calculated according to the following equation, called a triplet:

$$y_i^{obs} = ln\left(\frac{\sqrt{I(i,\lambda_{ref1})I(i,\lambda_{ref2})}}{I(i,\lambda_{abs})}\right) \quad \text{(Eq. 5.1)}$$

Similarly, SASKTRAN and the a priori profile to can be used to obtain measurement vectors of modeled data.

$$y_i^{mod} = ln\left(\frac{\sqrt{I(i,\lambda_{ref1})I(i,\lambda_{ref2})}}{I(i,\lambda_{abs})}\right) \quad \text{(Eq. 5.2)}$$

In this case, the same wavelength triplets are used, as well as the same altitudes.

In the work presented by *Degenstein et al.*, a weighting factor W_{ijk} is used to determine the ozone profile at an altitude, *i*, based measurement made at the look directions, *j*, and the wavelength triplet *k*. Therefore, the MART equation used in the process is

$$x_i^{(n+1)} = x_i^{(n)} \sum_k \left(\sum_j \frac{y_{kj}^{obs}}{y_{kj}^{mod}} W_{ijk} \right) \quad \text{(Eq. 5.3)}$$

where $x_i^{(n)}$ represents the ozone density after the nth iteration. In the current analysis, only one wavelength triplet will be used, and the altitudes will be defined by the look directions, so the *j* and *k* terms drop out of the equation and the weighting factor becomes 1. With these parameters, the iterative process can begin, starting with the simplified MART equation

$$x_i^{(n+1)} = x_i^{(n)} \left(\frac{y_i^{obs}}{y_i^{mod}} \right) \quad \text{(Eq. 5.4)}$$

The ratio of the two measurement vectors form the multiplicative factor, defined as

$$\alpha_i = \frac{y_i^{obs}}{y_i^{mod}} \quad \text{(Eq. 5.5)}$$

This ratio can then be used to scale ozone density. Hence, a better estimate of the ozone profile is achieved through each iterative step of the following equation:

$$x_i^{(n+1)} = x_i^{(n)} \alpha_i \quad \text{(Eq. 5.6)}$$

5.3.2 Ozone Retrieval

This ozone retrieval focused on the same zenith scan analyzed in Section 5.2. The analysis that follows investigates the spectrum measured by Slit 1.

In Figure 5.18, the a priori ozone profile shown in black in the right hand image is the starting point for the retrieval. This is defined as a previous profile because it is representative of $x_i^{(n)}$ from Equation 5.4 This profile is added to the SASKTRAN model to calculate a modelled radiance profile. Observed and modelled measurement vector profiles are then calculated from their respective sources and shown in the left panel of Figure 5.18. These are denoted "Balloon Data" indicating it is the measurement vector obtained from measurements, and "Updated Iterated Simulation" indicating that this is the measurement vector obtained from the most recent modeled data set. These two quantities define y_i^{obs} and y_i^{mod} in Equation 5.4. The radiance profiles used to calculate these measurement vectors have been normalized at 30 km. From these measurement vectors, the first multiplicative factor is calculated for each tangent altitude of interest. This is shown in the middle panel. This is defined as the updated iterated factor because it is obtained from the updated iterated simulation measurement vector to obtain an updated ozone profile. Finally, the a priori ozone profile is multiplied by the multiplicative factor to obtain an updated ozone profile as shown in red in the left panel of the image. This updated

profile represents $x_i^{(n+1)}$ from Equation 5.4, and is therefore the updated iterated solution for the ozone profile.

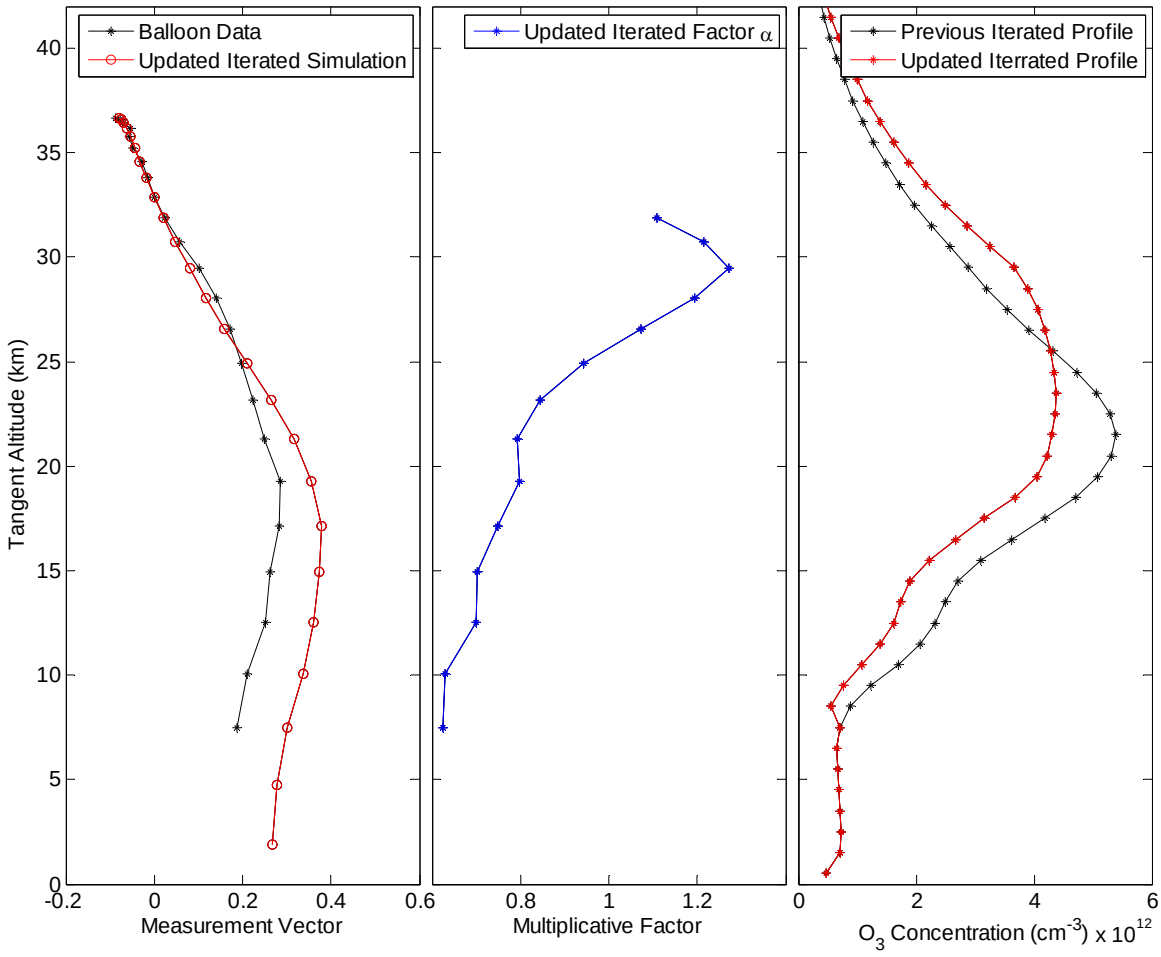

Figure 5.18: Ozone retrieval with 1 iteration of MART with Slit 1 data.

There are two aspects to notice about the updated profile. Firstly, the profile remains the same for tangent altitudes lower than those measured from balloon platform, and secondly, that a constant scaling factor is used for values higher than the normalization tangent altitude. This scaling factor is the multiplicative factor just below normalization tangent altitude. For this reason, the multiplicative factor has not been shown for any measurements made at tangent altitudes higher than the normalization altitude.

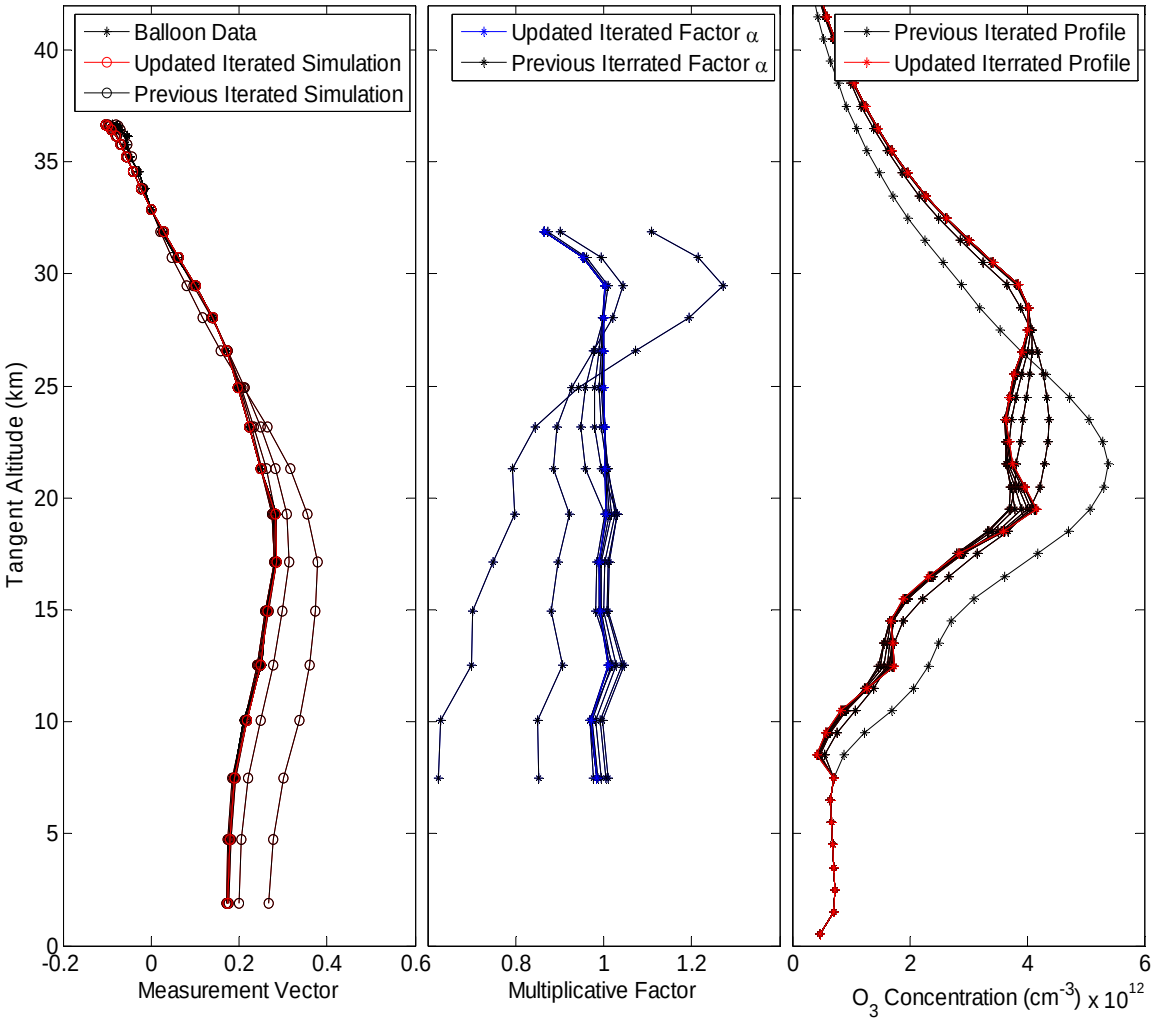

Figure 5.19: Ozone retrieval with 10 iterations of MART with Slit 1 data.

Figure 5.19 shows the first ten iterations of the MART retrieval. The second time through, the newly calculated ozone profile shown in Figure 5.18 is modelled in the SASKTRAN simulation. An updated measurement vector is then calculated for each tangent altitude. This is once again shown in the leftward panel of Figure 5.19. A new multiplicative factor is then calculated for each tangent altitude from the measured and newly modelled measurement vectors, as shown in the center panel. Finally, the ozone profile is updated according to the multiplicative factor, shown in the right panel. This procedure then repeats. After ten iterations, it is shown that the

multiplicative factor has approached 1 for most tangent altitudes. When this occurs, the simulated profile begins to match the measured profile, and thus the MART has provided a calculated ozone profile.

Figure 5.20 shows the results of 10 iterations of the MART process applied to the measurement data from Slit 2. As shown, a slightly noisier profile is obtained from the data collected through Slit 2. The exposure times used to collect this data are the same as those used for the Slit 1 retrieval, and therefore this data set has fewer counts collected on the CCD. This accounts for the increased noise seen in this retrieval. A retrieval was also attempted using the radiance measured through Slit 3, but with even less signal it was unattainable. The precision of this method can be performed to map the error in the measured radiance through to the error in the retrieved profile, as shown by *Bourassa et al.* (2012), but this is beyond the scope of this thesis work.

The ozone profile can now be compared to those retrieved by OSIRIS-FM during coincident overpasses of the satellite. It was not possible to obtain a profile from the flight model that corresponds to the exact location of the balloon, but there is however data pertaining to profiles in the relative vicinity of the balloon scan around the same date and time. The positions of the OSIRIS-FM ozone profiles that will be compared are shown in Figure 5.21, along with the balloon profile location and the city of Timmins for reference.

Table 5.1 shows the distance between the OSIRIS-FM ozone profiles and the OSIRIS-DM profile, as well as the times associated with each scan.

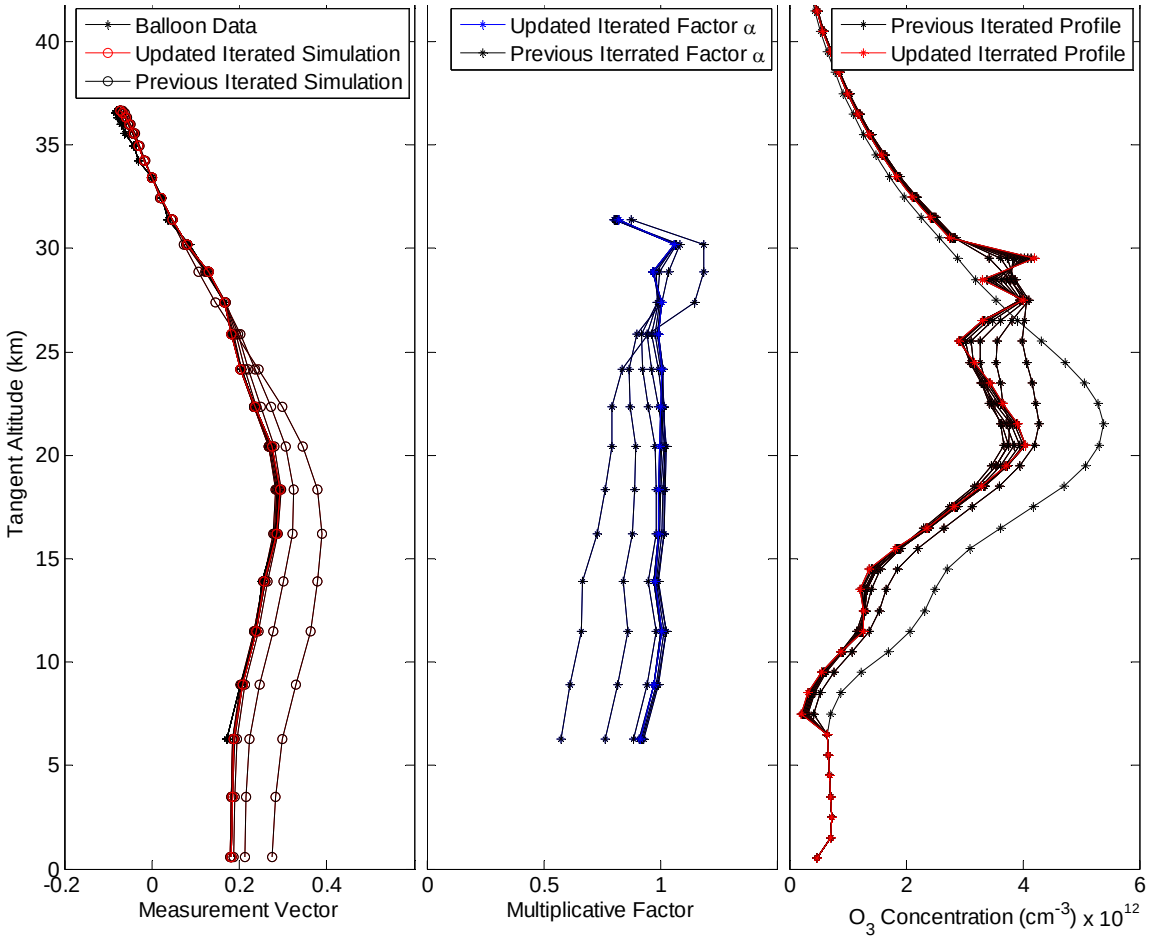

Figure 5.20: Ozone retrieval with 10 iterations of MART with Slit 2 data.

Table 5.1: OSIRIS-FM Scan Information

	Date	Time (UTC)	Distance (km)
OSIRIS-FM Scan 1	September 16, 2014	12:47:46	735
OSIRIS-FM Scan 2	September 16, 2014	23:36:54	855
OSIRIS-FM Scan 3	September 17, 2014	12:46:05	762
OSIRIS-FM Scan 4	September 17, 2014	12:48:03	670
OSIRIS-FM Scan 5	September 17, 2014	12:49:05	964
OSIRIS-DM	September 19, 2014	13:59:27	0

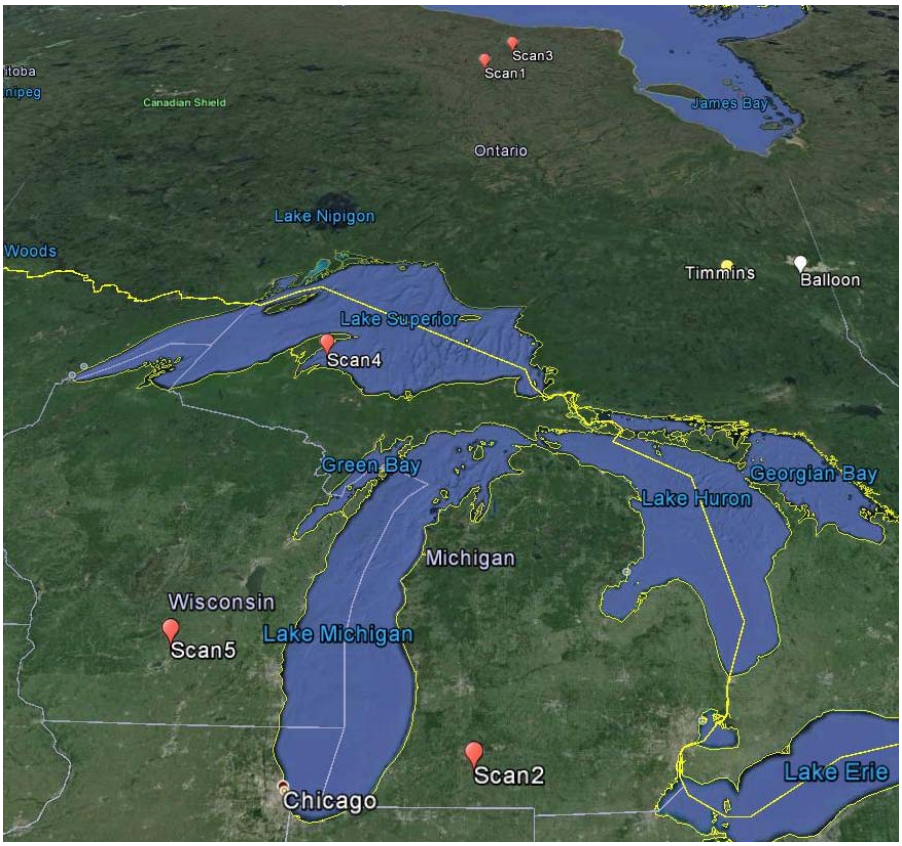

Figure 5.21: Locations of OSIRIS-FM and OSIRIS-DM ozone profiles.

As shown in Figure 5.21 and Table 5.1, the closest profile obtained from OSIRIS-FM is for a location 670 km WSW of the balloon location. These profiles however should give an estimate of the ozone profile in the region to compare the OSIRIS-DM profile to.

Figure 5.22 shows the 5 ozone profiles calculated from data retrieved with OSIRIS-FM. These profiles are shown with the dashed lines. It is important to note that the shape and magnitude of these trends are quite similar, especially when compared to the a priori profile that the retrieval started with. The differences reflect the differences in ozone profiles based on location. In this plot, the ozone profile calculated in this work from data collected by Slit 1 of OSIRIS-DM is also shown. These profiles have a similar overall trend to those calculated by

OSIRIS-FM. Aside from increased concentrations calculated for the Slit 1 profile at high altitudes, the OSIRIS-DM profiles indicate no more disagreement than any of the profiles calculated from OSIRIS-FM measurements. Upon close inspection of Figure 5.22, it should be noted that the OSIRIS-DM profiles has a very similar trend to the profile generated by OSIRIS-FM Scan 4. Overall the ozone profiles agree well enough to conclude that the multi-slit system has acceptable performance for retrieving ozone profiles from the balloon-borne platform.

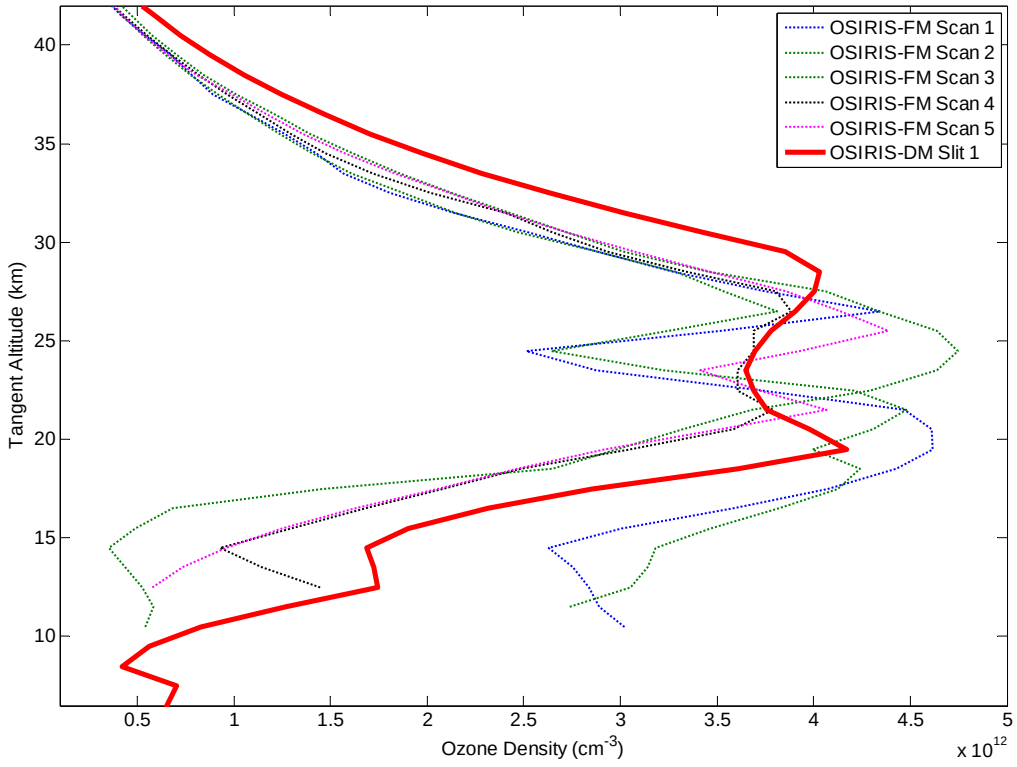

Figure 5.22: Ozone profiles retrieved by OSIRIS-FM and Slit 1 of OSIRIS-DM.

5.3.3 Modelling Radiance Profiles with SASKTRAN Revisited

The radiance profiles constructed in Section 5.2.5 can now be reconstructed using updated species profiles based on retrievals from flight data. Figure 5.23 shows the same discrete wavelengths with newly calculated radiance profiles from SASKTRAN.

In Figure 5.23, the ozone profile added to the simulation was generated from the profiles retrieved from OSIRIS-DM and OSIRIS-FM. The six profiles shown in Figure 5.22 were averaged to generate this profile. Similarly, the aerosol profile used in this model was generated using five profiles calculated by OSIRIS-FM data only. Aerosol has a scattering effect on longer wavelengths, and therefore is shown to make a difference in the 650 and 750 nm profiles (*Bourassa,* 2007). In addition to this, the simulation was also run with the a priori ozone profile that was used to generate Figure 5.12.

The addition of these calculated species profiles improve agreement between the measured and simulated data. For the 550, 650 and 750 nm cases, this figure shows that the SASKTRAN simulation has modelled the measured data very effectively for all altitudes above the cloud that was mentioned previously. For the 450 nm measurements however, the agreement is degraded in the lower regions of the atmosphere. This may be an effect of the cloud that could not be properly modelled. Regardless, the overall agreement of the radiance profiles has significantly increased when including these measured profiles, as expected.

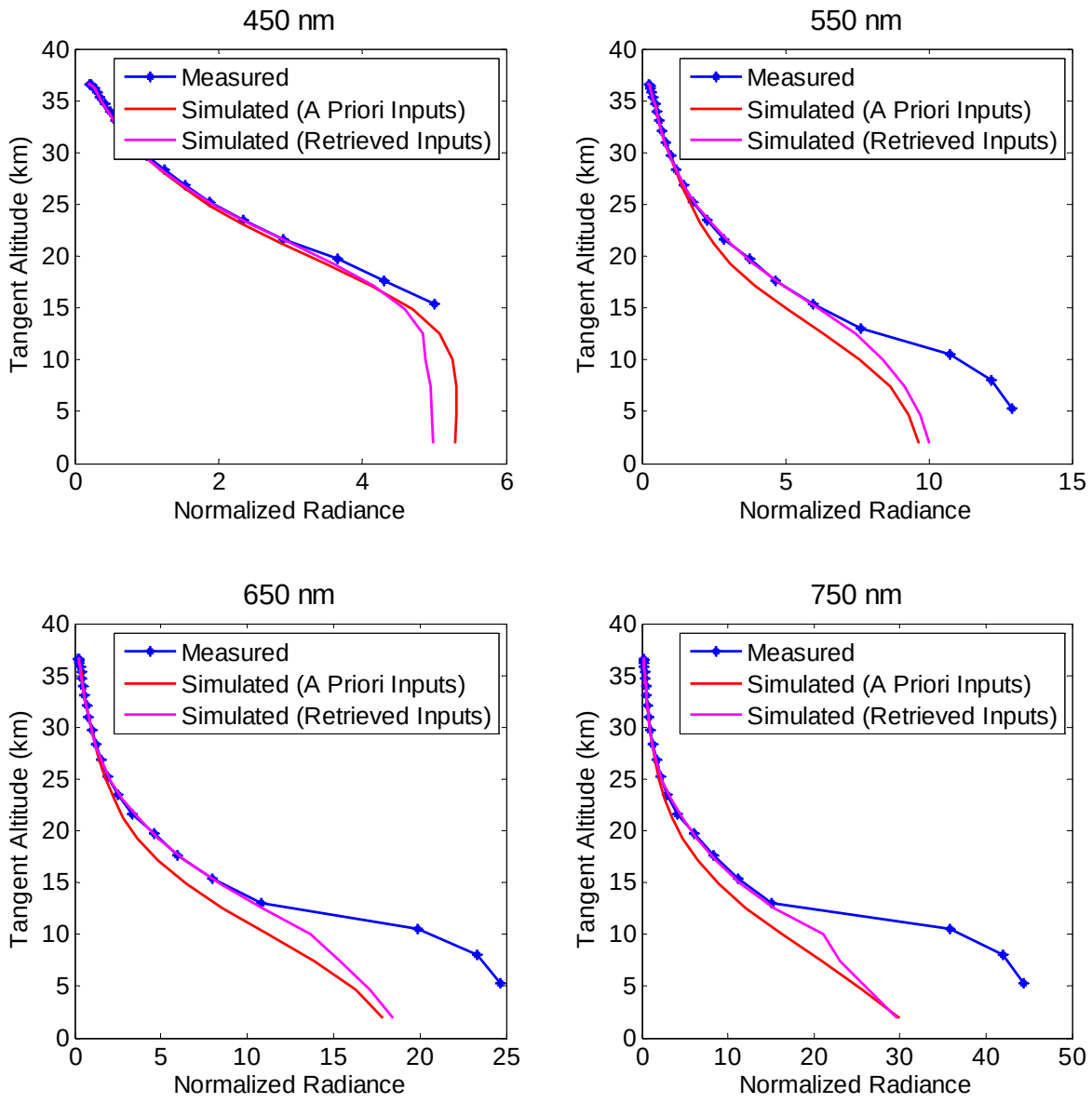

Figure 5.23: Normalized radiance profiles from balloon data and SASKTRAN simulations with measured ozone and stratospheric aerosols profiles added.

Through the stratospheric balloon campaign in Timmins, Ontario, and the post flight data analysis, the pointing system for OSIRIS-DM operated successfully. The system designed to redirect the line of sight for the instrument worked well during the mission. The two major components involved in this, namely the mirror pointing system and the shutter, each performed

without any significant issues during the flight. Post flight analysis also verified that the system worked as designed in the test environment. The atmospheric radiance was properly attenuated by the pointing system, and valid spectral profiles were collected. The data from this mission was also used to produce an ozone profile that was found to display similar characteristics to profiles produced by OSIRIS-FM. Overall, the stratospheric balloon mission for OSIRIS-DM was successful.

6. SUMMARY AND FUTURE WORK

In this project, an existing technology was modified to give new multi-slit imaging capabilities to the OSIRIS-DM instrument. This gave new life to an instrument with a long-standing legacy in the field of Canadian atmospheric studies. The intention of this project was to act as a proof-of-concept prototype for CATS, a new satellite instrument understudy for atmospheric limb profiling. This project took an instrument designed for lab based testing and modified it to operate on board a stratospheric balloon payload.

6.1 Summary of Thesis Work

This project started through funding provided through the Canadian Space Agency. In an initiative called FAST, the agency supplied university programs with funding to build capacity in the space sector for Canadian researchers. The goal of the initiative is to guide students towards careers in the Canadian space sector as well as to develop future space technology. These funds obtained were used to transform the developmental model of the notable Canadian satellite instrument OSIRIS from a single field of view instrument to one with the capabilities to view multiple fields of view. This new multi-slit instrument serves as a prototype for the CATS instrument.

In addition to funding the instrument development, the FAST grant from the CSA also came with an additional research opportunity in the field of high altitude ballooning. Through an agreement with the city of Timmins, Ontario and CNES, the CSA built a new ballooning facility in Northern Ontario. The multi-slit OSIRIS-DM project was selected to fly on one of these crafts as part of the “Strato” Science 2014 Campaign. This would allow for the new technology to be tested in the limb viewing geometry that would be required for a satellite version of CATS. The campaign required that the instrument be ready for launch in the late summer of 2014.

The transformation of the instrument was performed through collaboration with engineers at COM DEV International Ltd. COM DEV has a long standing relationship with the OSIRIS project, seeing as many members of the original design team work for the company. With this vested interest in the project, a team of COM DEV engineers from their Kanata branch assisted in the development of this new technology.

The major modification that was required was the design and replacement of the slit plate that is used to limit the light that passes through the instrument, and hence defines its field of view. The original slit plate housed within the OSIRIS-DM had a single rectangular slit, which defined a field of view that would image to 1 km by 15 km in the atmosphere when mounted on a satellite-based platform. The new slit plate would have multiple rectangular slits, which would collect light from varying tangent altitudes when imaging from an airborne environment. The multi-slit system would collect much more data simultaneously, which would improve the spatial resolution and therefore offer greater coverage throughout the atmosphere. After a few iterations between the teams at the University of Saskatchewan and COM DEV, a finalized slit plate was produced with four of these slits. The OSIRIS-DM instrument was then transported to Kanata to install the new slit plate into the instrument. Upon installation it was found that due to an unexpected obstruction in the optical chain, the slit plate had to be modified to only contain three slits. The unusable slit on the slit plate was masked, and then the plate was successfully installed in OSIRIS-DM.

Upon returning the multi-slit OSIRIS-DM to the U of S, preparations were made to launch the instrument on a gondola that would be connected to a stratospheric balloon. To make the most beneficial measurements from this environment, the instrument would be required to collect light from varying tangent altitudes in the atmosphere. The balloon mission would be a shared

experience for five instruments mounted to the same gondola, which meant that the orientation of the gondola had to be favorable for all the instruments on board. This meant that an additional pointing system would be required to adjust the line of sight of the multi-slit system while imaging in the atmosphere.

The system designed features a single mirror and a motorized actuator to adjust its position. The mirror is located directly in front of the aperture to the OSIRIS-DM system, and reflects light roughly 45° to enter the system. The pointing system also features a shutter system to reduce image smearing as a result of the new multiple fields of view that are imaged on the CCD. In addition to this, a light attenuation scheme was designed in the system to reduce the intensity of light entering the system. This aspect was required to ensure that the system could properly handle the varying intensity of light it would measure form the stratosphere while remaining in the exposure timing tolerances set forth by the shutter and the OSIRIS-DM system. The final system required was a front end baffling system to reduce the effects of external stray light on the system.

After full system tests, the instrument was shipped to Timmins in preparation for launch. The instrument spent a month at the Timmins Stratospheric Balloon Base where it was integrated onto CARMEN, the gondola that would hoist the instrument into the stratosphere. In the early hours of September 19th, 2014, the instrument began its ascent to 36 km to make measurements in the limb scattering geometry. All subsystems in the pointing system operated as expected. During the flight, there were no issues with the mirror positioning system or the shutter system. The images downlinked from the balloon also indicated that the light attenuation system was operating within the required tolerances.

Upon retrieving the instrument following its descent, the full data record collected during the flight was retrieved from the on board storage drive. The data was then analyzed to verify the operation of the system during the flight. The mirror system was first analyzed to verify that the pointing requirements were met. Although the feedback system for this aspect was crude, it offered sufficient evidence that the mirror was positioned in the correct orientation for each imaging process. Once the mirror positions were verified, the data collected in a zenith scan could be analyzed. The spectra of light measured through the three slits agreed with the predicted trend. The spectra got progressively brighter as the tangent altitude was lowered, just as expected. Individual radiance profiles were then validated against those predicted by SASKTRAN for select wavelengths. The general trends of these radiance profiles agreed with the predicted profiles.

The final item of interest to demonstrate with the collected data was to perform an ozone retrieval. The inversion technique known as MART was performed, which utilizes flight data and SASKTRAN to provided successively closer estimates of the ozone profile in the atmosphere the measurements were taken. The retrieved profile was then compared to profiles obtained from data collected by the OSIRIS-FM in regions nearby the location of the balloon mission. The closest profile available for comparison was collection for a region nearly 700 km away and two days before the OSIRIS-DM data, but the two ozone profiles still displayed similar characteristics. The data was therefore verified within an error margin defined by the agreement level of multiple OSIRIS-FM profiles for the surrounding region of the atmosphere.

The major successes of the project include the following:

- Multi-slit system effectively imaged separated sections of the atmosphere in the limb scattering viewing geometry.

- Mirror pointing system provided atmospheric profile scans throughout balloon mission.
- Radiance profiles measured from balloon match profiles predicted by SASKTRAN for each slit.
- The baffle removed external stray light from system.
- Multi-slit plate increased internal stray light with respect to original slit plate, but kept it within one order of magnitude.

6.2 Future Work

As explained in Chapter 4, the design of a dual axis scanning system was investigated but abandoned due to time constraints during the project. This system is open for reanalysis if the instrument were to fly on another stratospheric balloon. Additionally, further lab based measurements could be performed to better verify the fields of view for the installed slit plate. Such tests would require a collimated light source to be directed into the instrument with precise control over the angle at which it is entering. This would refine the tangent altitude calculation used from the balloon platform.

Overall, this project was a success. The project met its goal to revitalize the OSIRIS-DM as a proof-of-concept prototype for CATS, the potential successor to the OSIRIS legacy. This means that the goals of the FAST initiative were also met, both in training in the space sector as well as development of a new technology. The installation of the new slit plate, although slightly modified from its original design, operated well in the system and met the expectations set forth by ray tracing simulations. The pointing system built for the instrument met the requirements set forth in order to control the line of sight of the instrument on board the stratospheric balloon. In addition to this, it succeeded in reducing stray light, while attenuating the signal to levels

required by the OSIRIS-DM system. The balloon mission in itself was also a success and a testament to the feasibility of this new technology one day operating on a satellite platform.

LIST OF REFERENCES

Bass, M., Mahajan, V. N., Van Stryland, E. W. Li, G., Macdonal, C. A., DeCusatis, C. (2010), *Handbook of optics (Volume 1)*, New York: McGraw Hill.

Bourassa, A., D. Degenstein, R. Gattinger, and E. Llewellyn (2007), Stratospheric aerosol retrieval with Optical Spectrograph and InfraRed Imaging System limb scatter measurements, *J. Geophys. Res*, 112(D10), doi:10.1029/2006JD008079.

Bourassa A. (2007), Stratospheric aerosol retrieval from OSIRIS limb scattered sunlight spectra, Ph.D. thesis, University of Saskatchewan.

Bourassa, A., D. Degenstein, and E. Llewellyn (2008), SASKTRAN: A spherical geometry radiative transfer code for efficient estimation of limb scattered sunlight, *J. Quant. Spectr. & Rad. Trans*., 109, 52–73, doi:10.1016/j.jqsrt.2007.07.007.

Bourassa, A. E., C. A. McLinden, A. F. Bathgate, B. J. Elash and D. A. Degenstein (2012), Precision estimate for Odin-OSIRIS limb scatter retrievals, *J. Geophys Res*, 117(D4), doi:10.1029/2011JD016976.

Canadian Space Agency News Release (2012), Canada-France collaborate on balloon launches. Retrieved from Canadian Space Agency website: http://www.asc-csa.gc.ca/eng/media/news_releases/2012/0615.asp

Canadian Space Agency Announcement of Opportunity, (2013a), Flights for the advancement of science and technology (FAST 2013). Retrieved from Canadian Space Agency website: http://www.asc-csa.gc.ca/eng/ao/2013-fast.asp

Canadian Space Agency News Release (2013b), Space agencies launch first stratospheric balloon from Timmins. Retrieved from Canadian Space Agency website: http://www.asc-csa.gc.ca/eng/media/news_releases/2013/0912.asp

Centre national d'études spatiales (n.d.), La nacelle CARMEN. Retrieved November 17th, 2014. Retrieved from Centre national d'études spatiales website: http://www.cnes.fr/web/CNES-fr/10627-la-nacelle-carmen.php

Degenstein, D., A. Bourassa, C. Roth, and E. Llewellyn (2009), Limb scatter ozone retrieval from 10 to 60 km using a Multiplicative Algebraic Reconstruction Technique, *Atmos. Chem. Phys*, 9, 6521–6529, doi:10.5194/acp-9-6521-2009.

Degenstein, D (2013), Odin-OSIRIS: A summary of the past twelve years, *Proc. 7th annual atmospheric limb conference.*

Fischer, R. E., B. Tadic-Galeb, P. R. Yoder, R. and Galeb, (2000), *Optical system design,* New York: McGraw Hill.

Howell, S. B. (2006), *Handbook of CCD astronomy (Vol 5),* Cambridge University Press.

Llewellyn, E., N. Lloyd, D. Degenstein, R. Gattinger, S. Petelina, A. Bourassa, J. Wiensz, E. Ivanov, I. McDade, B. Solheim, J. C. McConnell, C. S. Haley, C. von Savigny, C. E. Sioris, C. A. McLinden, E. Griffioen, J. Kaminski, W. F. Evans, E. Puckrin, K. Strong, V. Wehrle, R. H. Hum, D. J. Kendall, J. Matsushita, D. P. Murtagh, S. Brohede, J. Stegman, G. Witt, G. Barnes, W. F. Payne, L. Pich´e, K. Smith, G. Warshaw, D. L. Deslauniers, P. Marchand, E. H. Richardson, R. A. King, I. Wevers, W. McCreath, E. Kyr¨ol¨a, L. Oikarinen, G. W. Leppelmeier, H. Auvinen, G. M´egie, A. Hauchecorne, F. Lef˙evre, J. de La N¨oe, P. Ricaud, U. Frisk, F. Sjoberg, F. von Sch´eele, and L. Nordh (2004), The OSIRIS instrument on the Odin spacecraft, *Can. J. Phys*, 82, 411–422, doi:10.1139/p04-005.

McPeters, R. D., G. J. Labow,, B. J. and Johnson. (1997), A satellite-derived ozone climatology for balloonsonde estimation of total column ozone, *J. Geophys. Res*, 102(D7), 8875-8885, doi:10.1029/96JD02977.

McPeters, R. D., P. K. Bhartia, A. J. Krueger, J. R. Herman, C. G. Wellemeyer, C. J. Seftor, G. Jaross, O. Torres, L. Moy, G. Labow, W. Byerly, S. L. Taylor, T. Swissler, R.P. Cebula, (1998), Earth probe total ozone mapping spectrometer (TOMS): data products user's guide. Documentation. National Aeronautics and Space Administration.

Murtagh, D., U. Frisk, F. Merino, M. Ridal, A. Jonsson, J. Stegman, G. Witt, P. Eriksson, C. Jim´enez, G. Megie, J. de La No¨e, P. Ricaud, P. Baron, J. R. Pardo, A. Hauchcorne, E. J. Llewellyn, D. A. Degenstein, R. L. Gattinger, N. D. Lloyd, W. F. J. Evans, I. C. McDade, C. S. Haley, C. Sioris, C. von Savigny, B. H. Solheim, J. C. McConnell, K. Strong, E. H. Richardson, G. W. Leppelmeier, E. Kyr¨ol¨a, H. Auvinen, and L. Oikarinen (2002), Review: An overview of the Odin atmospheric mission, *Can. J. Phys*., 80, 309–319, doi:10.1139/p01-157.

Riebeek, H. (2010) Global Warming. Retrieved from National Aeronautics and Space Administration website: http://earthobservatory.nasa.gov/Features/GlobalWarming/
Roth, C. Z. (2007) Atmospheric ozone retrieval using radiance measruements from Chappuis and Hartley-Huggins absorption bands, M.Sc. Thesis, University of Saskatchewan.

Stoicesu, M. B. (2006) Development and characterization of the OSIRIS USASK observatory, M. Sc. Thesis, University of Saskatchewan.

Taylor, B. J. A. (2015) The upgrade, calibration and evaluation of the multi-slit OSIRIS-DM for stratospheric balloon flight, M.Sc. Thesis, University of Saskatchewan.

Thomason, L. W., L. R. Poole, and T. Deshler (1997), A global climatology of stratospheric aerosol surface area density deduced from Stratospheric Aerosol gas Experiment II measurements, *J. Geophys. Res*, 102(D7), 8967-8976, doi: 10.1029/96JD02962.

Warshaw, G. D., D.-L. Desaulniers, and D. Degenstein, (1996), Optical design and performance of the Odin UV/visible spectrograph and infrared imager instrument, *Proc. 10th annual AIAA/USU conference on small satellites.*

Wilcox, B. A. (2002) Ground validation of Osiris scattered sunlight measurements, M. Sc. Thesis, University of Saskatchewan.